NASA-CR-54240

Summary Report

THE PLASMA SEPARATOR ION ENGINE

By

B. A. FREE, W. N. NEIMAN, G. P. KERR, JR.

FACILITY FORM 602

N65-19502 (ACCESSION NUMBER)

373 (PAGES)

CR-54240 (NASA CR OR TMX OR AD NUMBER)

1 (THRU)

(CODE)

18 (CATEGORY)

prepared for

NATIONAL AERONAUTICS AND SPACE ADMINISTRATION

CONTRACT NAS 3-3561

SPACE POWER AND PROPULSION SECTION

MISSILE AND SPACE DIVISION

GENERAL ELECTRIC

CINCINNATI, OHIO 45215

GPO PRICE $ _____

(CSFTI)

~~OTS~~ PRICE(S) $ _____

Hard copy (HC) $1.00

Microfiche (MF) $2.00

NOTICE

This report was prepared as an account of Government sponsored work. Neither the United States, nor the National Aeronautics and Space Administration (NASA), nor any person acting on behalf of NASA:

A.) Makes any warranty or representation, expressed or implied, with respect to the accuracy, completeness, or usefulness of the information contained in this report, or that the use of any information, apparatus, method, or process disclosed in this report may not infringe privately owned rights; or

B.) Assumes any liabilities with respect to the use of, or for damages resulting from the use of any information, apparatus, method or process disclosed in this report.

As used above, "person acting on behalf of NASA" includes any employee or contractor of NASA, or employee of such contractor, to the extent that such employee or contractor of NASA, or employee of such contractor prepares, disseminates, or provides access to, any information pursuant to his employment or contract with NASA, or his employment with such contractor.

Requests for copies of this report should be referred to:

National Aeronautics and Space Administration
Office of Scientific and Technical Information
Washington 25, D.C.
Attention: AFSS-A

CASE FILE COPY

NASA-CR-54240

SUMMARY REPORT

THE PLASMA SEPARATOR ION ENGINE
Period April 1, 1963 - June 30, 1964

prepared by

B.A. Free, W.N. Neiman, G.P. Kerr, Jr.

approved by

Dr. M.L. Bromberg
Manager, Electrical Space Propulsion Projects

prepared for

NATIONAL AERONAUTICS AND SPACE ADMINISTRATION

March 15, 1965

CONTRACT NAS 3-3561

Technical Management
NASA Lewis Research Center
Cleveland, Ohio
Electrical Propulsion Office
J.J. Ferrante

SPACE POWER AND PROPULSION SECTION
MISSILE AND SPACE DIVISION
GENERAL ELECTRIC COMPANY
Cincinnati, Ohio 45215

ACKNOWLEDGMENTS

The work described in this report was performed under Contract NAS 3-3561 funded by the National Aeronautics and Space Administration's Electric Propulsion Office at the Lewis Research Center. The authors gratefully acknowledge the guidance and counsel given by J. Ferrante, the NASA Project Engineer, and by D. Lockwood, R. Nicholls, E. Richley, P. Reader, A. Goldstein, and S. Jones of NASA in technical discussions during the course of the contract.

We are also indebted to General Electric Engineers, J. Kenney, M. Templeton, B. Merten, F. Cadek, R. Richter, and N. Jeffries for contributions in the design, consultation, and test areas, to engineering technicians G. Brown, K. Hake, and C. Schnell who handled most of the fabrication and test activities, and to Mrs. P. A. Stevens for preparing the manuscript.

TABLE OF CONTENTS

	Page No.
LIST OF FIGURES	vii
SUMMARY	xvii
INTRODUCTION	1
I. ION SOURCE DEVELOPMENT	7
Theory	9
Hardware	17
Experimental Procedure	20
Preliminary Experiments	23
Source Performance	27
II. AERODYNAMIC FLOW PATTERNS	39
Analytical Study	41
Hardware	61
Experimental Procedure	64
Experimental Results and Discussion	66
Evaluation of Results	75
III. ELECTROMAGNETIC NOZZLE DEVELOPMENT	83
Theory	85
Hardware	92
Experimental Methods	95
Experimental Results and Discussion	97
IV. ACCELERATOR STUDIES	107
Classical Theory	109
Theory of Auto Focussing Perforated Parallel Plate Electrode System	115
Hardware	119
Experimental Methods	125
Experimental Results and Discussion	127
V. ENGINE RUNS	133
General Methods of Operation	135
Engine Configuration I	139
Engine Configuration II	142

Table of Contents, Continued

	Page No.
Engine Configuration III	145
Application of Engine Performance to Specific Mission Requirements	164
VI. OVERALL EVALUATION, CONCLUSIONS, AND RECOMMENDATIONS	169
Evaluation and Conclusions	171
Recommendations	173
REFERENCES	175
APPENDIX I	305
APPENDIX II	329

LIST OF ILLUSTRATIONS

Figure No.		Page No.
1	Elements of the Plasma Separator Ion Engine	179
2	Source Design I	180
3	Source Design II	181
4	Source Design III	182
5	Source Designs IV, V, VI	183
6	Source Design VII and VIII	184
7	Multiple Anode Ion Source VII	185
8	Multiple Anode Ion Source - Exploded View	186
9	Multiple Anode Ion Source with Inner Anode Removed	187
10	Source Design IX	188
11	Source Design X	188
12	Source Design XI	188
13	Electron Emission From a Heated Tantalum Ribbon in Cesium Vapor. Gibbon[10]	189
14	Bell Jar Vacuum System for Source Studies	190
15	Modified Vacuum System for Sources and Flow Pattern Studies	191
16	High Vacuum Test Chamber for Source Studies	192
17	Boiler and Fuel Feed System	193
18	Boiler and Fuel Feed System with Inert Gas Purge	194
19	Large Boiler and Fuel Feed System Design	195
20	Fuel Line Detail - Orifice Cleanout and Argon Purge	196
21	Fuel Line Detail - Orifice Cleanout Plunger	197
22	Total Probe and Mounting Ring (Actual Scale)	198

LIST OF ILLUSTRATIONS (Continued)

Figure No.		Page No.
23	Stability of Arc and Probe Readings	199
24	Typical Total Probe Saturation Curves	200
25	Current Voltage Curves for Variations of Source Design I	201
26	Ionization vs. Arc Voltage for Variations of Source Design I	202
27	Performance Curves for Several Geometries of Source Design I	203
28	Effect of Flow Rate on the Performance of Source Design IA	204
29	Effect of Flow Rate on the Performance of Selected Ion Source	205
30	Electron-Ion Current Ratio vs. Ion Generation Power	206
31	The Effect of High Vacuum on Source Performance	207
32	Degree of Ionization vs. Arc Current Density	208
33	Reduction in Ion Generation Power by an Axial Magnetic Field	209
34	Molecular Flow Geometry in a Tube	210
35	Flux Projections on Flat Plates	211
36	Geometry of Spherically Symmetrical Molecular Expansion	212
37	Dayton's T Function for Cylindrical Tubes	213
38	Theoretical Flux Patterns from Tubular Sources on a Flat Normal Plane	214
39	Cross Section of a Typical Flux Distribution on a Flat Plate	215
40	Three-Dimensional View of Figure 39	216
41	Flux Within 3:1 Limits from a $\cos^n\theta$ Distribution	217
42	Flux Distribution over a Flat Plate from Spherically Symmetrical Expansions	218
43	Flux Projection on a Flat Plate Tilted to the Beam Axis	219

LIST OF ILLUSTRATIONS (Continued)

Figure No.		Page No.
44	Molecular Flow Pattern from a Tubular Source Projected at Selected Angles to a Flat Plate. Tube Length/Radius Ratio = 8	220
45	Molecular Flow Pattern from a Tubular Source Projected at Selected Angles to a Flat Plate. Tube Length/Radius Ratio = 10	221
46	Molecular Flow Pattern from a Tubular Source Projected at Selected Angles to a Flat Plate. Tube Length/Radius Ratio = 12	222
47	Molecular Flow Pattern from Two Independent Sources	223
48	Double Plate Distribution Probe	224
49	Plasma Distribution Probe Design	225
50	Shadow Shield Design	227
51	Multiple Ion Probe with Shadow Shielding	228
52	The Effect of Source to Probe Distance on Density Pattern	229
53	Density Patterns for Source Design III. Throat = .023"	230
54	Density Patterns for Source Design III. Throat = .047"	231
55	Flow Pattern from a Multiple Orifice Source at Low Flow Rate	232
56	Ion Density Pattern for Source VII. Tube Length/Radius Ratio = 2.5	233
57	Ion Density Pattern for Source VII. Tube Length/Radius Ratio = 5	234
58	Ion Density Pattern for Source VII. Tube Length/Radius Ratio = 10	235
59	Ion Density Patterns for Source VII. Variable Tube Dimensions	236
60	Density Pattern Variation with Nozzle Half Angle	237
61	Density Pattern Variation with Flow Rate	238

LIST OF ILLUSTRATIONS (Continued)

Figure No.		Page No.
62	The Effect of Nozzle Shortening	239
63	Density Pattern Variation with Tilted Beam Axis	240
64	A Single Source Flux Distribution. Source Located at ⊖ Shaded Area Within 3:1 Density Limits Represents 46.5% of Total Flow	241
65	Multiple Source Flux Distribution. Source Located at ⊖ Shaded Area Within 3:1 Density Limits Represents 78% of Total Flux	242
66	Current Density Correction Curve for Plasma Sheath Effect	243
67	A Selected Density Pattern and Matching Analytical Function	245
68	Percent of Integrated Flow Within Different Radii	246
69	Evaluation of Aerodynamic Flow Patterns	247
70	Shadow Shield and Multiple Ion Probe Design	248
71	Small Cylindrical Electromagnetic Nozzle	249
72	Large Cylindrical Electromagnetic Nozzle	250
73	Conical Electromagnetic Nozzle Design with Auxiliary Cylindrical Coil	251
74	Conical Electromagnetic Nozzle Design with Auxiliary Cylindrical Coil and Throat Coil	252
75	Plasma Flow Control in a Small Solenoid	253
76	Radial Electron Current Restriction in a Small Solenoid	254
77	Plasma Flow Control in an 8" Diameter Solenoid	255
78	Radial Electron Current Restriction in an 8" Diameter Solenoid	256
79	Aerodynamic Density Pattern for Source X	257
80	Density Patterns of Simple Electromagnetic Devices	258

LIST OF ILLUSTRATIONS (Continued)

Figure No.		Page No.
81	Density Patterns for Electromagnetic Nozzle Configurations	259
82	Axial Magnetic Field Along Axis of Coaxial Magnet Coils with only Cylindrical Coil Energized	260
83	Radial Magnetic Field Along Axis of Coaxial Magnet Coils with only Cylindrical Coil Energized	261
84	Axial Magnetic Field Along Axis of Coaxial Magnet Coils with only Conical Coil Energized	262
85	Radial Magnetic Field Along Axis of Coaxial Magnet Coils with only Conical Coil Energized	263
86	Magnetic Field Characteristics of Wire Wound Throat Coil of Figure 74	264
87	Magnetic Field Characteristics of Wire Wound Throat Coil of Figure 74	265
88	Magnetic Field of the Throat Coil of Figure 74	266
89	Magnetic Field of Conical Coil of Figures 73 and 74	267
90	Magnetic Field of the Downstream Solenoid of Figures 73 and 74	268
91	Combined Magnetic Field of the Throat and Conical Windings	269
92	Combined Magnetic Field of Throat, Conical, and Solenoid Windings	270
93	Evaluation of Electromagnetic Steering	271
94	Electromagnetic Nozzle Design Modification	272
95	Magnetic Field of the Throat Coil of Figure 94	273
96	Magnetic Field of the Throat Coil and Downstream Cylinder Coil of Figure 94	274
97	Magnetic Field of the Throat Coil and Downstream Cylinder Coil of Figure 94	275

LIST OF ILLUSTRATIONS (Continued)

Figure No.		Page No.
98	Magnetic Field of the Throat Coil and Downstream Cylinder Coil of Figure 94	276
99	Density Patterns of Electromagnetic Nozzle of Figure 94	277
100	Evaluation of Electromagnetic Nozzle of Figure 94	278
101	Field Characteristics of Perforated Plate Electrodes	279
102	Plasma Boundary Shapes Predicted by Classical Theory	280
103	Ion Currents vs. Accelerator Potential at Various Cesium Flow Rates	281
104	Comparison of Measured Accelerated Ion Current with Total Incident Flow by Calibration	282
105	Variation of Electron-Ion Density Ratio with Potential in the Transition Region from Neutral Plasma to Space Charge Limited Ion Flow	283
106	Vacuum System Used for Accelerator Studies and Engine Runs	284
107	Grid Suspension System for 19 Hole and 211 Hole Accelerator System	285
108	The Six Inch Accelerator System in Operating Position	286
109	The Ion Beam Examiner, Disassembled	287
110	Nineteen Point Ion Probe (Examiner)	288
111	Schematic Arrangement of the 6" Accelerator System Components	289
112	Density Patterns for Source IX	290
113	Schematic Arrangement of the 8" Accelerator System Components	291
114	Engine Configuration I	292
115	Engine Configuration II	293
116	Engine Configuration III	294

LIST OF ILLUSTRATIONS (Continued)

Figure No.		Page No.
117	Density Patterns for Source XI, Aerodynamic and Magnetically Controlled	295
118	Beam Current Density vs. Incident Density Ratio	296
119	Electrodes After EC III Run. Separator Upstream	297
120	Electrodes After EC III Run. Separator Downstream	298
121	Electrodes After EC III Run. Accelerator Upstream	299
122	Electrodes After EC III Run. Accelerator Downstream	300
123	Electrodes After EC III Run. Decelerator Upstream	301
124	Electrodes After EC III Run. Decelerator Downstream	302
125	The Target-Calorimeter After an Engine Run	303
126	Calculated Engine Efficiency for Two Values of Propellant Utilization and Two Values of Ion Generation Power	304

LIST OF TABLES

Table No.		Page No.
I	Selected Design Factors for Ion Sources of Moderate Performance	29
II	Performance of Source VII - Tantalum Orifice	30
III	Flux Distribution Parameters for $Cos^{n}\theta$ Functions	56
IV	Date for Sheath Effect Corrections to Observe Current Density Probe Radius = 0.277 cm.	79
V	Observed and Corrected Current Densities for a Selected Pattern with and without Shadow Shield.	80
VI.	Axial and Radial Field Strengths for Conical and Solenoid Coils, Calculated from Figs. 82 to 85.	103
VII	Selected Performance of the 6", 211 Hole Accelerator System	128
VIII	Evaluation of the Density Patterns of Fig. 117	129
IX	Selected Performance of the 8", 361 Hole Accelerator System.	130
X	Beam Current Density and Related Factors for 19 Hole, 211 Hole, and 361 Hole Accelerator Systems.	130
XI	Performance Data for Engine Configuration I	140
XII	Engine Performance Calculations for EC I	141
XIII	Performance Data for Engine Configuration II	143
XIV	Engine Performance Calculations for Engine Configuration II	143
XV	Voltage Breakdown Frequency During 50-Hour Run with Engine Configuration III.	150
XVI	Best Performance Data for Engine Configuration III.	151
XVII	Best Engine Performance for Engine Configuration III.	152
XVIII	50-Hour Run Data with Engine Configuration III.	153
XIX	Engine Performance Calculations for Data of 50-Hour Run with EC III	156
XX	Calorimeter Data and Calculations for 50-Hour Run with Engine Configuration III	160

SUMMARY

The inherent technical feasibility of the plasma separator engine has been demonstrated experimentally both in separate engine component development programs and in a final 50 hour engine run.

Peak ion source performance has been established well above that of any other source under development, at levels of ionization above 99% and power costs well below 100 electron volts per ion, and a theoretical interpretation of source performance characteristics has been developed. Aerodynamic flow control from a single source is restricted by the geometrical requirements for efficient ion production, but a multiple source approach analytically has been shown to improve flow patterns considerably, assuming collisionless flow. The theory of magnetic flow control is outlined and the concept experimentally demonstrated. The best electromagnetic density patterns produced to date are superior to any single source aerodynamic pattern.

Complete transmission of incident plasma through the separator electrode with good optics has been experimentally observed many times. This behavior is not in accord with commonly accepted perforated plate optics, and a new theory of plasma extraction optics has been proposed to account for it.

An engine run of 56 hours total duration was made with an overall thrustor efficiency of 83.1% at an engine specific impulse of 6360 seconds, using a predetermined level of propellant utilization. The propellant utilization was checked by a mass balance and the performance was verified calorimetrically.

Existing separate component performance indicates that a thruster efficiency of 86.5% is available by simultaneous component optimization. The capabilities of the plasma separator engine operating at this level of performance have been evaluated for several missions, including Navigator, and are shown in Appendix II.

Theoretical information is presented which shows that the low ion generation power required in the Plasma Separator Engine results in superior thruster efficiency in the low specific impulse region.

INTRODUCTION

Two major classifications of ion engine may be defined: contact engines, which depend on surface ionization, and electron bombardment engines, which ionize by electron collision. The latter class may be arbitrarily subdivided into devices which ionize in low density and high density plasma regions, since distinct problems are presented in each case. A brief description of the essential characteristics of each type is given below.

The Contact Engine

In the contact engine cesium vapor is permitted to interact with a surface of high work function which generally also serves as a shaped, rigid anode. Provided that the work function of the surface can be kept considerably larger than the ionization potential of the cesium, such interaction produces an equilibrium concentration of cesium ions which approaches 100%. This condition exists only when the surface temperature is kept above the minimum level necessary to prevent adsorption of cesium atoms, since the work function is drastically lowered by the presence of even trace amounts of cesium contamination of the surface[1][2]*. Severe ion generation losses in the form of radiation from the hot surface can be reduced somewhat by increasing the extraction potential and therefore the current density, but near perfect ion optics are then required to avoid rapid destruction of the electrodes by impingment of very high energy ions. Also at high current densities the work function of the surface is adversely

*Superscript parenthesized numerals denote references.

affected by the mere contact of the flowing cesium since each colliding atom interacts with the surface for a short residence time, even without adsorption. This factor necessitates operation at higher emitter temperatures. which decreases emitter lifetime via sintering.

Consideration of these factors leads to the conclusion that the basic problem with the contact ion engine is the necessity of generating and focusing a very high density ion beam in order to realize even moderately good thruster efficiency. The consequent problems described above are direct results of this restriction.

The Low Density Electron Bombardment Engine

In this type of engine ions are generated in the vapor phase by collision between neutral atoms and electrons of moderate energy. Ion beam current densities of the order of 1-10 milliamperes/cm^2 are common goals, with corresponding plasma densities of the order of 10^{15} - 10^{16} particles/cm^3. At these levels the ion optics and electrode erosion problems are not nearly as critical as with the contact engine, but the ionization cross section is so low that ion generation losses are severe. These losses can be reduced significantly by some variation of Kaufman's[3] original model, i.e., by magnetically or electrically restricting the electron to a trajectory of higher collision probability, but the basic problem remains the same - excessive ion generation losses due to low ionizing collision cross section in a low density plasma.

The Plasma Separator Engine

A schematic of a typical plasma separator ion engine is shown in Fig. 1, and consists of an ion source, a region of aerodynamic or electromagnetically controlled expansion, and an ion extraction and acceleration device. The key to the high performance potential of this engine is in the source, which combines the good points of the contact and bombardment engines in producing a dense plasma by effective bombardment, and in the expansion region, which eliminates the contact engine's problem of extracting a dense ion beam.

The similarity with the contact engine is that both devices generate high ion current densities at the ion source. But whereas the contact engine produces an ion beam and is thus limited by practical extraction potentials to several tens of milliamperes per square centimeter, the expanding arc source generates ions in a dense neutral plasma with ion currents in the range of several tens of amperes per square centimeter of radiating surface. Thus the radiation losses are reduced by two or three orders of magnitude and the severe optics and electrode erosion problems of the contact engine are avoided by expansion to a much lower density prior to extraction.

The similarity with the low density electron bombardment engine is that both devices ionize by electron collision and need extract only moderate ion currents. Comparison of cesium atom densities of the ionizing region of the two engines, however, show that the plasma separator engine ionizes plasma three orders of magnitude denser than does the low density electron bombardment engine, with a consequent very large increase in the ionizing collision probability.

Both the contact engine and the low density electron bombardment engine have source lifetime problems; in the contact engine the anode is subject to deterioration due to sintering, while in the low density electron bombardment engines a cathode design has not yet been developed which combines long life with high performance. In the plasma separator engine the source temperature and arc characteristics are such that no significant lifetime problems are expected, and none have been encountered.

Thus it appears that the plasma separator engine is at least in concept capable of exceeding the performance of both the contact engines and the low density electron bombardment devices. It is one of the purposes of this report to show that this type of engine will actually give performance superior to any other presently available, especially in the low specific impulse region. Since one of the advantages of the plasma separator engine is that the components can be developed more or less independently, the state of component development will be considered as well as the assembled engine.

Previous Work

Sometime prior to 1962, R. N. Edwards theorized that ion generation power levels could be reduced significantly if highly ionized cesium plasma could be generated at very high density and used before extensive recombination occurred, and in the same year he demonstrated the Plasma Separator Engine concept experimentally in a highly unoptimized assembly of the essential engine components. Majkowski and Donahue[6] suggested that high density plasmas could

be generated by simultaneous contact ionization and thermionic emission, and the recombination rate data then available[5] was shown by Bromberg[7] to predict little recombination during the flight time to an accelerator. Initial experimental efforts along these lines, however, showed only low degrees of residual ionization even a few centimeters downstream of the source. This behavior was confirmed by application of later and more accurate rate data in the recombination expression[8].

These early efforts, however, conducted under contract NAS 3-2504, showed fairly high residual degrees of ionization downstream when an arc discharge was passed through the expanding plasma, and the study was redirected along these lines. The development of a highly efficient ion source, based on an expanding arc mechanism, was completed under this contract and reported in detail[4].

Present Efforts

The goals of the present contract NAS 3-3561 originally were to produce and accelerate a directed plasma at least 80% utilized, with an average flux density ranging from 1 to 3 ma/cm^2, and a density variation no greater than 3:1 across the flow profile. A fifty hour engine run was included in the original goals to demonstrate that the source could be run in an engine configuration and to determine source erosion and wear effects, but no specifications were set on overall thruster efficiency. It was decided arbitrarily during the latter stages of the contract to aim for a thruster efficiency of 82% and a beam current of 350 ma. With the exception of the level of beam current all these figures were met or surpassed, as detailed in the various sections of the report.

Organization of the Report

The report is arbitrarily divided into sections covering coherent units of subject matter. The four main sections cover source development, plasma flow control devices, accelerator studies, and engine runs. Each main section is subdivided topically. Chronological order is followed only when it does not interfere with the logical presentation of related topics. Overall conclusions are based on the theoretical treatments given at the beginning of each of the main sections and the overall discussion at the end of the report.

I. ION SOURCE DEVELOPMENT

THEORY

General Description

Typical ion sources for the plasma separator engine are shown in Figs. 2 through 12. All these devices have in common a tubular fuel feed line which serves as a cathode, a nozzle or similar flow constriction device, and an anode, usually of the ring type. Activation of the electrodes while cesium is flowing produces an arc discharge from the cathode through the nozzle throat and nozzle expansion region to the anode. In some of the devices a magnetic field is used which reduces the arc current at any given arc voltage.

A rigid quantitative study of this discharge region would combine all the complexities of aerodynamic flow, both continuum and molecular, with those of plasma physics and electromagnetic field theory. Since this is clearly beyond the scope of the present study, the approach which will be followed is a reasonable, semi-quantitative explanation of the phenomena involved, based on established concepts in the pertinent fields of research.

The Cathode

Taylor and Langmuir[1] and later Houston[9] have demonstrated the large increase in thermionic emission which is obtained when cesium vapor interacts with a refractory metal surface at moderate temperatures (800-1800°K). Some recent results obtained by Gibbons[10] are indicated roughly in Fig. 13, where it can be clearly seen that overheating in any given area on the cathode would

automatically quench the current density by a factor of nearly two orders of magnitude, with consequent relocation of the arc. The overall effect of this phenomenon is to produce an equilibrium condition in which the electron discharge and ion bombardment is spread more or less evenly over the surface of the cathode. Thus, it is not suprising that the cesium coated hollow cathode used in these studies produces a steady uniform arc operating in the spotless mode, with an almost negligible cathode erosion rate.

Arc Current Requirements

Consider a plasma of cesium atoms, ions, and electrons flowing through a tube of length ℓ and radius r in the region of a coaxial arc with the anode downstream. The rate of ion production is equal to the rate of neutral decay, and is related to the arc current by:

$$(1) \quad -\frac{dn}{dt} = Pfnvt\ I_e$$

where n is the instantaneous neutral density at time t, P is the total probability for electron-neutral collisions per centimeter of electron travel at a neutral density n atoms/cm^3, f is the effective fraction of the collisions which results in ionization, I_e is the electron current in electrons/sec., and the product of ion velocity v and flight time t is equal to the arc length. It will be shown subsequently that no recombination term is necessary in this expression. Integrating (1) gives :

$$(2)\quad n = n_o e^{-PfvI_e \frac{t^2}{2}}$$

from which the degree of ionization d_+ can be estimated by:

$$(3)\quad d_+ = \frac{n_o - n}{n_o}$$

P is a complex function of the electron energy which ranges roughly from 1000 - 2000 collisions per centimeter per mm Hg[11]. In appropriate units of neutral cesium atom density this becomes 1.3×10^{-14} to 1.3×10^{-15} collisions per cm per electron per atom, assuming an average cesium pressure of 10^{-1} - 10^{-2} mm. Hg. The factor f includes single and multiple collision ionization. Francis[12] indicates that single electron ionization collisions are about 3 orders of magnitude less frequent than the total number of collisions, which establishes the lower limit for f at about 10^{-3}. The effective value is of course considerably higher due to multiple collision ionization. Sonic atom velocity is about 3000 cm/sec, the arc length is about 1 cm., and electron currents of about 20 amperes or 1.2×10^{20} electrons/sec. are passed through a source operating in the range of one ampere of ion current. The residence time t is the quotient of ℓ divided by the average atom velocity over a range of about 3000 - 5000 cm/sec. Typical ionization times are therefore about 3×10^{-4} sec. An atom density of 10^{14} - 10^{15} atoms/cm^3 which corresponds roughly to a cesium pressure of 10^{-1} - 10^{-2} Torr at 1300°K is common in the arc region.

Substitution of these values into equations (2) and (3) give expected ionizations of about 80-90% even when the ionization efficiency factor f is taken for single collision ionization only. A very moderate increase in the value of f, due to multiple collision ionization corresponding to 100 collisions per ionization, would result in a calculated ionization approaching 100% neglecting minor recombination terms in view of the high electron temperature of the arc.

Thus, it appears from these very approximate relationships that the electron currents necessary to produce high levels of ionization can be roughly calculated, and that the current levels in present use are more than adequate for complete ionization. These calculations could be made more exact by such methods as calculating the pressure as a function of distance, multiplying P by the resulting function, and integrating over the path length, but until the uncertainty in the value of f is resolved, such procedures are hardly justified.

Arc Voltage Requirements:

The arc voltage is required to produce two conditions. The first requirement is that a considerable portion of the electrons in the discharge must be accelerated to the first ionization potential, or at least to the first excitation potential, of the neutral atoms, in order to realize a high probability for ionization either by single or multiple impact. This is accomplished in the cathode fall region, where the width of the sheath is one to several mean free paths for electron-neutral collisions, and the potential drop is of the order of the least ionization potential of the gas[13]. Since no other region exists in the arc where the potential fall across a mean free path is larger than this

value, it is improbable that multiple ionized particles will be produced whenever the second ionization potential is greater than twice that of the first. In the case of cesium, the ratio of the second to first ionization potential is 6 and the production of doubly charged species is negligible.

The second requirement of the arc voltage is that it be sufficient to sustain a potential gradient along the length of the arc of such proportions that the electron acceleration along a mean free path will produce a terminal electron velocity high enough to prevent any significant recombination in the arc region. A form of the Saha equation:

$$(4)\quad \frac{x^2}{1-x^2} = \frac{3.16 \times 10^{-7} T^{2.5}}{P}\, e^{-\frac{eV}{kT}}$$

can be used to estimate the thermal degree of dissociation x at a temperature T and pressure in atmospheres P, where eV is the ionization energy in ergs and k is Boltzmann's constant. Temperatures as low as 5000 - 6000°K are sufficient to maintain nearly complete ionization for cesium. Cobine[13] shows in his treatment of the electric arc tnat the electron temperature of a typical arc at one mm gas pressure is above 7000°K, a value more than sufficient to maintain complete ionization. Since the arc in our source burns at a pressure considerably lower than this, our electron temperatures would be expected to be higher. Calculations based on the slopes of our experimentally measured probe saturation curves invariably show electron temperatures in excess of 10000°K, and the possibility of recombination may thus be neglected.

Anode Geometry

It is possible for the anode to be either above or below plasma potential, depending on whether the electron current to it is emission limited or space charge limited. If the plasma potential is higher than the anode potential random ions will freely strike the anode surface and be neutralized. This can be avoided by making the anode positive with respect to the plasma, causing all ions to be electrostatically reflected before they strike the anode. This situation is reached, according to elementary probe theory, only after the anode is accepting all the random electron current incident on its surface. Thus either the arc voltage and current may be increased or the anode surface area may be decreased to produce a positive anode with respect to plasma potential. This reasoning may be applied to any conductor immersed in the plasma floating at a potential negative with respect to the plasma. Any such conductor will serve to neutralize any ion which strikes it, as will be seen in connection with the experimental results described below.

Recombination in the Expansion Region

A conservative estimate of the degree of ionization of an expanding plasma was reported previously[4], based on a combination of standard equations for fluid flow through a nozzle with recombination coefficients reported by Hersnberg and Hinov[14]. This estimate is conservative because the electron temperature was assumed equal to the ion temperature. Throughout the present contract, however, degrees of ionization considerably higher than those predicted[4]

have been experimentally observed, and our elementary predictions must be abandoned in favor of negligible rates of recombination. Theoretical justification for the latter view is established by application of probe measurements and Saha's equation as follows:

Ionization Levels Indicated by the Saha Equation

A convenient form of Saha's equation relating the degree of ionization of a gas to the absolute temperature is:

$$(5)\quad \log_{10}\left(\frac{X^2}{1-X^2}\,p\right) = \frac{-5{,}050\ V_i}{T} + 2.5\log_{10} T - 6.5$$

where $X = \frac{n_i}{n} = \frac{n_e}{n}$ = fraction of atoms ionized, p is the pressure in atmospheres, V_i the ionizing potential in volts, and T the gas temperature in degrees Kelvin.

The table below gives the degree of ionization of cesium calculated from equation (5) at several moderate temperatures over the range of pressure existing in the expanding plasma.

	DEGREE OF IONIZATION		
Temp. (^{o}K)	1 Torr	0.1 Torr	0.01 Torr
5000	.9809	.9980	.9998
6000	.9972	.9997	.9999
7000	.9994	.9999	.9999

Electron Temperatures Calculated From Probe Measurements

Total probe measurements of the expanding plasma and the double probe configuration are shown in Fig. 24. The probe voltage-current characteristic is obtained by gradually increasing the cathode-anode voltage until current saturation is reached.

Assuming a Maxwellian distribution of electron energies, and that the number and temperature of the electrons are independent of probe voltage, the expected probe current density vs. probe volts is given by the Boltzman relation,

$\log_e j = B - \frac{Ve}{kT}$, where B represents a term which does not change with voltage. From this the electron temperature can be calculated from the slope of the voltage-log current plot.

In our experiments this slope is not a constant, but decreases as the probe approaches saturation, indicating that our electron energy distribution is not Maxwellian, but some other distribution containing a higher proportion of high energy electrons. Therefore the minimum value of the slope represents a conservative estimate of the electron temperature. The electron temperature we have calculated by this method for a typical ion source is about 12000^{o}K, a value far in excess of that required to maintain complete ionization according to Saha's relationship.

HARDWARE

Vacuum Tank

Source studies were initiated in an 18" diameter glass bell jar, shown schematically in Fig. 14. All penetrations were through one steel plate which blanked off the open end of the bell jar. This system was modified early in the program to the glass cylinder shown schematically in Fig. 15, a more versatile system necessary for the plasma density distribution studies described later. Operating pressures for both systems of 1×10^{-5} to 5×10^{-5} mm. Hg. were reached via a 4" silicone oil diffusion pump. Toward the end of the program the effect of lower pressure on source performance was tested in the tank shown in Fig. 16, at pressures in the range of 5×10^{-7} to 2×10^{-6}.

Boiler and Fuel Feed System

A typical cesium boiler and fuel feed system is shown in Fig. 17. Fig. 18 shows the same type of boiler (without line heaters and insulation), equipped with a second valve for an inert gas purge which was added to allow opening of the vacuum system for minor adjustments without cooling the lines.

Figs. 19, 20, and 21 show the design of a larger boiler which was built near the end of the program for use in long duration runs at high flow rates. The boiler is located outside the vacuum system and can be fabricated to any convenient size. Both the inert gas purge line and the cleanout plug and plunger design are

EXPERIMENTAL PROCEDURE

The experimental procedure for a source performance study is extremely simple. The bell jar is evacuated to the low 10^{-5} mm Hg range and the boiler is brought to a controlled temperature predetermined to give the approximate flow rate desired. The fuel lines and source are all kept hotter than the boiler to prevent condensation. A potential sufficient to start the arc is set across the electrodes and an electric timer is started automatically when the boiler valve is opened.

The source heater is turned off as soon as the arc is well established. The floating power supply to the total probe is activated until the saturation current is reached, and the arc voltage is adjusted until an optimum condition is reached (i.e. maximum probe current for least power expenditure). Probe current, arc voltage and current, and boiler temperature are monitored for a period of time long enough to minimize any startup or shutdown variations in the flow, and then the boiler valve is closed and the timer stopped. The cesium collected in the total probe is determined by hydrolysis and titration with standard acid.

The degree of ionization and ion production power efficiency are then calculated by the following formulae:

$$(6)\quad \eta_{+} = \frac{V_A \times I_A}{I_P}$$

where η_+ is ion production efficiency in either watts of power per ampere of ion current, or in the equivalent units of electron-volts per ion, V_A and I_A are arc voltage and current, and I_P is the saturated probe ion current.

$$(7)\quad D_+ = I_P/I_B$$

where degree of ionization D_+ is equal to the probe current I_P divided by the total flow of cesium from the boiler, calculated in units of current.

The total cesium flow for this purpose is now always determined by titration, a more accurate procedure than precalibration, and is established by:

$$(8)\quad I_B = \frac{\text{Vol.} \times N \times F}{t}$$

where the product of acid volume and strength N is equal to the number of millimoles of cesium, F is Faraday's number, 96,500 millicoulombs per millimole, and t is the time in seconds. The overall accuracy of these determinations is generally recognized to be better than $\pm$ 0.5%.

With some probe designs a small portion of the cesium ions will miss the probe, strike some other surface and be neutralized, and eventually migrate as neutrals to the cold probe. In these cases, the degree of ionization calculated by the above methods will be low. With the flat plate design shown in Fig. 49 the loss ranges up to 10% when the probe is located at typical accel system distances from the source. Under these conditions the fraction ionized cannot

be distinguished from the fraction of plasma incident on the probe and the two factors are lumped together.

It may be mentioned that the data reported below was gathered sometimes in consecutive runs with a fixed purpose, sometimes over the whole range of the program with extraneous variables not wholly controlled. Every attempt has been made to restrict comparisons to sets of data gathered under roughly comparable conditions with respect to all significant variables. The reader will realize that under these conditions some of the relationships reported are more exact than others.

PRELIMINARY EXPERIMENTS

Stability of the Arc and Probe Readings

Fig. 23 shows the results of experiments where the arc current and voltage and probe current are plotted along the time axis, proving that the ion flow rate is essentially constant over a period of time longer than an average source test. The periods before and after the recorded intervals were just as steady, but at slightly different arc settings. Since the ion flow rate is very nearly equal to the total cesium flow rate, it can be safely inferred that the total flow rate is also constant, thus validating the use of equation (7). In cases where small variations in arc behavior and probe current are encountered, they are never rapid fluctuations, and the average probe current value can always be used as a good estimate of the ion flow rate.

Probe Saturation Curves

The total probe used in these studies is nothing more than a floating double probe with a large cathode. From ordinary probe theory we know that both electrodes, before potential is applied, are covered with an electron sheath whose space charge limits the electron current to a value equal to the ion current. We also know that any isolated conductor in a plasma is negative with respect to the plasma potential because of the formation of this sheath, that such a conductor accepts all the random ion current to itself, and hence can be easily made more negative with respect to the plasma. In order to make such a conductor more positive than the plasma potential, however, one must

accept all the random electron current to it.

When these considerations are applied to a floating double probe whose electrodes are of equal size, it is apparent that at the saturation potential the cathode will be sufficiently negative to repel all electrons, and hence read only ion current, but that the anode will still be slightly negative with respect to the plasma.

Under these conditions both electrodes will accept all the random ion current incident on their respective sheaths. The sheath around the cathode will be slightly larger, and hence the ion current to the cathode will be slightly greater than the anode ion current. The anode will also accept sufficient electron current to exactly balance the ion current to both electrodes. Only the electron current necessary to neutralize the ion current to the cathode will be observed in the external circuit.

In a neutral cesium plasma, the random electron current density is about 500 times the random ion current density across any plane, even if the electrons are in thermal equilibrium with the ions. The total random current to any object, however, is dependent on the area, and naturally a small object can be biased positive with respect to the plasma without drawing the huge electron currents that would be associated with biasing a large object positive. Thus, in a floating double probe, when the cathode is enlarged or the anode decreased in size, the total random ion current to the cathode approaches the total random electron current to the anode. When the effective cathode/anode area ratio becomes

equal to the ratio of random electron current to random ion current, then the anode becomes positive with respect to the plasma just as easily as the cathode becomes negative, when a potential difference is applied between the electrodes. At saturation potential under these conditions, all electrons are reflected from the cathode and all ions are reflected from the anode, and the probe reads the total ion current. Experimental verification of the above description has only recently been obtained in even a sketchy manner, and is illustrated in Fig. 24. Curve (a) represents a probe with properly balanced electrode areas. If the anode surface area is too large, the random electron current to the anode will exceed the ion current to the cathode, and the excess electrons will be repelled by a space charge sheath while the random ion current to both electrodes will be accepted. Under these conditions the total ion current will be split between cathode and anode in proportion to their surface areas and a saturation curve similar to (b) in Fig. 24 will be obtained. If the anode surface is so small that the random electron current to it is not sufficient to neutralize the total ion flow, some of the electron current will be accepted by the cathode and a low value of ion current will be obtained at the saturation potential. As the potential is increased further, however, the sheath around the anode will increase in size, increasing its effective surface area until the electron current to the anode equals the total ion current. This situation is illustrated in curve (c) of Fig. 24 for the case where the anode is only slightly smaller than necessary.

The conclusion to be drawn from this discussion is that total probe readings are conservative, provided that only singly charged ions are present, since no

electrode geometry will allow a probe current reading higher than the total ion flow. If in addition the probe dimensions and geometry approximate those of an ion extractor, then probe measurements are a conservative measurement of ionization in an engine.

SOURCE PERFORMANCE

Sources of Moderate Performance

During this contract period, emphasis was laid on the study of aerodynamic and electromagnetically controlled flow patterns issuing from the sources studied, and not on ion generation efficiency. Consequently, a number of the sources tested were capable of only fair values for power efficiency and degree of ionization. These sources are mentioned only to illustrate the reasons for the lower performance values.

Sources of this type are illustrated in Figs. 3, 4, 5, and 6. The pertinent design factors and performance figures for source II through VI are given in Table I. In general, all these sources are larger than those reported below, leading to higher radiation losses and higher ion generation power requirements. More important factors, however, seem to be low arc current densities through the nozzle throat, and the presence of floating metal components which may cause low ionization probability and high recombination rates, respectively. Within groups of similar sources the following trends can be seen. In source type II a slight increase in ionization and power efficiency are observed as a result of an increase in arc current density and a reduction of the exposed floating conducting surface. The low degree of ionization is probably due largely to the low electron current density in relation to the levels shown in Fig. 32. In source type III, the floating tantalum plug is a large surface of recombination which causes low ionization levels. Grounding this plug to the cathode removes

this source of recombination, but the arc then probably travels from the plug to the anode, without going through the nozzle throat. The current density shown, therefore, is probably too high, and the high ion production cost is a reflection of the poor ionization probability along the electron path. For some unknown reason no arc was struck when a boron nitride plug was used in source III. It may be that the conduction path through the throat is too severely restricted when not supported by the metal plug. In sources IV, V, and VI a trend toward poorer ion generation efficiency occurs as the nozzle angle increases, i.e., as the anode moves out radially, as a result of higher arc voltage for any given current. The higher ionization levels are probably due to increased electron current density and the removal of the anode to the outer edge of the beam, where a minimum of recombination by anode impingement occurs.

Sources VII and VIII, illustrated in Fig. 6, were constructed to allow testing of the effect of the anode location on performance during single runs. It was found that activation of more than one anode simultaneously always resulted in poor performance, and hence the results reported below are for single anode operation with the other two floating. The anodes are designated 1, 2, and 3 starting from the downstream end of the source. Table II summarizes the behavior of several variations of Source VII with a tantalum insert.

TABLE I

Selected Design Factors for Ion Sources of Moderate Performance

Source Description	Arc Current Density, amp/cm^2	Exposed Anode Area, cm^2	Exposed Metal Surface (Floating)	Percent Ionization	Ion Generation Efficiency, Electron volts/Ion
II, Axial Anode Operating	135	0.051	Large	44	265
II, Ring Anode Operating	135	0.304	Small	46	220
II, Both Anodes Operating	142	0.355	None	52	204
III, Tantalum Plug Floating	195	2.12	Large	72	~600
III, Tantalum Plug Ground	(279)	2.12	None	81	~900
III, Boron Nitride Plug	No Arc	2.12	None	-	-
IV, Tantalum Insert	170	~ 0.30	Large	61	110
V, Tantalum Insert	196	~0.30	Large	74	192
VI, Tantalum Insert	196	~0.30	Large	83	348

TABLE II

Performance of Source VII - Tantalum Orifice

Run	Number of Anodes	Orifice L/R	Anode	Total Flow, ma	Percent Ionization	Ion Generation Power, El. V/Ion
C1	3	5	1	507	77	640
			2	507	75	947
			3	507	73	1015
			1	481	81	697
			2	481	98	326
			3	481	96	468
			1	552	85	1053
			2	552	85	563
			3	552	89	476
			2	1297	71	251
D1	3	10	1	(700)*	--	364
			2	(675)*	--	237
			3	(625)*	--	448
E1	3	2.5	1	583	94	392
			2	583	96	392
			3	583	91	510
C2	2	5	1	1020	67	370
			2	1020	67	252
D2	2	10	1	940	67	453
			2	940	67	399
C3,D3,E3	1	No Arc Struck				

* Ion flow rate, total unknown.

The relatively poor performance of this source does not permit a clear picture of the relationships among the various source design criteria and performance. The only trends which can be perceived are that at roughly comparable levels of ionization the ion generation efficiency is better at higher flow rates for these large sources, and that when the inner anode (Fig. 7) is removed, exposing the metal surface of the floating orifice insert as shown in Fig. 9 the degree of ionization falls. The effect of removing two anodes is to place the remaining one so far out radially as to remove it completely from the flow of cesium vapor, and under these conditions no arc is observed.

When orifice inserts of boron nitride were substituted for the tantalum inserts it was observed that the degree of ionization did not fall when one of the anodes was removed. No significant effects on source performance were noted when Source VIII was tested in place of Source VII.

High Performance Sources

The source shown in Figs. 2, 10, 11, and 12 were designed for both high performance and flow control. Geometrical variations of Source Design I are shown in Fig. 2. This source was used early in the present program to study the effect of electrode positioning, and its performance was probably measured with a total probe whose electrode areas were properly balanced, as indicated by the fact that degrees of ionization in excess of 99% were obtained in some cases.

The Effect of Electrode Geometry

It is apparent from the drawing that design 1A, and to a lesser extent 1D, allows direct contact of the plasma beam periphery with the anode, while in designs 1B and 1C the anode is further out radially. The effect of these geometries is shown in Fig. 25, where it is seen that the current voltage curve for design 1A is a straight line, which allows the generation of high arc current with increasing voltage. Curve 1D is also in this category but this design requires a higher voltage for a given current. The curves for designs 1B and 1C, however, show that as the arc voltage is increased the current level reaches a plateau where very little current increase can be generated with further increases in voltage. Since from equation (1) the rate of ion production is directly proportional to the arc current, the degree of ionization as a function of voltage also plateaus for design 1B and 1C, as shown in Fig. 26, before complete ionization is attained.

The effect of the electrode geometry on performance is illustrated in Fig. 27 in the critical region near complete ionization. Design 1A is apparently capable of nearly complete ionization at very low power levels. Designs 1B and 1C are apparently not capable of higher ionization levels than 95% at reasonable power levels. Source design 1D is capable of more complete ionization, since the curve is still rising at 96% ionization, but only at relatively high power levels. This behavior is expected from a comparison of the current voltage curves of design 1A and 1D in Fig. 25, where for any current level a higher voltage is required for 1D.

The Effect of Flow Rate and Source Size

It has been found in general that any given source design has a broad optimum flow rate range for maximum performance. Below this range the ion generation power requirements are significantly increased. It is expected that operation much above this range would eventually result in a plasma density high enough to promote significant recombination rates. Fig. 28 shows the effect of flow rate on performance for Source 1A. It is apparent that the optimum operating range for this source is well above 370 ma. Fig. 29 compares performance at various flow rates for Sources IX, X, and XI. The degree of ionization was measured with the total probe design shown in Fig. 24C, and may be somewhat low. However, in all cases where a valid check on the flow rate by titration was made, the maximum degree of ionization obtainable by arc control was somewhere between 90% and 100%. In a few cases, however, losses of cesium by spontaneous ignition prevented an accurate flow rate determination and degree of ionization could not be precisely determined. Fig. 29 therefore presents ion flow rate, not degree of ionization as a function of ion generation power. Assuming that all the points shown represent a degree of ionization above 90%, the maximum error in ion generation power is $\pm$ 10%. Two trends are apparent in Fig. 29: first, for any given source the performance improves with increasing flow rate, and second, at the lower flow rates the small sources give better performance than larger sources. It is noticeable that the minimum flow rate for highest power efficiency operation of the smallest source (XI) seems to be about 300 ma.

This behavior is explained as follows: For a given source, the range of cesium flow rate for efficient operation is between the level necessary to reduce the hollow cathode work function and the level where extensive recombination occurs due to interatomic collisions. Within this range there is a minimum necessary level of electron current density to effect complete ionization purely on the basis of ionization collision probability. This required level is easily attained in any well designed source as soon as the cesium flow rate becomes high enough to reduce the work function of the hollow cathode significantly, so that the arc current does not become emission limited before high ionization levels are reached. Since this required level of current depends on the ionizing collision probability for each atom considered singly it will not be affected strongly by increasing ion flow rate, as long as interatomic collisions are rare in comparison with electron - atom collisions. Thus, approximately the same arc current density will be required to effect complete ionization of both low and high flows of cesium up to the point where the ionization probability of a single atom is not an isolated chance. In equation (5) the arc current I_A remains essentially constant over the range of efficient operation, and the voltage V_A is slightly higher at low flow rates due to the higher resistance of the less dense plasma. The overall result is a steady decrease in ion generation power as the cesium flow rate increases, or in other words as the arc current to beam current ratio decreases.

$$(5)\quad \eta_+ = \frac{V_A \times I_A \ (\text{constant})}{I_P}$$

From Fig. 30 it appears that the electron current density/ion current density ratio is the basic criterion governing source design for high ion generation efficiency, although significant secondary effects due to minor variations in source

design are apparently present. It is probable that increasing the flow rate much further would result in either incomplete ionization or in poorer power efficiency due to recombination.

The Effect of Vacuum Tank Pressure

All the source data reported thus far were collected via experiments run at pressures in the low end of the 10^{-5} mm. Hg. range in the tank shown in Figs. 14 and 15. To demonstrate that the results are not prejudiced by pressures of this magnitude, several source tests were run in the tank shown in Fig. 16, at pressures in the 10^{-6} - 10^{-7} range. The most significant comparisons obtained are illustrated in Fig. 31 for comparable flow rates and levels of ionization. The source used in these experiments was design XI with a 0.020" thick anode. The variation in ionization level between the two curves is very likely due to total probe geometry variation rather than to source behavior variation, but in any event is not more than about 7%, which very nearly balances the slight variation in power efficiency. The difference between the two curves is not considered significant.

The Effect of Anode Surface Area

In the section on theory the possibility of neutralization on the anode surface was discussed, and it was concluded that one way to make the anode surface positive with respect to the plasma, thus preventing ions from striking it, was to decrease the anode surface area. A brief study of this effect was made with Source XI toward the end of the program, with anode thicknesses of 0.040", 0.020". and 0.010". The average degree of ionization in the case of

the 0.040" anode was 94.7% over five runs with a range from 91.8% to 96.1%, the average for the 0.020" anode was 95.7% for four runs, with a range from 92% to 99.9%. The values obtained for the 0.010" anode were 100% and 103% in two successive runs. The differences noted are near the limit of error for these experiments, but nevertheless may be significant because of the number of runs made consecutively under near identical conditions with the same equipment. The relatively high precision usually obtained in measuring degree of ionization is masked in the figures above by variation in flow rate, with the higher ionization levels in each series of runs corresponding to the lower flow rates. Further study is warranted before any firm relationship can be established.

Electron Current Density Requirements

Fig. 32 relates electron current density through the throat of the nozzle with degree of ionization for all the high performance sources. The values much above 200 amp/cm^2 indicate that performance could be improved by reducing the arc current without changing the voltage, since some of the sources reach high levels of ionization at current densities between 150-200 amp/cm^2. One way of accomplishing this is to restrict the arc current by means of an axial magnetic field.

The Effect of an Axial Magnetic Field

When an axial magnetic field is imposed on the arc region the radial motion of the electrons is suppressed. This has the double effect of reducing the arc current at any given voltage and of making the anode more positive with respect to the plasma at any given arc current level. Both effects should improve the

performance of any source in which the minimum required voltage produces an excess of arc current. Fig. 33 shows the effect of the magnetic field on source performance in terms of the reduction in ion generation power as a result of lowering the arc current. Each curve is for a single run with Source XI at constant ionization level above 90%. The highest current density and ion generation power shown represents the condition where no magnetic field is present. The beneficial effect of this technique is clear in all cases.

II. AERODYNAMIC FLOW PATTERNS

ANALYTICAL STUDY

General Description of the Flow Problem

In the previous section it was shown that one of the requirements for efficient ion generation is a reasonably high cesium atom density along the arc path, the magnitude of which has been found empirically to be of the order of 10^{14} - 10^{15} atoms/cm^3. Now the mean free path L of any randomly moving gaseous particle is given by:

$$(9) \quad L = \frac{2.33 \times 10^{-20}}{\sigma^2} \quad \frac{T}{P}$$

where σ is the collision diameter for the type of collision under consideration, T is the temperature in ^{o}K, and P is the pressure in torr. If σ for electron collisions with cesium atoms is taken as about 2×10^{-8} cm^2, the mean free path upstream of the throat, where the temperature is about $1000^{o}K$ and the pressure approximately 1 - 2 torr, is a fraction of a centimeter, well within the continuum range when flight paths of several centimeters are being considered. At the exit plane of a typical nozzle of the type used here, the value of T/P is roughly 5-10 times the value at the throat when calculated by ideal gas isentropic flow equations, the mean free path is consequently of the order of one to several centimeters, and the flow is within the transition region. Downstream of the nozzle the pressure rapidly decreases to the 10^{-5} mm Hg range, the mean free path becomes several tens or hundreds of centimeters, and molecular flow predominates.

Superimposed on this aerodynamic behavior is the electromagnetic field associated with the arc discharge, which will influence the ion trajectories strongly near the anode, to a lesser extent in the transition region just beyond the anode sheath, and very little in the relatively field free regions of dense neutral plasma.

The total problem thus posed is extremely complex, and a rigorous analysis clearly beyond the program scope. A brief study was made, however, concerning the portions of the problem described above, in an attempt to gain some insight into the more important phases of the problem.

The Continuum Flow Region

This area poses no problem in analysis. An existing computer program at this location, using essentially the method of characteristics, calculates pressure, temperature, mach number, and flow direction. From this information the number density and velocity distribution, hence flux, can be calculated at any point in the flow field. Thus, a flux profile could be constructed across any plane normal to the beam axis in this region. Analysis of the mean free path for ion-ion collisions at any selected plane would provide an approximate estimate of the appropriateness of either continuum or free molecular flow.

The Transition Flow Region

Over some region in the plasma expansion the flow regime changes from continuum through a transition region to free molecular flow. Although no exact methods are available for treating the transition region, the problem may be solved approximately by assuming that the transition is fairly sharp, and that the continuum flow parameters at the point of transition may be projected on the accelerator plane by a suitable free molecular flow analysis. The point of transition could be chosen empirically to agree best with experimental observations, or by setting some judicious limit on a suitably chosen parameter, say, Knudsen number or mean free path.

The Molecular Flow Region

A detailed literature search was conducted to find a suitable multi-dimensional analysis for molecular flow. The existing literature[16]-[31] can be broken up into two general categories as applying to our problem. Those references which consider pure molecular effusion, that is, no macroscopic or net mass flow velocity, and those which consider free molecular flow with a net macroscopic velocity superimposed on the random microscopic velocities. In the first category, E. H. Kennard[16], R. D. Present,[17] W. G. Pollard[18], and E. M. Sparrow[19] calculate total effusive flow through tubes of various lengths assuming pure specular reflection for particles hitting the wall, a rather poor assumption. These references do not calculate the distribution of molecular flux at the exit of the tubes, which is our primary interest.

C. A. Tsonis[20] calculates the projected distribution of molecular flux on curved surfaces of various shapes assuming a cosine distribution from a source. This information would be useful in studies involving dished or otherwise shaped accelerator systems.

Davis, Levenson, and Milleron[21] calculate flow rates and distribution patterns at the exit of complicated ducts, simple tubes and nozzles. These are lengthy, complicated calculations using Monte Carlo type techniques on a digital computer.

B. B. Dayton[22] derives an expression for distribution of molecular flux at the exit of a straight cylindrical tube. The departure of this distribution pattern from the cosine law depends on the ratio of length to radius of the tube. His calculations will be compared to some experimentally measured flow patterns in a later section of the report.

More recently Richley and Reynolds[31] have described molecular flow patterns from converging and diverging tubes by numerical methods. This work is applicable to neutral gases or slightly ionized plasmas in field free regions. All the foregoing methods are useful only in low density regions and cannot be used to analyse the flow from a typical expanding arc source.

In the second category, i.e., references which consider a macroscopic velocity superimposed on the random microscopic velocities, are the following:

H. W. Liepmann[23] calculates the total mass flow through the orifice where the gas expands to a lower pressure downstream of the orifice. No exit flux distribution calculation is attempted.

Kantrowitz and Grey[24] and Parker, Kuhlthau, and Zapata[25] have independently analyzed a nozzle assuming continuum flow in the nozzle and free molecular flow beyond the exit plane. Both analyses are one-dimensional assuming a uniform velocity and density profile (flux profile) at the exit plane, and are not adequate for the present problem.

H. S. Tsein[26] and H. Ashley[27] have derived expressions for the total flux incident on a surface from a given source but do not consider the directional distribution of velocities.

G. W. Patterson[28] derives a similar expression which is used to calculate total flow through an orifice inclined to the direction of macroscopic velocity.

Patterson and Harris[29] have derived an expression for total flow through a tube of arbitrary length where there is a constant macroscopic gas velocity normal to the tube inlet superimposed on the random thermal velocities. This derivation will be described in some detail as it illustrates the complexities involved in rigorous treatment of free molecular flow with a macroscopic velocity.

The author derives the following expression for the flow rate through a pipe:

$$(10)\quad N = \alpha\left[N_s + N_{cc}\,(S,D)\right] \;+\; (1 - 2\alpha)\int_o^1 N_{cc}\,(S,D/X)\,dx$$

N_s is the number of molecules/sec entering the tube and is evaluated by:

$$(11)\quad N_s = \frac{nC_m}{2\sqrt{\pi}}\,\pi r^2\left[e^{-S^2} + S\sqrt{\pi}\,(1 + \operatorname{erf} S)\right]$$

In these expressions, using the author's notation, erf S is the error function defined by:

$$(11a)\quad \operatorname{erf} S = \frac{2}{\sqrt{\pi}}\int_o^s e^{-Z^2}\,dz$$

$N_{cc}(S,D)$ is the function of S and D which describes the number of molecules that pass through the tube without hitting the walls, n is the atom density, and S is the molecular speed ratio of u, the constant macroscopic speed, to C_m, the most probable random speed. The geometrical characteristics of the tube are described by the dimensionless quantities D, the ratio of tube diameter to length, and X, the axial distance traveled divided by the tube length. α, a function of D, is a geometrical factor first calculated by Clausing[30].

The total number of molecules passing through a tube can be obtained from (10) once $N_{cc}\,(S,D)$ is evaluated. Referring to Fig. 34, the number of molecules which pass through an element of area dA of the inlet disc, with speeds between Λ and $\Lambda + d\Lambda$ directed between ϕ and $\phi + d\phi$, $\theta + d\theta$ in unit time is:

$$(12)\quad dA,\ n\pi^{-3/2}C_m\ e^{-\Lambda^2 + 2S\Lambda\cos\phi - S^2}\Lambda^3 d\sin\phi\cos\phi\,d\phi\,d\theta$$

Expression (12) is in spherical coordinates. The equivalent expression in rectangular coordinates is:

$$(13)\quad dA\ n\ \xi_x\ f\ (d\xi_x\ d\xi_y\ d\xi_z)$$

where f is Maxwell's distribution function:

$$(14)\quad f = \pi^{-3/2}\ c_m^{-3}\ e^{-\frac{c^2}{c_m^2}}$$

The molecular velocities are given in terms of the macroscopic and random components:

$$(15)\quad \xi_x = u_x + c_x,\ \xi_y = c_y,\ \xi_z = c_z$$

The transformation to spherical coordinates is:

$$(16)\quad \xi_x = \xi \cos\phi$$

$$\xi_y = \xi \sin\phi \cos\theta$$

$$\xi_z = \xi \sin\phi \sin\theta$$

$$d\xi_x\ d\xi_y\ d\xi_z = \xi^2 \sin\phi\ d\phi\ d\theta\ d\xi$$

$$\frac{c^2}{c_m^2} = \frac{c_x^2 + c_y^2 + c_z^2}{c_m^2} = \frac{\xi^2 - 2\xi u \cos\phi + u^2}{c_m^2} = \Lambda^2 - 2S\Lambda\cos\phi + S^2$$

To obtain $N_{cc}(S,D)$, expression (11) must be integrated over all possible speeds ($0 \le \Lambda \le \infty$), over the outlet area ($0 \le \phi \le \phi_1$, $0 \le \theta \le 2\pi$), and over the

inlet area expressed as a function of the outlet area. Needless to say this is not a simple integration. The author obtains the following expression which is not in closed form:

$$(17)\quad N_{cc}(S,D) = \frac{nCm\pi r^2}{2\sqrt{\pi}} \left[e^{-S^2} + S\sqrt{\pi}\,(1 + \operatorname{erf} S) - e^{-S^2}\ \frac{2(\sqrt{1+D^2}-1)}{D^2} - \frac{4S}{\sqrt{\pi}}\ \eta\,(S,D) \right]$$

where

$$\eta\,(S,D) = \frac{1}{D} \int_0^1 dy \int_0^{\phi} (1 + \operatorname{erf} S \cos \phi_1) \cos \phi_1 e^{-S^2 \sin^2 \phi_1}\, d\phi_1$$

$\eta\,(S,D)$ is evaluated by expanding the integrand in several series expansions which hold for small D (i.e., long tubes) and small S and integrating each term. The final result is of the form:

$$(18)\quad \eta(S,D) = \pi(1 + \operatorname{erf} S) \sum a_i\ I_i + 2\sqrt{\pi}\ e^{-S^2} \left[\frac{F'(u_o)}{1!} \sum b_j I_j + \frac{F''(u_o)}{2!} \sum C_k\, I_k + \frac{F'''\,(u_o)}{3!} \sum d_e\, I_e + \frac{F'''\,(u_o)}{4!}\ \sum e_m\, I_m + \cdots\cdots \right]$$

The coefficients and first few terms of each series is listed in the appendix of reference (29).

The fairly rigorous derivation above can be extended to our analysis of free molecular flow from the transition plane on out to the plate. One can visualize the transition plane as the tube entrance plane in Fig. 34 and the collecting plate as the exit plane of the tube where the exit diameter of the tube is now larger than the inlet diameter as illustrated in Fig. 35. N_{cc} (S,D), the number of molecules that pass through the diverging tube without hitting the walls, would be the number that hit a plate of the same diameter as the exit plane.

The number density, n, and the macroscopic speed, u, are known from the continuum analysis. Expressions analogous to (9) and (10) could be written, but complicated by three additional considerations. (a) The inlet diameter is not equal to the outlet or plate diameter. (b) The number density n is not constant over the transition plane (inlet area), but is a function of the radius $n=n(r,\theta)$. (c) The macroscopic velocity is neither constant nor normal to the transition plane. Thus, $u=u(r,\theta,\phi)$.

While reference (29) calculates the total flow only, the exit angular flux distribution corresponding to a flux distribution on a plate could be obtained by integrating over all speeds and over the inlet area only. In general, even relatively simple expressions for $n=n(r,\theta)$ and $u=u(r,\theta,\phi)$ would increase the difficulty of already complex integrations beyond the point of practicality.

A numerical computer study might be attempted in the following way. For an axisymmetric source, n and u would be known at the transition plane

at each infinitesimal dA. Assuming n and u constant over dA, the number of molecules which pass through the element of area dA_1 with speeds between Λ and $\Lambda + d\Lambda$ directed between ϕ and $\phi + d\phi$, $\theta + d\theta$ in unit time is:

$$(19)\quad dA_1 n_1 T_1^{-3/2} C_m e^{-(\Lambda^2 - S_1^2)} \Lambda^3 \, d\Lambda \sin\phi \cos\phi \, d\phi \, d\theta$$

where the molecular velocities are:

$$(20)\quad \xi_{1x} = u_{1x} + C_x,\ \xi_{1y} = u_{1y} + C_y,\ \xi_{1z} = u_{1z} + C_z$$
$$C_x = \xi_{1x} = (\xi_1 - u_1)\cos\phi$$
$$C_y = \xi_{1y} - u_{1y} = (\xi_1 - u_1)\sin\phi\cos\theta$$
$$C_z = \xi_{1z} - u_{1z} = (\xi_1 - u_1)\sin\phi\sin\theta$$

Integration of (19) over all speeds and over the inlet area only would give the flux distribution at the plate contributed by dA_1. Integration of (19) over all speeds ($0 \leq \Lambda \leq \infty$) can be accomplished by a simple substitution. dA_1, once expressed as a function of the outlet area, could be integrated from r_1 to r_o and with respect to θ from $0 \leq \theta \leq 2\pi$ because of the axisymmetric source.

This procedure could be repeated for a number of dA's along the radius. The number of dA's required for accuracy would depend on the steepness of the velocity and density (flux) distribution at the transition plane.

The total flux distribution at the plate is obtained by adding the individual contributions from each ring shaped area of the transition plane.

Practical Considerations

All the methods described above are too complex for practicality even when the effect of the electromagnetic field is neglected, and when the added complexities of the field are taken into account the feasibility of a rigorous solution of the problem by purely analytical means is doubtful.

An alternate empirical approach is possible, in which the flow pattern issuing from each source is determined once by experimental means, and then described and projected, using the assumption of collisionless flow, on any desired surface at any desired angle by appropriate analytical expressions.

Analytical Expressions for Axisymmetric Flow Patterns

Uniform Flux

The simplest flow pattern possible is of course one in which the density is a constant over the entire area of any cross section normal to the flow path. This situation may be approached eventually in a very large multiple-source engine, or by electromagnetic control, but at present somewhat more complex flow patterns must be considered.

Spherically Symmetrical Expansion for a Point Source

For a point source of plasma expanding with spherical symmetry the particle flow rate is the same in all directions per unit solid angle. The flux normal to any spherical isobaric surface is inversely proportional to the square of the distance from the source, since the spherical area intercepted by the constant solid angle, dw, is directly proportional to the square of the distance from the source. The geometry of this pattern is illustrated in

derived in Ref. (22), to construct distribution curves for interception of the beam by a flat plate normal to the beam axis. Typical results are shown in Fig. 38 for a few length to radius ratios. It can be seen qualitatively from these curves that the more desirable flat distributions associated with small L/R ratios lead to a very undesirable gradual density fall-off at the perimeter of the beam. It will be seen later that this characteristic is retained in the experimentally determined flow patterns.

Evaluation of Flow Patterns

Assume that we have some known flux distribution $F(\theta)$ across a flat plate. Fig. 39 shows a cross section of a typical distribution where the total flux corresponds to the volume enclosed when this curve is rotated around the central axis. Fig. 40 shows the geometry of the following derivation. The total flux through an incremental area is given by the product of the flux per unit area and the area:

$$(28) \quad F_A = F(\theta_A)\, dA$$

where dA is equal to $2\pi x\, dx$, but $x = r \tan \theta$ and $dx = r \sec^2 \theta\, d\theta$, so that (28) becomes:

$$(29) \quad F_A = 2\, F(\theta_A)\, r^2 \tan \theta \sec^2 \theta\, d\theta$$

The total flux over the whole plate is equal to the integral of (29).

$$(30)\quad F_{total} = 2\ r^2 \int_0^{\pi/2} F(\theta)\ \tan\theta\ \sec^2\theta\ d\theta$$

and the flux within the limits set by, for example, a 3/1 density ratio is

$$(31)\quad F_o = 2\ r^2 \int_0^{\theta} F(\theta)\ \tan\theta\ \sec^2\theta\ d\theta$$

The decimal fraction of allowable flux is given by dividing (31) by (30):

$$(32)\quad \frac{F_\theta}{F_{total}} = \frac{\int_0^{\theta} F(\theta)\ \tan\theta\ \sec^2\theta\ d\theta}{\int_0^{\pi/2} F(\theta)\ \tan\theta\ \sec^2\theta\ d\theta}$$

A similar process to this can be followed for any analytically described flux function.

Evaluation for $F(\theta) = \cos^n\theta$

Equation (32) can be evaluated for $F(\theta) = \cos^n\theta$. Where n is less than three, the total flux is infinite, corresponding to uniform flux between infinite plane parallel plates. If we arbitrarily limit the density ratio to 3:1, evaluation of (29) for n = 3 becomes:

$$(33)\quad \frac{F_\theta}{F_{total}} = \frac{\int_0^{\theta} \cos^3\theta\ \tan\theta\ \sec^2\theta\ d\theta}{\int_0^{\pi/2} \cos^3\theta\ \tan\theta\ \sec^2\theta\ d\theta}\ ,\ \theta = 43.9^\circ$$

$$(34)\quad \cos^3\theta\ \tan\theta\ \sec^2\theta = \sin\theta$$

and (33) becomes:

$$(35)\quad \frac{F_\theta}{F_{total}} = \frac{\left[-\cos\theta\right]_0^{43.9}}{\left[-\cos\theta\right]_0^{\pi/2}} = \frac{\left[-.6938+1\right]}{\left[0+1\right]} = 0.3062$$

Similar integrations have been performed for n = 4, 5, 6, 10, and 15 and the results are given in Table III.

TABLE III

Flux Distribution Parameters for $\cos^n\theta$ Functions

n	$\theta_{1/3}$	F_o/F_{total}	n	$\theta_{1/3}$	F_o/F_{total}
3	43.9°	.306	6	33.6°	.511
4	40.5°	.422	10	26.4°	.584
5	36.6°	.484	15	21.7°	.615

These results are plotted in Fig. 41, where it can be seen that the desirable flat distributions, corresponding to lower powers of n, result in poor propellant utilization. With steeper distribution functions, which are intrinsically undesirable, the curve asymtotically levels off. The height of the horizontal portion of the curve could be improved only by accepting a larger flux ratio. It appears therefore, that single sources producing any kind of a $\cos^n\theta$ pattern will not be suitable when projected on flat accelerator systems normal to the beam axis. Two alternate methods around this difficulty are tilting the beam axis and using multiple sources.

Projections of Flux Distribution on a Flat Plate Tilted to the Beam Axis

Since the accelerator plane will always be normal to the accelerated beam axis, a "tilted" plate in the following derivations means that the plasma beam axis from a single source is directed at an angle to the plate.

In the case of a spherically symmetrical distribution, tilting the source has no effect on the flux distribution over the plate, except for a linear displacement of the peak of the $\cos^3\theta$ curve, corresponding to the shift in location of the source exit. Fig. 42 illustrates this.

For the cases where there is some jetting, i.e., the cosine distribution for a knife edge orifice or some higher power of the cosine, the distribution on a plate tilted to the beam axis is derived as follows:

Consider the situation sketched in Fig. 43. The beam axis r_o is tilted at an angle α from the perpendicular distance to the plate, and the angular distribution function around r_o is some function of θ'. By simple addition:

$$(36) \quad \theta' = \theta - \alpha$$

for all positions, if signs are preserved.

Thus $F(\theta') = F(\theta - \alpha)$. The perpendicular area intercepted by a solid angle dw is proportional to the distance squared, so that:

$$(37)\quad \frac{dA_1}{dA} = \frac{r_1^2}{r^2} = \cos^2\theta$$

and the projection of this area on the flat plate is expressed by:

$$(38)\quad dA = dA_p \cos\theta$$

Combination of (37) and (38) leads to:

$$(39)\quad \frac{dA_1}{dA_p} = \cos^3\theta$$

Dividing the flux per unit solid angle by these areas and multiplying by the appropriate functions, the flux ratio per unit area is seen to be:

$$(40)\quad \frac{F_p}{F_1} = \frac{F(\theta-\alpha)}{F(\alpha)} \cos^3\theta$$

where the factor $F(\theta - \alpha)/F(\alpha)$ describes the flux density at angle θ, and the $\cos^3\theta$ represents projection on the plate, as was shown previously for a simpler case.

Theoretical density patterns similar to those of Fig. 38 have been projected at various angles in Figs. 44, 45, and 46. The variety of the patterns can be best explained with reference to Fig. 45. Two factors leading to high density are present; the nearness of the source to the plate at a given angle, and the higher flux near the axis of the beam issuing from the source. When the angle of projection is moderate (e.g. 40°-50°) the distance from source to

plate along the beam axis is only slightly lengthened, and the dominant factor is the density peak at this angle. At larger angles of projection (e.g. 60°) the distance from source to plate along the beam axis is considerably elongated, and neither factor is dominant. Beyond this point the angle of projection is so large (e.g. 70°) that the nearness of the plate at angles less than the beam inclination, becomes the dominant factor. Comparison of patterns among the three figures at equal angles of inclination shows that the tube geometry as well as the angle of inclination is critical.

In judging the desirability of a given pattern, it must be remembered that tilting the source destroys the axisymmetry, and that the projections shown are central cross sections of the long dimension of a three-dimensional pattern. Also it is helpful to remember that just about 50% of the flux falls on either side of the point of impingement of the beam axis. This latter fact detracts from the suitability of even the best single pattern of Fig. 45 on the grounds of poor propellant utilization. Tilting of the source, therefore, does not solve the problem of plasma flow control, but merely provides an additional method of producing versatile density patterns.

Density Patterns from Multiple Sources

The concept of using multiple sources, based on the assumption that collisionless flux from several independent sources can be added numerically, is illustrated in a simplified manner in Fig. 47. This figure shows a cross section of the density pattern coplanar with the two sources producing it. In practice, as will be shown later, the measured patterns from three or more sources are used, and the overall density pattern is determined numerically

on a digital computer. Very good overall density patterns may be obtained by this method if many sources are used and a wide selection of individual density patterns is available.

HARDWARE

Fuel Feed System, Sources, and Vacuum Chamber

The sources and fuel feed system described in the previous section were used to study aerodynamic flow patterns. The sources are illustrated in Fig. 2 through Fig. 12, some of which were designed primarily for source performance and/or electromagnetic flow control. Boiler and fuel feed systems are illustrated in Fig. 17 through Fig. 21. The vacuum system used exclusively to determine density pattern variation is sketched in Fig. 15.

Distribution Probes

The double plate distribution probe sketched in Fig. 48 was used early in the program to outline rough density patterns. The plates are operated as total probes independently, and the sum of the ion current to both plates is a measure of the ion flow rate. The plates are located close enough together so that cesium flowing through the holes in the front plate is collected in separated spots on the back plate. These spots are individually hydrolysed and titrated as total cesium flow to the area in question, which at high degrees of ionization is a good approximation to the ion flow as well. The total cesium found on each plate by titration may be checked against the ion current to each plate. This probe was replaced early in the program by the more versatile and efficient design described below.

The plasma distribution probe design used in most of the density pattern studies is shown in Fig. 49. This probe consists of a liquid nitrogen cooled 12" diameter circular steel plate, mounted on the vacuum system through a double O-ring vacuum seal. Across one diameter of the plate, and electrically insulated from it by means of boron nitride inserts, is a series of 28 small probes, spaced at intervals equal to those of our present accelerator elements. The high thermal conductivity of the boron nitride inserts permits cooling of these point probes without direct contact with the liquid nitrogen. The whole apparatus can be rotated 180° around its central axis or translated normal to the axis a distance of about 12 inches without breaking the vacuum seal. Thus, the density of any point in the expanding plasma may be examined.

This device also serves as a total probe. The 28 small probes and the plate itself are connected in parallel to the cathode of a floating power supply, and a 0.020" tantalum wire is suspended across the face of the plate above and below the line of point probes. This wire serves as the anode for all the probes, and above the saturation potential collects all the electrons necessary to neutralize the ions flowing to the plate and point probes. When the plate is close enough to the source to receive all the plasma, the sum of ion currents to all the probes (including the plate) is a measure of the total ion flow. At the conclusion of a run, the total cesium flow can be determined by collection and titration of all the cesium condensed on the probe. The electrons reflected from the large cathode surface freely move throughout the expanding plasma region, and may help to reionize small percentages of neutrals which may be present. However, this same phenomenon will occur when the plate probe is replaced by a floating perforated plate electrode.

In the original design it was assumed that the probe heads themselves would provide sufficient shadow shielding for the insulating boron nitride inserts, but the first few runs were terminated after about 20-30 minutes due to a cesium film buildup and consequent shorting between plate and probes. The running time was extended to about one hour by the shadow shield design shown in Fig. 50 (top sketch). This design did not allow for the angle of incidence of the beam at the peripheral probe locations, and was modified as shown in the bottom sketch. With this design, runs of two hours duration were routine before shorting of the probes. A fixed source to probe distance is one of the factors in the design. The final design of the probe itself, with wire anodes and shadow shield in place, is shown in Fig. 51. The four inch wide radial extension spot welded to the outer circumference of the plate insures collection of nearly all the plasma.

EXPERIMENTAL PROCEDURE

Source Performance Determination

It is necessary to determine degree of ionization and ion generation power as well as density pattern in all tests to insure that desirable overall performance is maintained. In a typical run, the distribution probe is first located close enough to the source to collect all the plasma, and the source performance characteristics are recorded briefly as described in the previous section. Sufficient readings are usually taken at this time to optimize the degree of ionization with respect to arc controls, but the probe is not kept in the close up position for any longer than necessary, to avoid rapid coating of the probe insulators. At some suitable larger distance the density pattern is then examined, at which time a small part of the plasma misses the outer edge of the probe, is neutralized on some other warm surface, and migrates eventually to the cold probe. At the conclusion of the run the source characteristics are examined in more detail with the probe in the close up position, using the probe as a total probe only. Coating of the individual probe insulators does not affect the total ion current readings.

Density Pattern Representations

Each probe is connected to a monitoring milliammeter and through a switching arrangement to a single more sensitive milliammeter. Each probe current is therefore read on the same meter to a precision of $\pm$ 0.05 ma. When a cursory examination of the distribution as a function of the probe rotation indicates axisymmetry, a

single cross section is read and assumed to be representative. When the distribution is not axisymmetric the beam axis may be normal to the probe but displaced radially, in which case the probe angle at which the readings are highest is assumed to represent the axisymmetric cross section. Only if the beam axis is at an angle to the probe plane is it necessary to take readings at numerous settings of probe rotation.

Therefore, the beam axis is always closely aligned normal to the probe plate and pointed directly at the probe axis of rotation. This is accomplished by inserting a snug fitting pointer in the source orifice which reaches to within a few millimeters of the probe plane. The source alignment is then adjusted until the pointer is aimed normal to the central probe, then the tank is evacuated and the source heated to make sure that neither operation distorts the alignment. It has been found experimentally that when a run is made under these conditions, the density pattern is close to axisymmetric.

Axisymmetric density patterns from single sources are shown in cross section. More complex patterns are illustrated as contour diagrams. In the first few cases, before the source to probe distance was fixed, the normalized flux was plotted against the tangent of the angle off the beam axis. This technique makes all patterns comparable at any flow rate and any source to probe distance. After the source to probe distance was fixed, the normalized flux was generally plotted against probe location for convenience.

EXPERIMENTAL RESULTS AND DISCUSSION

The Effect of Source to Probe Distance

In order to eliminate the need for examining each source at various source to probe distances, it is necessary to show that the distribution pattern plotted in normalized or dimensionless terms is not changed by varying the source to probe distance. Fig. 52 illustrates that this is so when the normalized flux is plotted against the tangent of the angle of impingement for two different source to probe distances. The two experimental patterns are identical except for a slight lateral displacement due to source alignment. These particular results have been corrected for sheath error, the validity of which is established later, to bring out the identity of the pattern.

The Necessity of High Ionization Levels

The necessity of maintaining high levels of ionization from the point of view of power efficiency and propellant utilization is obvious. In addition, high ionization levels are required for adequate measurement of plasma density distribution, since it is not known at present if the ionization level is constant at all locations in the beam. Therefore, only at high levels of ionization can the total distribution, which is the required quantity, be approximated by the ion distribution, which is the measured quantity.

In this report, no density pattern measured below 80% ionization is included. This is an arbitrary limit and more confidence should be placed in validity of the patterns measured at the higher degrees of ionization.

Source Design I and II

These sources were built and tested during the source development phase of the program, and were not examined for density pattern. Source III will be recognized as a more sophisticated version of Source II, without the axial anode, and Sources IX, X, and XI are merely advanced versions of Source I. Density patterns of all types of source shown in Fig. 2 through Fig. 12 are therefore represented.

Source Design III

Source III is the "plug nozzle" design shown in Fig. 4. The location of the plug determines the annular throat width and to some extent the direction of the flow. Fig. 53 shows typical patterns* obtained with the plug position set to produce an annular gap of 0.023". There is some evidence that the presence of the plug contributes to beam spreading. Fig. 54 shows similar results for an annular gap of 0.047" at a higher flow rate. Here either the higher flow rate or the wider opening has destroyed the effect of the plug.

*Aerodynamic density patterns are not corrected for sheath effects unless otherwise specified. Since none of the patterns approach the desired shape even remotely, the slight sheath corrections would be trivial.

It is probable that the presence of the metallic plug, either grounded to the source or floating, interferes with the passage of the arc through the throat. The relatively low degrees of ionization shown in Table I may confirm this. Several runs were attempted with the plug made of boron nitride, but no arc was struck under these conditions, possibly due to high resistance over the arc path through the throat. Further study with sources of this type is needed before their ultimate usefulness can be decided.

Multiple Orifice Source Designs

The source shown in Fig. 5 with a nozzle half angle of 25° and the peripheral openings pitched 15° off axis, was tested for performance and density pattern early in the program. The possibility that the arc current might be too intense through some of the openings and too weak through others was recognized, and one of the main purposes of the tests was to ascertain whether sources of this type were at all feasible. The best levels of ionization obtained with this source were only 60%-65%, which may have been due to either poor arc current distribution or to the floating metal orifice plate acting as a deionizing surface. The only significant density pattern* was obtained at a low flow rate, where the flow through the openings may have been collisionless. This pattern is shown in Fig. 55, compared with the pattern calculated by adding the theoretical flow from the individual openings, assuming

*This pattern is reported despite poor ionization, since it seems to confirm the likelihood of molecular flow at low ion currents.

molecular flow. The effect of the nozzle was neglected in calculating the predicted curve. At higher flow rates, where the flow through the plate openings was not molecular, there was no similarity between the predicted and observed pattern.

Further work on this type of source was cancelled, in view of the poor performance and undesirable density pattern.

Source Designs VII and VIII

Source Design VII and VIII are illustrated in Fig. 6. The interchangeable orifice inserts are used to see if the flow approximates that predicted by Dayton, i.e., molecular flow from tubes for different length to diameter ratios. The multiple anode design allows the use of any single anode or any anode combination for a given assembly. One or two of the upstream anodes can be removed as shown in Fig. 9. The effect of these variations on source performance has been discussed in the previous section (see Table II). The effect of the nozzle dimensions on flow pattern will be covered in this section.

The only difference between Source VII and VIII, is the nozzle half angle. The boron nitride plugs were later substituted for tantalum plugs in an attempt to improve ion generation efficiency.

Effect of Orifice Dimensions and Nozzle Shortening

Figs. 56, 57, and 58 are cross sections of the density measured using Source VII shown in Fig. 6, with orifice inserts of different length/radius ratio compared with the theoretical distribution predicted for molecular flow through tubes in flat plates. With a constant orifice radius the flow in theory should jet more with increasing tube length, as can be seen from the theoretical curves shown. The notation "shortened nozzle" on the curve indicate that the rear two removable sections of the nozzle, consisting of a boron nitride spacer and a tantalum anode, have been removed. The effect of this change is to shorten and widen the nozzle without changing the half angle and to move the anode, which is part of the nozzle wall, upstream and out radially. It can be seen that the overall effect of this change with any of the three inserts is negligible, indicating that the nozzle has little effect on the flow, and that the flow is molecular downstream of the orifice exit. Fig. 59 shows the pattern for all three tube geometries, among which there is little variation. Comparison with the theoretical curve shown for a knife-edge orifice indicates that there is some jetting effect, i.e., that molecular flow does not start at the tube exit, but exists part way up the tube. The effective length/ratio for all three tubes, i.e., the length over which molecular flow dominates, appears to be about 2.5. For these inserts, this corresponds to a tube length of 0.125", which is almost equal to the mean free path at the pressure of 1 torr near the orifice exit.

The Effect of Nozzle Half Angle

Fig. 60 was constructed from data taken with Source VII and Source VIII, both shown in Fig. 6. The only difference between the two sources is nozzle half angles of 30° and 15° respectively. The tests were run with all three anodes in place. The more acute nozzle gives rise to a steeper density pattern as expected, despite the fact that the flow rate through the 30° nozzle was 1360 ma. and that through the 60° nozzle was 1620 ma. It will be seen below that steeper patterns are usually associated with high flow rates.

The Effect of Flow Rate

The density pattern variation with flow rate is shown in Fig. 61. The highest flow rate gives a distribution which is somewhat more peaked than the other two which, may be due to partial continuum flow in the nozzle and a jetting effect. The patterns for the two lower flow rates are roughly similar; toward the center of the beam the lowest flow rate pattern seems steeper but toward the periphery of the beam the medium flow pattern seems steeper. These variations may be due to either complex continuum versus molecular flow relationships or to a sheath effect near the probes.

Nozzle Shortening Effect with 15° Half Angle Nozzle

The nozzle shortening effect discussed above for the 30° half angle nozzle was re-examined for the 15° half angle nozzle. The results, shown in Fig. 62, confirm that this effect is minor.

The Effect of Tilting the Beam Axis

Fig. 63 shows the effect of directing the beam axis at an angle to the collector. The density peak is shifted toward the direction of the beam axis and the curve shows slower decay in the direction of the beam axis as predicted from theoretical projection. The rate of decay of the beam from the tilted source is slightly steeper than that predicted. This is due to the fact that the shadow shield for the probes was not designed for this angle of incidence.

The effect of larger angle of tilt, say 60°, would probably be very much greater as predicted in Figs. 44, 45, and 46 but our present setup makes investigation above a tilt of 45° difficult. It may be noted here that the equations for theoretical projection are entirely valid in a region of molecular flow and since the experimental data presented above indicates molecular flow, experimental confirmation of the predicted patterns is not essential at present.

Source Designs IX, X, and XI

These sources, shown in Figs. 10, 11, and 12 were designed mainly for high performance, not for aerodynamic study. Aerodynamic density patterns of Source IX, and XI were determined, however, the first for use in conjunction with an accelerator study, the second as a base for comparison with electromagnetic patterns. These experiments are not pertinent to this section of the report and will be covered later. It may be stated here that the aerodynamic density patterns are of the same type as those shown above, and add nothing to the present series.

Multiple Source Patterns

Despite the wide variety of sources and conditions tested the density patterns described above follow the same general pattern, varying only in steepness. It was shown in Fig. 41 and the associated discussion that no simple distribution curve of this type will satisfy the requirements for good performance since integration of the curves between any reasonable density variation limits leads to plasma utilization of the order of 50-60%. However, since the beams are in molecular flow downstream of the source, multiple or compound sources can be placed so as to produce distributions of any desired flatness and propellant utilization, by algebraic addition of the flow from the individual sources. Since it is necessary to use as few sources as possible to keep the fuel feed system simple, the wide selection of measured patterns available from the aerodynamic survey is desirable.

A program has been designed and tested on an IBM 7090 digital computer which computes the total flux through any point in a plane from an unlimited number of sources located anywhere and oriented at any angle with respect to the plane. The patterns from the individual sources need not be identical.

An early sample calculation by this method is illustrated in Figs. 64 and 65. Fig. 64 is an axial view of a contour diagram secured by rotating a cross section of a selected measured density pattern 360° around the beam axis. Fig. 65 is a contour diagram secured by superimposing the patterns of Fig. 64. The increase shown, from 46.5% to 78% of the total flow within the arbitrary 3:1 density limits, was obtained with only four identical simple patterns at unoptimized locations.

Optimization with respect to number, type, and location of sources, angle of inclination, and flow rate would undoubtedly raise the propellant utilization considerably. Further work along these lines was postponed pending the outcome of the electromagnetic nozzle study described in a later section.

EVALUATION OF RESULTS

General Method

The general method of evaluating the density patterns shown in Figs. 52 through 63 is to symmetrize the curve, rotate it around the axis of symmetry, and evaluate the volume thus enclosed as a function of the distance from the beam axis. If the flux density determination is fairly accurate, the integrated total flux should approach 100% as the off axis distance increases. When this method was first applied, using the ion current densities calculated from the probe currents and the area of the openings in the shadow shield, low results were obtained when the integrated flux was compared to the total ion current. When no shadow shield was used and the ion current densities were calculated from the probe currents and the exposed area of the probe faces, high results were obtained. This was interpreted as a sheath effect, since in the former case the sheath around the shadow shield would reduce the effective area of the opening, while in the latter case the sheath at the probe edges would increase the effective area of the probe.

This interpretation was confirmed by the fact that when the shadow shield was allowed to float instead of being negatively charged, the ion current to the distribution probes increased.

When the shadow shield is in place, this sheath cannot be eliminated electrically without forcing the shadow shield to plasma potential, in which case the entire random electron current to the shadow shield would be accepted - an in-

conveniently large amount. Removing the shadow shield does not help either, since the probes themselves are subject to this edge effect and the current density measurements would be high instead of low. Nor can a constant correction to the area be made since the sheath thickness is a function of the current density which is variable.

Sheath Correction

If the approximate assumption is made that the sheath is parallel to all charged surfaces, correction can be made to the current density with the aid of Child's Law in the form:

$$(41) \quad X^2 = \frac{(2\ e/m)^{1/2} V^{3/2}}{9\ j}$$

where X is the sheath thickness, e/m the charge to mass ratio for the ions, and V the potential difference for a current density j. The apparent current density is related to the actual current density by:

conveniently large amount. Removing the shadow shield does not help either, since the probes themselves are subject to this edge effect and the current density measurements would be high instead of low. Nor can a constant correction to the area be made since the sheath thickness is a function of the current density which is variable.

Sheath Correction

If the approximate assumption is made that the sheath is parallel to all charged surfaces, correction can be made to the current density with the aid of Child's Law in the form:

$$(41) \quad X^2 = \frac{(2\ e/m)^{1/2} V^{3/2}}{9\ j}$$

where X is the sheath thickness, e/m the charge to mass ratio for the ions, and V the potential difference for a current density j. The apparent current density is related to the actual current density by:

$$(42) \quad j_i = j_o \frac{(R - X)^2}{R^2}$$

where R is the uncorrected radius of the perforation in the probe shield, X is sheath thickness, and j_o and j_i are true and observed current densities, respectively. To secure a correction curve over a range of current density with potential as parameter, a series of true current density values are assumed, sheath thickness is calculated for a range of potential, and equation (42) is solved for corresponding values of observed current density. The results are

shown in Table IV and Fig. 66, illustrating the range of correction from a few percent at high current density to values more than double the observed values in the low 10^{-5} ampere range.

The approximate nature of these corrections makes it desirable to check the validity of results insofar as they are related to the pertinent parameters of the program, namely, density pattern and percent of flow within prescribed density limits. The effect on density pattern and the validity of the corrections were checked experimentally as follows: One run was made at a given flow rate with the shadow shield in place, and a second run was made with the shadow shield removed. In the latter case, sheath corrections are negative, i.e., the observed current densities are higher than the true values. The observed and corrected current densities for these two runs are shown in Table V. Comparison of the corrected columns shows close correlation despite the somewhat erratic observations obtained without shadow shielding. The probe to plasma voltage in both cases was approximated by the voltage between the cathode (probe) and the anode (wire) of the total probe.

The validity of the space charge corrections was checked by a second, independent method. If valid probe readings are plotted against probe radius, and the resulting curve rotated 360° around the beam axis, the volume thus generated from $0 < R < \infty$ represents the total flow, which is also measured directly as the sum of the distribution probe and total probe readings. Two methods of securing the total flow by this method are illustrated in Fig. 67. The circles represent actual data points, corrected for Child's Law as described above, and the curve is the graph of the analytical function:

TABLE IV

Date for Sheath Effect Corrections to Observed Current Density

Probe Radius = 0.277 cm.

J_o	V = 15 Volts			V = 20 Volts			V = 25 Volts		
Amp/cm^2	X, cm	(R - X)	J_i	X, cm	(R - X)	J_i	X, cm	(R - X)	J_i
10^{-5}	0.1775	.0995	1.29×10^{-6}	.205	.0720	6.75×10^{-6}	0.242	.035	1.6×10^{-7}
2×10^{-5}	0.1257	.1513	0.58×10^{-5}	.1448	.1322	4.55×10^{-6}	0.171	.106	2.93×10^{-6}
5×10^{-5}	0.0795	.1975	2.53×10^{-5}	.0915	.1855	2.24×10^{-5}	0.108	.169	1.86×10^{-5}
1×10^{-4}	0.0562	.2208	0.635×10^{-4}	.0647	.2123	$.587\times10^{-4}$	.0768	.2002	4.00×10^{-5}
2×10^{-4}	0.0397	.2373	1.46×10^{-4}	.0458	.2312	1.39×10^{-4}	.0543	.2227	5.21×10^{-5}
5×10^{-4}	0.0252	.2518	4.13×10^{-4}	.0289	.2481	4×10^{-4}	.0344	.2426	3.83×10^{-4}
1×10^{-3}	0.0178	.2592	0.875×10^{-3}	.0205	.2565	$.857\times10^{-3}$	.0242	.2528	8.31×10^{-4}
2×10^{-3}	0.0126	.2644	1.81×10^{-3}	.01448	.2625	1.79×10^{-3}	.0171	.2599	1.756×10^{-3}
5×10^{-3}	0.0080	.2690	4.70×10^{-3}	.00915	.2678	4.67×10^{-3}	.0108	.2662	4.61×10^{-3}
1×10^{-2}	0.0056	.2714	0.959×10^{-2}	.00647	.2705	$.953\times10^{-2}$	.0077	.2693	9.43×10^{-3}
2×10^{-2}	0.0040	.2730	1.94×10^{-2}	.00458	.2724	1.93×10^{-2}	.0054	.2716	1.92×10^{-2}
5×10^{-2}	0.0025	.2745	4.90×10^{-2}	.00289	.2741	4.89×10^{-2}	.0034	.2736	4.87×10^{-2}

$$(43)\quad F_R = 10^8 F_o / (R^2 + 100)^4$$

which is slightly lower than the experimental points. Here F_o is central flux and F_R is flux at a radius R. One method of securing the total flow is to integrate equation (43) from $0 < R < \infty$ and $0 < \theta < 2\pi$ where θ is the angle of rotation of the curve about the beam axis. An alternate method is to integrate numerically, using the probe current densities to approximate the average current density over the area corresponding to the probe distance. In the example illustrated, the values obtained by integrating the analytical expression are about 90% of the values obtained by numerical integration. This discrepancy can be made as small as desired by matching the measured pattern and analytical expression more precisely by computer methods.

TABLE V

Observed and Corrected Current Densities for
A Selected Pattern With And Without Shadow Shield

With Shadow Shield		Without Shadow Shield	
Observed	Corrected	Corrected	Observed
.722	.84	.85	.897
.618	.73	.77	.807
.564	.67	.71	.807
.519	.62	.63	.673
.490	.59	.63	.673
.440	.54	.54	.583
.386	.48	.55	.594
.311	.39	.40	.426
.232	.30	.31	.336
.079	.12	.18	.202
.050	.08	.06	.067

Analytical expressions such as equation (43) are useful in evaluating multiple source patterns. The numerical method of integration is more convenient in evaluating single patterns.

The validity of the sheath correction method given above is supported by Fig. 68, where the percent of flow within a given radius is plotted against the radius. The corrected curve approaches the theoretical level of 100% at large radius within a few percent. This behavior is typical of every curve evaluated to date.

Specific Method of Comparison

The density patterns and contour diagrams shown in Figs. 52 through 65 serve the purpose of presenting a physical picture of the flow pattern, while curves similar to that of Fig. 68 illustrate ultimate propellant utilization. Neither of these methods, however, are very useful for comparison or overall evaluation of flow patterns, since propellant utilization and beam current density, hence density variation, must be considered simultaneously.

The percentage of the total flow within selected density variation limits is the primary criterion for evaluating flow patterns. Fig. 69 illustrates a comparison based on this criterion, of the steepest and the flattest single aerodynamic density pattern obtained in this study. A curve for a multiple source pattern is also included which is the result of a calculated superposition of four of the steepest aerodynamic patterns obtained. The superiority of the multiple source in producing higher cumulative flux at any level of density variation is at once obvious when this method of presenting the data is used.

III. ELECTROMAGNETIC NOZZLE DEVELOPMENT

THEORY

Electrostatic Reflection of Plasma Ions

Consider a neutral collisionless plasma drifting through a cylindrical or conical tube. Ions and electrons strike the wall at random but the velocity of the electrons is so much greater than that of the ions that the electron current density is several hundred times the ion current density. If this current is not drained from the tube walls a space charge sheath is quickly established by the bombarding electrons which limit the electron flow to a level which exactly balances the ion flow, and the wall assumes the potential of an insulated probe, negative with respect to the plasma.

At this point all the random thermal ion current to the wall is accepted and neutralized. Any attempt to reflect ions by forcing the wall potential more positive than the plasma will result in electron currents to the wall equal to the random electron current which strikes the wall in the absence of a space charge sheath. Some method of limiting this current is obviously desirable.

Magnetic Control of Electron Current

If the plasma is contained in a solenoidal magnetic field the charged particles of both species will describe spiral paths around the magnetic lines of force between collisions which depend on the angle of motion to the field, the velocity and mass of the particles and the magnetic field strength. Equation

(44) describes the spiral trajectories of single particles in terms of a radius of curvature r.

$$(44) \quad r = \frac{100}{H} \sqrt{2.07\ MV}$$

where H is the magnetic field strength in gausses, M is the molecular weight per unit electronic charge, and V is the component of the voltage normal to the magnetic field through which the particle has been accelerated. The parallel components of the motion are of course not affected by the field. For cesium ions and electrons nearly in thermal equilibrium, equation (44) predicts an average electron radius of curvature some 500 times smaller than that of the ions.

Consider the experimental arrangement of Fig. 71. If the field strength due to the magnetic coil is set at a very low value, electrons and ions both travel helical paths of radii bigger than the apparatus and the phenomena at the cylinder wall described earlier is largely unchanged. As the field strength is increased some of the slower moving electrons and those which have small velocity components normal to the field are confined to helical paths which do not intercept the wall, thus reducing the total possible random electron current to the wall. This effect will continue with increasing field strength until the random electron and ion currents to the wall are equal. At any point during this process the wall could be positively charged with a smaller penalty in electron current than before.

If the field strength is increased beyond this point the theory predicts, neglecting plasma instabilities and collisions, that the random ion current will exceed the random electron current, a positive potential will be assumed by the wall and some ions will be reflected. Eventually, some field strength would be reached where even the most energetic electrons would be constrained from reaching the wall and the wall could be positively charged with respect to the plasma with no resulting electron current penalty. This condition would result in total reflection of all ions.

Finally, if the field is made sufficiently strong, ions as well as electrons will be restrained from striking the wall by magnetic forces alone.

Quantitative Aspects

Although the basic principles of operation of an electromagnetic nozzle, described qualitatively above, indicate the feasibility of ion trajectory control in a neutral plasma, the more quantitative aspects complicate the problem considerably. To begin with, frequent collisions in the plasma would more or less destroy any effective control, and the electromagnetic nozzle is fully effective only in a region of molecular flow, and only partially effective in continuum flow whenever the radius of curvature of the particle trajectories is much smaller than the mean free path. This latter statement is justified by the fact that axially directed collisions are not restricted by the magnetic field. Further complications are introduced by the knowledge that the ions and electrons are not in thermal equilibrium, and that the velocity distribution

for both particles is determined by superposition of complex field effects on the aerodynamic expansion. Furthermore, the circular spiral paths predicted by equation (44) are distorted into elliptical spirals or cycloids by radial components of the electric field.

Finally, the shape and penetration into the plasma of the potential field arising from the charge on the nozzle form cannot be predicted from any simple form of Child's Law, since the motion and hence the density distribution of the electrons is restricted.

Although a fairly rigorous treatment of the electromagnetic nozzle problem is feasible, a separate program of considerable scope would be required to realize a satisfactory solution. The present program is restricted to a development of a qualitative knowledge of the principles involved, an empirical program to confirm or suitably modify these principles, and an experimental development of a workable electromagnetic nozzle.

Methods of Attack

Two general methods of attack on the problem may be described. The first method is to control entirely the motion of all the ions, either directly or by control of the electrons, from as far upstream as possible. The second method is to create a magnetic field which is very weak within some arbitrary radius, and then increases rapidly, forming a kind of electromagnetic wall. In the former case the particle/magnetic flux ratio is held constant, the electron

trajectories are fixed along lines of magnetic force, and the ions follow trajectories determined largely by the electric field. In the latter case, the central portion of the plasma is in molecular flow in a relatively field free region. Electrons are restricted from moving across the magnetic field near the wall, and ions are reflected from this region by an imposed electrostatic field.

The Method of Magnetic Steering

If the plasma flow is uniform over the cross section normal to the flow at the point where magnetic control is assumed, a constant field which expands uniformly to the accelerator system is desired. This type of magnetic field is relatively easy to form and maintain, but the initial uniform plasma flow cannot be generated conveniently from a single expansion device. This method may serve well in conjunction with a multiple source of the type described in the previous section.

If the plasma flow is a function of the distance from the beam axis at the plane in the stream where magnetic control is assumed, then a magnetic field is required such that the field strength is proportional to the particle flux. Downstream this field would expand in such a manner as to blend with a uniform magnetic field normal to the plane of the accelerator system. An alternate scheme for a jetting flow pattern is a uniform magnetic field upstream blending into a non-uniform field downstream which is weakest at the beam axis. Construction of magnetic fields tailored to a specified strength and shape can be accomplished with the aid of high speed computer studies such as those

reported by Calhaghan and Maslen[32] and Sass and Stoll[33].

No matter what the shape of the plasma density pattern or magnetic field, the method of magnetic steering requires that either the ions or the electrons be magnetically controlled for a considerable distance downstream of the source. Solution of equation (44) for cesium ions with energies of the order of one electron-volt shows that restriction of ions to circular paths of radius = 1 cm. would require about a 2000 gauss field over the controlled expansion area, clearly an impractical figure. Similar magnetic control for electrons, however, requires only a few gauss which can be easily maintained across a wide diameter. Stronger fields, approaching several thousand gauss, can be maintained upstream over a much smaller area whenever required for a high electron current density. Thus, this method implies magnetic control of electrons only, and electrostatic control of the ion flow.

The Method of Magnetic Containment

The central core of almost any aerodynamic pattern is fairly uniform, hence, there is no need to control this portion of the plasma at all, provided that the outer edges of the plasma beam are reflected or otherwise steered so as to avoid excessive propellant losses while preserving an overall uniform current density. One method of accomplishing this is to construct a magnetic field which is very weak for some distance normal to the axis of the plasma beam, but which increases sharply at some selected distance.

Aerodynamic flow is allowed in the central weak-field region and ions are reflected by a positive potential imposed on a conducting form of selected shape in the strong field region. Electron currents to the form are kept low, as usual, by the restricting magnetic field. Construction of fields approaching this particular shape may be somewhat more of a problem, and more study along these lines is indicated. It is especially desirable that the properties and dimensions of the sheath region be investigated in a study similar to that of Goldstein[34].

HARDWARE

Auxiliary Equipment

All electromagnetic plasma flow control studies were conducted in the vacuum tank shown in Fig. 15, described previously in Section II. Boiler and fuel feed systems, (Figs. 17, 18) and the titration equipment are unchanged from the source performance and aerodynamic nozzle studies. The sources used mainly in this study are shown in Figs. 10, 11, and 12.

Distribution Probe

The basic design of this device shown in Fig. 49 and described in the previous section is unchanged. The fact that some of the plasma is reflected, however, makes a change in the shadow shield design necessary. In Fig. 70, the primary beam falls on the probe surfaces at any radial distance because of the properly offset openings in the shadow shield, but the reflected beam is partly lost. This was corrected by placing the shadow shield holes directly over the probes, and decreasing the space between the probe faces and shadow shield to the point where no offset is required.

Magnetic Coils

The first electromagnetic coil tested was a 3" diameter, 6" long stainless steel cylinder wound with sheathed low resistance heating wire to prevent condensation of the cesium. This design, shown in Fig. 71, was not intended to produce any flow pattern improvement, but merely to demonstrate the concept.

The next simple device tested is shown in Fig. 72, and consists of an 8" diameter 5" long stainless steel cylinder wound with insulated copper wire. This device represents an early attempt to secure a combination of aerodynamic expansion and ion reflection.

Fig. 73 is a combination of a conical coil and a large, short, cylindrical coil downstream, and represents an early attempt to control the entire plasma from source to accelerator. The cylindrical coil was generally activated in opposition to the conical coil to produce defocussing. Fig. 74 shows a further modification of the same idea. The throat coil was included when tests showed the magnetic field was too weak near the source. Both designs were equipped with cooling coils.

Fig. 94 is a design consisting of a single strong coil at the nozzle throat and two large cylindrical coils downstream. A fairly wide variety of magnetic fields can be produced with this device by varying the relative strength and direction of the three fields. An unwound, ion reflecting stainless steel form can be so placed in the field that the magnetic lines of force lie parallel to

the form. Under these conditions the form can be placed at positive potential without accepting an excessive electron current flow.

EXPERIMENTAL METHODS

General Method

The general method of operation in these tests has been described in the two previous sections and is largely unchanged. Fuel flow rate is roughly set by precalibration of a thermostatted boiler, monitored for stability by frequent ion current readings for the highly ionized plasma, and determined accurately by titration at the conclusion of the run, since all the flowing cesium eventually condenses on the cold probe. Ion currents are determined by total probe readings and checked by integration of the flow patterns.

Preliminary Operations

Prior to installation of a given electromagnetic device, the source performance and aerodynamic density pattern for the ion source in use are defined at several flow rates by the methods described in the two previous sections. Then the electromagnetic device is installed and the magnetic field strength and shape are determined in air.

Axial and radial field strengths are determined by the use of a magnetic probe with a Bell Model 120 gaussmeter.

Magnetic field shapes are determined by the simple method of mounting a flat surface across the horizontal diameter of the axially symmetric field,

sprinkling with iron filings, and vibrating the surface with the field on. The resulting pattern is fixed by spraying with a fast drying clear lacquer.

Magnetic Nozzle Studies

Magnetic nozzle experiments are generally confined to studying some combination of three areas of interest: the effect of the field on source operation, correlation of the magnetic nozzle effects with theory, and the effect of the magnetic nozzle on flow pattern. Data pertinent to all three areas are recorded for each combination of the magnetic and electric fields, then extracted from the raw record and regrouped for reporting clarity.

When simple devices such as those shown in Figs. 71 and 72 are tested, readings are generally recorded for several combinations of coil current and coil form bias. More complicated combinations such as those shown in Figs. 73, 74, and 94 are usually studied only at settings which produce high propellant utilization, and data is recorded only for settings producing some desirable combination of propellant utilization and density pattern.

EXPERIMENTAL RESULTS AND DISCUSSION

Qualitative Effects of the Electromagnetic Nozzle

The first electromagnetic nozzle runs were made with the experimental setup shown in Fig. 71, using Source Design X of Fig. 11. The purpose of this series is to show qualitatively that the electromagnetic nozzle behaves as predicted by theory, and to survey any gross effects of the magnetic field on source and probe behavior.

Wada and Knechtli[5] showed some time ago the lack of effect on probe measurements of fairly large magnetic fields normal to the probe surface, and more recently Goldstein[34] has predicted considerable sheath effects when the probe surface is parallel to the magnetic field. The latter effects occur because the magnetic field restricts electron flow normal to the surface for considerable distances, and as the space charge limited current is decreased, the sheath is enlarged. Ordinary sheath dimensions should be restored by a magnetic field which has sufficient components pointing normal to the probe surfaces, since the space charge limitations are only imposed on this component of the electron current. In the present experiments fairly large axial and radial magnetic fields both exist in the probe region, and sufficient components of the magnetic field exist normal to any given surface of the probe to produce ordinary sheath dimensions. This hypothesis cannot be confirmed by observing probe current changes with increasing field strength, since the magnetic field increases the true ion current density by focussing. However, the ion density

pattern, corrected for ordinary sheath effects and integrated to fairly large radius, agrees within a few percent with the total ion flow measured by the total probe in all the cases calculated for electromagnetically controlled flow patterns. This shows that no gross errors in the assumed sheath dimensions and corrected probe measurements are introduced by the magnetic field.

The effect on source behavior, as discussed in a previous section, is to reduce the arc current by restricting radial electron flow. This effect can be used to decrease ion generation power requirements.

Concept Demonstration

When the e/m nozzle is biased sufficiently negative with respect to the plasma, it acts as a total probe and measures ion current. In one series of experiments with the apparatus shown in Fig. 71 the ion current to the negatively biased e/m nozzle was 180 ma and that to the total probe 160 ma with the magnetic coil not activated. Thus the total ion flow rate was 340 ma. As the magnetic coil was activated and the power level was raised to a high value without changing the total flow rate or bias the ion current to the e/m coil form gradually dropped to below 10 ma while the total probe current rose to 330 ma. In the same series of experiments, biasing the e/m nozzle a few volts more positive than its floating potential resulted in 340 ma of ion current to the total probe at a much lower coil power than when the e/m nozzle was floating or biased negative. Titration of all the cesium collected in all parts of the apparatus after the run showed that the flow had been 342 ma.

This behavior is in accord with the theory, which predicts that the plasma may be steered entirely by the magnetic field at high power levels, but that the electrons may be steered magnetically and the ions reflected electrostatically at lower power levels.

Fig. 75 shows the same behavior in a more quantitative manner at low magnetic field strengths. These data were collected at constant boiler temperature (i.e., total flow rate), using the apparatus of Fig. 71. As in the previous case the total probe current without any appreciable electromagnetic focussing is somewhat less than half the maximum level reached. It can be seen that increasing either the magnetic field strength or the nozzle positive bias alone results in a small steering effect, as indicated by the probe current increase, but selected combinations of the two effects are much more effective in steering large fractions of the total beam. In these experiments a source was used which was pretested at ionization levels above 80%, so that the effects observed are not explainable by an increase in ionization due to magnetic field.

Fig. 76 shows electron current to the e/m nozzle form of Fig. 71 as a function of positive bias above floating potential for two levels of coil power. At zero net electron current to the nozzle form, the device is floating. Two facts are noteworthy: the floating potential is increased with increasing magnetic field, and the electron current to the nozzle is considerably reduced by increasing magnetic field strength, at any selected nozzle bias. Both effects confirm the theoretical prediction that the random electron current is restricted in a direction normal to a magnetic field.

The following behavior of the large solenoid sketched in Fig. 72 also demonstrates the electromagnetic nozzle concept, but the effects are not as pronounced due to the use of a weaker magnetic field in an attempt to produce a desirable density pattern.

Fig. 77 shows the increase in ion steering, as measured by probe current increase, with increasing field strength. In this test the current to the coil form was held constant by increasing the bias to compensate for increasing magnetic field strengths. As in Fig. 75, the general observation can be made that selected combinations of magnetic field strength and bias are more effective than either when applied alone. It can be seen that a larger percentage of the flow is received aerodynamically in this arrangement than in the previous one, and that the electron current to the coil form is not as sensitive to increase in potential. Both these effects are due to the large dimensions of the solenoid. The peculiar behavior at zero magnetic field with increasing bias was checked several times. The authors have no explanation for this small reverse.

Fig. 78 confirms Fig. 76, i.e., that radial electron current is restricted by a solenoidal magnetic field. Here it is apparent that the restriction is not a linear function of the field strength. This is to be expected, since the electron energy distribution is at least as complicated as a Maxwellian function.

Density Pattern for Cylindrical and Conical Coils

Fig. 79 shows the aerodynamic density pattern for Source X at three different flow rates, corrected for sheath effect. The source to probe distance was 9". The integrated flow rate represents the ion flow rate to the probed area, a circle of radius 4". The ion flow rate to the probe includes the amount impinging on the extension to the probe, shown in Fig. 51, which at this source to probe distance is a significant amount. The total ion flow rate is secured at a much smaller source to probe distance, say about 5". At this distance the three figures would coincide within a few percent but the central probes would be very quickly shorted by the high cesium flow. The effect of high flow rates is to produce slightly steeper patterns as noted in the previous section. The density patterns all have the desired flatness, but are useless for ion engine purposes because of the low propellant utilization of 70% - 75%.

Fig. 80 illustrates the best density pattern obtained with the large cylindrical coil shown in Fig. 72, in terms of flatness and high propellant utilization. It is somewhat steeper than the aerodynamic pattern, but still fairly flat. Propellant utilization for this device, however, is only about 70-80% due to losses outside of the solenoid. Note that for this device and those following, which restrict the probe current to the area surveyed by the point probes, the integrated ion current agrees with the total probe current. The patterns are corrected for sheath effects.

The second curve of Fig. 80 shows the best density pattern obtained in a series of tests with the conical design shown in Fig. 73. The conical coil alone was used for this series. The curve shown corresponds to only 86% propellant utilization, but complete propellant utilization was obtained in an even more focussed pattern. The lower curves of Figs. 82 and 83 give some idea of the relative magnetic field strength at various locations within this design. The coil current corresponding to the pattern in Fig. 80 is 4.0 amperes, which produce axial field strengths in the range of 5-15 gauss and radial field strengths of less than 2 gauss. The Larmor radius normal to the resultant field for one volt electrons is less than 1 cm. The focussing tendency of the conical coil is illustrated in Fig. 89, where it can be seen that the magnetic field lines are more convergent than the coil form.

Fig. 81 illustrates the best density patterns obtained with the compound electromagnetic devices shown in Figs. 73 and 74, corrected for sheath effect.

The purpose of the downstream cylindrical coil is to defocus the plasma by creating a magnetic field in opposition to that of the conical coil. The pattern shown for the conical and cylindrical combination is much less peaked than that of the conical coil alone, and in addition the propellant utilization is increased to 80%. The higher propellant utilization is explained by algebraic addition of the lower curves of Figs. 82 through 85., for conical and cylindrical coil currents of 14 and -20 amperes, respectively. When the two coils are activated in opposition, the axial fields nullify and the radial fields reinforce as shown in Table VI.

TABLE VI

Axial and Radial Field Strengths for Conical and Solenoid Coils, Calculated from Figs. 82 to 85

Distance From Source, cm.	5	10	15	20	24
Axial Field, Gausses	47	37	20	7	0
Radial Field, Gausses	8.5	12	12	—	—

Table VI shows the increased field strength responsible for tighter flow control over most of the source to probe distance, which explains the higher propellant utilization. Also apparent is the marked reduction in axial to radial field strength ratio as the downstream distance increases, corresponding to a divergent magnetic field with consequent beam spreading. The divergent magnetic field is apparent in the downstream section of Fig. 92, which is a combination of the conical coil field of Fig. 89 and the solenoid field of Fig. 90 acting in opposition.

The second density pattern shown in Fig. 81 is the best obtained for the throat, conical, and solenoid coil combination shown in Fig. 74. The purpose of the throat coil, the characteristics of which are shown in Fig. 86 and Fig. 87, is to increase the field strength upstream until the magnetic field is parallel to the conical walls. The magnetic field produced by a balanced combination of currents through the three sets of windings is shown in Fig. 92. When this condition is maintained, the electron current to the conical coil form increases the ion generation power considerably.

The devices described above are evaluated in Fig. 93 in terms of propellant utilization vs. density ratio for sheath corrected calculations. The effect of the sheath corrections alone can be seen by comparing the aerodynamic curve of Fig. 93 with those of Fig. 69 which were not corrected for sheath effect. The solenoid coil alone is worse than the aerodynamic due to excessive propellant loss outside the coil. The conical coil alone is worse than aerodynamic due to excessive focussing. The cone and cylinder combination, designed to defocus the flow, produces a pattern very much like the aerodynamic flow, perhaps indicating that plasma flow control was assumed after the aerodynamic pattern had already taken shape. The increased field strength and further shaping of the field due to the use of the additional windings at the throat effects a considerable improvement, as indicated by the highest curve in the figure.

Magnetic Nozzle Modification

Fig. 94 is a simplified diagram of an electromagnetic nozzle designed to produce a wide variety of magnetic and electric fields. The throat coil shown consists of 100 turns of 1/4" wide, 0.010" thick copper strip wound on a half inch core, and is capable of producing over 900 gauss at the throat of the source. The cylindrical coils are available for defocussing or otherwise shaping the magnetic field. Some of the fields produced by various dual combinations of the throat coil and downstream cylindrical coil are shown in Figs. 95, 96, 97, and 98, which give some idea of the variety of magnetic field shapes which could be produced.

The electrostatic fields for reflecting and steering ions are produced by charging the cylinder walls and the conical form to various potential levels. The conical form shown is arbitrary, and may be replaced with any desired shape. There is no need to wind the form electrically, since the magnetic field requirements are fulfilled by the throat and cylinder coils.

The source to probe distance was shortened to 7" in this design to reduce the electron current to the coil form noted in the previous design. It is recognized that this may result in a more highly peaked distribution.

Density Patterns

The possibilities of this device have not been fully explored at the present writing. Reinforcing combinations of the magnetic fields with various cone-shaped forms inserted in the field have been investigated in some detail and the two best resulting density patterns, corrected for sheath effect, are shown in Fig. 99, and evaluated in Fig. 100. In this device, the cylindrical coil forms were not cooled, and any cesium impinging on them was neutralized, re-evaporated, and condensed on the probe as neutrals. Thus, the difference between measured ion current to the probe and cesium current by titration is partly due to incomplete ionization, partly to incomplete focussing of the primary plasma beam on the probe. In the curves of Fig. 100 therefore, the cumulative flux represents the product of degree of ionization and fraction focussed. These results are not as good as the top curve of Fig. 93 when propellant flow control alone is considered, but the overall performance of these

devices is superior to that of the device using the conical coil discussed above, because of lower ion generation power requirements.

IV. ACCELERATOR STUDIES

CLASSICAL THEORY

Experimental Background

The present project scope does not include accelerator development except for casual improvements necessary for successful engine runs. Under contractor's Independent Research and Development Funding, however, a separate program was conducted to develop an ion accelerator suitable for eventual use in an assembled plasma separator engine. This program is reported in detail by Neiman[35] in his final report, but the three major results of the program, i.e., experimental confirmation of perforated plate electrode theory, development of an accelerator system, and experimental evidence leading to a modification of ion optical theory, are summarized in this report as background to the present program.

Extraction of Ions from a Plasma

The space charge theory governing ion extraction from a neutral plasma by perforated electrodes has been described in detail by Kerslake[36], Kerslake and Pawlik[37], Gabovich[38], Prince[39], and others, and need only be summarized briefly.

Consider an ion accelerating electrode array consisting of two or more uniformly perforated plane parallel plates suspended normal to a flowing neutral plasma. If the downstream electrode is placed at a high negative potential with respect to the plasma and the upstream electrode allowed to float, the

field generated upstream will repel electrons and accelerate ions, thus effecting separation of the oppositely charged plasma particles. This situation is illustrated in Fig. 101, where it can be seen that the "electrodes" of this system across the hole area are equipotential surfaces in space. For monoenergetic plasma, the virtual anode would be the surface at which the electrons are repelled, and the cathode would be the most negative equipotential surface through which the ions travel.

This situation differs from that of plane parallel electrodes in two respects: the anode to cathode distance is neither fixed nor equal to the plate to plate distance, and the virtual electrode surfaces can be curved. Thus, Child's Law for plane electrodes

$$(45)\quad j = \frac{4.73 \times 10^{-9}\ V^{3/2}}{X^2}$$

can only be considered a good approximation, where j amps/cm^2 of cesium ions are extracted by a potential of V volts across an electrode distance of X cm, when the virtual electrodes are approximately parallel, fairly flat, and separated by a distance equal to the plate to plate distance. When the first two conditions are met, but the virtual interelectrode distance is different from the actual plate to plate distance, equation (45) will be followed with an appropriate constant correction factor.

It can be assumed, since the virtual anode can adjust freely to accomodate any ion flow, that the flow through the holes of perforated plate electrodes is always space charge limited for plasma extraction.

Confirmation of Classical Optics

Consider the electrode arrangement shown in Fig. 102. Classical theory says that the floating upstream electrode for all three cases shown will be at wall potential, i.e., slightly negative with respect to the plasma, will therefore be surrounded by a positive space charge sheath, and will accept all the random ion current impinging on it together with an equal number of neutralizing electrons.

The top diagram illustrates the case where the balance between current density and applied potential is such as to drive the virtual anode concave in order to satisfy space charge requirements at the center line. Thus, the flow is space charge limited but the optics are very bad, i.e., a highly underfocussed condition. This situation corresponds to the steeper portions of the two lower experimental curves shown in Fig. 103, obtained with uniform density plasma incident on a small perforated plate electrode system. The total extracted current is indicated by the square points, and includes impingement currents. This region of the curves does not necessarily follow any power law, since the curvature as well as the spacing of the virtual electrode system is changing with increased potential. Indeed the only requirement on the behavior is that the slope be at all times less than 3/2, since the increasing

electrode spacing compensates partly for the increasing extraction potential. That this region is underfocussed is shown by two observations together; (a) the wide disparity between the total extracted current and the current focussed through the entire system, and (b) the fact that more total extracted current is observed than is predicted by the theoretical line for this electrode spacing. This latter behavior can only happen when the virtual electrodes assume a closer spacing than the real spacing of the perforated plates.

The beam current is indicated by the circles in Fig. 103, and represents only that portion of the ions which does not impinge. The sharp decrease in these curves is of course due to the rapidly diverging optics which occurs with decreasing potential, and is not at all related to any space charge controlled power law.

The second diagram of Fig. 102 illustrates the situation where the beam is properly focussed, i.e., where the virtual anode is slightly convex and practically all of the ion current incident on its surface is accelerated through the electrode system. This situation predicts good optics and mild focussing, i.e., and beam current/total current ratio slightly greater than hole area/total area ratio. This is experimentally confirmed by reference to the two complete lower curves of Fig. 103. At the knee of the curves good optics are first observed, as indicated by the convergence of beam current and total accelerated current. The ratios of the beam current at this point to the highest beam current observed (for the same cesium flow rate) are 0.65 for the lower curve and 0.69 for the upper curve, while the ratio of hole area

to total accelerator area is 0.58. Extraction of only an extra 10-12% of the total beam via slight bulging of the virtual anode would account for this.

Confirmation of Classical Space Charge Theory

Under these conditions, i.e., Case II of Fig. 102, corresponding to the knee of the experimental curves, the virtual electrodes should be fairly flat and parallel and spaced at a distance slightly larger than the spacing of the perforated plates. A line drawn through the knees of a family of such curves constructed at different flow rates should therefore roughly follow some power law close to the 3/2 power law, but should be displaced slightly to the right of a line drawn for the perforated plate spacing.

In Fig. 103 the two lower curves are completed into the underfocussed region, and the knees of the curves are adequately shown. The upper curves, however, were investigated only from just above the knee joint, i.e., the point where good optics begins, for fear of electrode damage due to high impingement currents. If the lowest points of these curves are assumed to be at the knee of the curve, which involves only a slight error, then a line can be drawn through the knee area of the curves which is perhaps slightly steeper than the 3/2 slope line, but displaced to the right as it should be. This very rough degree of confirmation of space charge theory is about all that should be expected with perforated electrodes of this design. If the first electrode were held at plasma potential or if the holes were small in comparison with the electrode spacing, results closer to flat plate electrode behavior would be observed.

Deviation from Classical Optics

The third diagram of Fig. 102 indicates the physical situation described classically as overfocussed or overpowered. Here the applied potential is too great for the current flow, and the virtual anode balloons upstream to satisfy the space charge equation by increasing the electrode spacing. This situation predicts extraction of a larger than geometrical percentage of the total plasma incident with gradually deteriorating optics as the potential is increased. The experimental data of Fig. 103 is at variance with this prediction, since the upper legs of the curves were all obtained with low impingement levels up to the incidence of breakdown between the electrodes at high potential. This is illustrated in the two lower curves where in this region the beam current through the accelerator electrode is almost identical with the total extracted current.

Classical treatment also predicts that not much more than geometrical throughput will be observed before serious overfocussing is observed. In the present case, however, the total ion current incident on the entire grid surface is accelerated through the holes. This is illustrated in Fig. 104 taken from Neiman[35], for a series of runs at different boiler temperatures. It can be seen that the maximum beam currents all coincide with careful calibration before and after the accelerator runs, within limits of experimental error. The experimental points were all taken in a region of good optics.

The observations summarized briefly above have led to the tentative theory for perforated parallel plate electrode optics described in the next section.

THEORY OF AUTO FOCUSSING PERFORATED PARALLEL PLATE ELECTRODE SYSTEM

The Virtual Anode

In ion extraction from a plasma, the virtual anode is usually understood to be an equipotential surface from which all electrons are reflected. Strictly speaking, this is only true for monoenergetic electrons, and in most cases electron reflection takes place within a transition region instead of at a single surface, the higher energy electrons penetrating further. This transition region will be described further below, but for the present let us define the virtual anode as the potential surface beyond which only an arbitrarily negligible fraction of the plasma electrons penetrate. As defined in this manner, the virtual node is not the same as the plasma boundary shown in Fig. 103. The plasma boundary is at plasma potential and is the surface at which the reflection of the lowest energy electrons occurs. The virtual anode as defined above is further downstream, at a potential sufficiently negative with respect to the plasma to reflect the remaining electrons. The volume between the plasma boundary and the virtual anode is the transition region.

The overfocussed picture shown in Fig. 103 makes the tacit assumption that the plasma boundary can only be separated from the floating upstream electrode by an electron sheath width. This is equivalent to saying that the virtual anode must be attached to the electrode and that the floating electrode will accept ion and electron currents both equal to the random ion current in the plasma.

An alternate interpretation is possible. There is no basic law that says the virtual anode need remain attached to the separating electrode, given a suitable potential field. On the assumption that the virtual anode can be detached from the separator by high accel potential and occupy a stable position upstream, it can be hypothesized that no ion impingement will occur on a floating separator, or on one on which the floating potential is enforced.

It has been confirmed by preliminary computer studies, in a joint effort by NASA and G.E. personnel, that no impingement on a floating separator, and very little accel or decel impingement, results when a space charge limited ion flow is directed normal to the type of virtual anode described above.

The hypothesis is also strongly supported by elementary probe theory. If all the electrons are reflected in the transition region, then only charges of one kind (+) impinge on the separator. If no mechanism is available to neutralize the charge buildup then further ion buildup is prevented by space charge limitation. In this case the ions will be either reflected back into the plasma or steered through the separator holes. The experimental evidence of 100% propellant utilization shown in Neiman's[35] report supports the latter mechanism.

What needs further explanation is how the ions are steered into the holes without violating the laws for space charge limited flow, since it is clear that very substantial radial field gradient components would be necessary if the ion flow were abruptly turned in the region downstream of the virtual anode,

which are clearly not present if the virtual anode shape is determined by a uniform plasma flux.

Pre-Steering in the Transition Region

The explanation lies in the transition region mentioned above, where the electron population is not negligible, but where definite changes in the potential field occur, since it is this very field which eventually reflects all the electrons before the virtual anode is reached.

In this transition region the densities of electrons and ions vary as a function of the potential. In the neutral plasma region the electron and ion densities are approximately equal, i.e., $n_e/n_i = 1$. However, in the space-charge limited flow region downstream of the virtual anode, the number of electrons present is very small so that $n_e/n_i \longrightarrow 0$. Between these two regions the electron density decreases because of the opposing potential; and the ion density also decreases because the ions are accelerated.

It is of interest to determine the charge density and potential field through the transition region where n_e/n_i decreases from one to zero. This can be done by first finding the charge density as a function of potential and then using this information to solve Poisson's equation for the potential as a function of position. If it appears that there is a region where the electron density exceeds or equals the ion density, while at the same time a potential field exists, then the possibility exists that the ion can be pre-directed toward the holes in the separator without space charge flow re-

strictions. The first step of this process has been completed and is shown in Fig. 105, from which it can be seen that the transition region does indeed contain a volume where electron density is greater than ion density. In this region the objection to ion steering on the basis of space charge limited considerations is removed.

It is recognized that the above description constitutes only the essential elements of the theory, and that further theoretical or experimental study is needed to adequately define the transition region field and ion trajectories. As it stands, however, it explains a good many experimental observations not in harmony with former theory, some of which have been included above out of context as illustrative examples.

HARDWARE

Vacuum Tank

The 3' x 4' vacuum tank used for the test program is described in detail by Jasper[40] and illustrated schematically in Fig. 106. A stationery end plate is equipped with an auxiliary mounting plate to accomodate the cesium boiler and source feed system, the source, and the accelerator and beam control units. The main tank, mounted on a movable dolly, contains a stainless steel target near the downstream end, and since the target is constructed as a calorimeter to measure beam power, fluid lines and thermocouples are led to it through the side of the tank.

A copper liner with passages for liquid nitrogen coolant is insulated from the tank body and encompasses the accelerator system. It can be operated at a selected potential to minimize stray currents. In addition to this, accelerator parts are locally shadow shielded to further minimize undesirable stray currents such as electron backstreaming.

Two viewing windows are in the side of the tank.

The present pumping system is capable of maintaining a pressure of approximately 10^{-5} mm. Hg. during testing.

Instrumentation and Controls

The details of the instrumentation and control system are given by Sabin, Templeton, and Scheffer[41]. The low voltage power supplies used for cesium supply line heaters, source, anode, and separator voltages, are protected from internal arc discharges by isolation transformers. The high-voltage power supplies (5 kv, 2 amp) used for ion accelerating voltages are provided with overload voltage disconnects which must be manually reset. A 5000 ohm power resistor is in the accelerator circuit to attenuate discharge currents. Ion currents within the engine system are read on calibrated multiple-range Sensitive Research Corp. ammeters whose accuracy is better than 1%. Less sensitive data is read on standard $\pm$ 2% meters. All thermocouple reference junctions are immersed in ice baths, and cesium supply system temperatures are monitored on a recorder. Calorimeter temperatures are read on a precision potentiometer.

Accelerator System

The performance of the accelerator systems is dependent on the prevention of electrical leakage and breakdown during operation and on the density distribution of the incident ion beam. Design changes affecting insulation, cesium buildup, electrostatic shielding, and beam distribution were made as the work progressed, and are described along with the accelerator system being tested when they were incorporated.

A. 361-Hole Grids with 19 Holes Exposed

The first high performance accelerator grid system consisted of three parallel plates, each containing 361 holes, 0.313 inches in diameter, with 19 holes exposed to limit the system to the flat portion of the ion beam. The grid system is pictured in Fig. 107. The insulators are fairly remote from the beam, and each insulator is protected from cesium depositing by a cylindrical metal shield. The cesium flow not incident on the central 19 holes of the separator electrode was condensed on a liquid nitrogen cooled coil placed between the source and separator. The separator holes outside the 19-hole area were covered with thin foil.

The source to anode distance was 9-3/4 inches, giving a beam intensity spread at the separator of about 10 percent as determined by the distribution probe described below. A stainless steel shield, held at source potential, surrounded the source in all directions except downstream.

B. 361-Hole Grids with 211 Holes Exposed

Exposing 211 holes of the grids to the cesium flow increased the exposed separator area to 164.2 sq. cm. A 6-inch cooling coil was installed to condense the portion of cesium flow outside the exposed area. This configuration is shown in Fig. 108. The mechanical suspension of the electrodes was improved to provide a fine tension control by a machine screw adjustment.

A mask consisting of a thin metal cylinder 6 inches in diameter and 1-1/2 inches long was attached to the upstream side of the separator as a cesium shield.

This accelerator system was used with an aerodynamic plasma distribution from the source at different source to separator distances.

C. 361-Hole Grids with all Holes Exposed

The foil blocking 150 peripheral grid holes was removed to produce this configuration. The use of the entire grid area was associated with magnetic nozzle development described elsewhere in the report. The various magnetic nozzles used consisted of a coil or group of coils energized electrically to minimize electron current to the coil form, with the coil form biased positively with respect to the plasma to focus ions on the separator.

Insulator shielding was further improved by replacing the outer metal cylinder around the support insulators by glass cylinders, and by mounting the insulators more remotely.

Probes

A. The total probes used in the accelerator studies are of the type shown in Fig. 22, and have been described in the section on source development. Two sizes of probes were used in accelerator studies. The one shown

in Fig. 22 is used in some cases to calibrate the total cesium flow rate against boiler temperature for various fuel feed systems, and in other cases to determine the total ion current incident on the 19 hole accelerator system as a function of boiler temperature as shown in Fig. 104. An 8" diameter probe of the same design was used in conjunction with the 211 hole and 361 hole accelerator systems.

B. The 12" diameter distribution probe described in the section on aerodynamic flow and shown in Fig. 49 was used to determine density distribution for the 211 hole and 361 hole accelerator systems.

A probe for determining beam density distribution was developed specifically for the program with 19 hole electrodes. It is shown disassembled in Fig. 109 and in cross section in Fig. 110. The negative electrode can be any or all of 19 screw heads or "buttons" in a configuration identical to the 19 hole electrodes. Ions not incident on the buttons strike a metal screening plate. By reversing polarity, the ion impingement on the screen is measured. The whole assembly is cooled by liquid nitrogen.

Target-Calorimeter

The target used for all accelerator and engine tests to date was also designed as a calorimeter, in order to verify ion beam power measured electrically. Recently ion source and accelerator development reached a point where accurate calorimeter confirmation became of paramount importance.

Consequently, the entire calorimeter system was redesigned to increase accuracy to a point close to the limit for such measurements. The improved design is given in detail in Appendix I.

EXPERIMENTAL METHODS

361 Hole Grids with 19 Holes Exposed

The cesium ion current incident on the 19 hole hex area is determined by a thorough previous calibration with a total probe, and is double-checked by measurements with the distribution probe, which also gives the density ratio across the system. Backstreaming around the outside of the electrodes is effectively prevented by the 8" diameter of the plates compared to the active electrode diameter of less than 2". In general, the accel potential is set 200 volts more negative than the decel, a condition which had been found sufficient to prevent electron backstreaming through the grids during Neiman's[35] accelerator development program.

System behavior is examined over a range of grid spacing and boiler temperature. At each boiler temperature for each grid spacing electrode potentials are raised and balanced until either the transmitted current reaches a maximum or excessive impingement or breakdown currents are observed.

361 Hole Grids with 211 Holes Exposed

This system was examined to determine the effect on performance of a wider variation in ion current density across the face of the accelerator. Density patterns at source to accel distances of 5-3/8" and 2-7/8" were determined in the vacuum system shown in Fig. 15, from which the current density variation and propellant utilization could be estimated.

With this exception, the experimental methods for this system are much the same as those for the smaller system above.

361 Hole Grids with all Holes Exposed

This system was examined in preparation for engine runs with electromagnetic flow control. Preliminary tests were made using an aerodynamic flow at a source to accel system distance of 8-3/8", with the peripheral portions of the beam condensed on an 8" diameter liquid nitrogen cooled cylinder. Density variation and propellant utilization were estimated as above. Later tests were made with more or less electromagnetic focussing, which resulted in higher propellant utilization and wider density variations. Some of these runs provide useful data for both accelerator studies and engine runs, and are therefore considered in both sections.

All other experimental methods for this system are the same as those for the 211 hole system.

EXPERIMENTAL RESULTS AND DISCUSSION

Results of the CIRD Program

The development of the nineteen hole perforated plate accelerator system is given in detail in Neiman's[35] final report. Those results which were most illustrative of the theory have already been given out of context. The only other results pertinent to the present study are:

(1) The density variation of 1.0/0.89 measured across the face of the accelerator by the ion examiner of Fig. 109 and 110.

(2) The highest average beam current density, measured at 4.85 ma. per square centimeter of electrode area.

(3) The peak axial ion current density corresponding to the highest average, measured at 5.5 ma/cm^2.

Results Using the 6", 211 Hole Accelerator System

The experimental arrangement of the apparatus is shown in Fig. 111. Two source to accelerator distances of 5-3/8" and 2-7/8" were used in separate tests. The density patterns for these two conditions with Source IX, as determined with the distribution probe of Fig. 49 in the vacuum tank of Fig. 15 are given in Fig. 112. Evaluation of these patterns for a 3" radius shows a density variation of 2.5 and a propellant utilization of 54% for the larger source to probe distance, and a density variation of 20 with a propellant utilization of 80% for the smaller.

The best accelerator performance secured with these arrangements, in terms of maximum beam current with reasonable optics is given in Table VII.

TABLE VII

Selected Performance of the 6", 211 Hole Accelerator System

Source/Accel Distance, In.	2-7/8"	5-3/8"
Accel Voltage KV	4.5	3.3
Accel Current MA.	4.4	2.5
Decel Volt KV	3.6	3.1
Decel Current MA	2.7	3.4
Transmitted Current, MA	190	280
Transmitted Current Density, MA/CM^2	1.15	1.70

Results Using the 8", 361 Hole Accelerator System

Whereas in the case above density variation was obtained by varying the source to accelerator distance, with the 8" accelerator system it is obtained by varying the magnetic focussing. The source in use is Source XI.

For aerodynamic runs the experimental arrangement of the source and accelerator is shown in Fig. 113, and the other components are arranged as in Fig. 111. The arrangement shown in Fig. 114 we shall call Engine Configuration I, or ECI. The arrangements of Figs. 115, and 116 are those used in the final engine runs, and will be designated Engine Configurations II and III.

The density patterns for these configurations are given in Fig. 117, some of them repeated from the electromagnetic nozzle section. Evaluation of these patterns for a 4" radius is given in Table VIII.

TABLE VIII

Evaluation of the Density Patterns of Fig. 117

Configuration	Density Variation $(\frac{Min}{Max})$	Incident on Separator
Aerodynamic	0.37	57%
EC I	0.06	95%
EC II	0.04	93%
EC III	0.04	93%

The best accelerator performance for these configurations, is given in Table IX.

Effect of Density Variation on Beam Current Density

Selected data from various accelerator runs are summarized in Table X, where it is apparent that a high density variation leads to low average beam current, as might be expected. Also, more or less expected is the fairly constant maximum axial current density for the 6" and 8" accelerator systems, despite wide variations in the peripheral minima and the steepness of the density patterns. The apparent ability of the electrode system to handle highly skewed patterns is evidence for the auto-focussing extraction theory described earlier. Classical perforated plate theory does not explain this ability.

TABLE IX

Selected Performance of the 8", 361 Hole Accelerator System

	Aerodynamic	EC-I	EC-II	EC-III
Accel Voltage, KV	3.5	4.2	3.5	3.2
Accel Current, MA	9.0	7.0	5.4	0.9
Decel Voltage, KV	2.5	3.2	3.2	3.2
Decel Current, MA	9.0	5.5	6.6	5.0
Transmitted Current, MA	350	199	187	197
Transmitted Current Density, ma/cm^2	1.28	0.73	0.68	0.72

TABLE X

Beam Current Density and Related Factors for

19 Hole, 211 Hole, and 361 Hole Accelerator Systems

Active Grid Dia. Inches	Grid Spacing, In.	Max/Min. Density Ratio	Average Current Density, ma/cm^2	Max. Current Density, ma/cm^2	Extraction Potential, KV
2	0.250	1.11	4.85	5.5	4.2
6	0.168	2.63	1.75	2.3	3.3
6	0.168	20.0	1.25	2.7	4.5
8	0.168	33.3	0.52	2.8	3.5
8	0.168	2.33	1.20	2.4	4.5
8	0.148	2.0	1.25	2.5	3.5
8	0.168	16.6	0.76	2.3	4.2
8	0.168	13.3	0.72	2.2	3.2

If the density ratios of Table X are plotted against average beam current density, as in Fig. 118, it can be seen that the curves for the 6" and 8" grid systems are displaced. This is understandable, since for equal distribution ratios, the average incident current is lowered for the eight inch system by the larger low current density area around the bigger circumference. Neither curve, however, shows any tendency to reach the average current density of 4.9 ma/cm^2 observed with the 19 hole system.

A possible cause of the current density limitation observed with the larger grids is departure from parallelism during operation. Impingement heating and the strong electrostatic field between grids are two factors which could contribute to this. Although the grids are quite parallel when installed, it is not possible at present to observe the degree of non-parallelism during operation.

V. ENGINE RUNS

GENERAL METHODS OF OPERATION

Selection of Engine Runs

In the plasma separator engine the dividing line between accelerator studies and engine runs is arbitrary, since all accelerator studies are necessarily associated with some ion source and some level of propellant utilization. In the present program three experiments were chosen to represent the Plasma Separator Engine, using the criteria of high propellant utilization, efficient and complete ion production, and low impingement current on the accelerator system. All three runs use some kind of electromagnetic flow control, since the multiple source concept has not yet been tried experimentally.

Hardware

All engine runs were made in the vacuum tank used for the accelerator studies (Fig. 106), but the plasma density patterns were determined in the tank shown in Fig. 15. Instrumentation and controls are identical to those used in accelerator studies.

The accelerator system consisting of separator, accel, and decel plates containing 361 holes and spaced 0.168 inches was used for all the engine runs. The accel and decel in all cases were 0.01 inches thick, non-magnetic stainless steel; in the first two engine runs reported, the separator was 0.060 inch magnetic steel, and for the remainder of the runs was 0.010 inch non-magnetic stainless steel.

Shielding of the space between the electrodes and source was provided as for the accelerator studies. In some cases, however, removal of the decel shield cap did not noticeably affect the operation.

General Experimental Methods

The rate of fuel flow was maintained in every case by thermostatically controlled boiler temperature setting. Auxiliary heaters maintained the valve and remainder of the fuel flow line up to the nozzle at higher temperature than the boiler to prevent cesium condensation.

Several variables were optimized in the small tank to produce the best combination of propellant utilization and flat density pattern and then duplicated in the large tank. They were:

1. Arc current, controlled through a separate isolated power supply.
2. Magnetic coil currents.
3. Bias on metal forms, including the magnetic coil forms, inserted in the magnetic field.

The variables optimized to produce the best combination of high beam current and good optics were separator bias (sometimes left floating), accel grid potential, and decel grid potential.

In the case of the final 50 hour duration run with EC III, the beam power as measured electrically was checked a number of times with the calorimeter system and methods described in Appendix I, confirming that shielding in the tank and electrode voltage applied were adequate to prevent backstreaming of electrons.

Evaluation Criteria

The overall evaluation of ion engine performance is given by:

$$(45)\quad \eta_T = \eta_P \times \eta_u$$

where the total engine efficiency is the product of the power efficiency (η_P) and propellant utilization (η_u). Power efficiency is further defined by:

$$(46)\quad \eta_P = \frac{W_B}{W_B + W_D + W_+ + W_F}$$

where W_B is accelerated beam power, W_D is drain power, W_+ is ion generation power and W_F is flow control power. In the case of the last factor, magnetic coil power will not be included as is conventional with similar engines, based on the assumption of eventual replacement with permanent magnets.

Propellant utilization is simply the accelerated beam current divided by the total fuel flow rate in the same units. In the plasma separator engine

it can be expressed as the product of four contributing factors, namely, degree of ionization, fraction incident on the separator plane, fraction transmitted through the separator, and fraction which does not impinge on the accel and decel electrodes.

ENGINE CONFIGURATION I

This configuration represents the best engine performance obtained with the multiple coil nozzle shown in Fig. 74 using Source XI. The purpose of the throat coil is to strengthen the upstream regions of the conical coil's magnetic field so as to produce a field parallel to the conical walls. The downstream cylindrical coil is activated in opposition to the conical coil and its purpose is to defocus the plasma and produce some beam spreading. The positioning of the engine components is shown in Fig. 114.

The best performance of this system in terms of good optics and high propellant utilization was secured when the throat coil current was 11.8 amperes, the conical coil current 9.3 amperes, the downstream solenoid current -18.8 amperes, and the conical form bias 13.6 volts above ground. The fractional flow incident on the separator of 95% was secured by integration of the density pattern of Fig. 117 over a 4" radius. This pattern was secured at a flow rate of 175 ma, which is somewhat lower than the flow rate in the engine run, but density patterns are not strongly dependent on moderate variations in the flow rate. A more accurate determination of this factor was not made because the ion generation power was too high for efficient engine performance.

The degree of ionization for this source was determined separately as 95.7%, an average of four runs made with the total probe as described in the source development section. The flow rate range over these runs was 200 ma to 400 ma.

Pertinent accelerator performance data for this run is given in Table XI.

TABLE XI

Performance Data for Engine Configuration I

Total Flow Rate, MA (Calc.)	233	Ion Beam Voltage, KV	3.2
Ion Flow Rate, MA (Calc.)	223	Ion Beam Current, MA	199
Incident on Separator, MA.	211	Arc Voltage, Volts	8.2
Accel Potential, KV	4.2	Arc Current, Amps.	0.8
Accel Current, MA	7.0	Coil Form Bias, Volts	13.6
Decel Potential, KV	3.2	Coil Form Current, Amps.	7.5
Decel Current, MA	5.5		

Engine performance data is calculated in Table XII, using the data of Table XI and equations (45) and (46). The ion beam potential is not corrected for voltage at which neutralization takes place. Ion generation power is arbitrarily designated as that associated with the arc, and flow control power is associated with the current and voltage of the coil form, although both currents pass through the nozzle throat to the cathode. Ion generation efficiency is secured by dividing the sum of the arc and coil form power in watts by the total ion current from the source in amperes. The fraction through

the separator is assumed as unity on the evidence of Fig. 104. Propellant utilization is the product of the four factors preceding it, power efficiency is derived from equation (46) and total efficiency is given by equation (45).

TABLE XII

Engine Performance Calculations for EC I

Accelerated Beam Power (W_B), Watts	636	Degree of Ionization	0.957
Grid Drain Power (W_D), Watts	47	Fraction on Separator	0.95
Ion Generation Power (W_+), Watts	6.6	Fraction Thru Separator	1.0
Flow Control Power (W_F), Watts	102	Fraction Not Impinging	0.941
Ion Generation Efficiency, EV/ION	487	Propellant Utilization	0.855
Power Efficiency (η_P)	0.805	Total Engine Efficiency	0.688

The advantage of splitting up engine performance into its contributing factors is that the areas which need improvement can be immediately identified. Thus, for Engine Configuration I the relatively poor performance arises largely from excessive electron current to the coil form, and from rather high impingement currents. Since nothing can be done to prevent electron impingement on the coil form without raising the magnetic field or lowering the coil form voltage, Engine Configuration I is not a satisfactory design.

ENGINE CONFIGURATION II

This configuration and the one following represent the best engine performance obtained with the design shown in Fig. 94. As far as performance is concerned, the main purpose of this design is to maintain high ionization levels at much lower power levels by restricting excessive current from the hollow cathode to either the anode or to any ion reflecting surfaces in the magnetic field. In this run the source was kept at ground potential and the accel and decel electrodes set at high negative potential. The positioning of the engine components is shown in Fig. 115.

The best performance of this system, in terms of good optics, propellant utilization, and low power requirements, was secured when the throat coil current was held at 21.5 amperes, the cylindrical coil current at 30 amps, the coil form floating, and the bias on the cone form 3.5 volts above ground.

Under these conditions the ion flow incident on the separator was only 86.6% of the total cesium flow, secured as usual by integration of the density pattern over a 4" radius. This factor is the product of the degree of ionization and fraction focussed, since the integrated ion flow was compared to the total cesium fuel flow rate.

The duration of this run was 15 continuous hours, before termination due to faulty operation of the calorimeter. Performance varied little over this period, and is summarized in the following tables.

TABLE XIII

Performance Data for Engine Configuration II

Total Flow Rate, MA	230	Ion Beam Voltage, KV	3.2
Ion Flow Rate, MA	(220)*	Ion Beam Current, MA	187
Incident on Separator, MA	199	Arc Voltage, Volts	7.3
Accel Potential, KV	3.5	Arc Current, Amps	3.5
Accel Current, MA	5.4	Coil Form Bias, Volts	3.5
Decel Potential, KV	3.2	Coil Form Current, Amps	0.0
Decel Current, MA	6.6		

*Assuming source performance of 95.7% ionization as in EC I.

Engine performance data is calculated in Table XIV from the data of Table XIII and equations (45) and (46), in the same manner as described for EC I.

TABLE XIV

Engine Performance Calculations for Engine Configuration II

Accelerated Beam Power(W_B), Watts	599	Degree of Ionization	(.957)*
Grid Drain Power (W_D), Watts	40	Fraction on Separator	.866**
Ion Generation Power (W_+), Watts	25.6	Fraction Thru Separator	1.0
Flow Control Power (W_F), Watts	0	Fraction Not Impinging	.940
Ion Generation Efficiency, EV/ION	(116)*	Propellant Utilization	.814
Power Efficiency (η_P)	.902	Total Engine Efficiency	.734

*Assuming source performance identical to EC I.

**Integrated value of ion flow compared to total flow, therefore includes degree of ionization.

It is apparent that this engine design improves the power efficiency considerably over that of EC I, but that the electromagnetic control settings are too mild to produce good propellant utilization.

ENGINE CONFIGURATION III

General Description

EC III was run in conjunction with accurate calorimeter readings, with all components functioning well over a longer period of time than the preceeding runs, and is reported in much more detail. Also, since the engine performance is fairly good, more pains were taken to confirm the accuracy of the various factors used to calculate it. The positioning of the engine components for this run, shown in Fig. 116 are identical to EC II. In this case, the source was placed at a high positive potential with respect to ground, and the decel electrode, decel shield, tank liner, calorimeter and tank wall were all at ground potential but isolated from each other. The purpose of this arrangement was to prove that the insulation and shielding of all former runs was adequate to prevent spurious electron currents between the tank and the engine components which were at high negative potential.

Between EC II and EC III the calorimeter was redesigned to improve accuracy and reliability as described in Appendix I. Frequent calorimeter confirmation of the beam power was obtained during the run.

Propellant Utilization

The ratio of ion flow rate incident on the separator plane to the total fuel flow rate was established by integration of the density pattern of Fig. 117 over a 4" radius, and also by direct measurement of the total ion

current incident on a total probe (Fig. 49) in the same position as the separator. This factor includes degree of ionization since it is secured by dividing the ion current to the probe by the total flow from the source. The ion density pattern was determined in four separate tests using the total probe of Fig. 49 in the vacuum tank of Fig. 15. Integrated ion flow rates corresponding to 93.3% and 93.1% were calculated for the range of magnetic control settings used in the engine run, and a value of 86.4% was obtained at control settings lower than any used in the engine run. Directly measured total probe currents in these four runs corresponded to 89.6%, 89.9%, 90.2%, and 88.9%* of the total flow, with the total probe masked so as to receive only the flow incident on the separator plane. Total flow in these cases was determined by titration of the cesium.

The figure of 90%, an average of the three directly measured currents, was adopted for this engine run rather than the values of 93% secured by integration. The factor, corrected for impingement currents, is the calculated value for propellant utilization in the tables below.

Propellant utilization was also checked by a rough mass balance as follows:

The contents of three 50 g. ampules of cesium were transferred under argon to a glass cylinder equipped with a pouring spout, and this amount was added to a clean boiler. The losses involved in the transfer process were

*Magnetic controls relaxed for this run until 1% of the ion current was lost.

obtained by titration of the amount of cesium which clings to the ampules and the glass cylinder, and were equal to 4.8 grams, 4.1 grams clinging to the glass cylinder and 0.22 grams clinging to a 50 gram ampule. All three ampules were assumed to retain this latter amount within small limits of error. Thus, the amount of cesium added to the boiler before the 50 hour run and preliminary operations was very close to 145 grams.

After the run the amount of cesium remaining in the boiler was transferred under argon to a volumetric cylinder, and the volume was measured as 42 ml. at room temperature, equal to 78.5 grams. The cesium remaining in the boiler was determined by titration to be equal to 9.7 grams, giving a total of 88.2 grams remaining after the run.

By subtraction, the amount of cesium used was 57.0 grams. This figure is not corrected for the cesium which clings to the fuel line and valve, which was later shown by titration to be about 1 gram. The integrated flow rate over the running time was secured as follows:

For each data point the beam current, accel drain current, and decel drain current were added to give the ion current through the separator. By dividing by the factor of 0.90 for the product of degree of ionization and fraction focussed, the flow rate through the separator was converted back to total flow rate issuing from the source. This flow rate for each data point was multiplied by the running time and the total flow secured by adding all the increments. The total flow secured by this method was 54 grams. This

check shows, within the broad limits of error of the volumetric-titrimetric method used, that the factor of 0.90 is correct for the product of the three factors: (a) degree of ionization, (b) fraction of total flow incident on the separator, and (c) fraction of incident propellant which is extracted.

Controls and Duration

The total running time for this run was 56 hours during which the only engine component replacement was a burned out cesium valve heater. The run was initiated with a two hour period of electrode conditioning and gradual increase in beam current. Following this the fuel flow was discontinued and the data examined in order to select suitable operating conditions, but the vacuum tank was kept sealed and none of the engine components was disturbed. Next an eight hour run was initiated to determine by gradual increase the limit of beam current that the system could handle. Again the vacuum system and engine components were undisturbed at shutdown. The next start up was interrupted after 3-1/2 hours by the valve heater burnout mentioned above. The tank was opened and the valve heater replaced without disturbing the other components. Inspection at this time showed no electrode damage except a faint buildup of dark material on the downstream side of the electrodes, probably due to sputtering of the collector.

The final 42-1/2 hours of running time was continuous, and the run was terminated by choice, after a final period of about 4 hours of control variation requested by the NASA observer, J. Ferrante. During the last 48 hours of operation complete sets of pertinent data were recorded at selected intervals, and are shown in Tables XVIII and XIX.

Voltage Breakdown

The high voltage power supplies used in this run are protected against overloads by automatic disconnect switches which are reset manually. In practice inter-grid voltage breakdowns seldom tripped the accel disconnect switch, on account of the attenuating effect of the 5000 ohm series resistor. However, the decel power supply did trip out at intervals.

During the 50 hour run with Engine Configuration III a record was kept of the time of each trip-out and the interval between them. It should be noted that voltage breakdowns were spontaneous at irregular intervals and did not in general follow any noticeable deteriorating conditions. The longest interval recorded during the 50 hour run was 176 minutes. The complete record is given in Table XV.

Manual reset was successfully accomplished within 2 or 3 seconds after each shutdown.

These data compare favorably with the shutdown experience encountered with the electron-bombardment thrustor described in the SERT-I test[42], where 10 shutdowns were experienced in 14 minutes with about 2 to 16 seconds elapsing before reinitiation.

TABLE XV

Voltage Breakdown Frequency During 50 - Hour Run

With Engine Configuration III

Breakdown Occurence	Interval Preceding Breakdown, Minutes	Breakdown Occurence	Interval Preceding Breakdown, Minutes
11:40 AM		11:30 PM	30
2:36 PM	176	12:05 AM	35
2:37	1	12:50	45
3:05	28	1:05	15
3:25	20	3:18	133
4:00	35	3:47	29
4:20	20	4:05	18
5:30	70	5:37	92
5:40	10	6:40	63
5:50	10	7:35	55
6:20	30	8:30	55
6:40	20	8:52	22
7:05	25	9:05	13
8:00	55	9:25	20
8:08	8	9:58	33
9:45	97	10:17	19
10:45	60	11:00	43
11:00	15		

Engine Performance and Discussion

The best performance obtained with this engine is given in Tables XVI and XVII for both the highest beam current and the highest engine efficiency. All other data sets are given in Tables XVIII and XIX.

TABLE XVI

Best Performance Data for Engine Configuration III

	Data Set No.			Data Set No.	
	55	7		55	7
Total Flow Rate, MA	225	210	Ion Beam Voltage, KV	3.2	3.2
Ion Flow Rate, MA	(215)*	(201)	Ion Beam Current, MA	197	184
Incident on Separator, MA	203	189	Arc Voltage, Volts	7.0	7.0
Accel Potential, KV	3.2	3.4	Arc Current, Amps	2.5	2.0
Accel Current, MA	0.9	0.9	Coil Form Bias, Volts	6.2	6.2
Decel Potential, KV	3.2	3.2	Coil Form Current, Amps	0.5	0.6
Decel Current, MA	5.0	3.8			

*Assuming Source Performance of 95.7% ionization as in EC-I.

In these tables the current assumed incident on the separator is the sum of the beam, accel, and decel currents. The total flow rate is secured by dividing by 0.90, the product of the degree of ionization and fraction focussed, previously determined. The degree of ionization calculated above does not enter directly into the engine performance calculation.

TABLE XVII

Best Engine Performance for Engine Configuration III

	Data Set No.			Data Set No.	
	55	7		55	7
Beam Power (W_B), Watts	630	589	Deg. of Ionization	(95.7)*	(95.7)
Drain Power (W_B), Watts	18.9	15.2	Fraction on Separator	.90**	.90**
Ion Generation Power (W_+), Watts	17.5	14.0	Fraction thru Separator	1.0	1.0
Flow Cont. Power (W_F), Watts	3.1	3.7	Fraction not Impinging	.971	.975
Ion Generation Effic., EV/Ion	95.8	88.1	Propellant Utilization	.874	.878
Power Efficiency (η_P)	0.941	0.947	Total Engine Efficiency	.822	.831

*Assuming source performance identical to EC I.

**Measured ion flow compared to total flow, therefore includes degree of ionization.

The gradual increase in boiler temperature is deliberate, to offset the slightly lower delivery rate as the boiler empties, a previously observed characteristic of the present system.

From the Tables it is apparent that the observed drain power loss is nearly as large as the ion generation power, and that this factor is influenced by the tank pressure. Later it will be seen that decel electrode damage is not nearly as great as would be expected from the apparent levels of impingement. Thus, it is possible that the decel drain power is spurious, and may be eliminated with better vacuum and/or insulation. A possible increase of about 2% overall engine efficiency is indicated here.

TABLE XVIII

50 - Hour Run Data with Engine Configuration III

Set No.	ACCEL		DECEL		TRANSMITTED BEAM CURRENT, MA.				ARC		Vacuum mm. Hg. ($x10^{-6}$)	Boiler Temp. °C	Throat Coil Amps	Cylinder Coil Amps	CONE BIAS	
	KV*	MA	KV*	MA	Target	Liner	Decel Shield	Total	Volts	Amps					Volts	Amps
1	3.4	0.9	3.2	4.2	94.0	2.8	9.5	106	7.3	2.0	18	289	30	2.2	12.0	0.6
2	3.4	0.7	3.2	7.7	137	4.4	13.9	155	7.0	2.0	19	302	30	2.2	12.0	0.7
3	3.4	0.7	3.2	3.5	150	6.9	15.1	172	7.2	2.0	16	306	30	8.5	12.0	1.3
4	3.4	0.9	3.2	4.0	160	7.7	16.2	184	7.1	2.0	23	309	30	9.3	10.0	1.3
5	3.4	1.0	3.2	4.3	164	7.8	16.6	188	7.1	2.0	23	311	25	9.0	9.0	1.7
6	3.4	0.8	3.2	6.0	137.5	5.9	13.9	157	7.1	2.0	37	301	30	5.3	12.0	0.7
7	3.4	0.9	3.2	3.8	159	8.6	16.1	184	7.0	2.0	26	314	30	9.0	6.2	0.6
8	3.4	2.0	3.2	6.3	143	6.4	3.4	153	9.5	2.0	42	300	29	10.0	9.3	0.3
9	3.4	2.0	3.2	6.3	161	7.7	4.3	173	9.0	2.1	44	301	29	9.7	9.3	0.4
10	3.4	1.0	3.2	6.4	144	7.3	3.8	155	9.4	1.8	37	297	28	13.5	8.5	0.5
11	3.4	1.25	3.2	6.2	136	8.6	4.1	149	9.5	2.0	41	294	28	14.3	8.0	0.5
12	3.4	1.25	3.2	5.8	137	7.4	3.8	148	9.5	2.0	39	294	28	14.3	8.0	0.6
13	3.4	1.40	3.2	5.8	173	11.6	5.4	190	9.5	2.0	39	301	28	14.3	8.0	0.6
14	3.4	1.1	3.2	6.6	136	5.2	3.8	145	8.8	2.4	32	297	29.5	6.4	10.0	0.1
15	3.4	1.3	3.2	6.0	171	7.3	4.8	183	8.5	2.5	38	304.3	29.5	6.5	10.0	0.1
16	3.4	1.0	3.2	4.8	164	6.3	4.2	174	8.5	2.6	27	304.5	29.0	6.4	10.0	0.2
17	3.4	1.2	3.2	4.2	162	6.0	4.1	172	8.5	2.7	22	303.8	29.5	6.5	10.0	0.3
18	3.4	4.4	3.2	3.0	161	6.4	2.5	170	8.1	2.7	13	306	26.5	6.7	8.9	0.5
19	3.4	2.4	3.2	3.1	160	6.0	2.2	168	7.0	2.5	13	306	30	3.0	9.0	0.6
20	3.2	0.5	3.2	2.6	159.5	6.6	2.2	168	7.2	2.5	15	306	30	5.0	9.0	0.7
21	3.2	0.4	3.2	2.7	160.5	6.6	2.3	169	7.3	2.6	14	306	30	5.0	9.0	0.7
22	3.2	0.6	3.2	2.6	162	6.4	1.4	170	7.1	2.5	10	307	29	5.0	9.0	0.7

Table XVIII, Cont'd

Set No.	ACCEL		DECEL		TRANSMITTED BEAM CURRENT, MA				ARC		Vacuum mm. Hg. ($x10^{-6}$)	Boiler Temp. °C	Throat Coil Amps	Cylinder Coil Amps	CONE BIAS	
	KV*	MA	KV*	MA	Target	Liner	Decel Shield	Total	Volts	Amps					Volts	Amps
23	3.2	0.6	3.2	2.6	162	6.5	1.3	170	7.0	2.5	10	308	28	5.0	9.0	0.7
24	3.2	0.5	3.2	2.6	163	6.8	1.2	171	6.9	2.5	10	308	28	5.2	9.0	1.0
25	3.2	0.5	3.2	2.6	164	1.7	1.2	172	9.0	2.5	9	308	28	5.0	9.0	0.8
26	3.2	0.6	3.2	2.6	160	6.8	1.2	168	9.0	2.5	10	308	28	5.0	9.0	0.8
27	3.2	0.5	3.2	2.5	160	6.5	1.1	168	9.0	2.5	8	307	28	5.0	9.0	0.8
28	3.2	0.4	3.2	2.6	167	7.1	1.2	175	8.9	2.6	7	310	28	5.0	9.0	0.8
29	3.2	0.4	3.2	2.5	162	6.8	1.1	170	7.9	2.4	7	308.3	28	13.0	9.1	0.8
30	3.2	0.3	3.2	2.4	160	6.3	1.2	168	8.1	2.8	7	307.3	28.5	13.0	9.2	0.8
31	3.2	0.2	3.2	2.3	158	6.3	1.0	165	8.0	2.7	6	306.0	28.5	13.4	9.5	1.0
32	3.2	0.5	3.2	2.8	152	7.2	3.1	162	7.2	2.5	14	306	26.5	5.0	7.0	0.6
33	3.2	0.8	3.2	2.6	158	7.7	2.1	168	7.2	2.5	13	309	30.0	5.5	7.0	0.6
34	3.2	1.0	3.2	3.1	159.5	7.1	1.2	168	7.1	2.5	11	309	31.5	4.3	7.0	0.5
35	3.0	0.9	3.0	2.4	152	6.9	1.1	160	7.1	2.5	8.8	309	29.0	7.0	7.0	0.7
36	2.8	0.6	2.8	1.8	137	6.6	1.0	145	6.9	2.5	8.7	309	29.0	10.5	5.0	0.2
37	2.6	0.5	2.6	1.5	122	6.4	0.9	129	6.8	2.5	8.2	309	29.0	8.7	4.5	-0-
38	3.2	1.2	3.2	2.5	148	7.0	0.9	156	7.0	2.5	8.7	309	29	6.0	6.0	0.2
39	3.4	1.8	3.4	2.8	151	7.2	0.9	159	7.0	2.5	9.1	309	29	6.0	6.0	0.3
40	3.6	2.2	3.6	3.3	154	7.6	1.0	163	7.0	2.5	9.5	309	29	6.0	6.0	0.3
41	3.8	3.1	3.8	3.9	158	8.0	1.0	167	7.0	2.5	10	309	29	6.0	6.0	0.3
42	4.0	2.6	4.0	4.2	162	8.2	1.6	172	7.0	2.5	12	309	29	6.0	6.0	0.3
43	3.7	3.0	3.2	2.6	150	6.2	1.1	157	7.0	2.5	10	309	29	6.0	6.0	0.3
44	3.5	2.4	3.0	2.1	148	5.6	0.9	154	7.0	2.5	8.4	309	29	6.0	6.0	0.3
45	3.3	2.0	2.8	1.7	144	5.5	0.8	150	7.0	2.5	8.3	309	29	6.0	6.0	0.3
46	3.1	1.6	2.6	1.5	140	5.1	0.8	146	7.0	2.5	8.0	309	29	6.0	6.0	0.3
47	3.3	2.4	2.6	1.4	140	4.1	0.7	145	7.0	2.5	7.8	309	29	6.0	6.0	0.3

Table XVIII, Cont'd

Set No.	ACCEL KV*	ACCEL MA	DECEL KV*	DECEL MA	TRANSMITTED BEAM CURRENT, MA Target	Liner	Decel Shield	Total	ARC Volts	ARC Amps	Vacuum mm. Hg. ($x10^{-6}$)	Boiler Temp. ^{o}C	Throat Coil Amps	Cylinder Coil Amps	CONE BIAS Volts	CONE BIAS Amps
48	3.5	3.2	2.6	1.4	140	3.3	0.6	144	7.0	2.5	7.8	309	29	6.0	6.0	0.3
49	3.7	3.9	2.8	1.6	143	3.7	0.7	147	7.0	2.5	7.8	309	29	6.0	6.0	0.3
50	3.9	4.4	3.0	1.8	147	3.9	0.7	152	7.0	2.5	7.8	309	29	6.0	6.0	0.3
51	4.1	5.5	3.2	2.4	148	4.3	0.7	153	7.0	2.5	7.8	309	29	6.0	6.0	0.3
52	4.2	5.4	3.3	2.6	149	4.4	0.8	154	7.0	2.5	7.8	309	29	6.0	6.0	0.3
53	4.3	5.9	3.4	2.7	151	4.5	0.8	156	7.0	2.5	8.3	309	29	6.0	6.0	0.3
54	4.2	5.5	3.2	2.4	150	3.1	0.7	154	7.0	2.5	7.7	309	29	6.0	6.0	0.3
55	3.2	0.9	3.2	5.0	185	10.5	1.7	197	7.0	2.5	9.7	322**	34	11.5	6.2	0.5

*The KV potentials of accel and decel are the negative values with respect to the source.

**This increase in boiler temperature should have resulted in a flow rate increase of 40 - 60%, based on previous experience, instead of the 28% shown here. The propellant utilization for this one data point may therefore be somewhat lower than the value assumed. This does not affect the overall run, since these conditions were maintained for only a few minutes.

TABLE XIX

Engine Performance Calculations for Data of
50 - Hour Run With EC-III

Data Set No.	1	2	3	4	5	6	7	8
Accel Beam Power (W_B) Watts	340	396	551	590	602	503	590	490
Grid Drain Power (W_D), Watts	16.3	26.9	13.4	15.7	16.9	21.8	15.0	26.6
Ion Gen. Power (W_+) Watts	14.6	14.0	14.4	14.2	14.2	14.2	14.0	19.0
Flow Control Power (W_F) Watts	7.2	8.4	15.6	13.0	15.3	8.4	3.7	2.8
Ion Gen. Effic., Ev/Ion	185	129	160	136	145	130	88.4	127
Power Effic. (η_P)	.90	.91	.928	.932	.928	.920	.948	.910
Fraction Not Impinging	.954	.949	.975	.974	.977	.958	.975	.948
Propellant Utilization (η_U)	.859	.854	.878	.876	.880	.862	.877	.854
Total Engine Effic. (η_T)	.773	.776	.815	.816	.816	.792	.832	.778

Data Set No.	9	10	11	12	13	14	15	16
Accel Beam Power (W_B) Watts	554	496	477	475	609	465	585	557
Grid Drain Power (W_D), Watts	26.6	23.6	22.8	28.6	18.9	24.6	23.4	18.6
Ion Gen. Power (W_+) Watts	18.9	16.9	19.0	19.0	19.0	21.3	21.2	22.1
Flow Control Power (W_F), Watts	3.7	4.2	4.0	4.8	4.9	1.0	1.3	2.0
Ion Gen. Effic., Ev/Ion	118	122	138	145	115	138	112	126
Power Effic., (η_P)	.918	.916	.910	.912	.935	.910	.928	.928
Fraction Not Impinging	.954	.954	.952	.955	.963	.950	.962	.968
Propellant Utilization (η_U)	.859	.859	.856	.860	.866	.855	.865	.871
Total Engine Effic., (η_T)	.789	.786	.780	.785	.810	.778	.802	.809

Table XIX, Cont'd

Data Set No.	17	18	19	20	21	22	23	24
Accel Beam Power (W_B), Watts	554	545	538	538	540	545	545	547
Grid Drain Power (W_D), Watts	17.3	24.6	17.6	9.9	9.9	10.2	10.2	9.9
Ion Gen. Power (W_+), Watts	23.0	21.8	17.5	18.0	19.0	17.7	17.5	17.2
Flow Control Power (W_F), Watts	3.0	4.4	5.4	6.3	6.3	6.3	6.3	9.0
Ion Gen. Effic., Ev/Ion	138	139	124	134	139	131	130	142
Power Effic., (η_P)	.929	.915	.930	.942	.940	.940	.940	.937
Fraction Not Impinging	.969	.958	.968	.982	.982	.982	.982	.982
Propellant Utilization (η_U)	.872	.862	.871	.885	.885	.885	.885	.885
Total Engine Effic., (η_T)	.810	.789	.810	.833	.832	.832	.832	.829

Data Set No.	25	26	27	28	29	30	31	32
Accel Beam Power (W_B), Watts	554	538	538	560	544	538	528	518
Grid Drain Power (W_D), Watts	9.9	10.2	9.6	9.6	9.3	8.6	8.0	8.0
Ion Gen. Power, (W_+), Watts	22.5	22.5	22.5	22.2	19.0	22.7	21.6	18.0
Flow Control Power (W_F), Watts	7.2	7.2	7.2	7.2	7.3	7.4	9.5	4.2
Ion Gen. Effic., Ev/Ion	160	164	164	156	144	166	175	127
Power Effic., (η_P)	.932	.931	.933	.935	.936	.934	.931	.940
Fraction Not Impinging	.982	.981	.982	.983	.983	.984	.985	.980
Propellant Utilization (η_U)	.885	.884	.885	.885	.885	.885	.886	.882
Total Engine Effic., (η_T)	.824	.822	.825	.827	.829	.826	.825	.829

Table XIX, Cont'd

Data Set No.	33	34	35	36	37	38	39	40
Accel Beam Power (W_B) Watts	538	538	480	406	335	500	540	587
Grid Drain Power (W_D) Watts	10.9	13.1	9.9	6.7	5.2	11.8	15.6	15.3
Ion Gen. Power (W_+), Watts	18.0	17.7	17.7	17.2	17.0	17.5	17.5	17.5
Flow Control Power (W_F) Watts	4.2	3.5	4.9	1.0	0	1.2	1.8	1.8
Ion Gen. Effic., Ev/Ion	122	116	142	117	123	111	112	109
Power Effic., (η_P)	.943	.942	.934	.942	.940	.944	.941	.945
Fraction Not Impinging	.980	.975	.980	.984	.985	.977	.972	.967
Propellant Utilization (η_U)	.882	.876	.881	.885	.885	.879	.875	.870
Total Engine Effic., (η_T)	.832	.825	.822	.832	.831	.829	.824	.822

Data Set No.	41	42	43	44	45	46	47	48
Accel Beam Power (W_B) Watts	635	688	502	462	420	379	377	374
Grid Drain Power (W_D) Watts	26.6	27.2	20.0	14.7	11.4	8.8	11.4	14.9
Ion Gen. Power (W_+) Watts	17.5	17.5	17.5	17.5	17.5	17.5	17.5	17.5
Flow Control Power (W_F) Watts	1.8	1.8	1.8	1.8	1.8	1.8	1.8	1.8
Ion Gen. Effic., Ev/Ion	105	103	102	115	118	122	122	122
Power Effic., (η_P)	.935	.936	.929	.931	.932	.928	.923	.915
Fraction Not Impinging	.960	.962	.966	.976	.976	.979	.975	.969
Propellant Utilization (η_U)	.864	.869	.878	.878	.880	.877	.870	.867
Total Engine Effic., (η_T)	.807	.810	.806	.819	.820	.817	.809	.795

Table XIX, Cont'd

Data Set No.	49	50	51	52	53	54	55
Accel Drain Power (W_B) Watts	412	455	490	510	532	492	632
Grid Drain Power (W_D) Watts	19.0	22.7	30.3	31.3	34.6	30.8	18.9
Ion Gen. Power (W_+) Watts	17.5	17.5	17.5	17.5	17.5	17.5	17.5
Flow Control Power (W_F) Watts	1.8	1.8	1.8	1.8	1.8	1.8	3.1
Ion Gen. Effic., Ev/Ion	119	115	113	112	111	113	94.2
Power Effic., (η_P)	.914	.916	.908	.910	.909	.909	.943
Fraction Not Impinging	.964	.961	.951	.951	.948	.951	.971
Propellant Utilization (η_U)	.865	.855	.855	.853	.853	.855	.875
Total Engine Effic., (η_T)	.790	.794	.775	.779	.775	.776	.825

TABLE XX

Calorimetric Data and Calculations for 50 Hour Run With Engine Configuration III

Data Set No.	1	2	3	4	5	7	14	15
Target Current, MA	89	134	149.5	162.5	165	158.5	136	169
Accel Potential, KV	3.2	3.2	3.2	3.2	3.2	3.2	3.2	3.2
Beam Watts	285	430	479	520	529	508	436	541
Calibrator Watts	320	448	492	527	536	527	463	561
Calibrator - MV	.50	.69	.71	.75	.74	.79	.73	.82
Calorimeter - MV	.56	.76	.82	.85	.86	.85	.76	.865
Watts Absorbed in Calorimeter								
Gross	359	494	569	598	625	568	483	593
Tare	63	59	57	55	51	58	58	54
Net	296	435	512	543	574	510	425	539

Data Set No.	18	19	20	21	22	23	24	25
Target Current, MA	159	160.5	160	160	162	162	162	164
Accel Potential, KV	3.2	3.2	3.2	3.2	3.2	3.2	3.2	3.2
Beam Watts	510	515	512	512	559	519	519	525
Calibrator Watts	526	526	526	526	526	528	528	535
Calibrator - MV	.80	.77	.84	.82	.80	.82	.79	.79
Calorimeter - MV	.89	.87	.90	.95	.93	.91	.91	.89
Watts Absorbed in Calorimeter								
Gross	585	595	564	610	614	587	609	604
Tare	54	52	56	56	55	53	52	52
Net	531	543	508	554	559	534	557	552

Table XX, Cont'd

Data Set No.	26	27	29	30	32	33	34	35	36	37
Target Current, MA	160	160	162	161	150.5	158.5	158	152	133.5	121
Accel Potential, KV	3.2	3.2	3.2	3.2	3.2	3.2	3.2	3.2	3.2	3.2
Beam Watts	512	512	519	515	482	508	516	487	427	388
Calibrator - Watts	528	526	537	537	495	517	522	460	391	320
Calibrator - MV	.79	.76	.81	.82	.73	.76	.75	.68	.57	.48
Calorimeter - MV	.86	.83	.91	.90	.85	.86	.86	.82	.77	.67
Watts Absorbed in Calorimeter										
Gross	574	575	604	589	577	585	600	555	528	446
Tare	52	55	52	44	55	57	53	53	55	58
Net	522	520	552	545	522	528	547	502	473	388

Propellant utilization losses in these runs are much more serious than ion generation power losses. It has already been experimentally demonstrated that the degree of ionization can be increased to above 99%, with the expanding arc source at higher flow rates, or even at the present flow rates, given time to develop a better low flow source. This alone would raise engine efficiency another 3%. Thus, an increase in engine efficiency of at least 5% over the levels reported can be predicted even without further development of flow control methods. Flow control development is necessary before engine efficiencies above 90% can be reached.

Extent of Electrode Erosion

Figs. 119 through 124 illustrate the electrode condition after the run. The black deposit on the upstream side of the separator and accel electrode may be organic decomposition products due to occasional overheating of the throat coil, which was insulated with a silicone rubber. The slight warping at the center of the separator electrode is the result of severe discharge currents to this area during the preliminary cleanup operations, and may be the reason for the slight electrode erosion of the central holes of the accel and decel electrodes. In Fig. 121 the upstream side of the accel electrode is slightly polished in a pattern around each hole. This pattern is more extended in a radial direction at the peripheral holes, perhaps as a result of the skewing of the virtual anode due to the gross angle of approach of the ions. The small amount of deposit on the downstream side of the accel electrode and the much larger amount on the decel electrode downstream is probably material sputtered from the collector. On the upstream side of the decel electrode there is slight visible electrode erosion around the central and peripheral

holes, separated by a region of less erosion. This may be due to slight underfocussing at the beam axis followed by optimum focussing and overfocussing as the radius increases.

Fig. 125 is a photograph of the target calorimeter after an engine run, after all soluble material had been washed off. The visible image of the electrode system was caused by ion bombardment, and could only be obtained if the ion beam was neutralized a very slight distance downstream of the decel electrode, i.e., before complete dispersion of the beam was effected by charge repulsion. The central region of the image is completely opaque due to high ion density.

Calorimeter Confirmation of the Beam Power

Beam power measurements with the calorimeter system described in Appendix I were made simultaneously with electrical beam power measurements for 26 sets of data points during the run with EC III. Table XX shows the data and calculated beam power readings. The average difference between the electrical and calorimetric measurements for the 26 sets of data was 4.3 percent, and the standard deviation from the average difference was 3.8 percent. This is considered excellent confirmation of the ion beam measurements, and demonstrates that the measured currents were true ion beam currents, uncomplicated with electron backstreaming. Thus, the degree of shielding outside the electrodes, and the relation of the electrode potentials was apparently adequate to prevent electron backstreaming.

APPLICATION OF ENGINE PERFORMANCE TO SPECIFIC MISSION REQUIREMENTS

The performance of the plasma separator engine has been compared with that of the electron bombardment engine for specific missions in a separate study by H. I. Brown. His analysis showing considerably higher performance capabilities for the plasma separator engine is given in detail in Appendix II and need not be repeated here.

A few words are in order, however, on the assumed performance of the plasma separator engine. As indicated in equations (45) and (46), the engine efficiency depends largely on three factors; propellant utilization, ion impingement, and ion generation and flow control power. In the plasma separator engine these factors can be optimized simultaneously with the single restriction that the flow control process must be limited by the density pattern. Thus an overall propellant utilization of 0.90, which has already been demonstrated experimentally in several engine runs, has been assumed. This figure is conservative by about 3%, since it includes degree of ionization, because this latter factor is a function of source performance alone, and the capability to produce levels of ionization above 99% has been experimentally verified several times.

Drain power is a function of accelerator performance alone, and has on many occasions been observed well below the 2% level, even with the present background tank pressures.

Ion generation and flow control power has already been recorded at 88 electron volts/ion in the EC III run, and this was at a low ion flow rate. It is known from the source performance studies that this factor can be lowered to below 70 Ev/Ion either by increasing the flow rate or by continuing the development of a low flow source, and this is the factor used by Brown in his analysis. However, even if the already measured factor of 88 Ev/Ion were used, the engine efficiency would be decreased by only 1%.

A most important factor to be noted in Brown's analysis is that the optimum specific impulse for the missions examined is low, where the Plasma Separator Engine, because of low ion generation power requirements, is capable of superior performance. A brief illustration of the effect of specific impulse on engine performance may clarify this point.

The Effect of Specific Impulse on Ion Engine Efficiency

The overall efficiency of an ion engine may be estimated by:

$$(47)\quad \eta_T = \eta_P \times \eta_U$$

where total engine efficiency is the product of the power efficiency (η_P) and the propellant utilization (η_U). Propellant utilization is simply the accelerated beam current divided by the total fuel flow rate in the same units, and a given constant propellant utilization affects the overall engine efficiency equally at high specific impulse and low.

Power efficiency can be further defined as

$$(48)\quad \eta_P = \frac{P_B}{P_B + P_D + P_+}$$

where P_B is the accelerated beam power, P_D the drain power on the electrodes, and P_+ the ion generation power. Other power losses can of course occur and enter into equation (48) in the same manner, but the simplified equation above serves to illustrate the point. The beam power in watts is of course the product of beam current and decel voltage, and the specific impulse is given by:

$$(49)\quad I_{sp} = 125\sqrt{V_D}$$

If we assume that the drain power is some constant small fraction of the beam power, say $\sim$1%, then (49) and (48) can be combined to give:

$$(50)\quad \eta_P = \frac{I_{sp}/125}{1.01\, I_{sp}/125 + v_+}$$

where v_+ is the ion generation power in electron volts per ion.

Fig. 126 shows the ion engine efficiency as a function of specific impulse for two different values of propellant utilization assuming constant ion generation power of 100 electron-volts per ion (2 upper curves). It can be seen that this factor is equally important at all specific impulses. Fig. 126 also shows the same relationship for two values of ion generation power using equation (50) and assuming constant propellant utilization and 1% drain power (2 lower curves).

Here it can be seen that the low ion generation power of the Plasma Separator Engine is essential for high engine efficiency at low specific impulse. If all other power losses were included this effect would be modified in degree only.

VI. OVERALL EVALUATION, CONCLUSIONS, AND RECOMMENDATIONS

EVALUATION AND CONCLUSIONS

An unoptimized engine configuration of the plasma separator type has been already tested at above 83% thrustor efficiency using a predetermined figure for degree of ionization and propellant utilization. A combination of the highest component performances which have been separately demonstrated, namely, 99% ionization, 70 ev/ion, $<$ 2% impingement currents, and 94% ion flow control would result in an electrical efficiency of 95%, a propellant utilization of 91%, and a thrustor efficiency of 86.5% at present beam current and specific impulse levels.

Reasonable progress in either the flow control or the accelerator areas described above would result in engine efficiencies above 90%, which Mickelson[43] has described as a necessary capability if electrical propulsion is to assume a significant role in space exploration activities. The plasma separator engine is the only ion engine under present development which gives promise of approaching this level of operation at low specific impulse because of the inherent operating characteristics of its components.

Peak ion source performance has been established for several specific conditions at levels of ionization above 99% at a power cost well below 100 electron volts/ion. No other ion source reported to date approaches this level of performance. A theory which explains source performance characteristics in some detail has been developed, and it predicts further source improvement, especially at low flow rates.

A modification in the theory of plasma extraction optics has been suggested which explains a number of observed experimental facts. Even with a simple perforated plate design, the electrode erosion rates are low. Extension of this theory in a combined analytical and experimental study are expected to lead to the low impingement designs necessary for long lifetime thrustors.

The capabilities and limitations of aerodynamic flow control from single sources have been thoroughly explored, and a computer program has been established which is capable of efficient study of the multiple source concept. It has been shown that the use of multiple sources improves propellant utilization considerably at any density ratio, but this area has not been fully explored.

Since magnetic flow control is the only method capable of effecting complete propellant utilization, in this type engine, its continued development is necessary for the realization of very high engine efficiency levels. The concept of electromagnetic flow control has been verified qualitatively, but an extensive investigation of the electromagnetic field is necessary before flow control can be improved to the desired level.

Further study of either of these methods of flow control will result in the necessary higher levels of propellant utilization and beam current density.

RECOMMENDATIONS

It is recommended that the potential of the plasma separator engine in the low specific impulse region be fully explored without delay in an adequate engine component optimization program followed by construction and testing of a complete engine. The component optimization programs prerequisite to the engine design are:

1. A combined analytical and experimental study to solve the problem of the autofocussing optical theory described previously. The successful solution of this problem will lead for the first time, to the design of a plasma extraction electrode system with near perfect optics.

2. An experimental study to confirm the theory of source performance described previously, and thus establish design criteria for sources operating at any reasonable flow rate.

3. An experimental study of source materials and long range durability.

4. A computer optimization of the multiple source concept, using a variety of the density patterns already established, followed by experimental verification. This study will establish the practical limit of propellant utilization for this method.

5. A combined analytical and experimental study of electromagnetic flow control, designed to establish the characteristics of the electric and magnetic field in the plasma and sheath regions. Even a semi-quantitative solution of this problem would result in considerable improvement in electromagnetic nozzle design.

6. An experimental study to design and test the electromagnetic flow control of plasma from a multiple source. There is every reason to believe that this concept will eventually lead to levels of propellant utilization approaching 100%.

REFERENCES

1. J. B. Taylor, and I. Langmuir, Phys. Rev. 44, 423, (1933).

2. B. A. Free, J. W. Carter, and M. L. Bromberg, Final Report, "Effect of Impurities of Cesium Fuel Upon Ion Engines", Contract # AF 33(657)-9163, June 1964, General Electric Company.

3. H. R. Kaufman, "The Electron-Bombardment Ion Rocket", Paper presented to AFOSR Symposium on Advanced Propulsion Concepts, Cincinnati, Ohio, (1962).

4. M. L. Bromberg, B. A. Free, and G. R. Brown, "A Program of Ion Source Research and Development", Final Report, Contract # NAS 3-2504, January, 1963, General Electric Company.

5. J. Y. Wada and R. C. Knechtli, "Generation and Application of Highly Ionized Quiescent Cesium Plasma in Steady State", Proc. IRE 49, 1926, (1961).

6. R. J. Donahue and R. I. Majkowski, "Spectroscopic Measurements of Temperatures and Densities in a Cesium Plasma", J. Appl. Phys. 33, 3, (1962).

7. M. L. Bromberg, "Analytical Study of Ionization in Cesium Plasma", General Electric Company, Report # R63FPD130, Cincinnati, Ohio, (1962).

8. J. Y. Wada and R. C. Knechtli, "Cesium Plasma Studies for Thermionic Energy Conversion", Final Report, Contract # NONr-3501(00), (1962).

9. J. M. Houston, "Thermionic Emission of Refractory Metals in Cesium Vapor", General Electric Research Laboratory, (1961).

10. M. D. Gibbons, "Experimental Studies of the Emission and Discharge Characteristics of the Ta-Cs System", Advanced Energy Conversion 1 Pergaman Press, Great Britain, (1962).

11. "Research on the Collision Probabilities of Electrons and Cesium Ions in Cesium Vapor", Final Report, Contract NASr-112, May 31, 1963.

12. G. Francis, "Ionization Phenomena in Gases", Butterworth Scientific Publications, London, 1960.

13. J. D. Cobine, "Gaseous Conductors", Dover Publications, Inc., New York, 1958.

14. J. G. Hershberg and E. Hinov, Phys. Rev. 125, 3, Feb. 1, 1962.

15. G. Kuskevics, "Calibration of Cesium Flow in the Ion Engine", General Electric Company, Report No. R61FPD106, February 1961.

16. E. H. Kennard, "Kinetic Theory of Gases", McGraw-Hill, Inc., New York, 1938.

References, (Cont'd)

17. R. D. Present, "Kinetic Theory of Gases, McGraw-Hill, Inc., New York, 1958.

18. W. G. Pollard and R. D. Present, "On Gaseous Self-Diffusion in Long Capillary Tubes", Phys. Rev., V. 73, April 1948.

19. E. M. Sparrow, V. K. Jonsson, And T. S. Lundgren, "Free Molecule Tube Flow and Adiabatic Wall Temperatures", Journal of Heat Transfer, Trans. ASME, 118, May, 1963.

20. C. A. Tsonis, General Engineering Laboratory, General Electric Company, Schenectady, New York, "Molecular Flux Distribution in an Aerospace Chamber-Analysis of Gas Kinetics-Summary Report", AEDC-TDR-63-88, April, 1963.

21. D. H. Davis, L. L. Levenson, and M. Milleron, "Theoretical and Experimental Studies of Free Molecular Flow Through Short Ducts", Rarified Gas Dynamics, Edited by L. Talbot, Academic Press, New York, 1961.

22. B. B. Dayton, "Gas Flow Patterns at Entrance and Exit of Cylindrical Tubes", Proc. Symp. Vac. Tech., Pergamon Press, 1960.

23. H. W. Liepmann, "Gas Kinetics and Gas Dynamics of Orifice Flow", J. Fluid Mech., February, 1961.

24. A. Kantrowitz and J. Grey, "A High Intensity Source for the Molecular Beam", Part 1. Theoretical, Rev. Sci. Instru., 22, No. 8, May, 1951.

25. H. M. Parker, A. R. Kuhlthau, and R. Zapata, "The Application of Supersonic Beam Sources to Low Density, High Velocity Experimentation", Rarified Gas Dynamics, Edited by F. M. Devienne, Pergammon Press, 1960.

26. H. S. Tsein, "Superaerodynamics, Mechanics of Rarified Gases", J. Aero. Sci., 16, No. 95, 1949.

27. H. Ashley, "Application of the Theory of Free Molecule Flow to Aeronautics", J. Aero. Sci., 16, No. 95, 1949.

28. G. M. Patterson, "Theory of Free-Molecule, Orifice-Type Pressure Probes in Isentropic and Non-isentropic Flows", Institute of Aerophysics, University of Toronto, UTIA Report No. 41, AFOSR TN 57-13, April 1959.

29. G. M. Patterson and E. L. Harris, "Properties of Impact Pressure Probes in Free Molecule Flow", Institute of Aerophysics, University of Toronto, UTIA Report No. 52, April 1958.

30. P. Clausing, "Uber der Stromung Sehr Verdunter Gase Durch Rohren von Beliebieger Lange", Ann. der Physik, V. 12, 1932.

References, (Cont'd)

31. E. A. Richley and T. W. Reynolds, "Numerical Solutions of Free Molecule Flow in Converging and Diverging Tubes and Slots", NASA Technical Note TN D-2330, 1964.

32. Edmund E. Callaghan and Stephen H. Maslen, "The Magnetic Field of a Finite Solenoid," Report No. NASA TN D-465, October, 1960.

33. A. R. Sass and J. C. Stoll, "Magnetic Field of a Finite Helical Solenoid", NASA Report TN D-1993, October 1963.

34. Arthur W. Goldstein, "Sheath Near a Plane Electrode Bounding a Collisionless Plasma in a Magnetic Field", NASA Technical Note TN D-1992, October 1963.

35. W. N. Neiman, "Development of a Cesium Plasma Accelerator System", General Electric Company Report 64SD3001, Missile and Space Division, Cincinnati, Ohio, Jan 23, 1964.

36. W. R. Kerslake, "Accelerator Grid Tests on an Electron-Bombardment Ion Rocket", NASA Technical Note TN D-1168, February 1962.

37. W. R. Kerslake and V. Pawlik, "Additional Studies of Screen and Accelerator Grids for Electron Bombardment Ion Thrustors", NASA Technical Note TN D-1411 August 1963.

38. M. D. Gabovich, "Extraction of Ions from Plasma Ion Sources and Primary Formation of Ion Beams", Pribory i Tekhnika Eksperimenta 2, March-April, 1963.

39. D. C. Prince, Jr., "Analytical Development of Ion Optical Systems for the XE-705 Plasma Separator Engine," General Electric Company, Report R62FPD380, (1962), Evendale, Ohio.

40. P. E. Jasper, "A Bakeable 800-Liter Vacuum Tank for Ion Engine Testing", Report R60FPD546, General Electric Company, Cincinnati 15, Ohio.

41. W. Sabin, R. Templeton, and R. Scheffer, "Instrumentation and Control System for Ion Engine Development Laboratory", Report R63FPD181, General Electric Company, Cincinnati 15, Ohio.

42. H. Gold, R. J. Rulis, F. A. Maruna, Jr., W. H. Hawersat, "Description and Operation of Spacecraft In SERT-I Ion Thrustor Flight Test", NASA TM X-52050, Lewis Research Center, Cleveland, Ohio.

43. Missiles and Rockets, September 7, 1964, p 32.

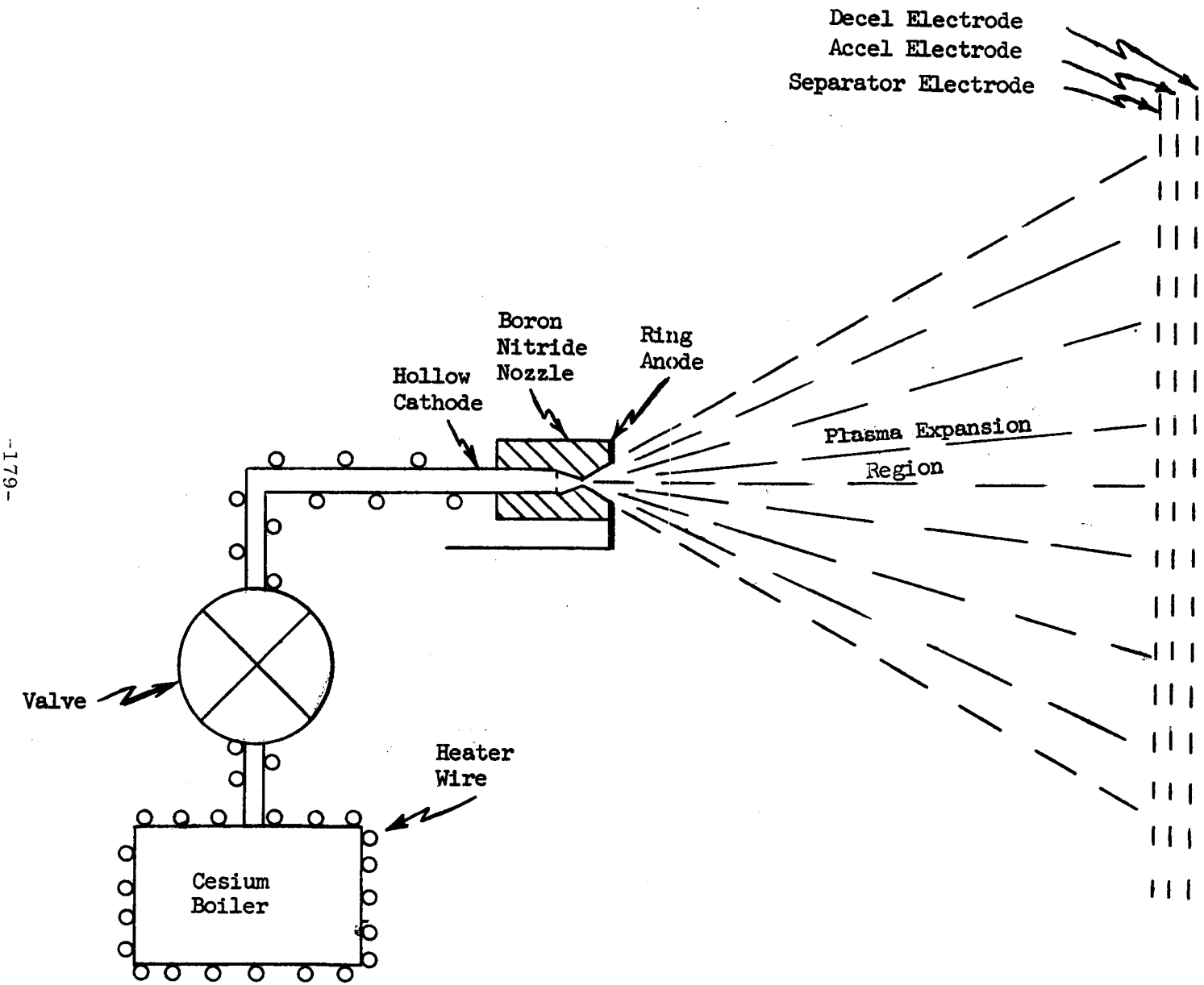
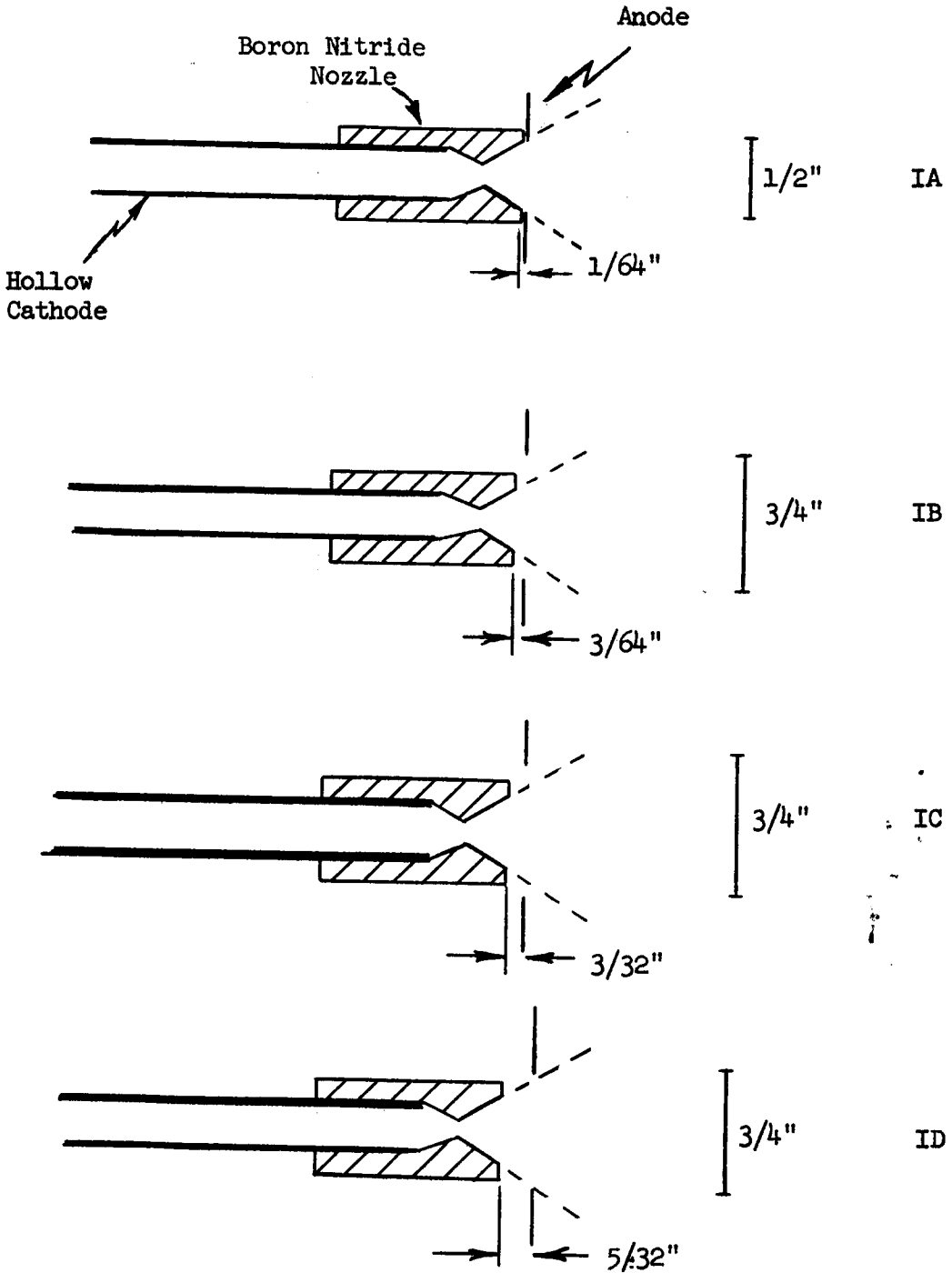
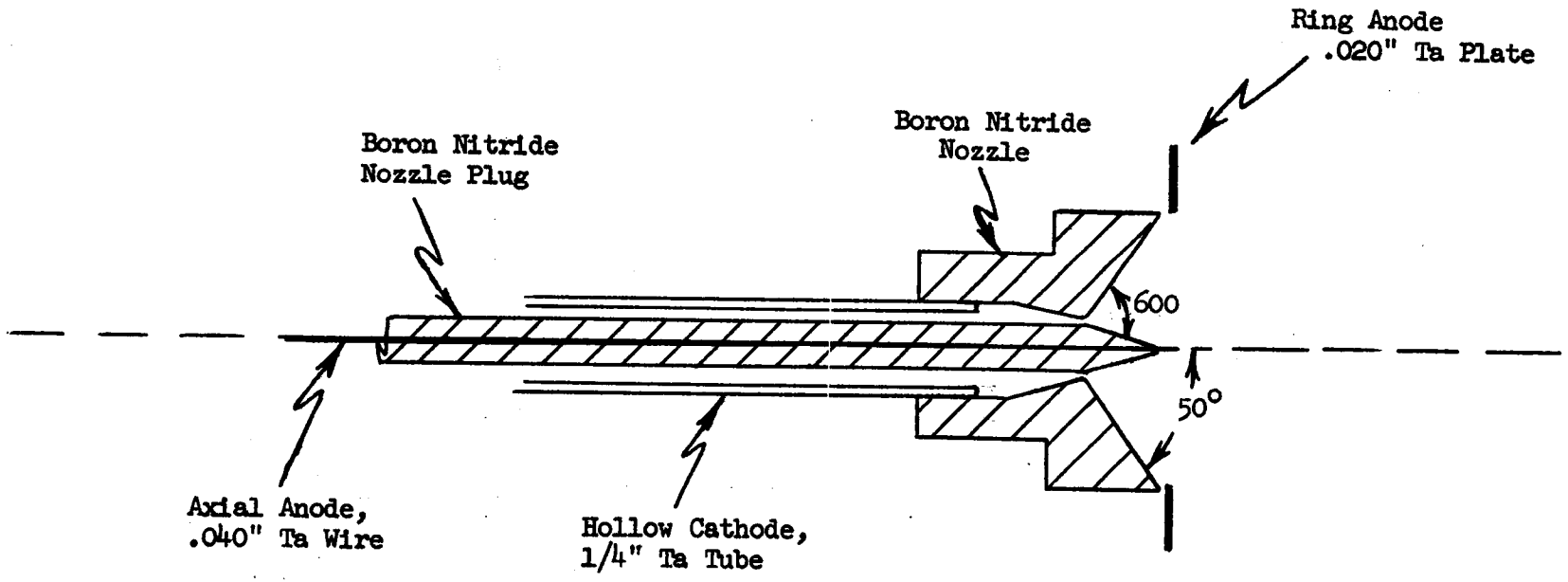


Fig. 1: Elements of the Plasma Separator Ion Engine



Cathode: 1/4" Ta Tube, .010" Wall.
Nozzle: .109" Throat, 60° Nozzle.
Anode: .020" Ta Plate.

Fig. 2: Source Design I



Scale 2:1

Fig. 3: Source Design II

Scale 2:1

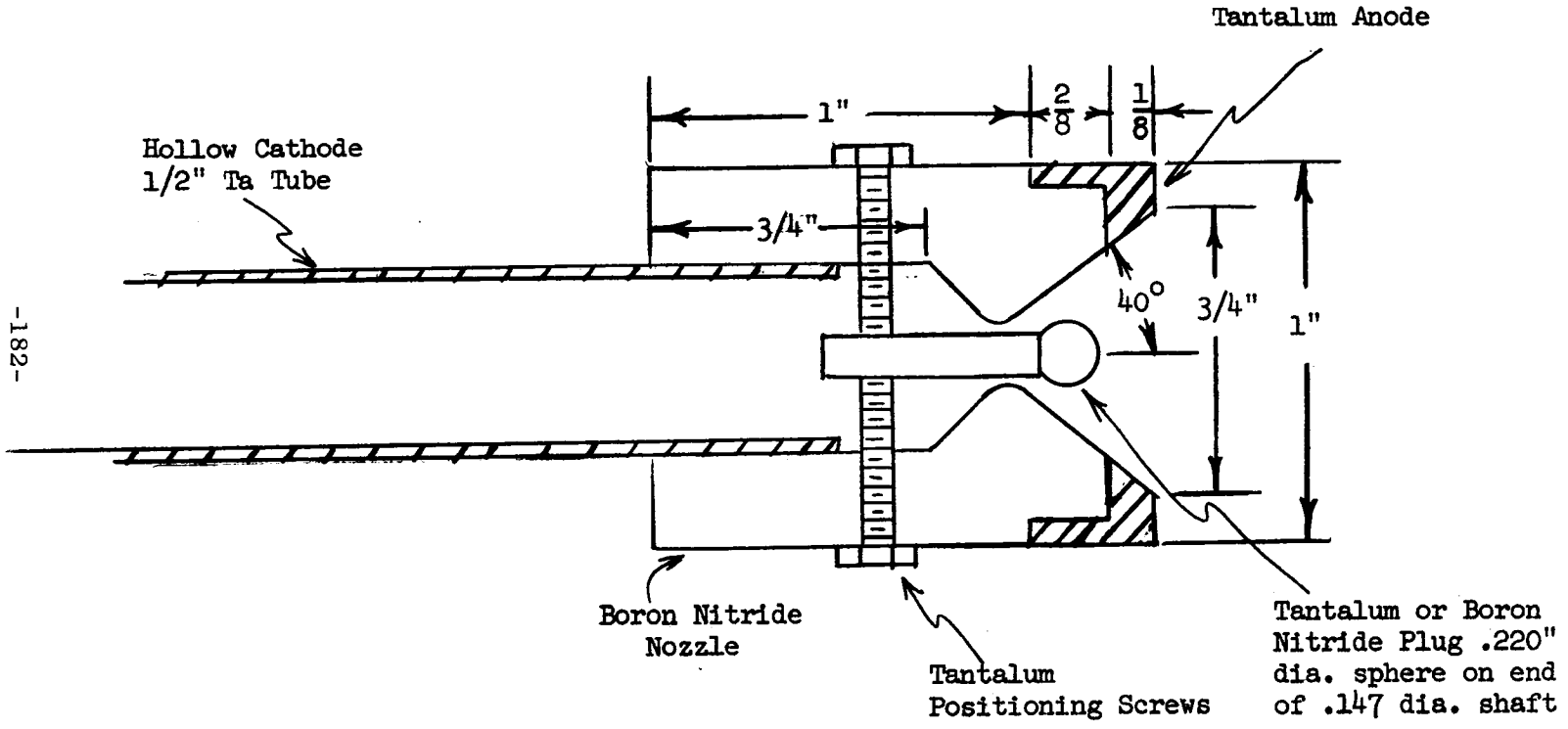
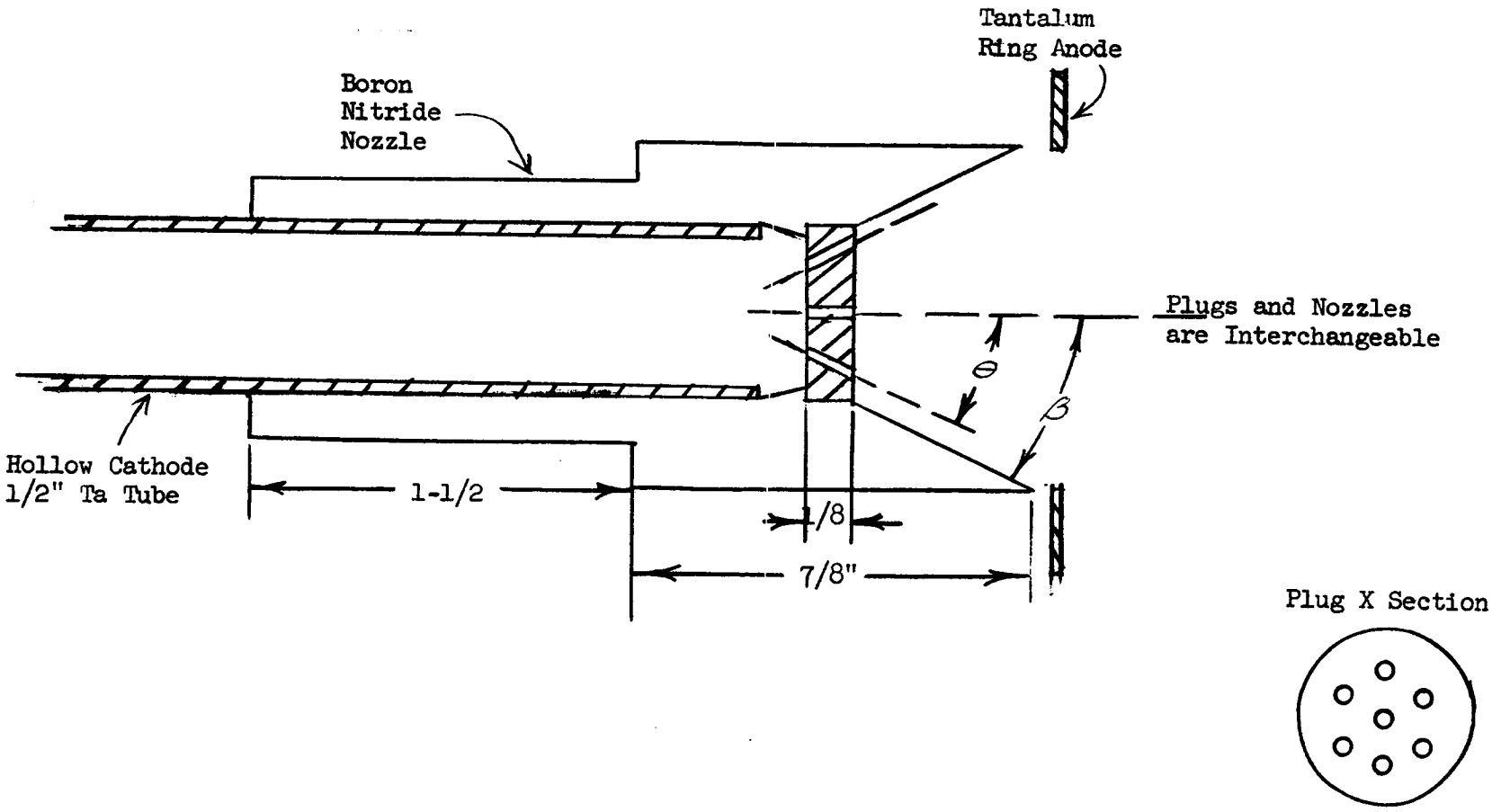


Fig. 4 : Source Design III

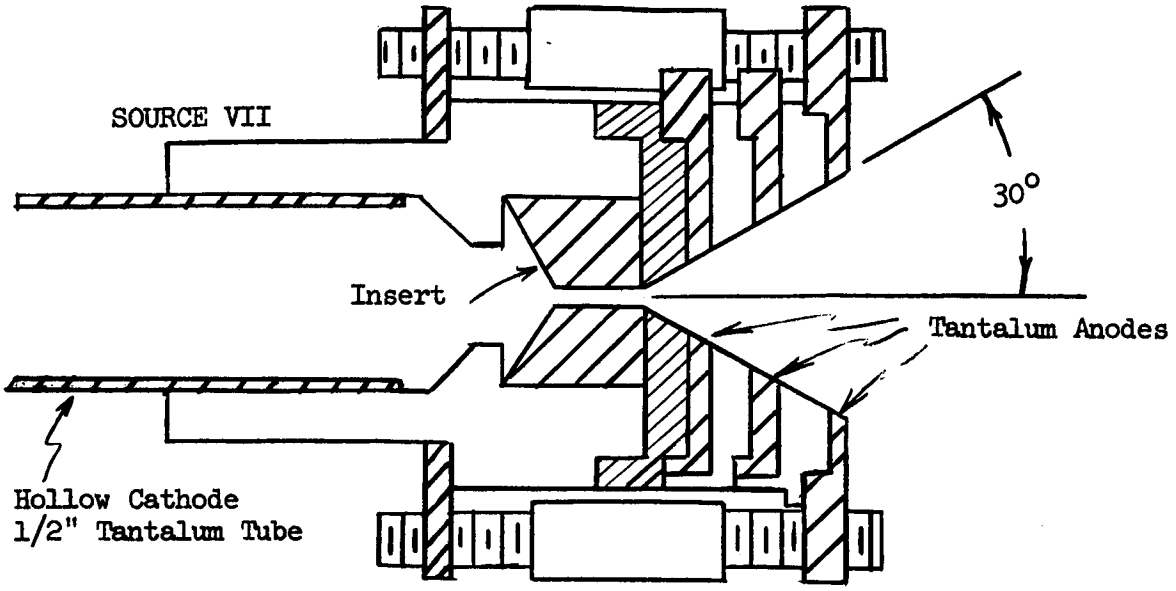
		θ	β
Noz. IV	(a)	15°	15°
	(b)	20°	15°
	(c)	25°	15°
Noz. V	(a)	20°	20°
	(b)	25°	20°
	(c)	15°	20°
Noz. VI	(a)	25°	25°
	(b)	20°	25°
	(c)	15°	25°

Scale 2:1

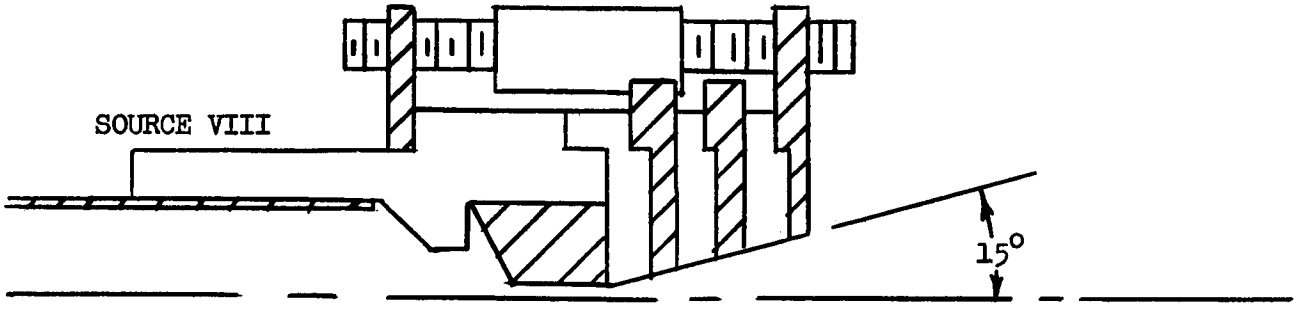


Plug X Section

Fig. 5 : Source Designs IV, V, VI



Scale 2:1



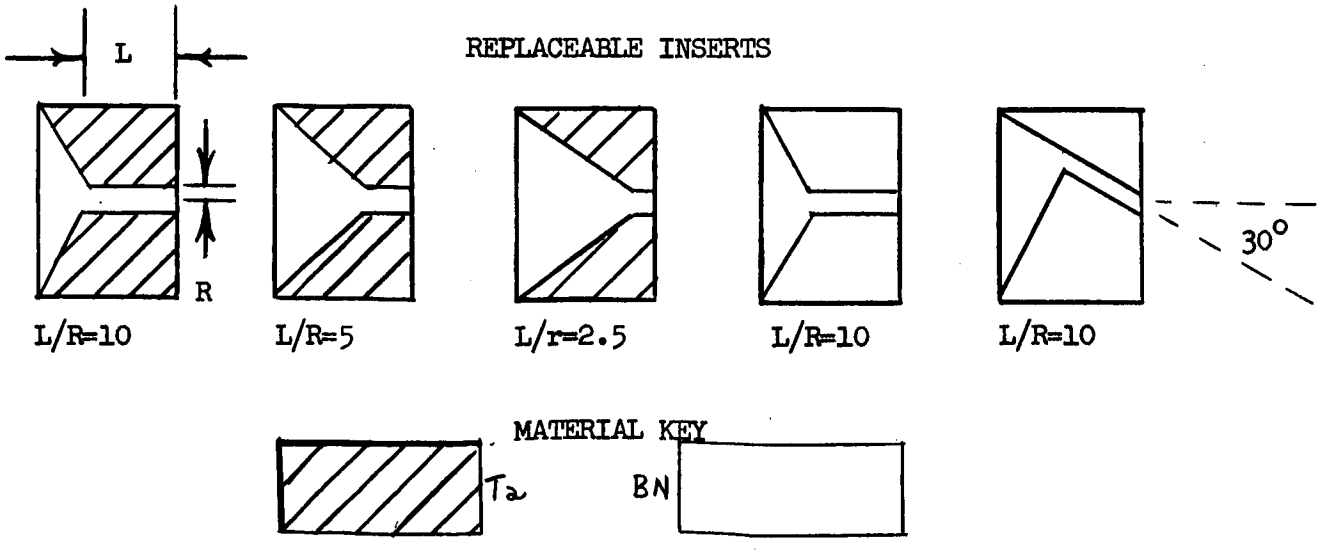


Fig. 6 : Source Design VII and VIII

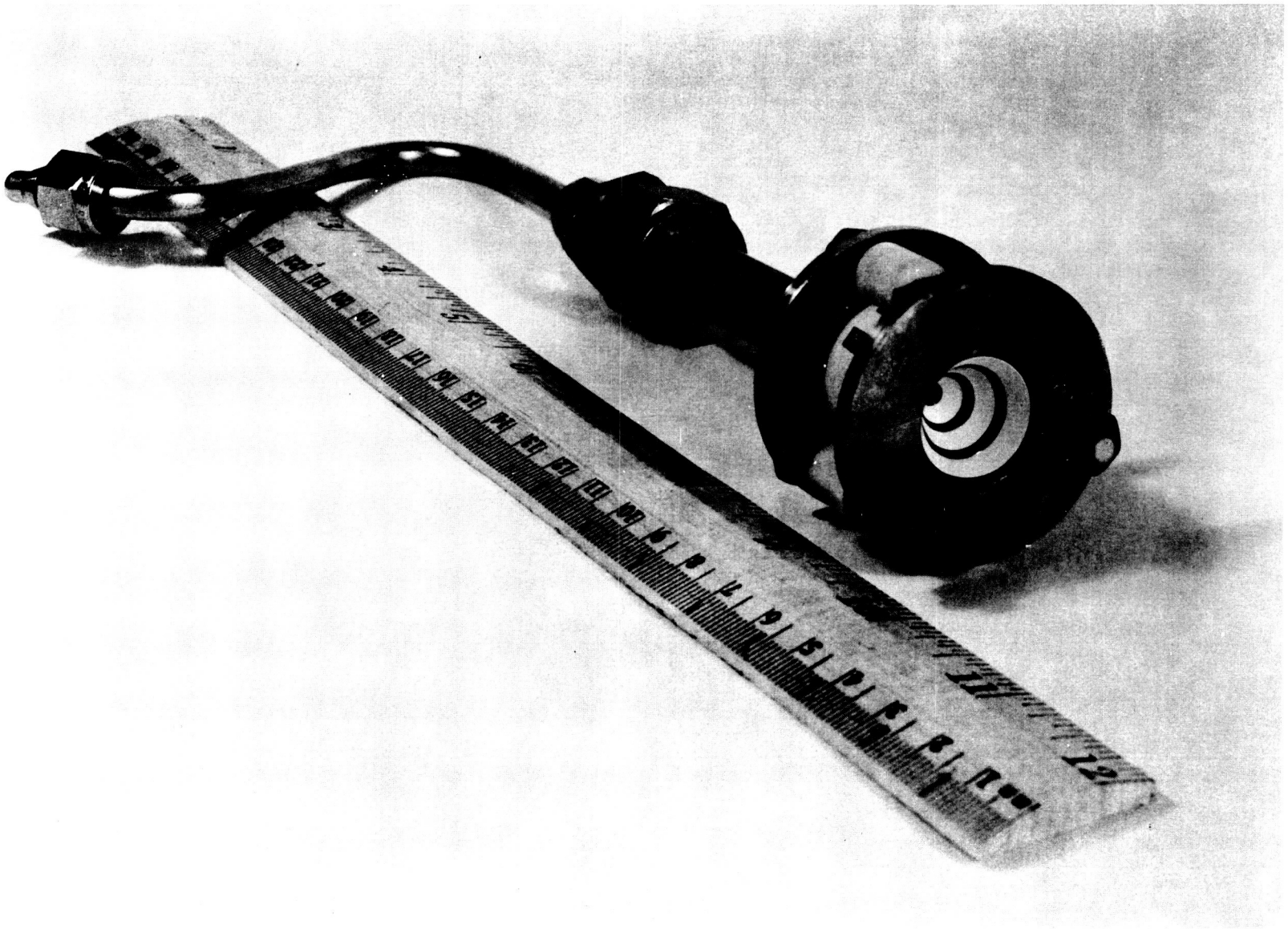


Fig 7: Multiple Anode Ion Source VII.



Fig 8: Multiple Anode Ion Source - Exploded View.

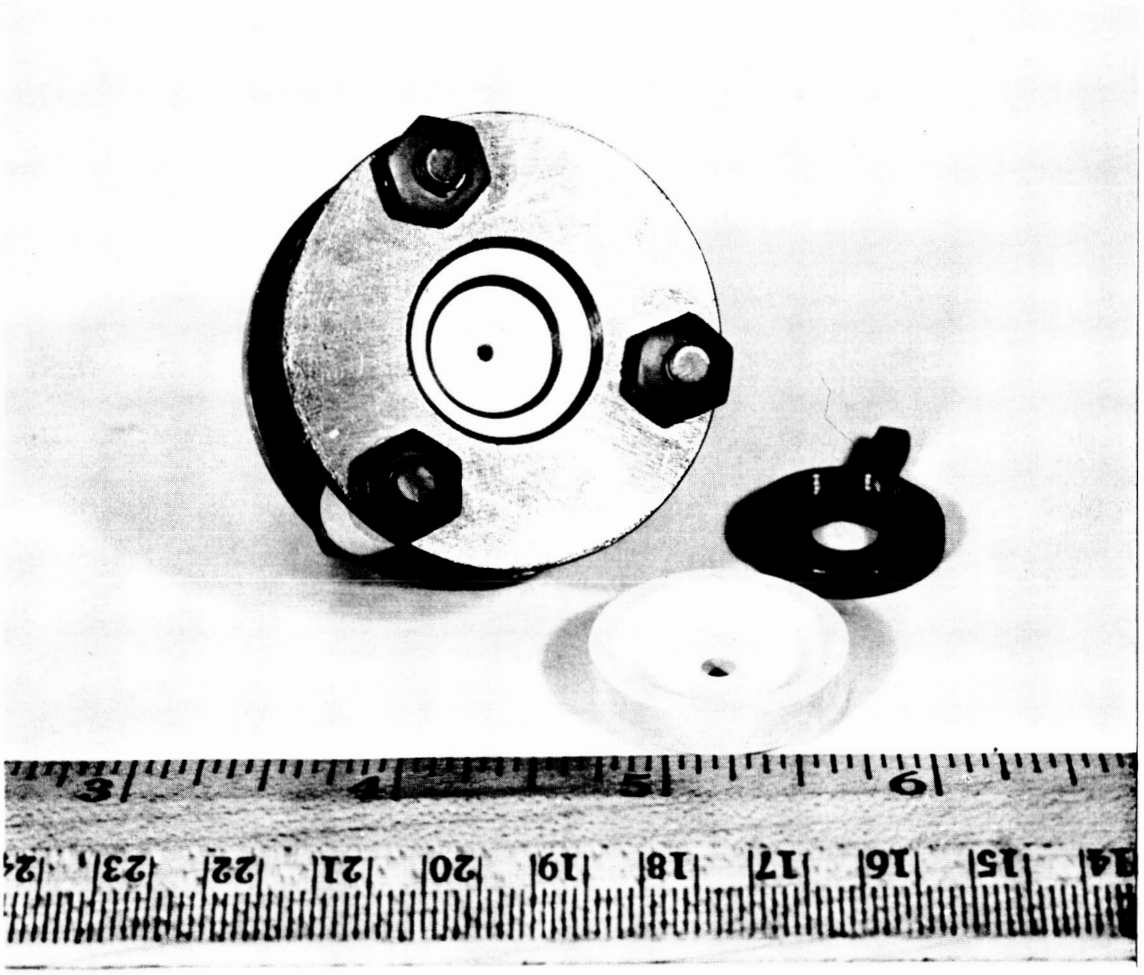


Fig. 9: Multiple Anode Ion Source with Inner Anode Removed

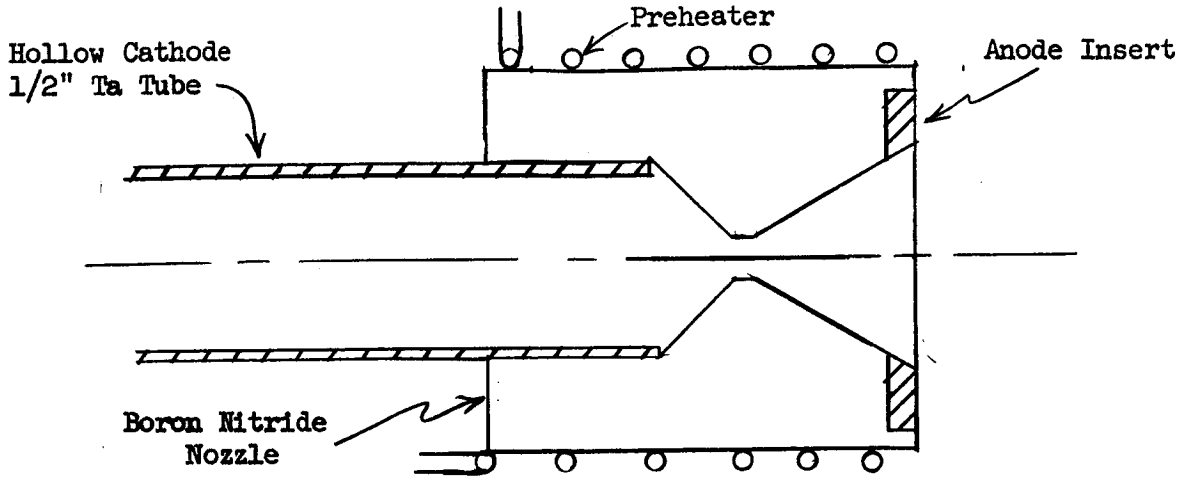


Fig. 10: Source Design IX

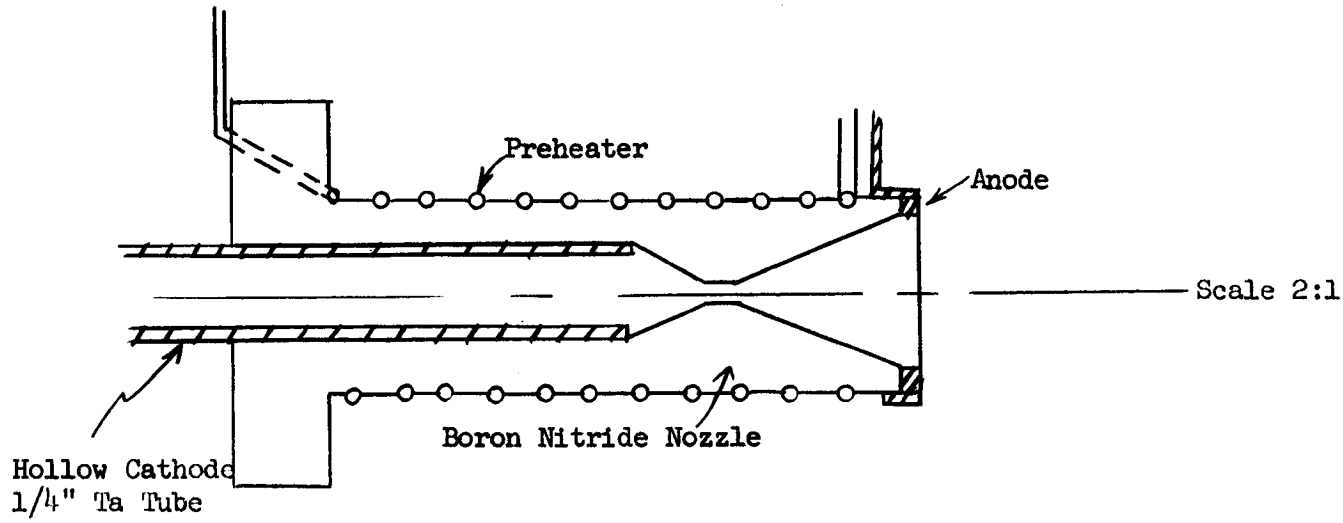


Fig. 11: Source Design X

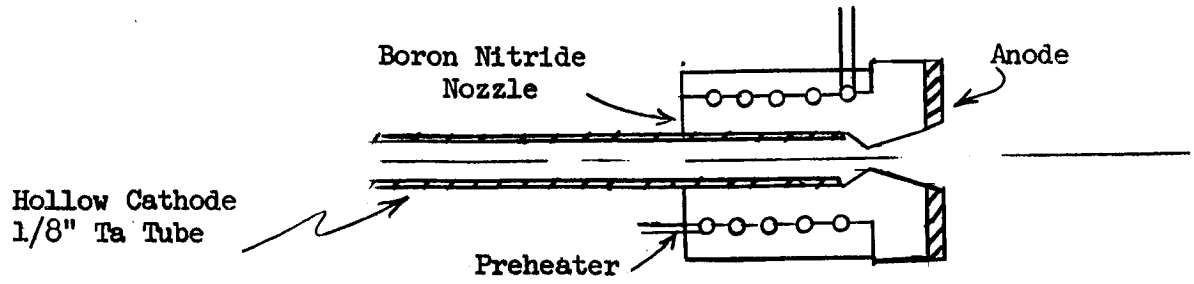


Fig. 12: Source Design XI

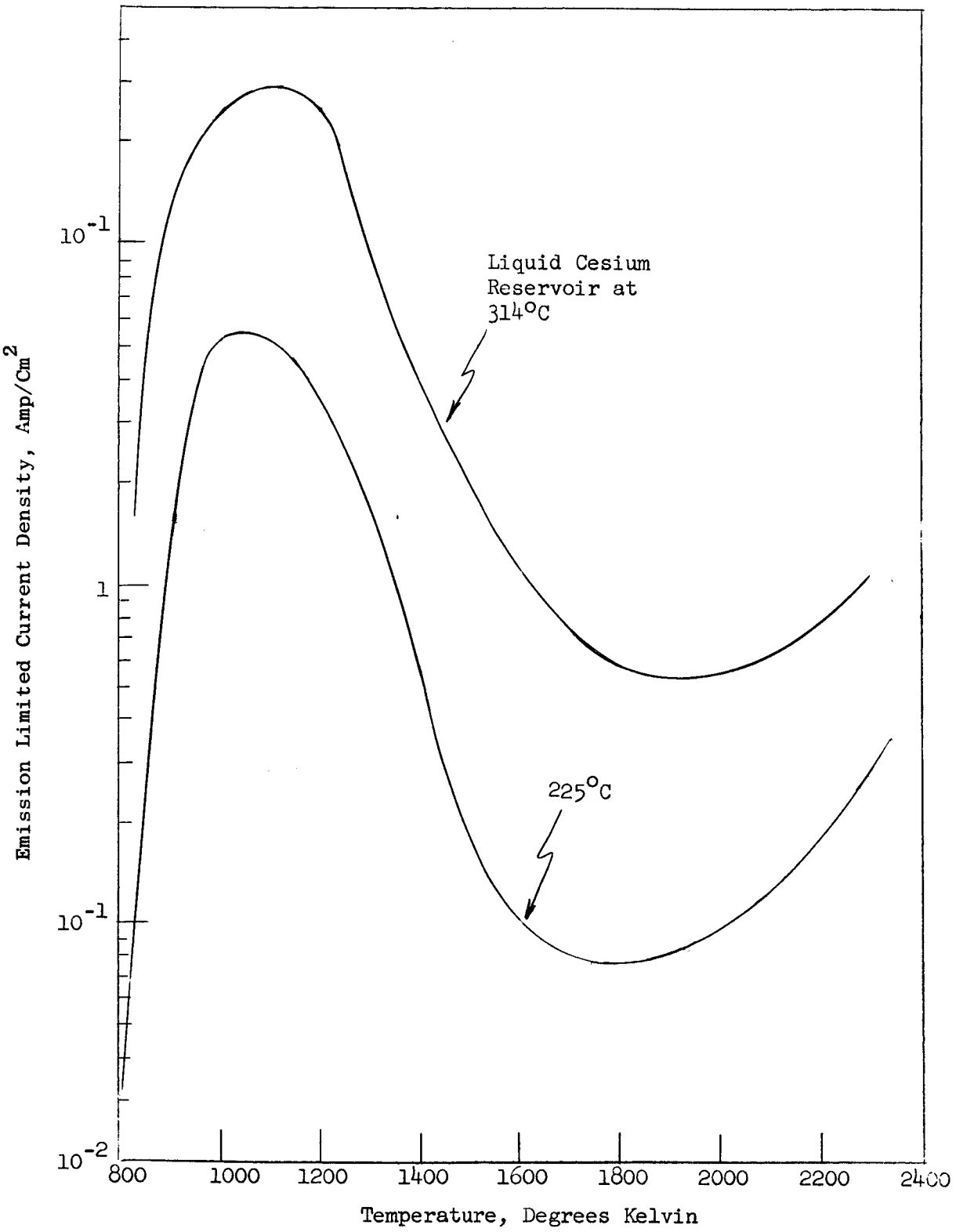


Fig. 13: Electron Emission From a Heated Tantalum Ribbon in Cesium Vapor. Gibbon (10)

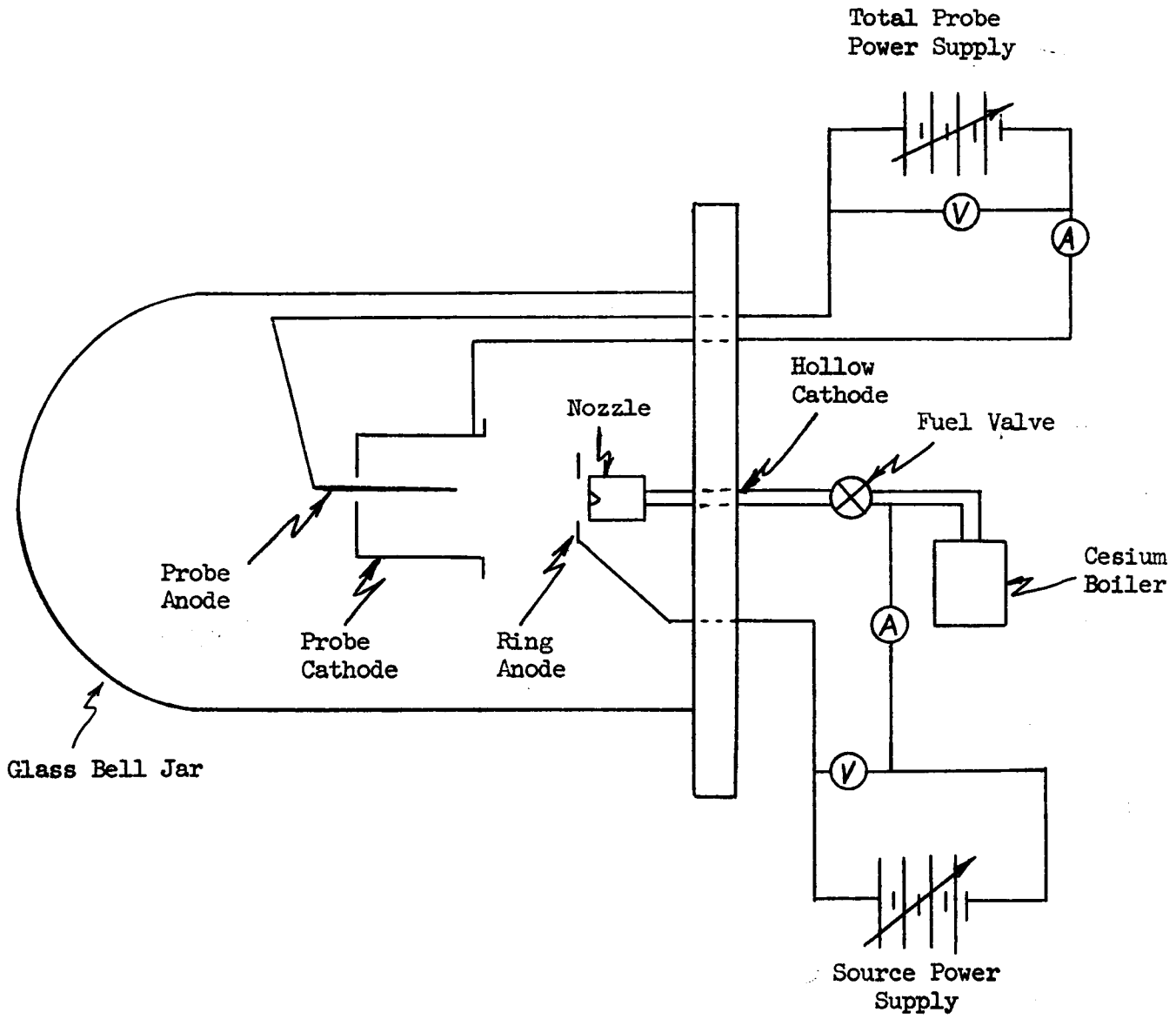


Fig.14 : Bell Jar Vacuum System for Source Studies

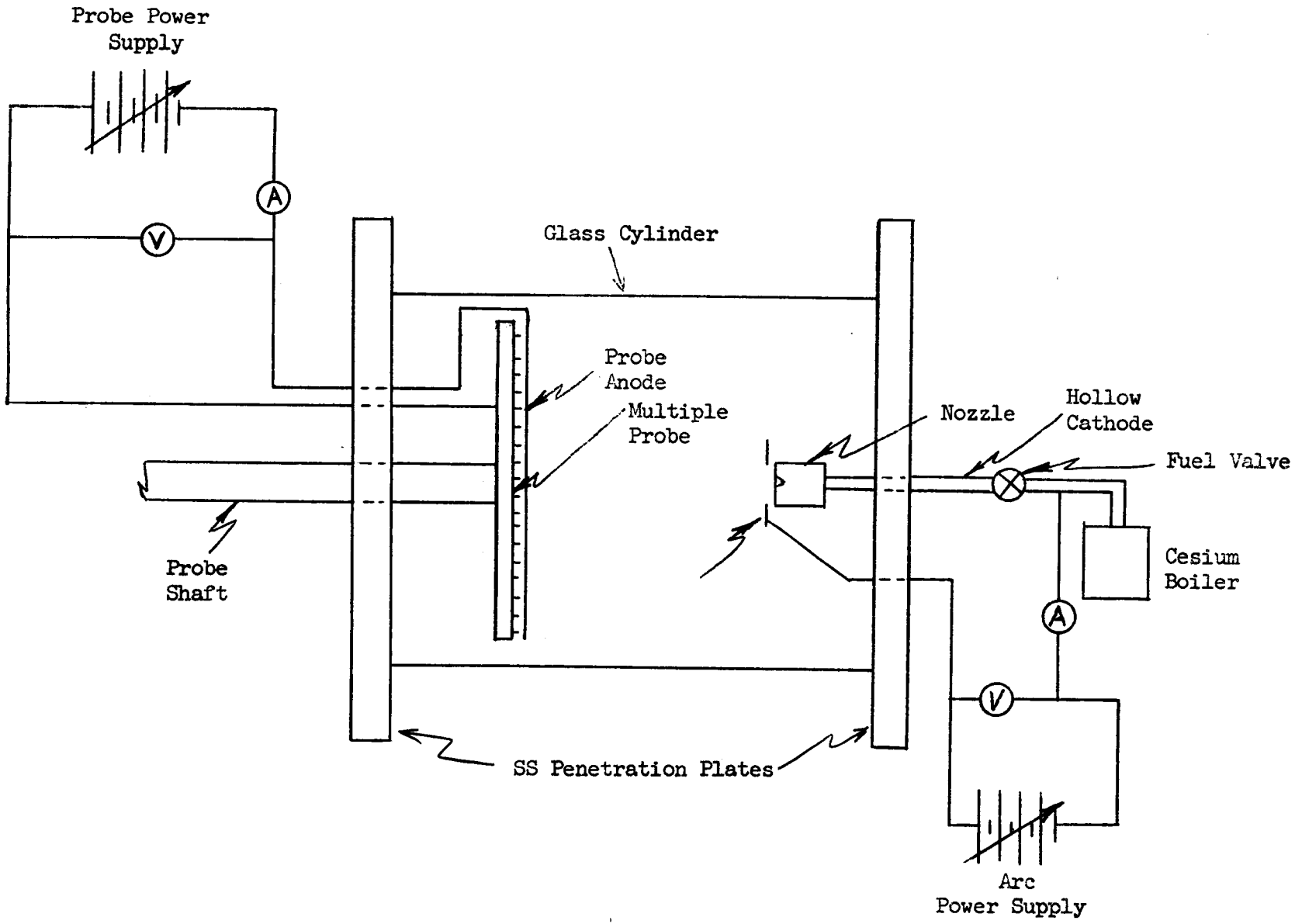


Fig. 15 Modified Vacuum System for Sources and Flow Pattern Studies

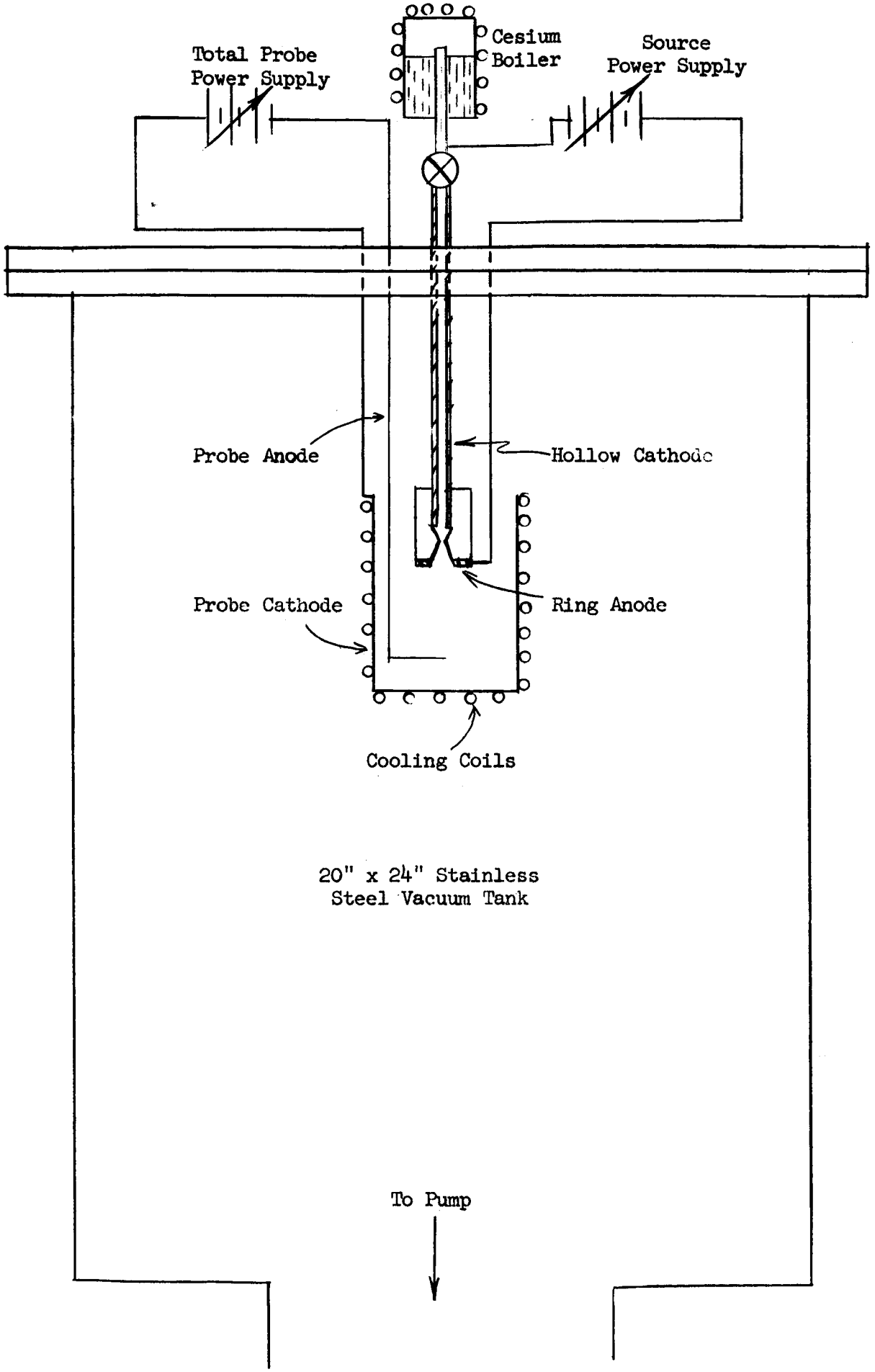


Fig. 16. High Vacuum Test Chamber for Source Studies

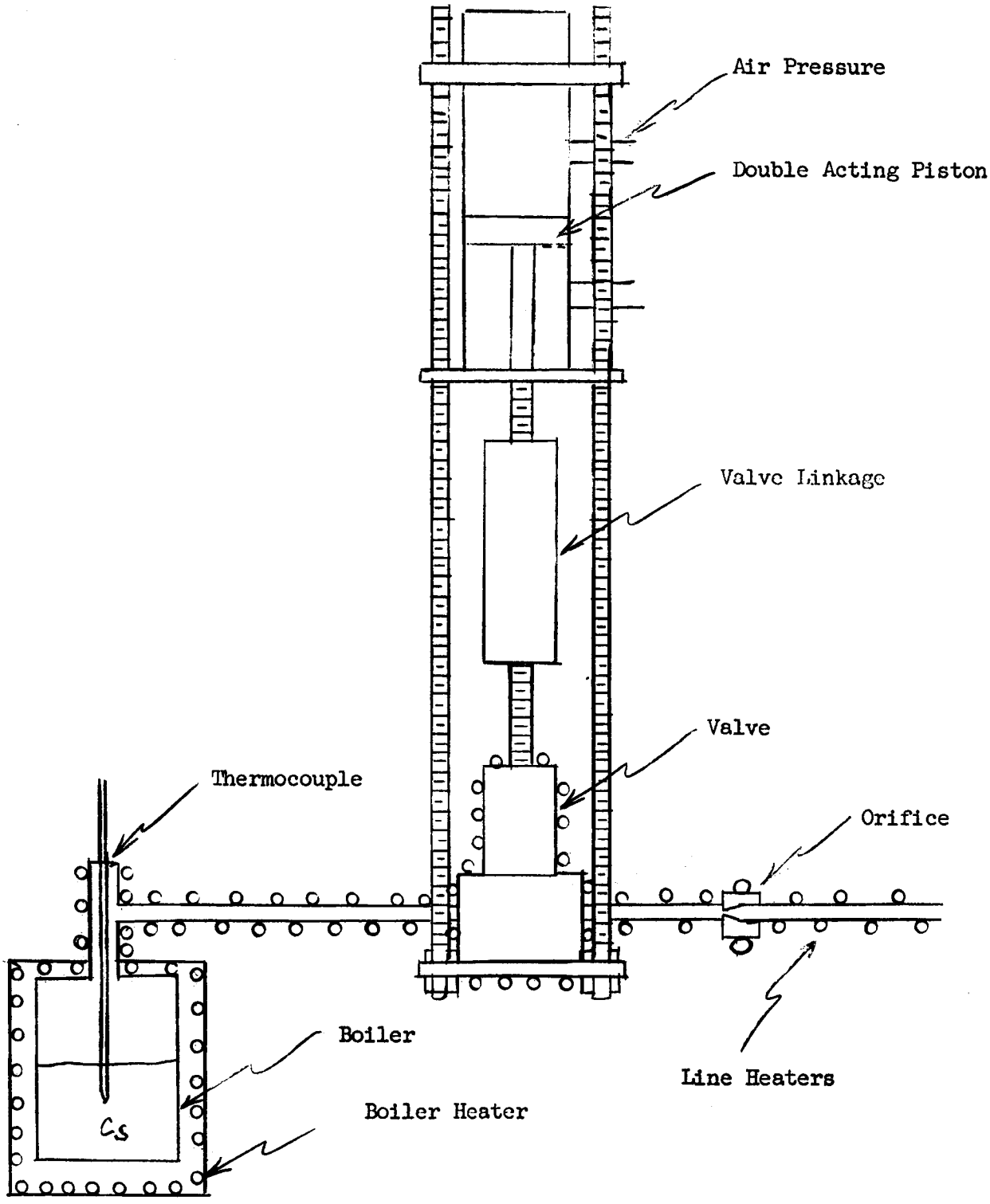


Fig. 17: Boiler and Fuel Feed System

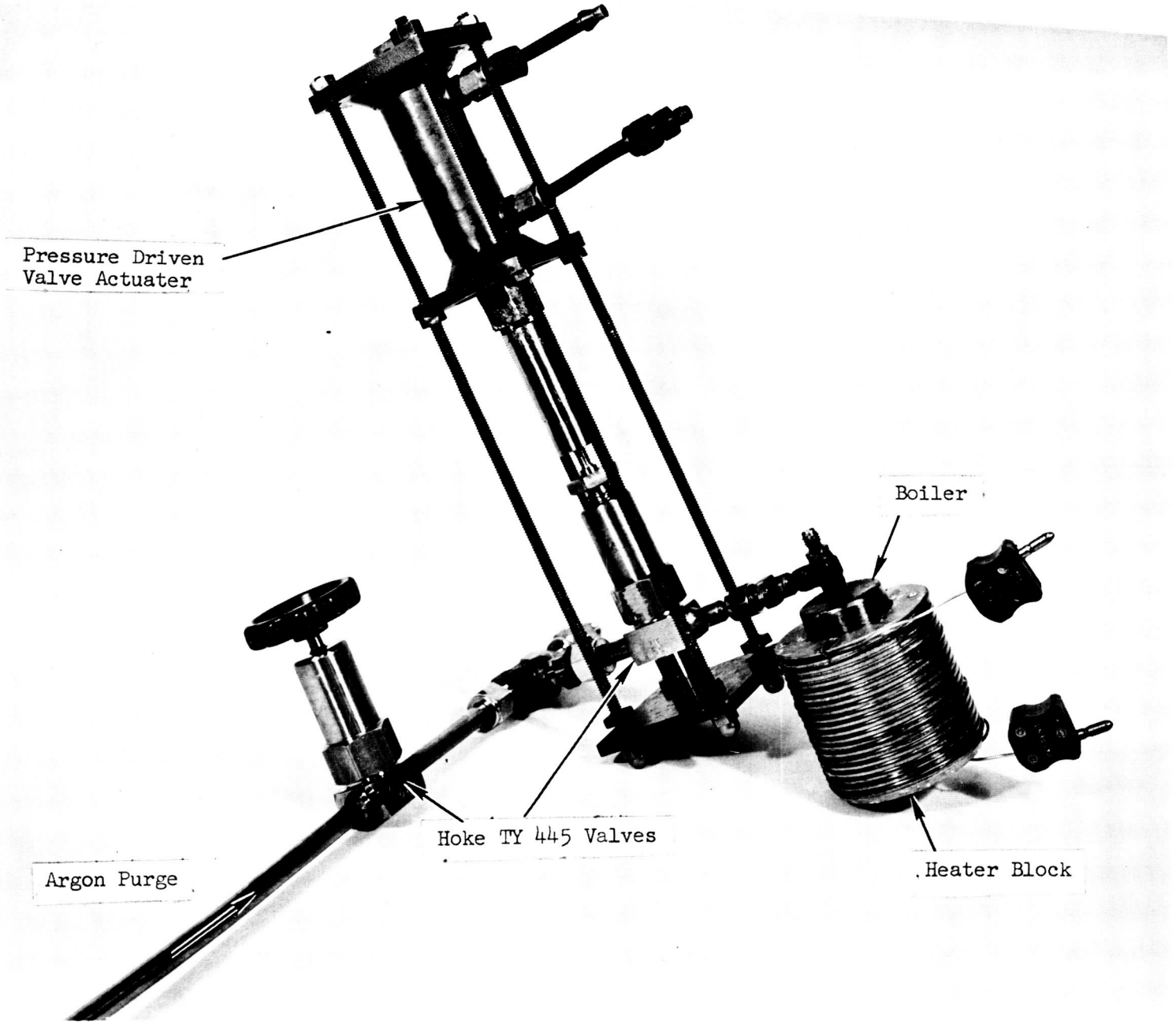


Fig. 18 Boiler and Fuel Feed System with Inert Gas Purge

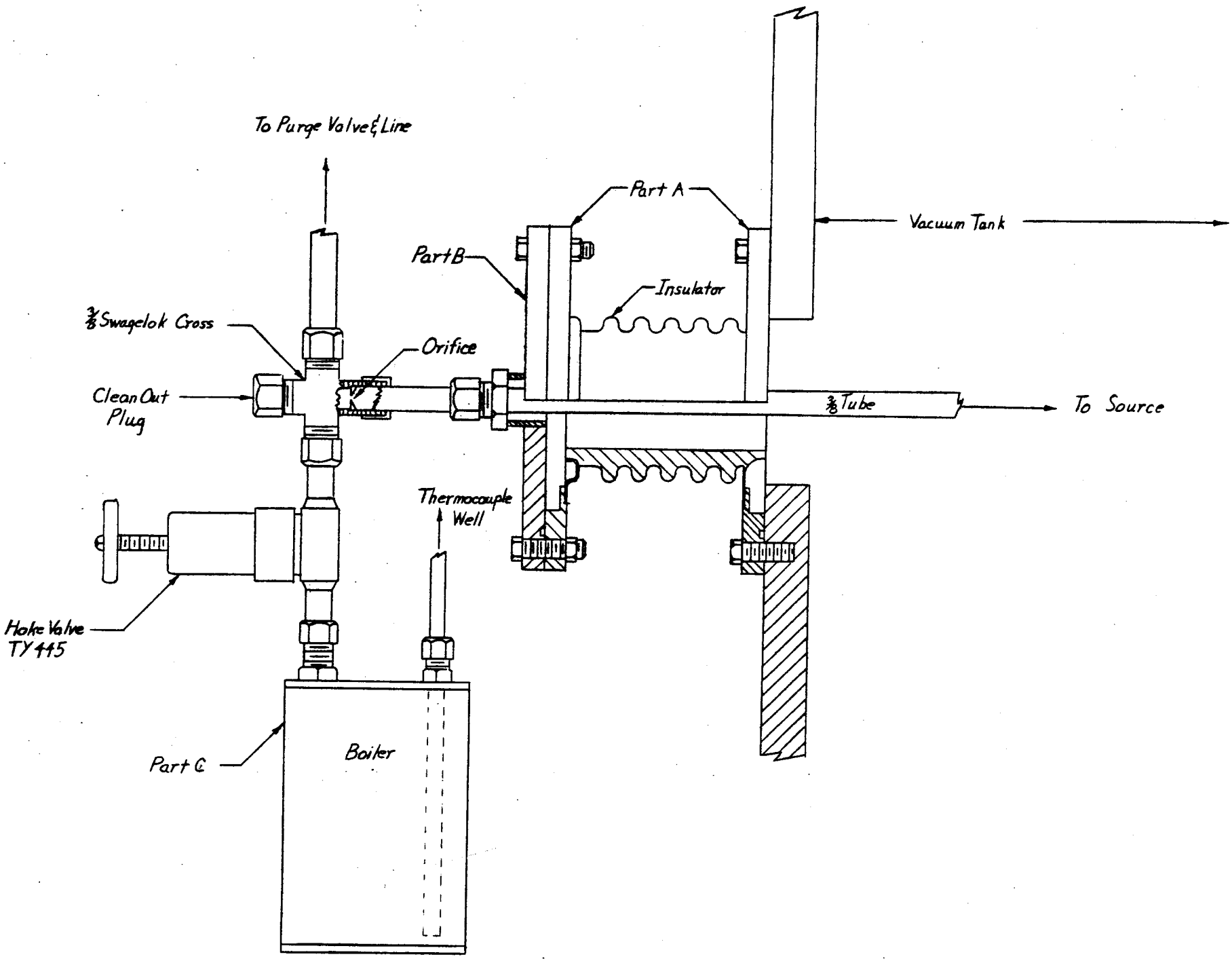


Fig.19: Large Boiler and Fuel Feed System Design

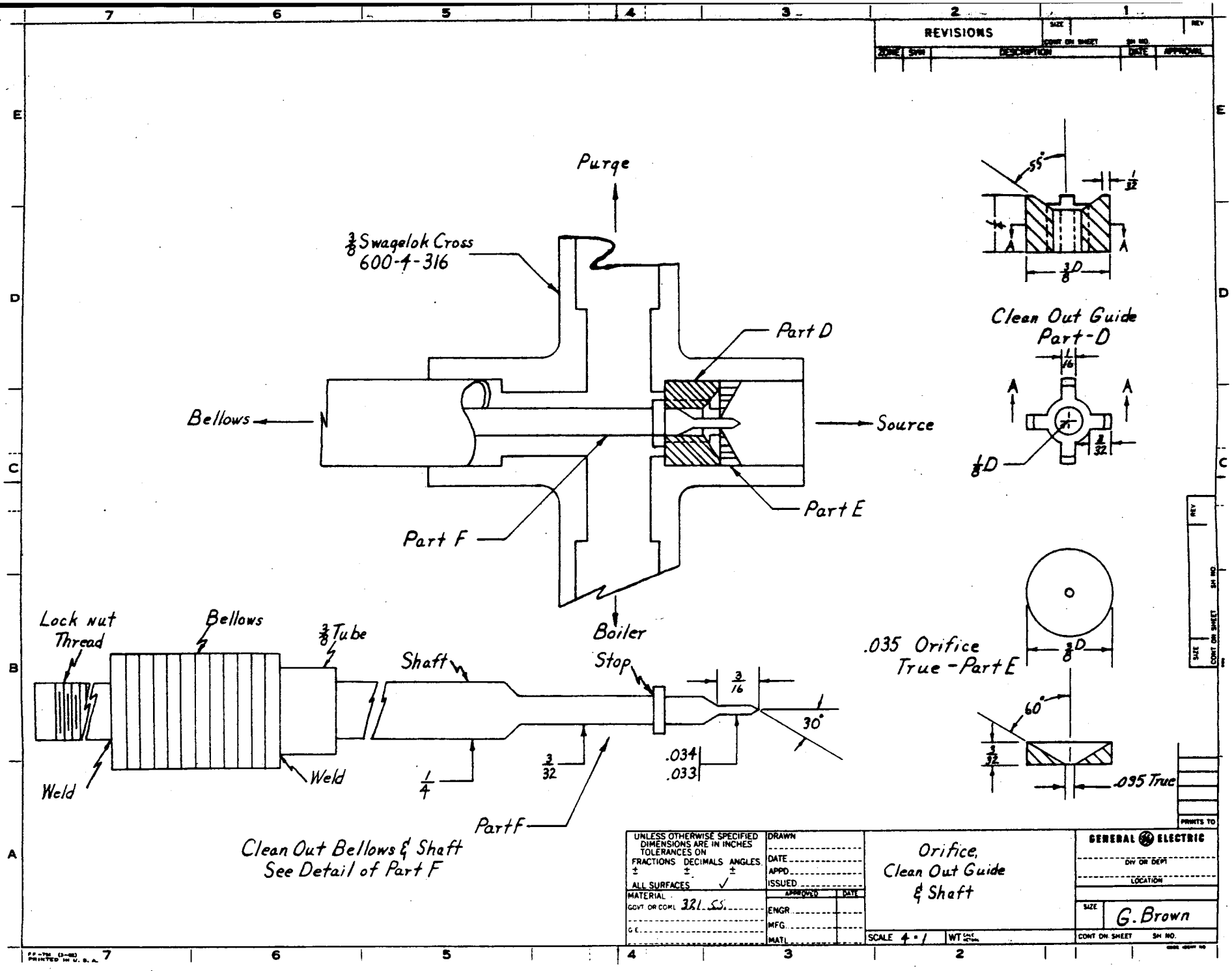


Fig. 20 : Fuel Line Detail - Orifice Cleanout and Argon Purge

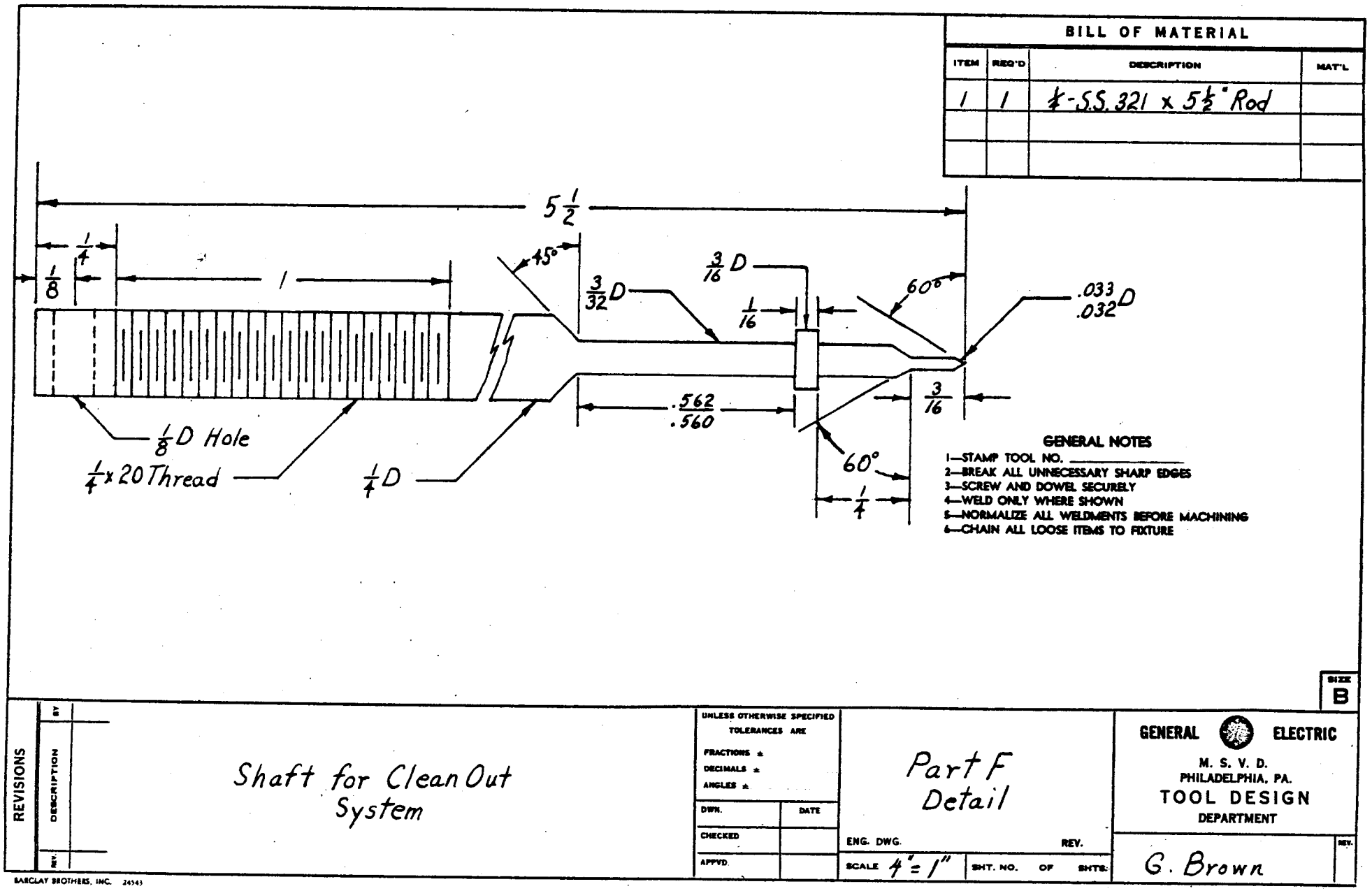


Fig. 21: Fuel Line Detail - Orifice Cleanout Plunger

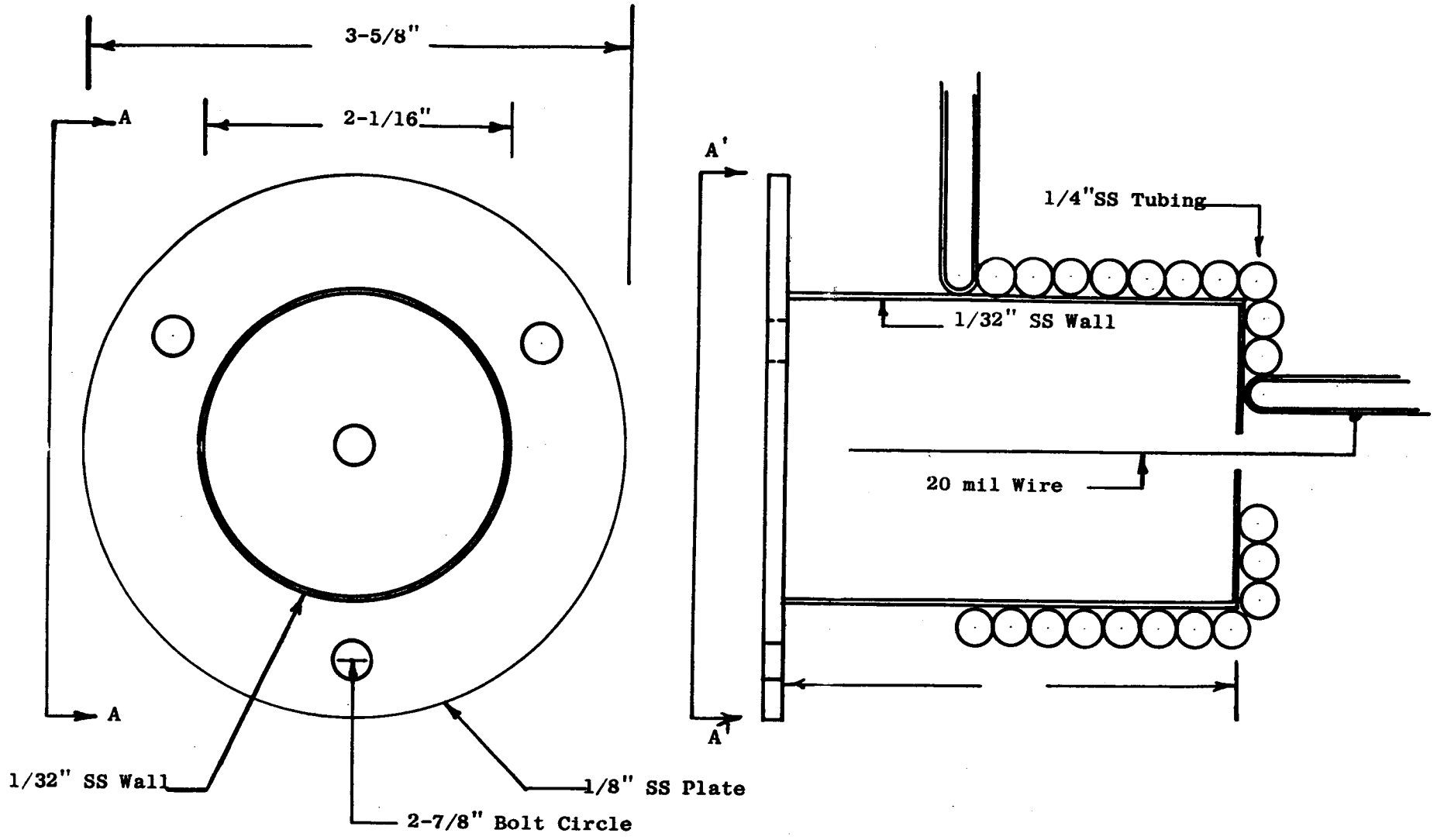
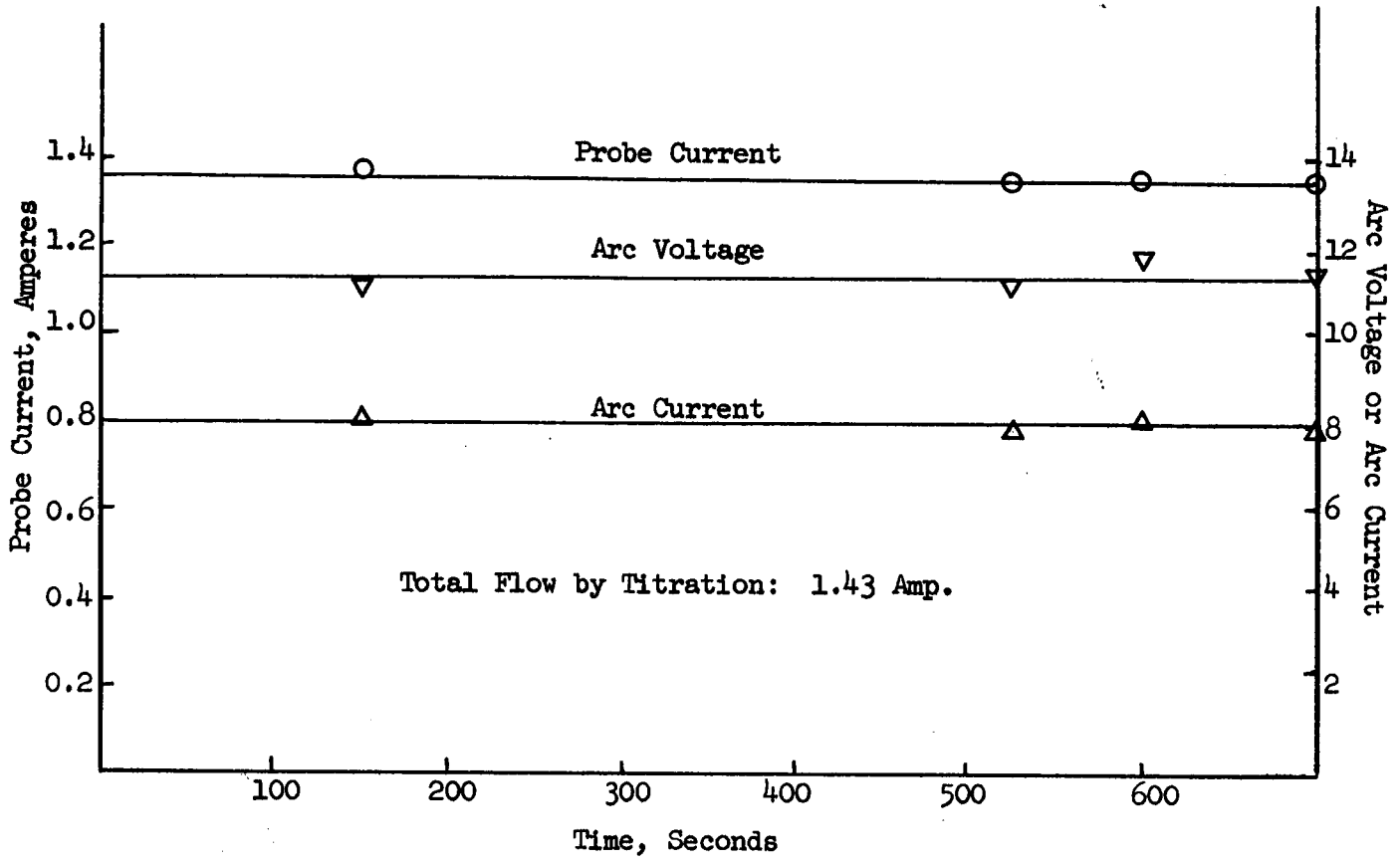


FIGURE 22

TOTAL PROBE AND MOUNTING RING
(Actual Scale)



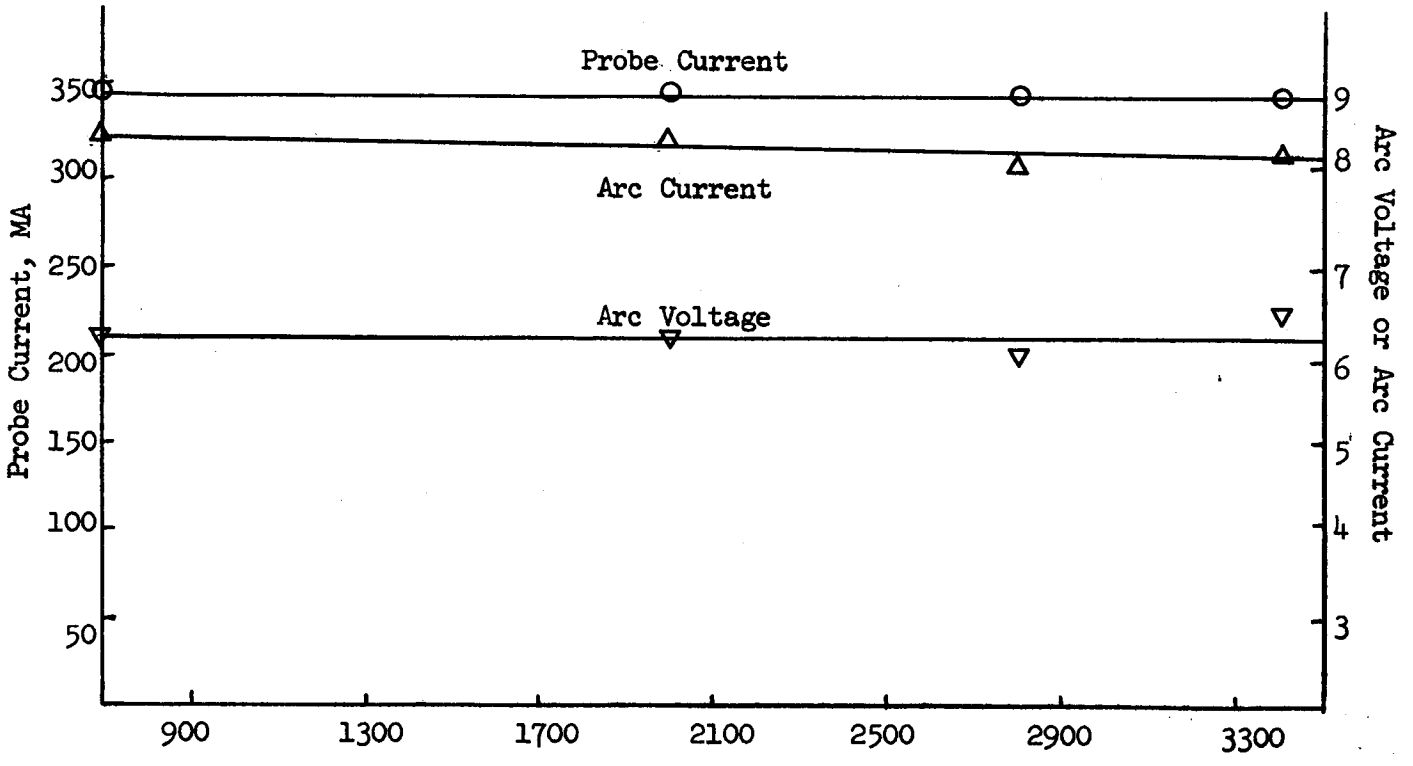


Fig. 23: Stability of Arc and Probe Readings

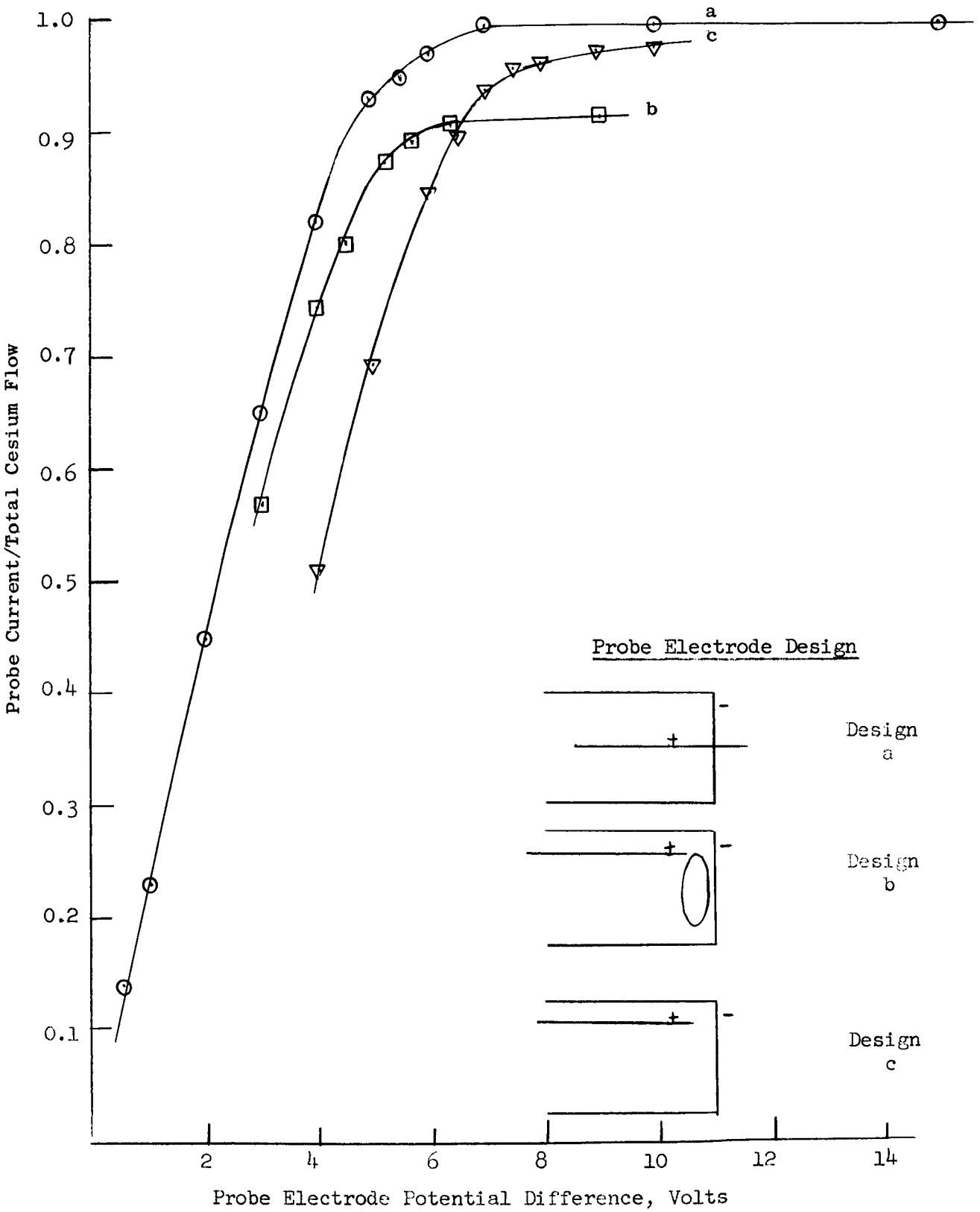


Fig. 24: Typical Total Probe Saturation Curves

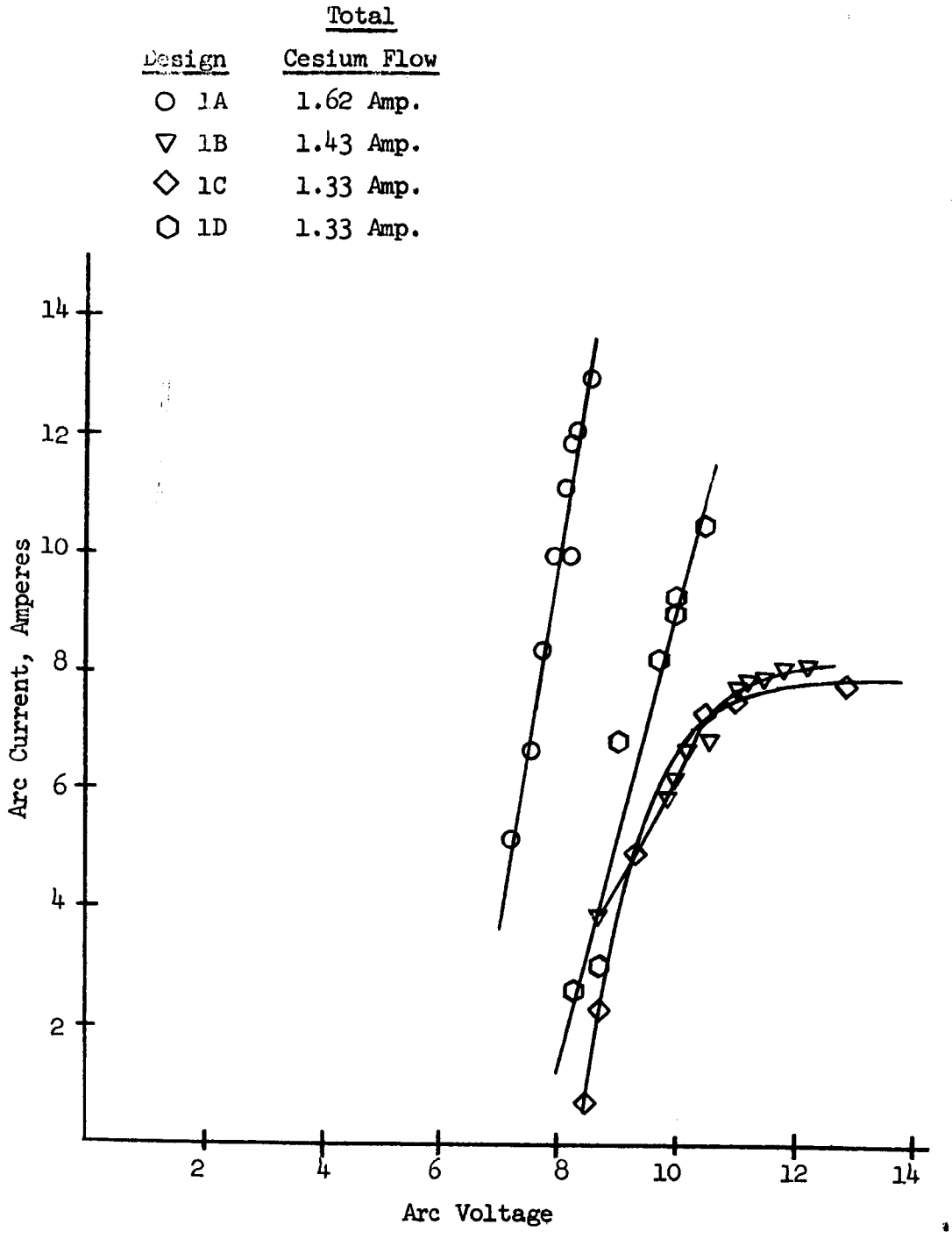


Fig. 25: Current Voltage Curves for Variations of Source Design I

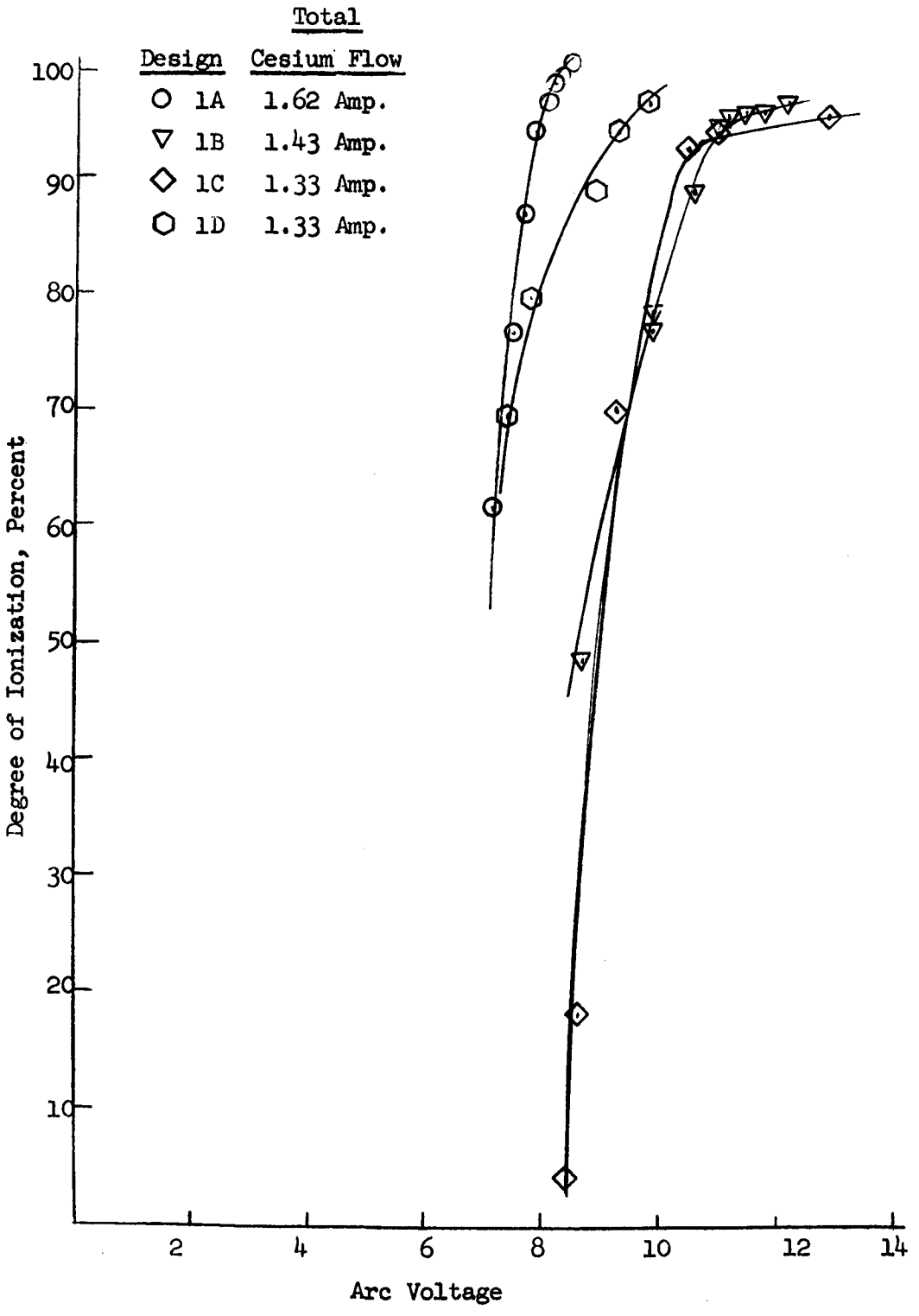


Fig. 26: Ionization vs. Arc Voltage for Variations of Source Design I

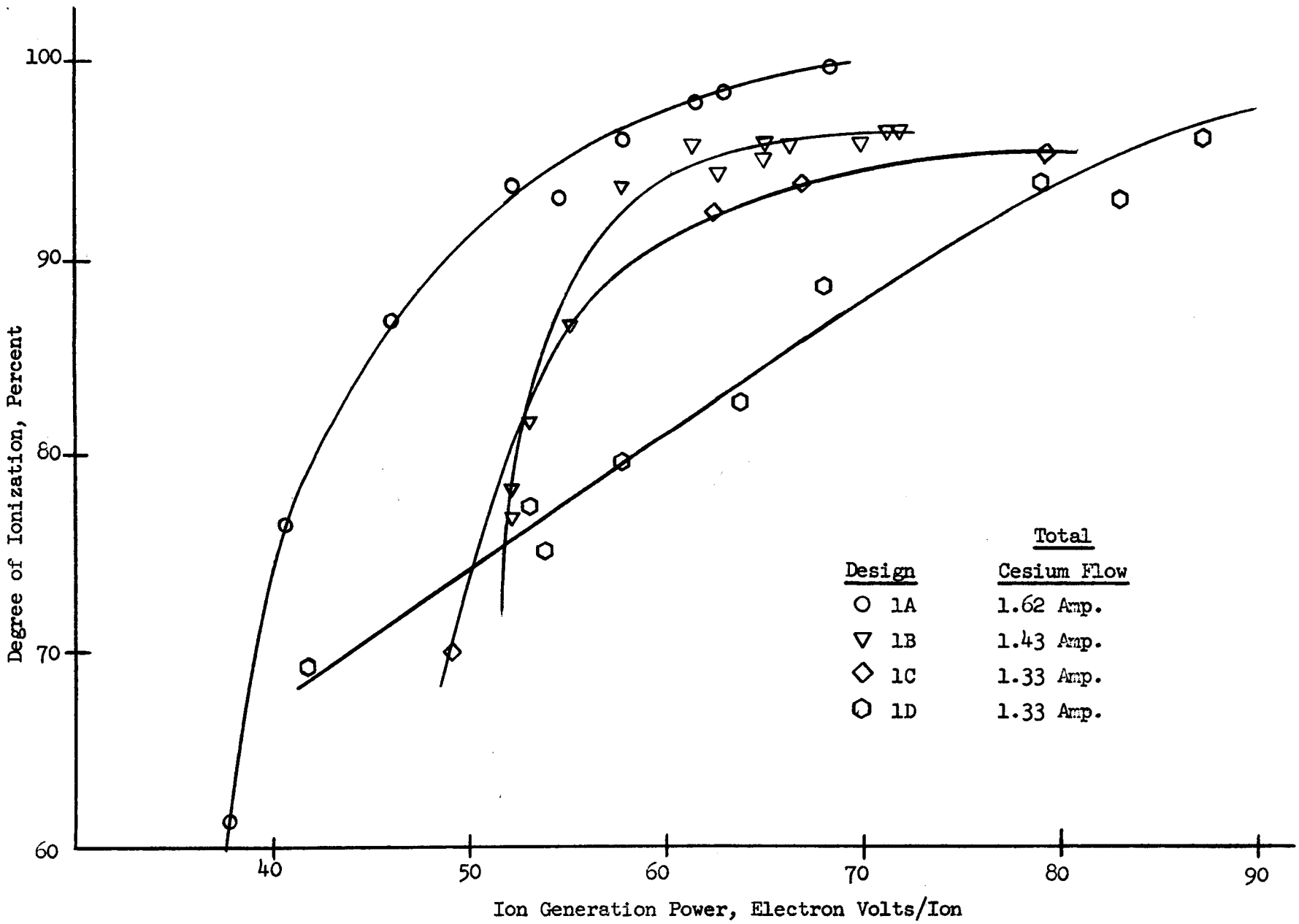


Fig. 27: Performance Curves for Several Geometries of Source Design I

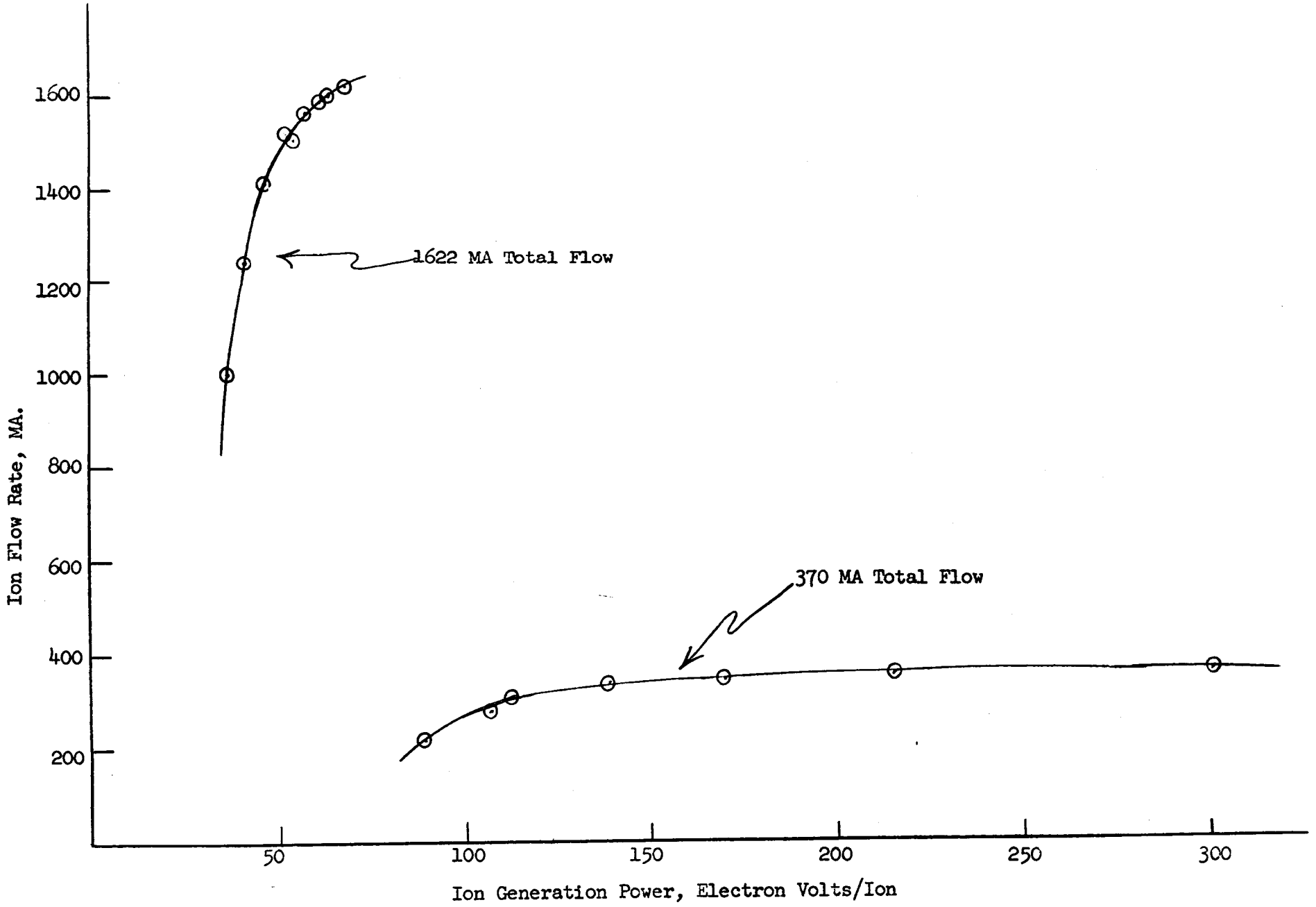


Fig. 28: Effect of Flow Rate on the Performance of Source Design 1A

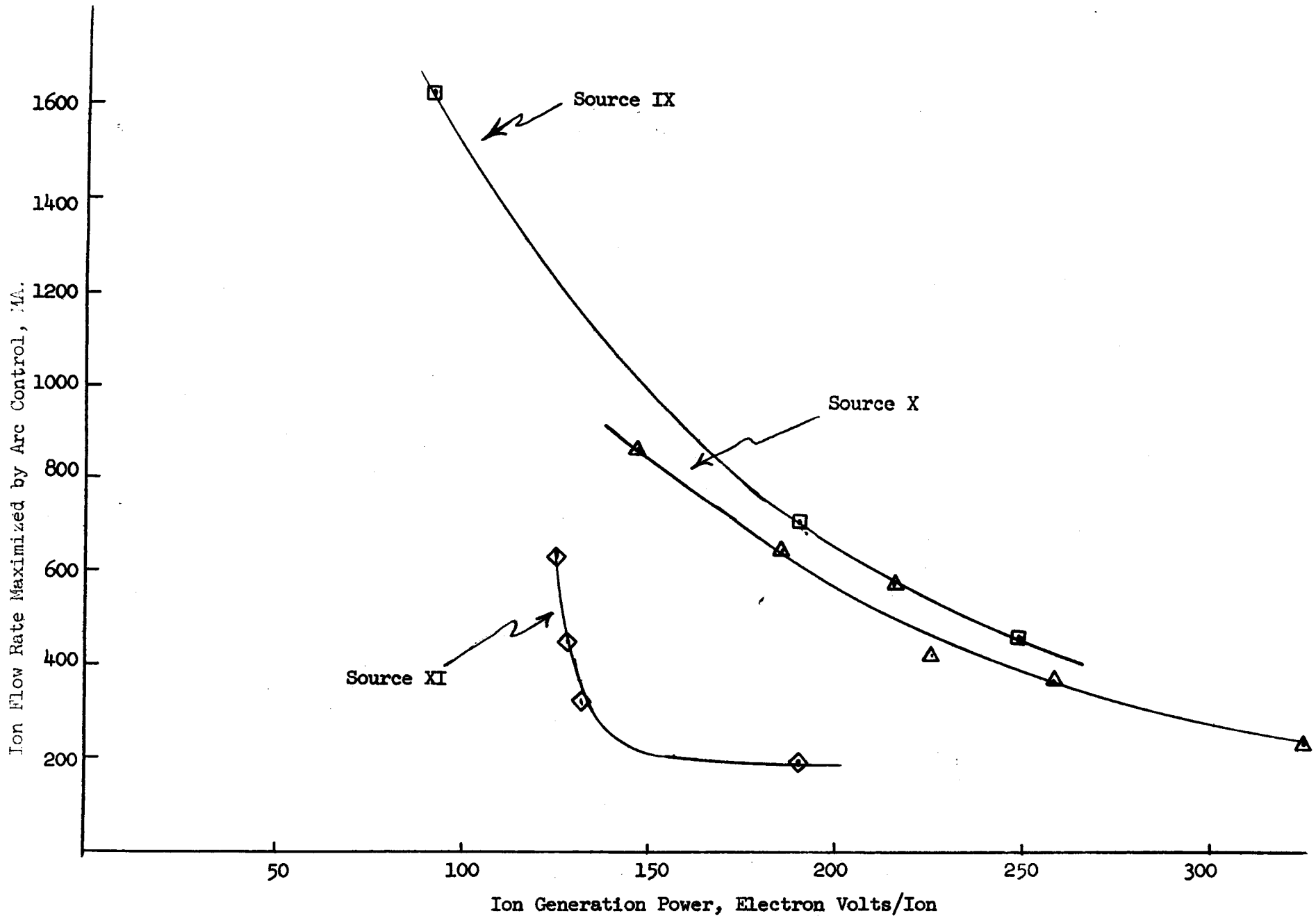


Fig. 29: Effect of Flow Rate on the Performance of Selected Ion Sources

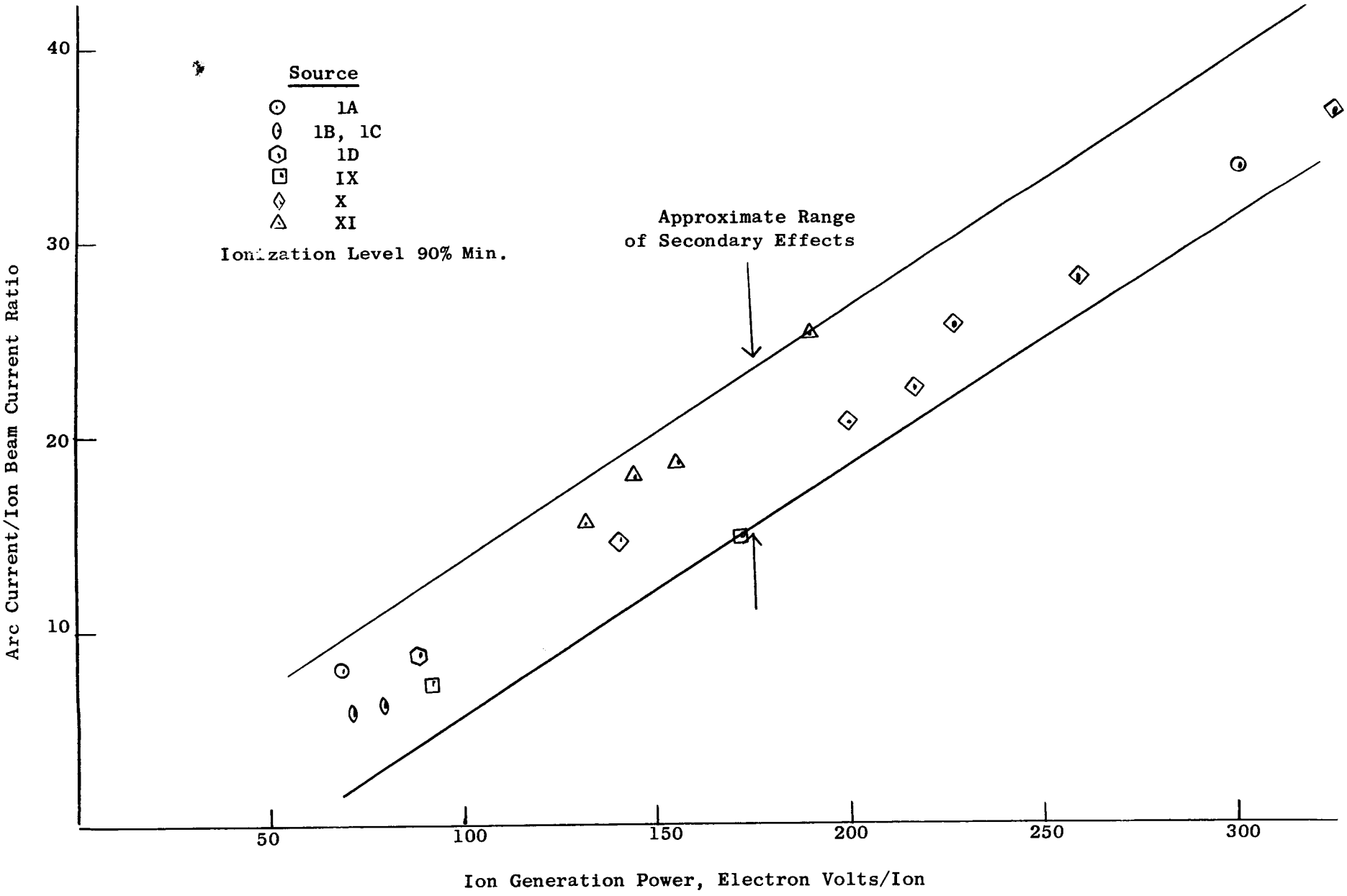


Fig. 30: Electron-Ion Current Ratio vs. Ion Generation Power

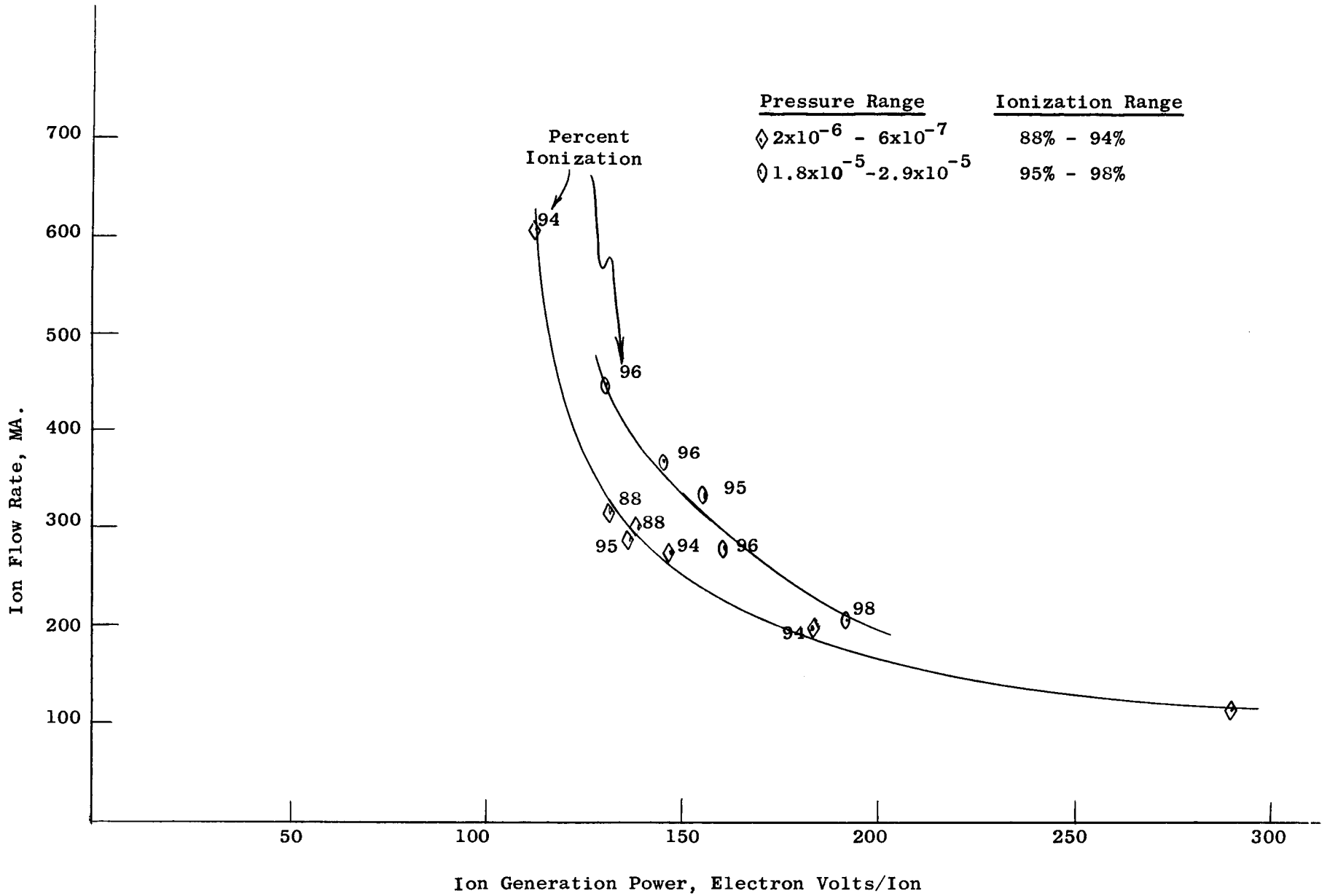


Fig. 31: The Effect of High Vacuum on Source Performance

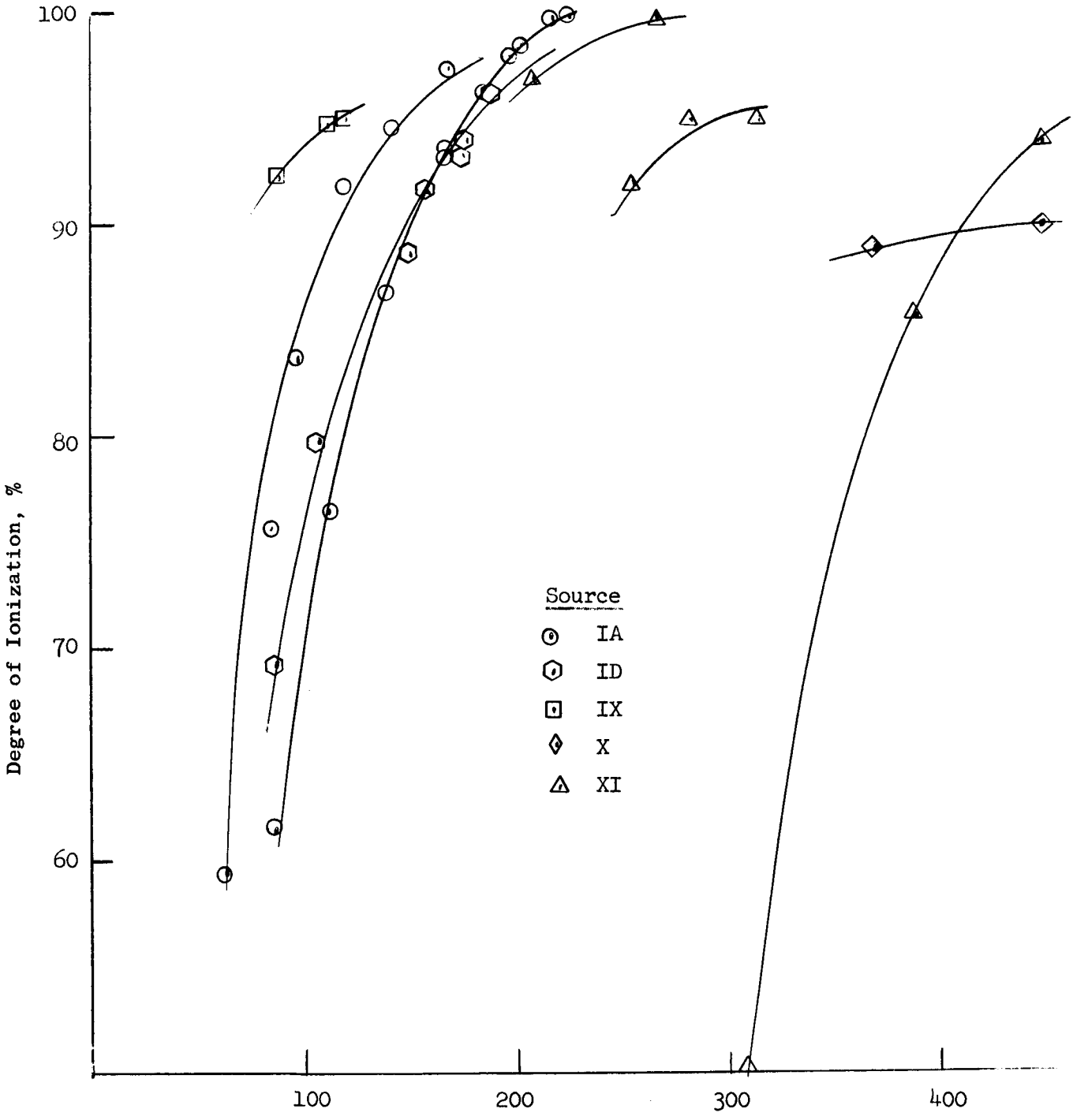


Fig. 32: Degree of Ionization vs. Arc Current Density

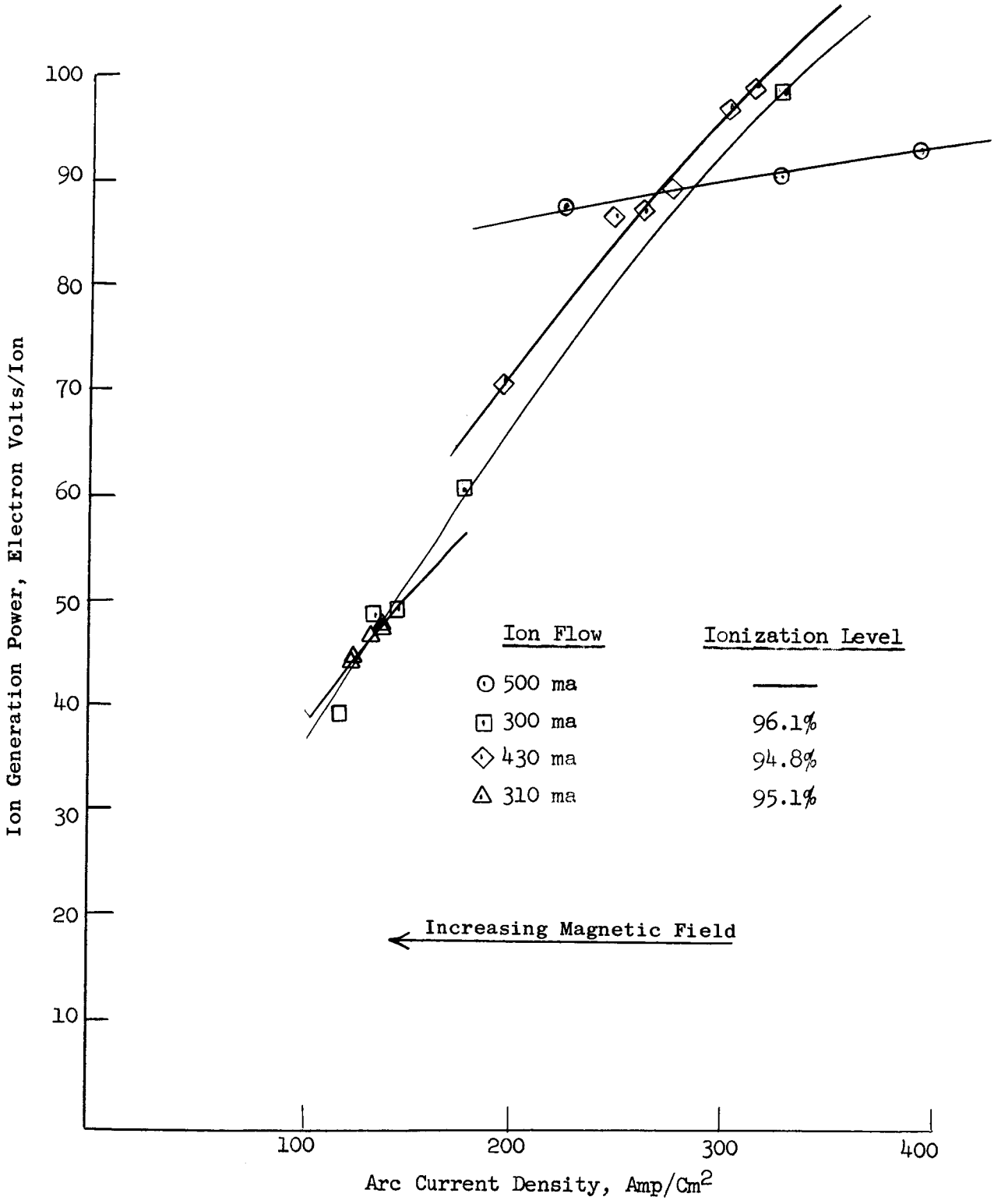


Fig. 33: Reduction in Ion Generation Power by an Axial Magnetic Field

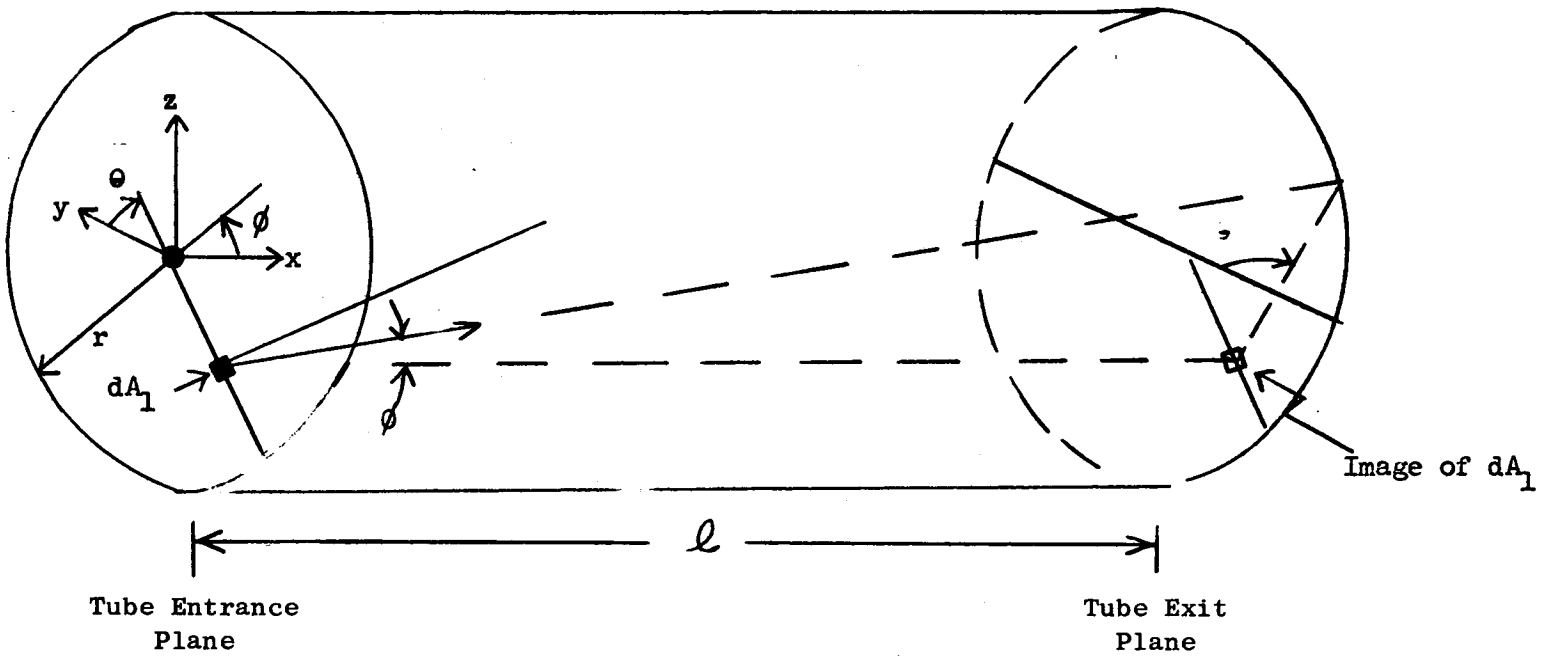


Fig. 34: Molecular Flow Geometry in a Tube

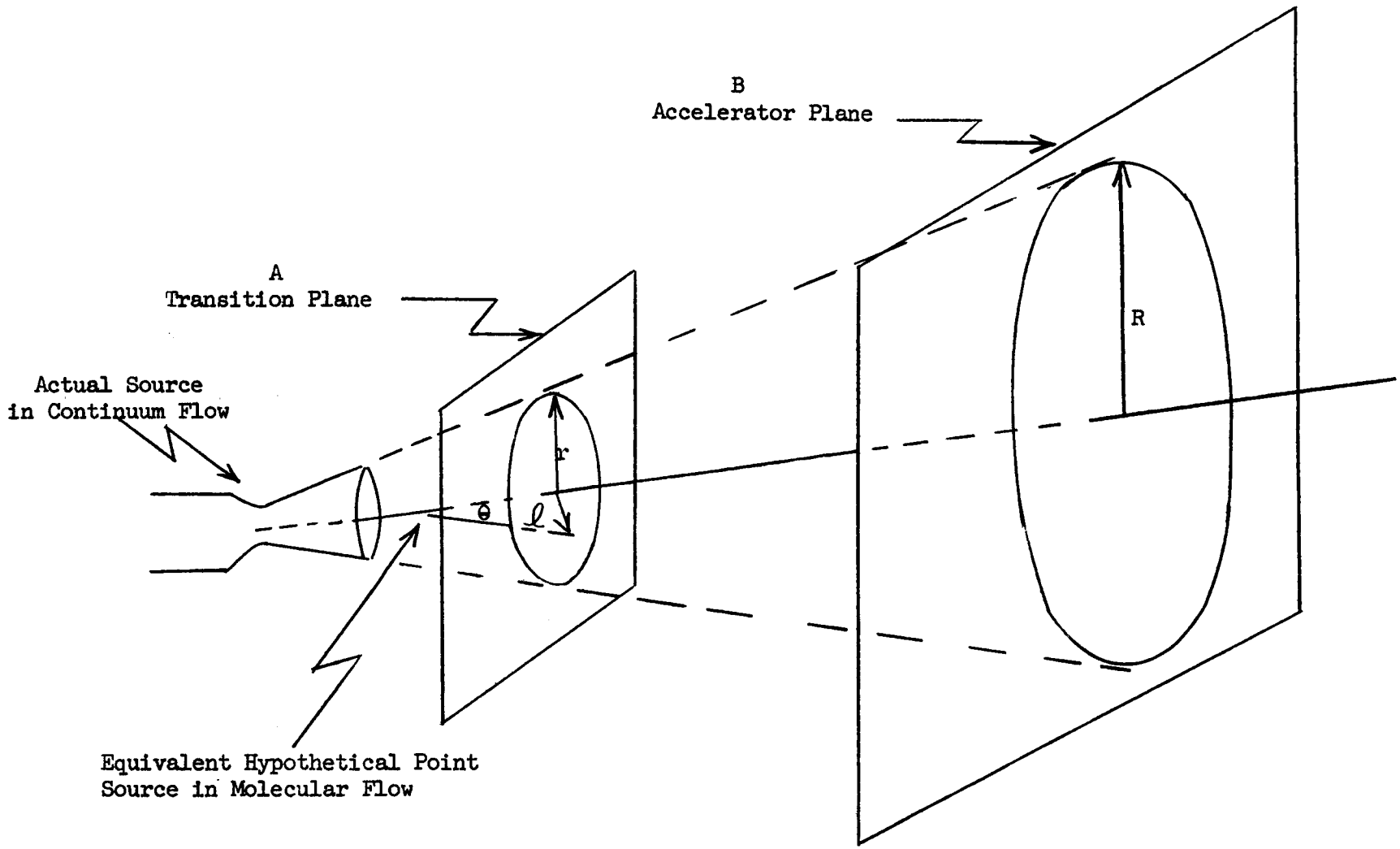


Fig. 35: Flux Projections on Flat Plates

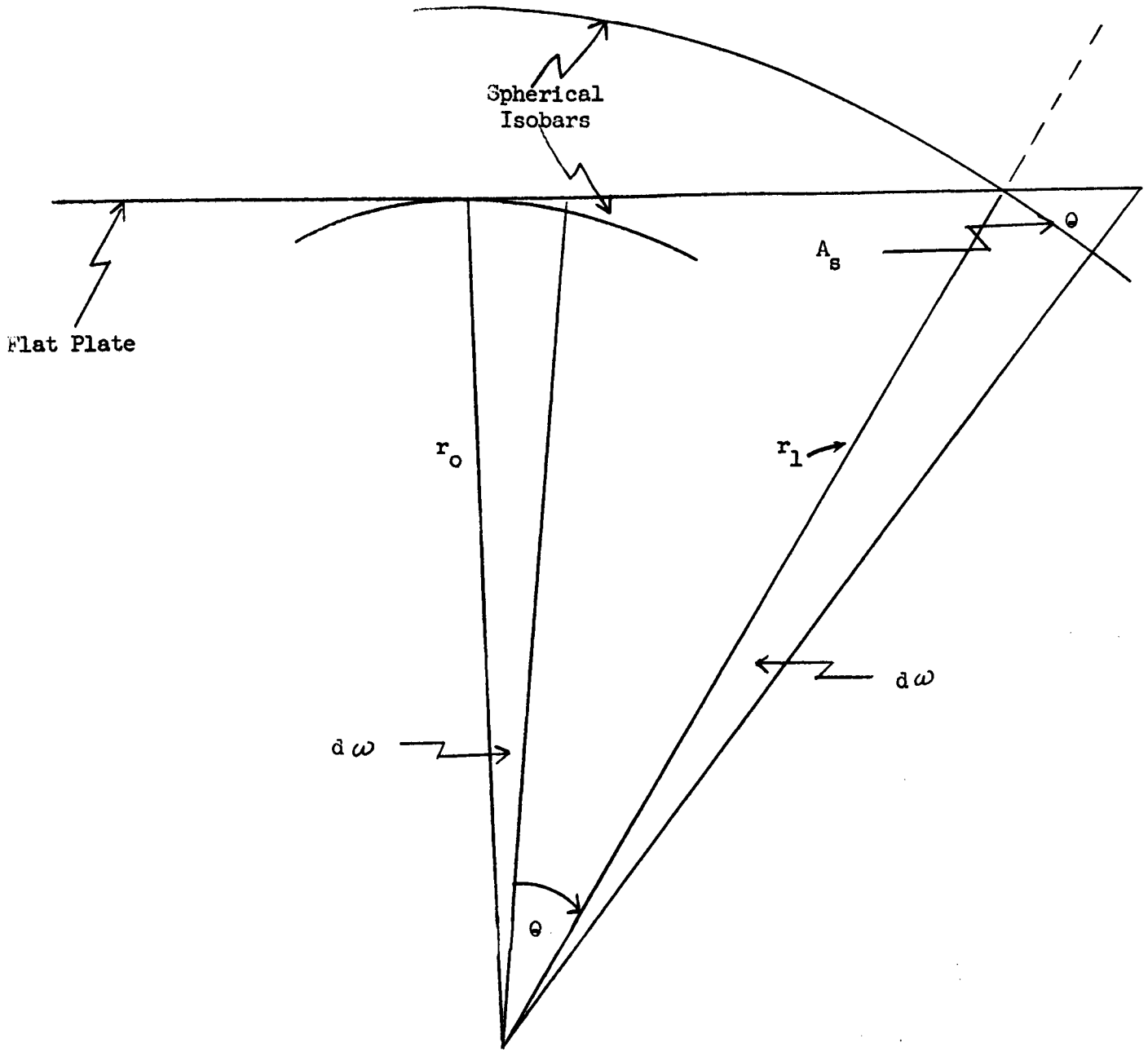


Fig. 36: Geometry of Spherically Symmetrical Molecular Expansion

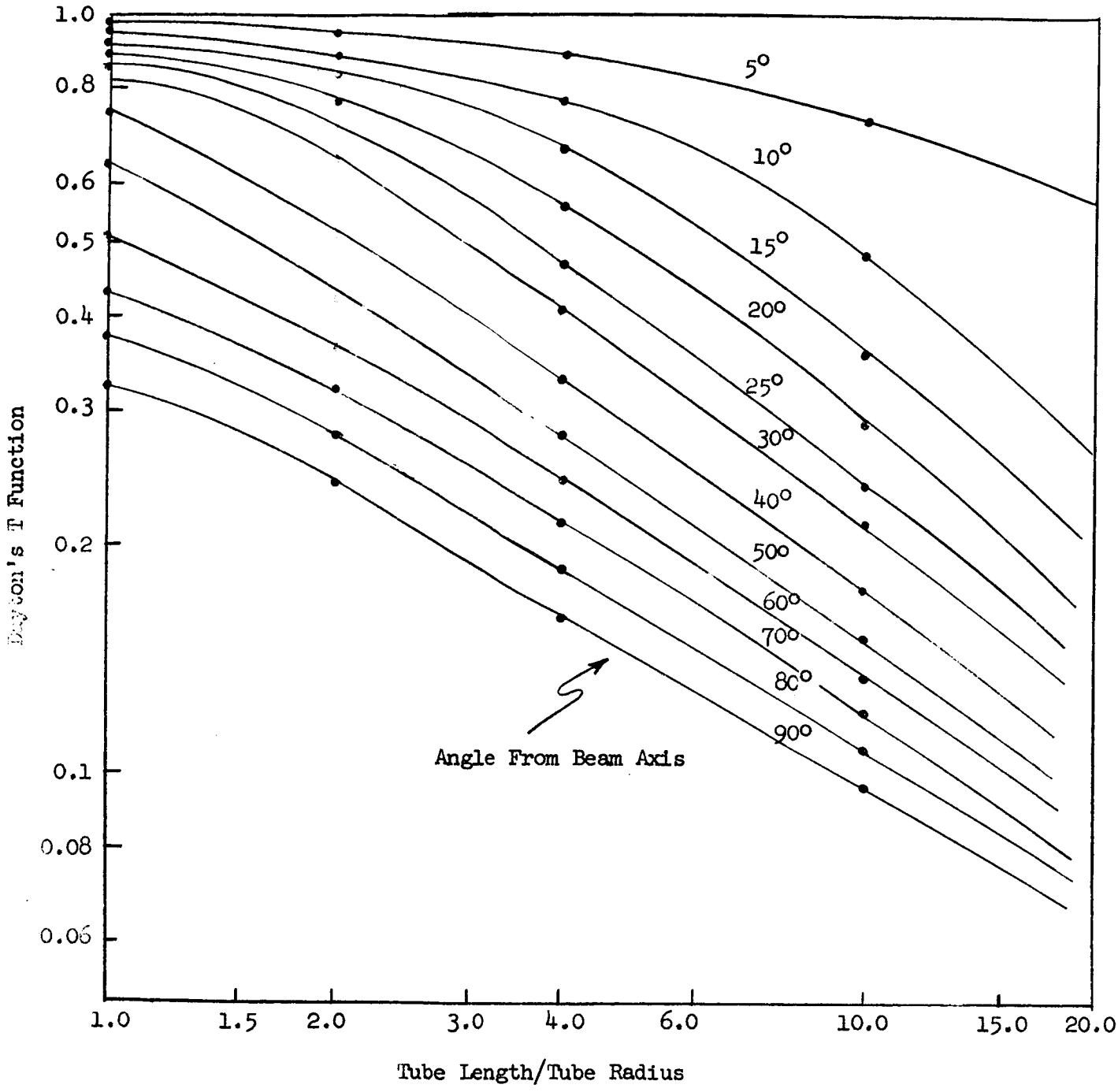


Fig. 37: Dayton's T Function for Cylindrical Tubes

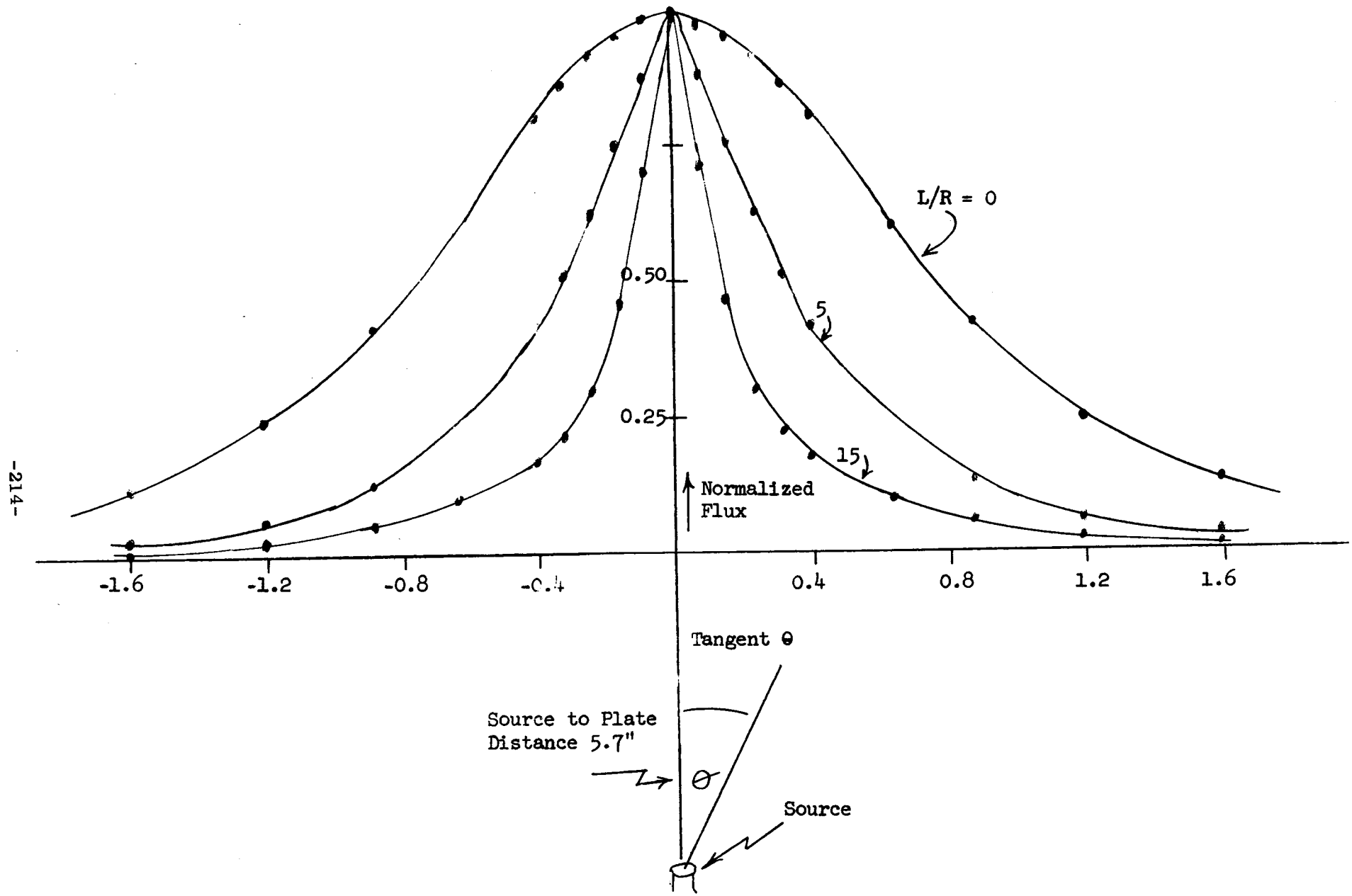


Fig. 38: Theoretical Flux Patterns from Tubular Sources on a Flat Normal Plane

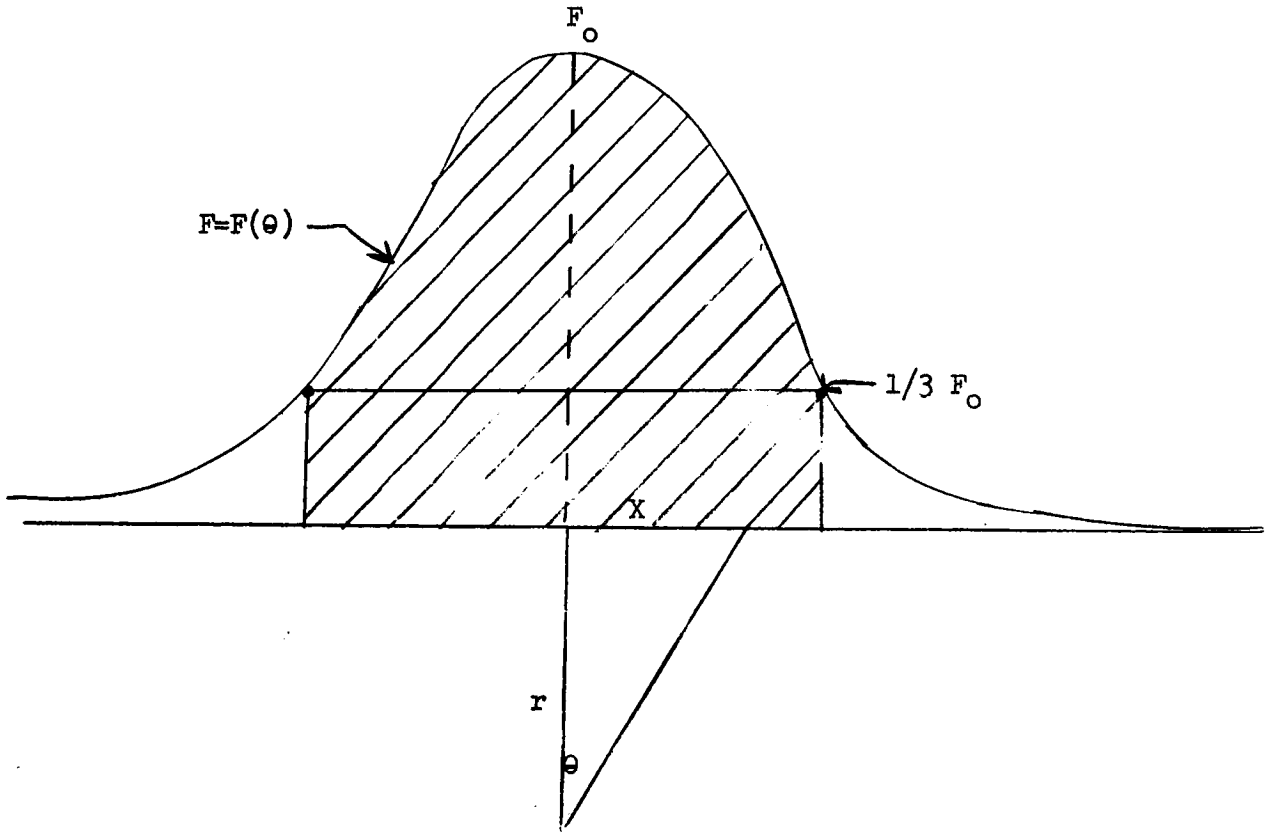


Fig. 39: Cross Section of a Typical Flux Distribution on a Flat Plate

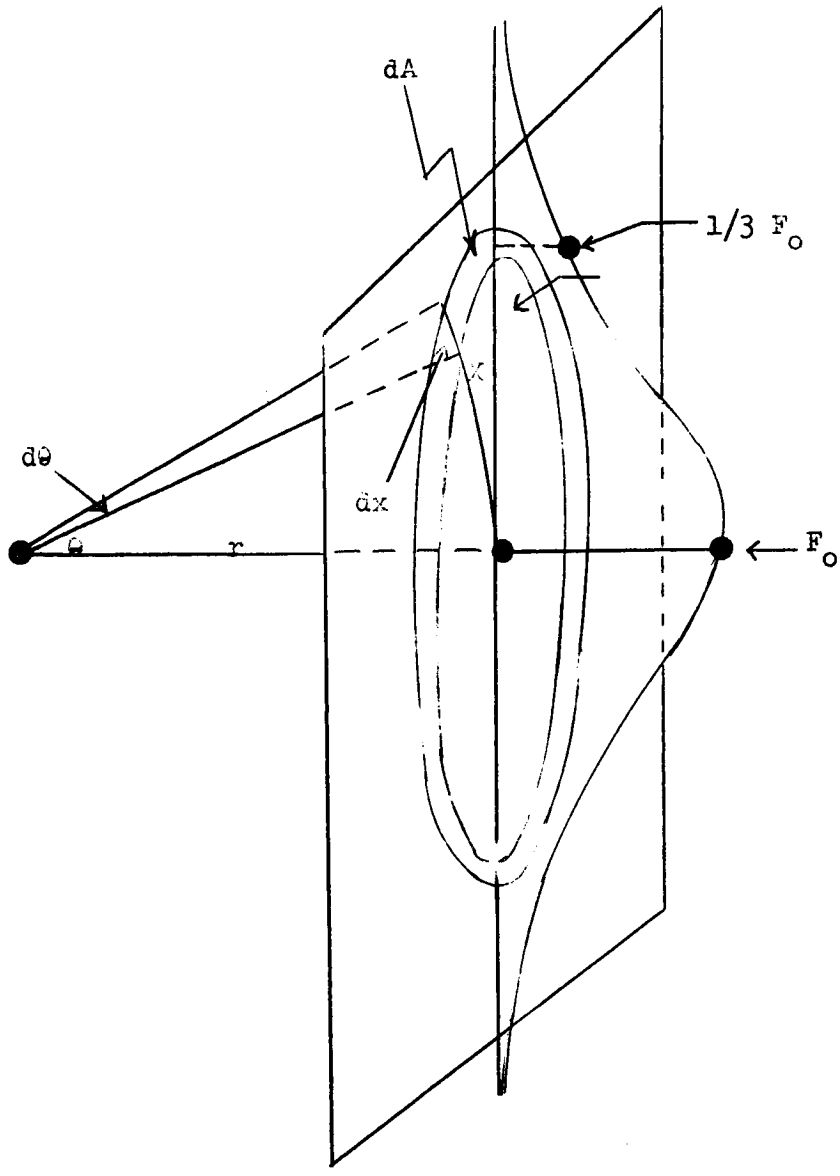


Fig. 40: Three-Dimensional View of Fig. 39

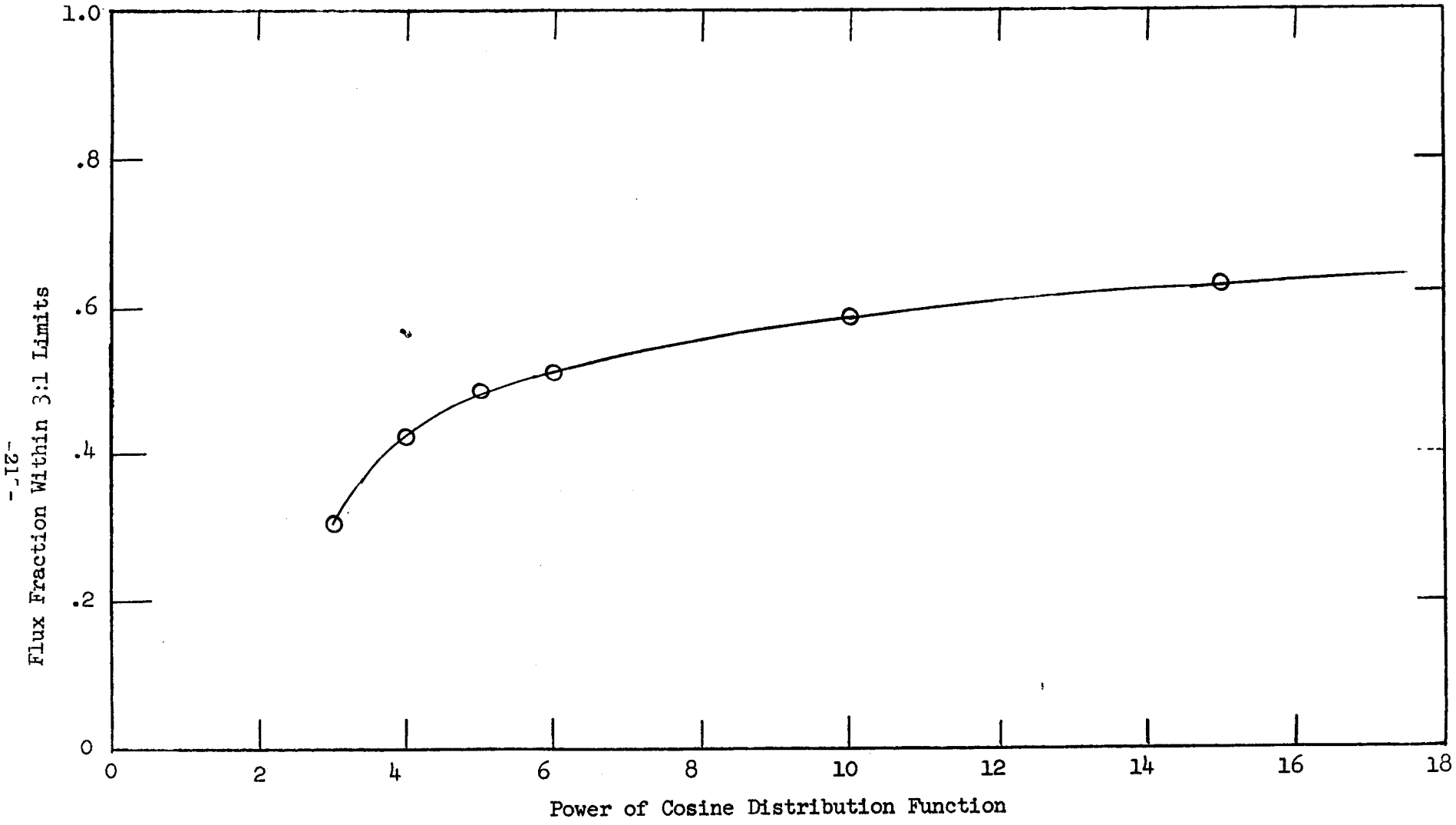


Fig. 41: Flux Within 3:1 Limits from a $Cos^{n}\theta$ Distribution

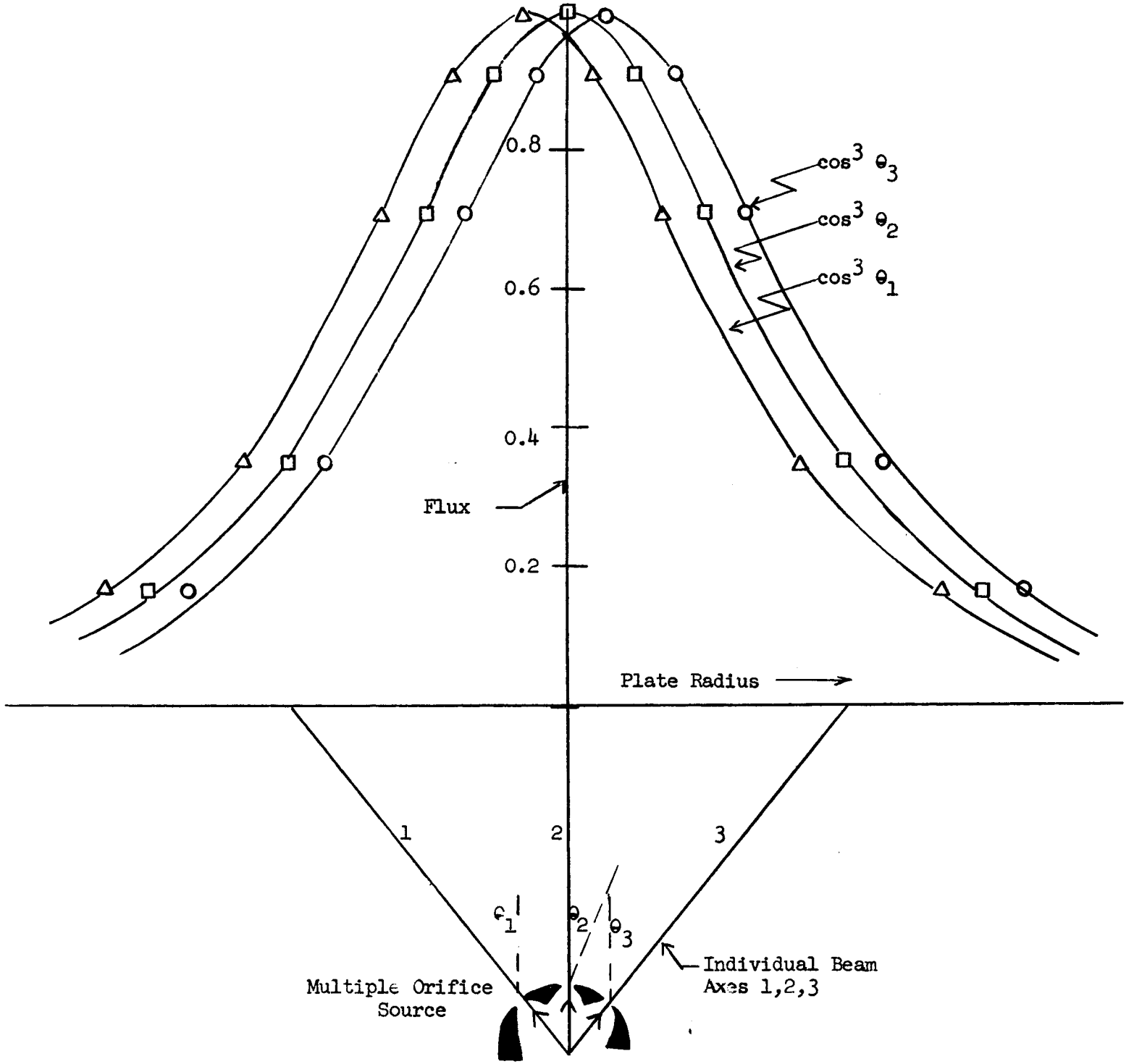


Fig. 42: Flux Distribution over a Flat Plate from Spherically Symmetrical Expansions

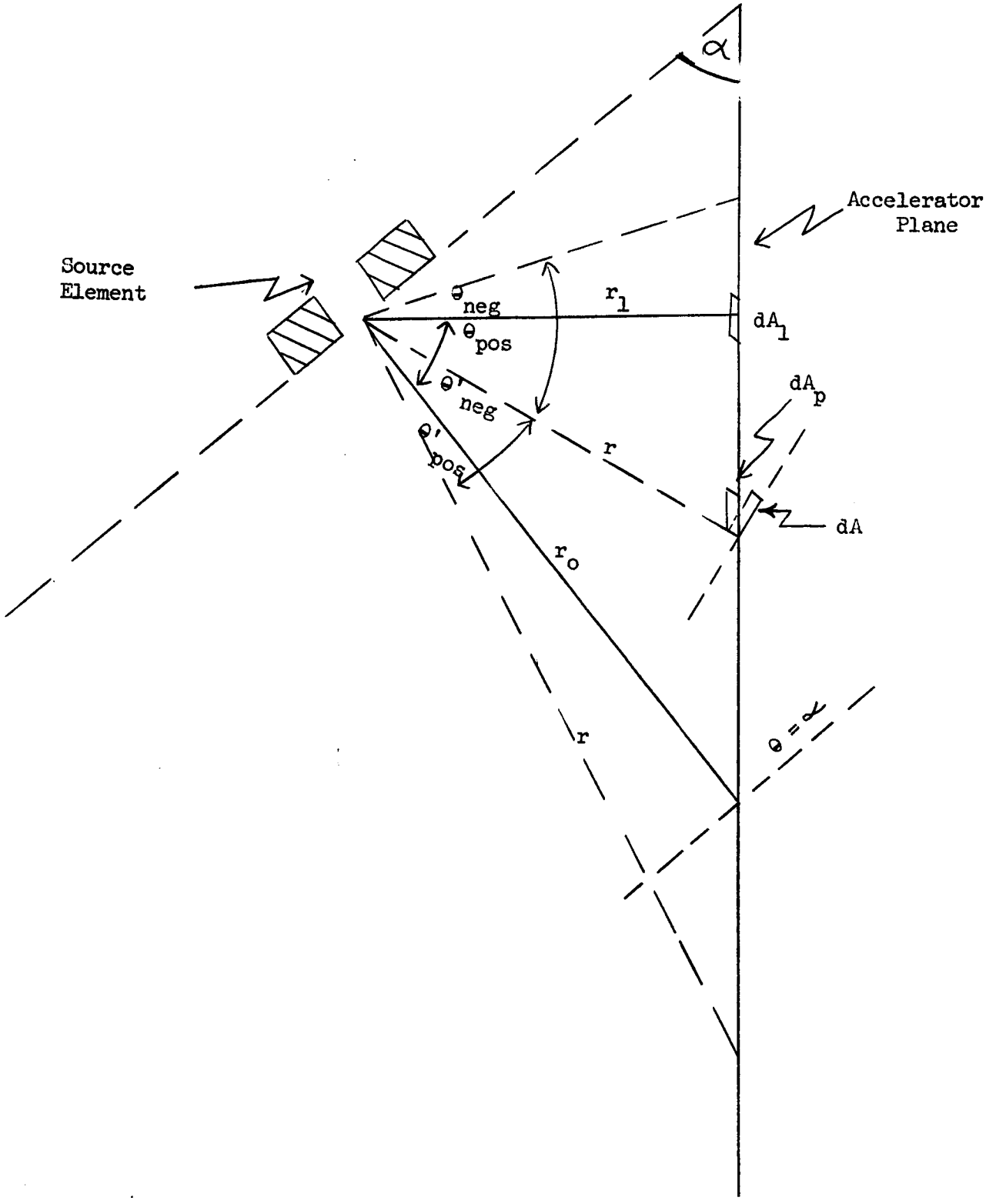


Fig. 43: Flux Projection on a Flat Plate Tilted to the Beam Axis

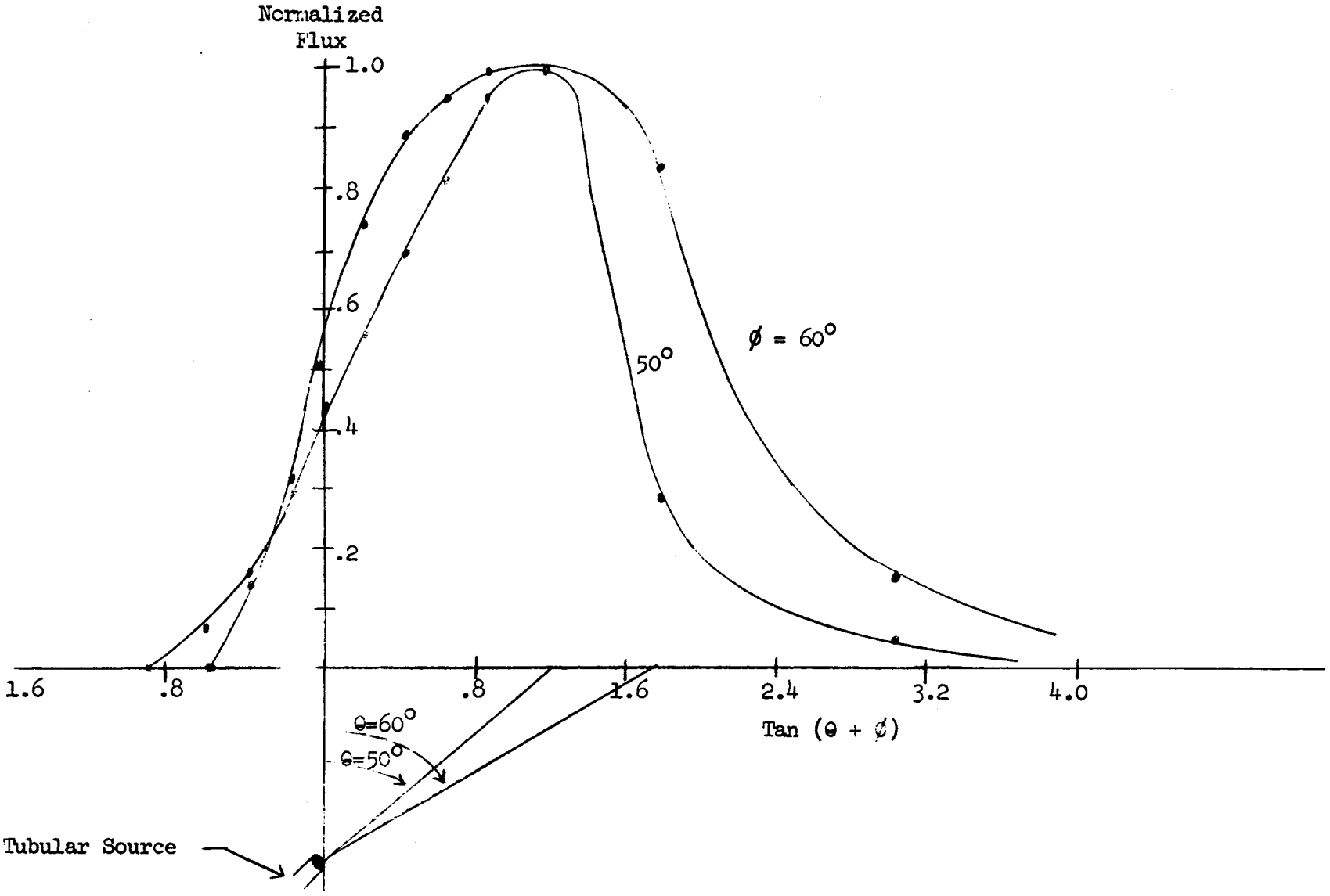


Fig. 44: Molecular Flow Pattern from a Tubular Source Projected at Selected Angles to a Flat Plate. Tube Length/Radius Ratio = 8.

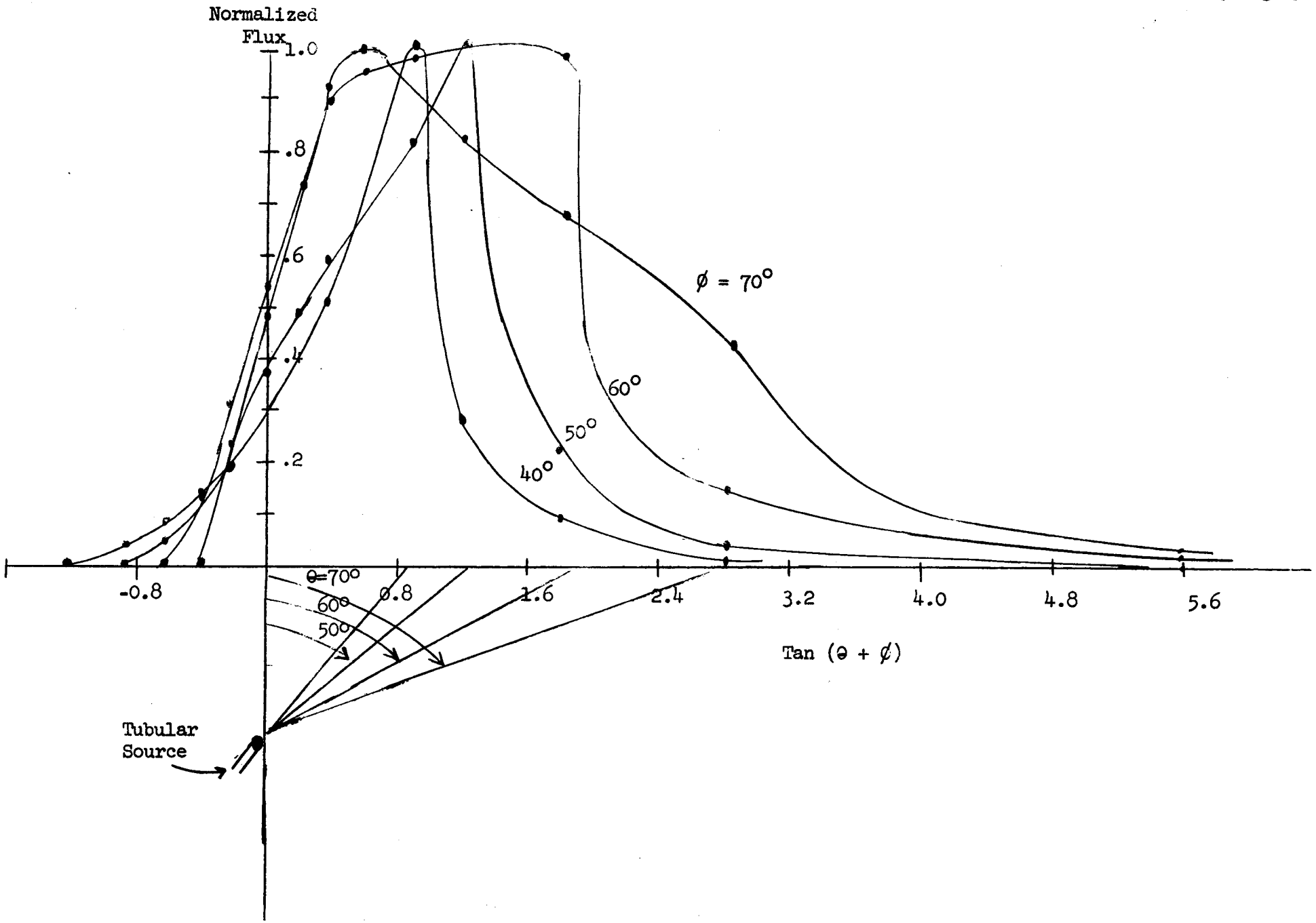


Fig. 45: Molecular Flow Pattern from a Tubular Source Projected at Selected Angles to a Flat Plate. Tube Length/Radius Ratio = 10.

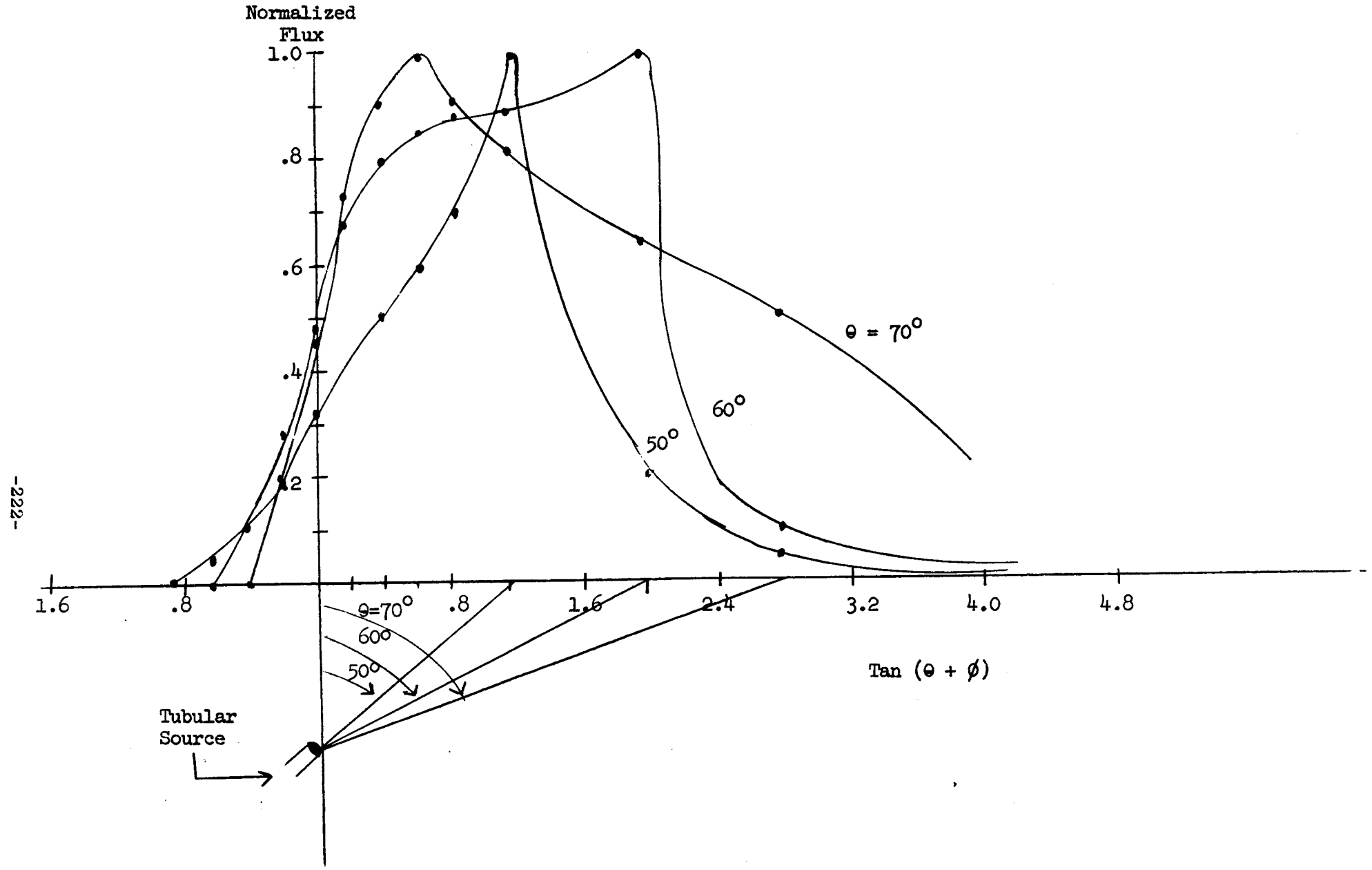


Fig. 46: Molecular Flow Pattern from a Tubular Source Projected at Selected Angles to a Flat Plate. Tube Length/Radius Ratio = 12.

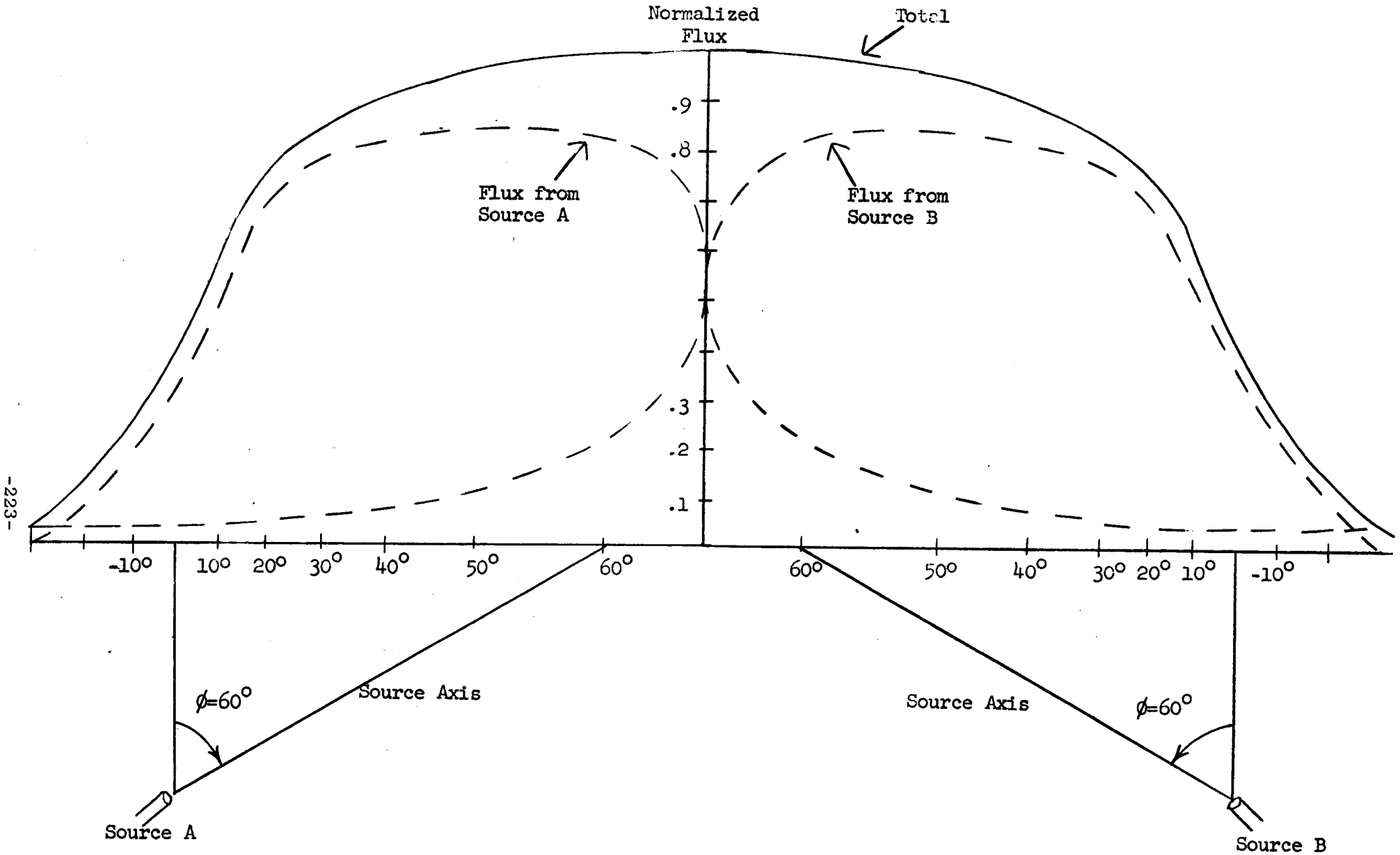


Fig. 47: Molecular Flow Pattern from Two Independent Sources

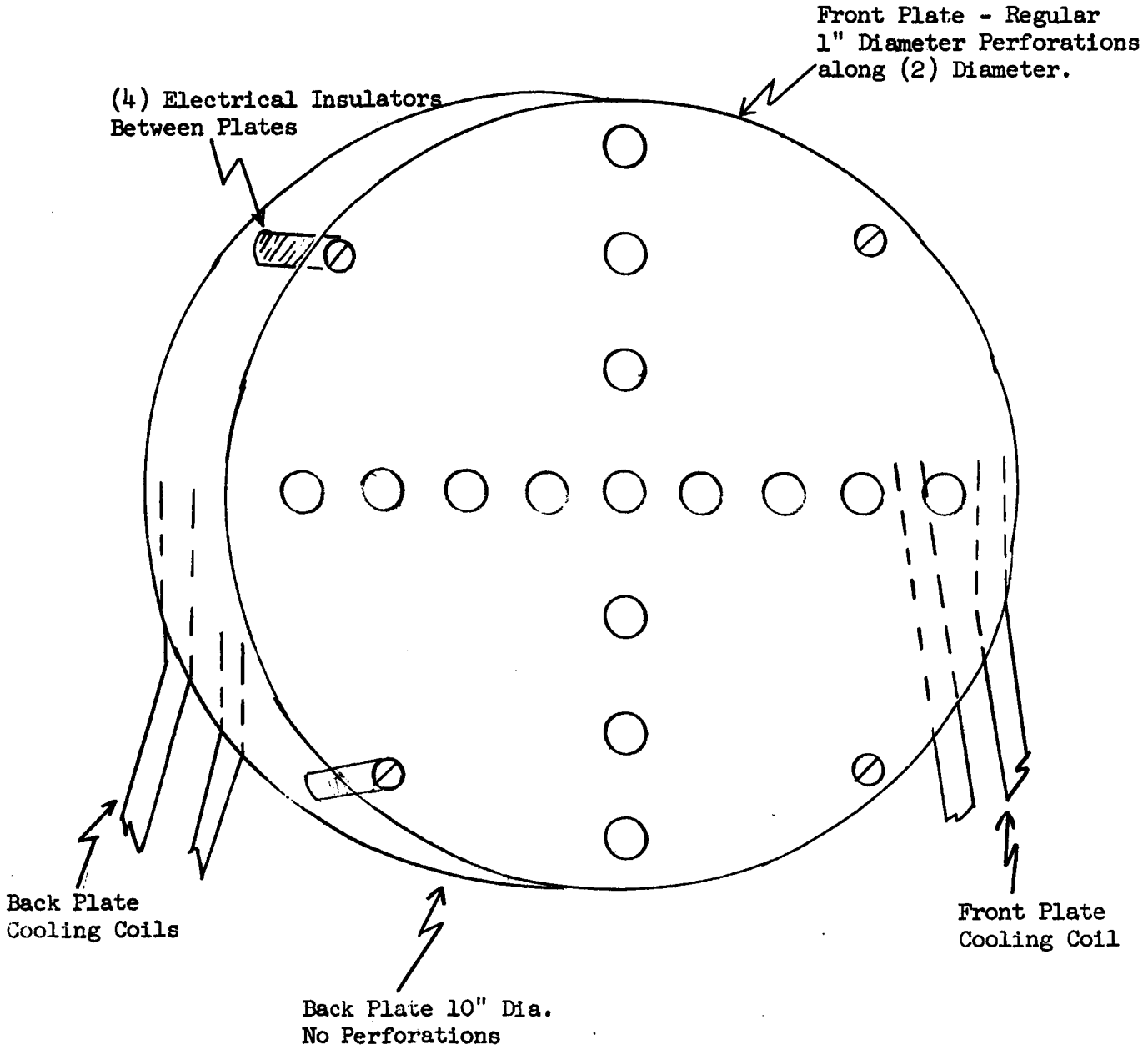


Fig. 48: Double Plate Distribution Probe

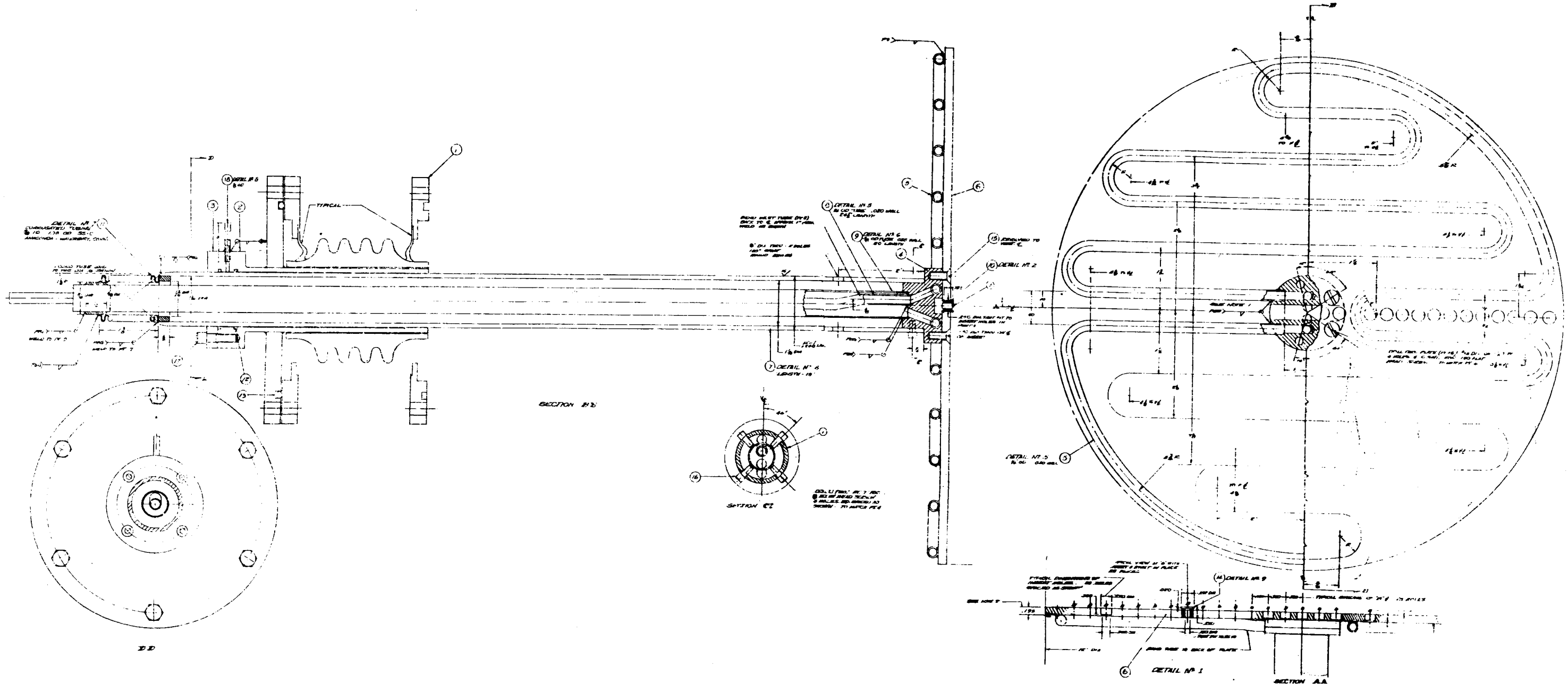
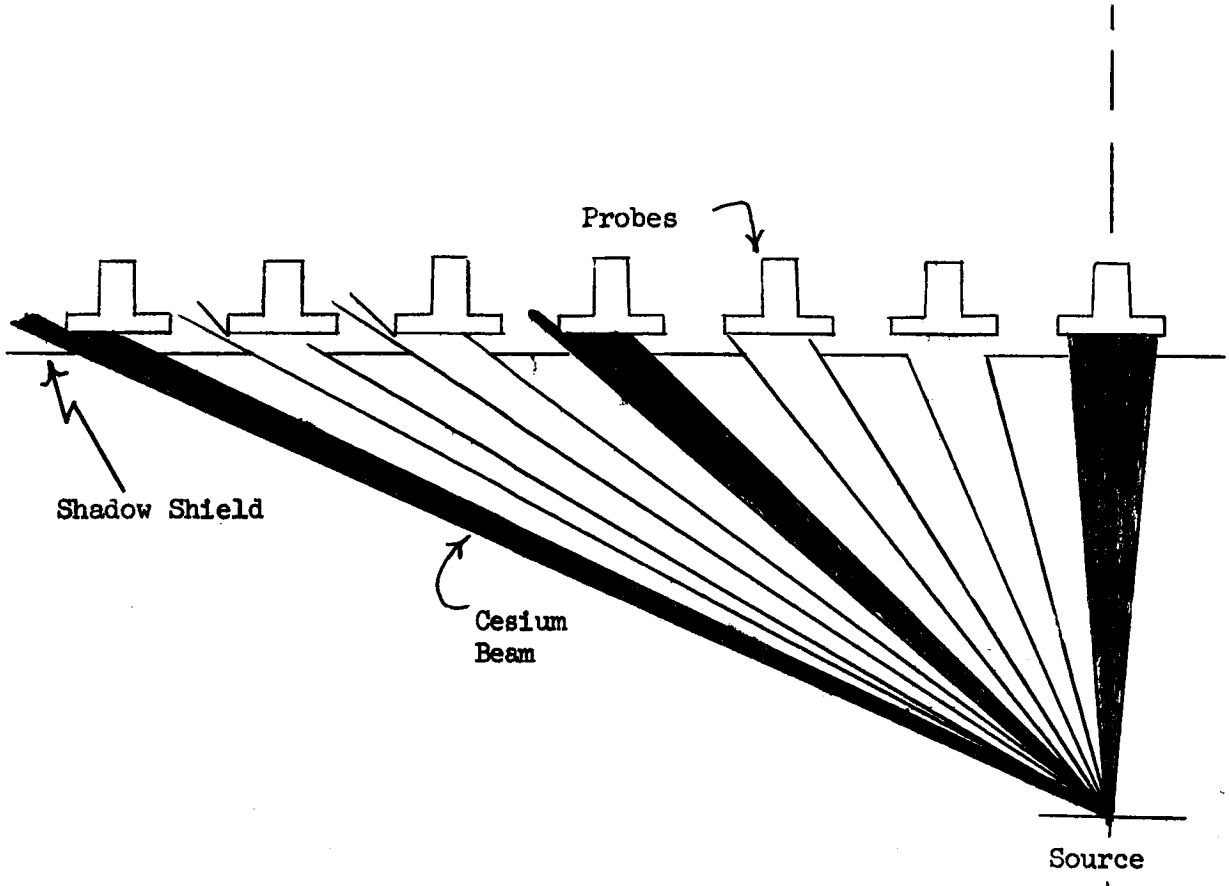
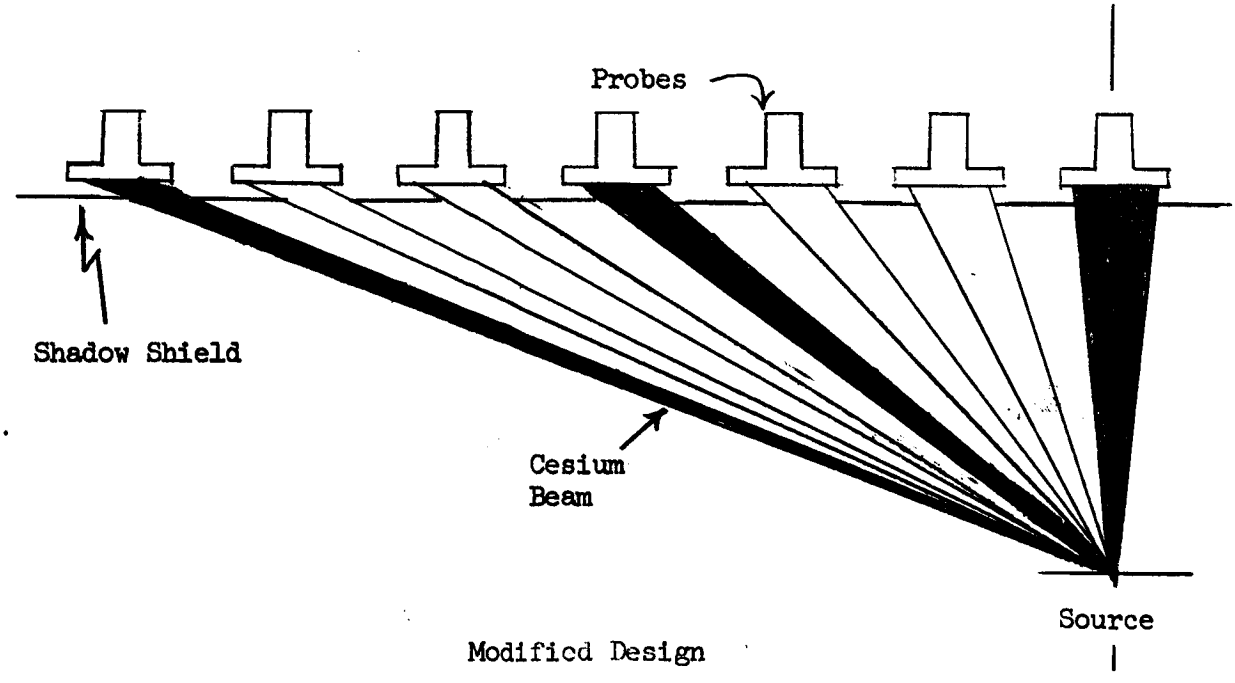


Fig. 49. Plasma Distribution Probe Design



Original Design



Modified Design

Fig. 50: Shadow Shield Design

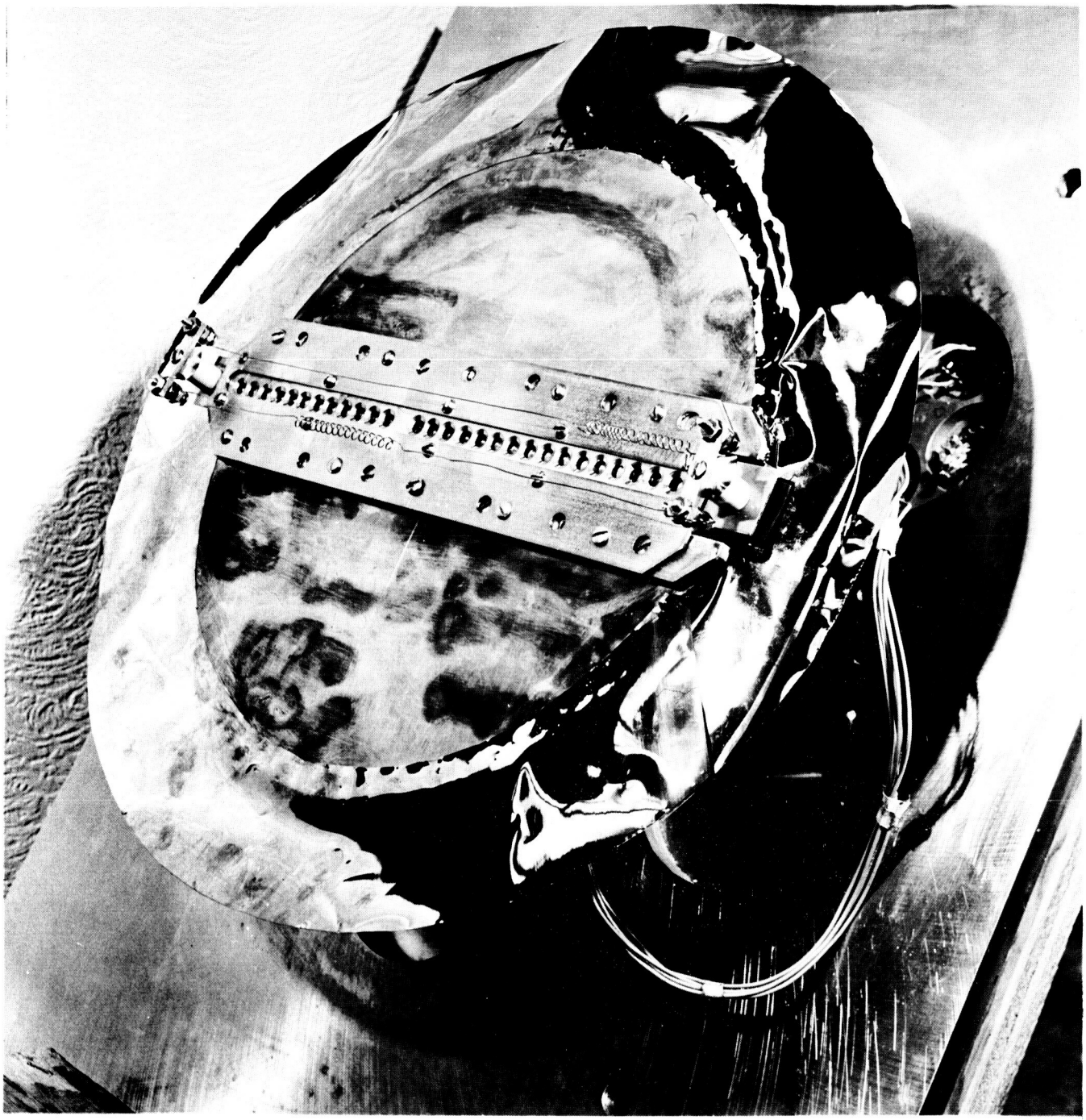


Fig. 51: Multiple Ion Probe with Shadow Shielding

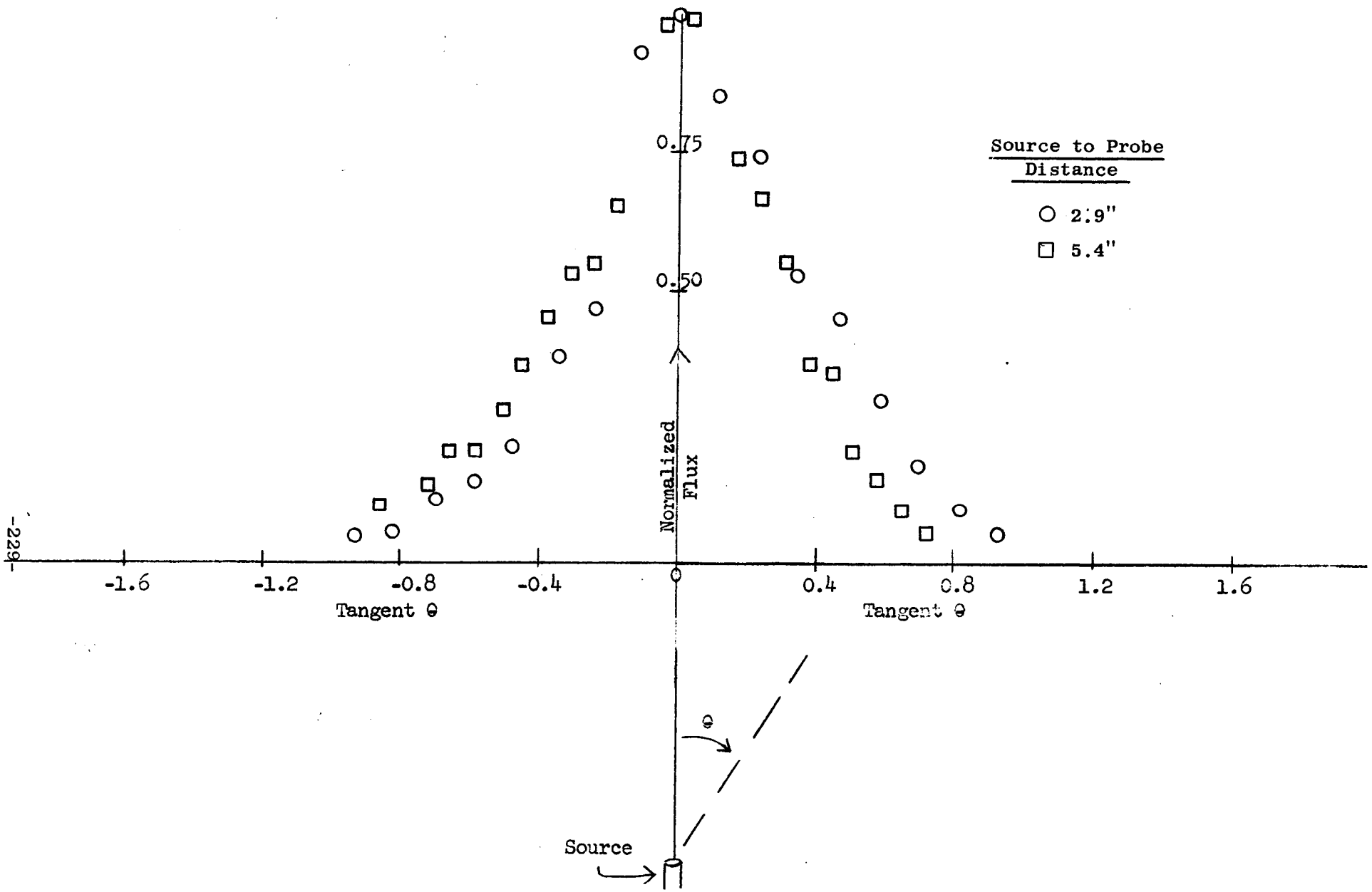


Fig. 52: The Effect of Source to Probe Distance on Density Pattern

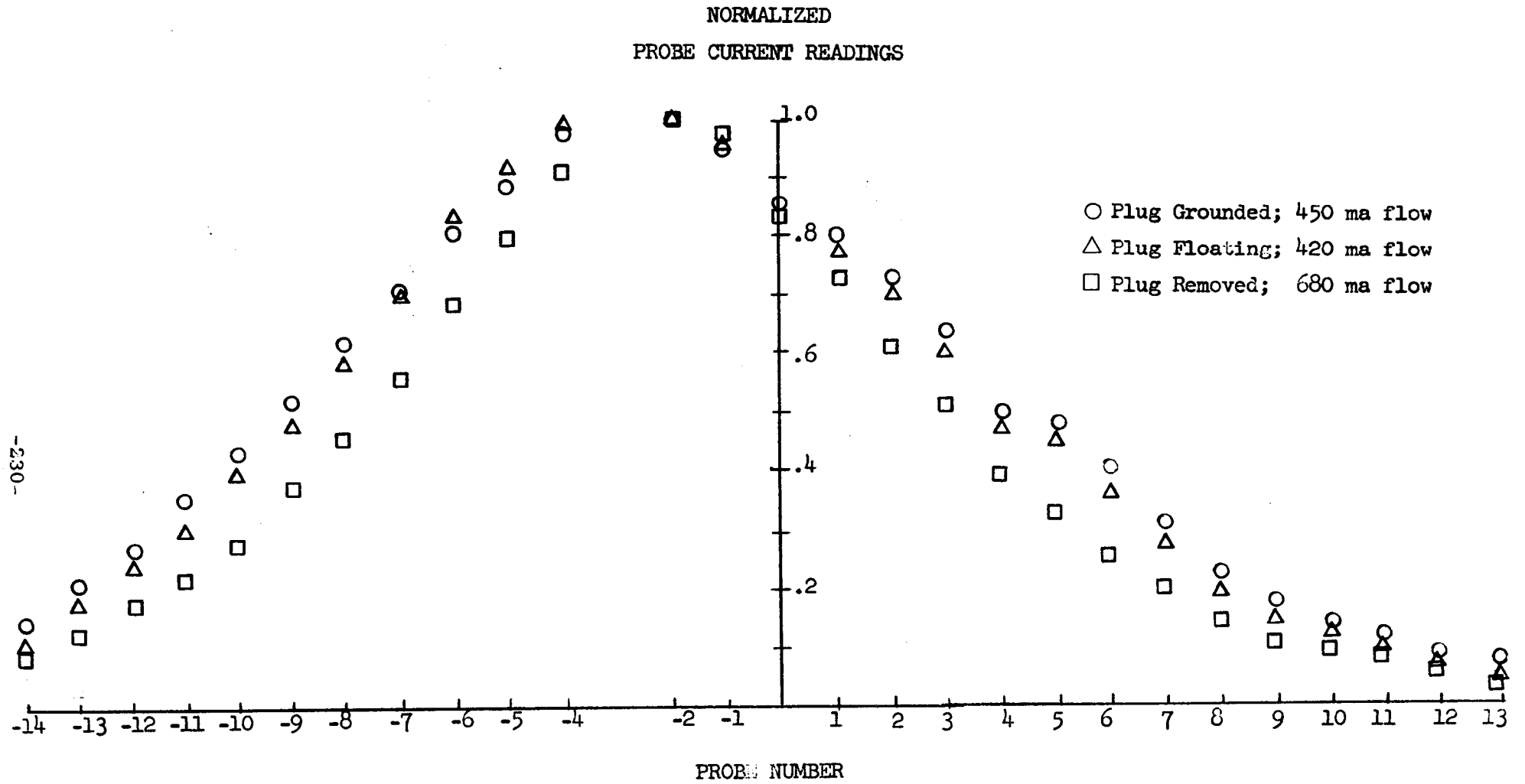


Fig. 53: Density Patterns for Source Design III. Throat = .023"

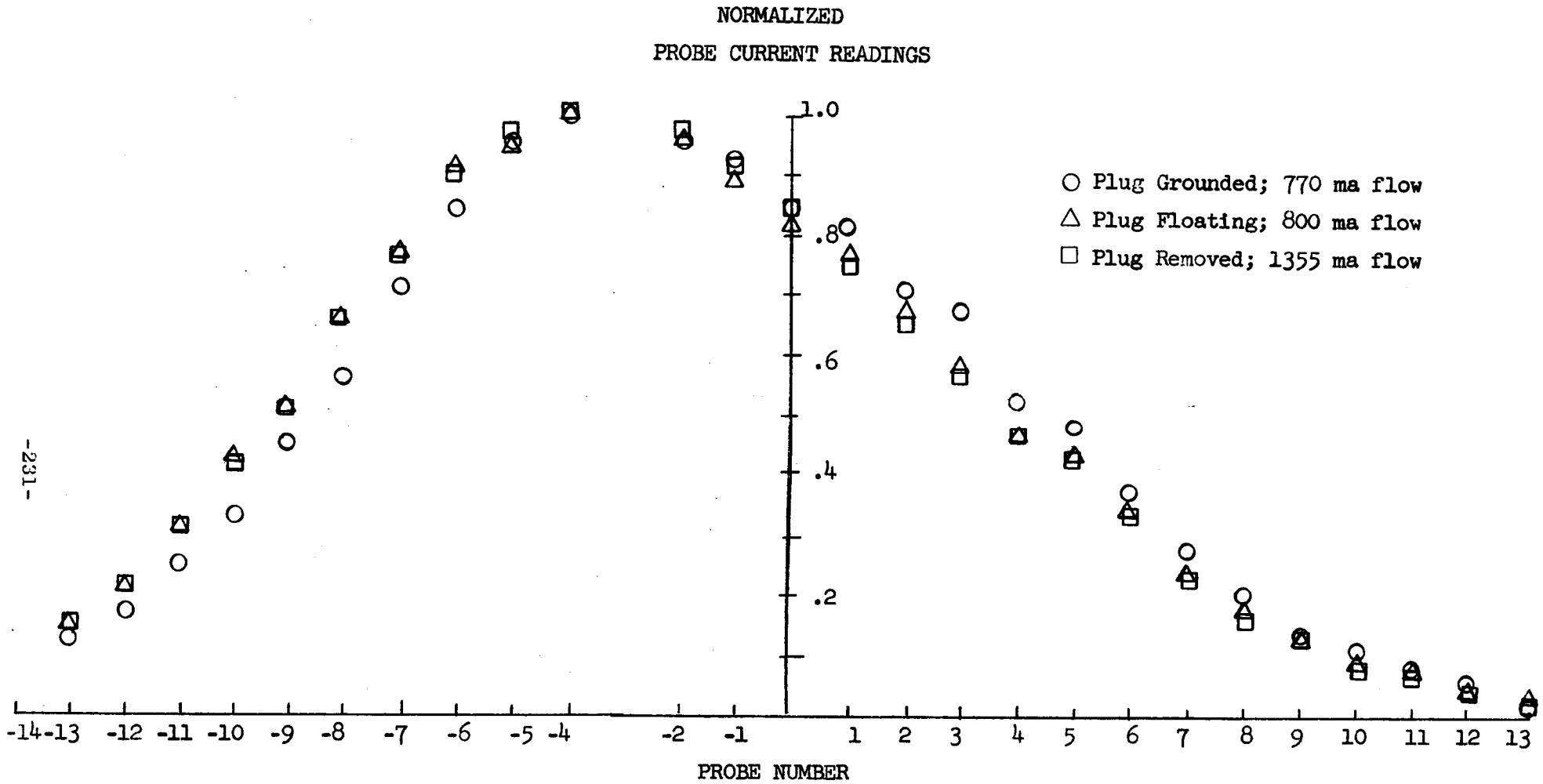


Fig. 54: Density Patterns for Source Design III. Throat = .047"

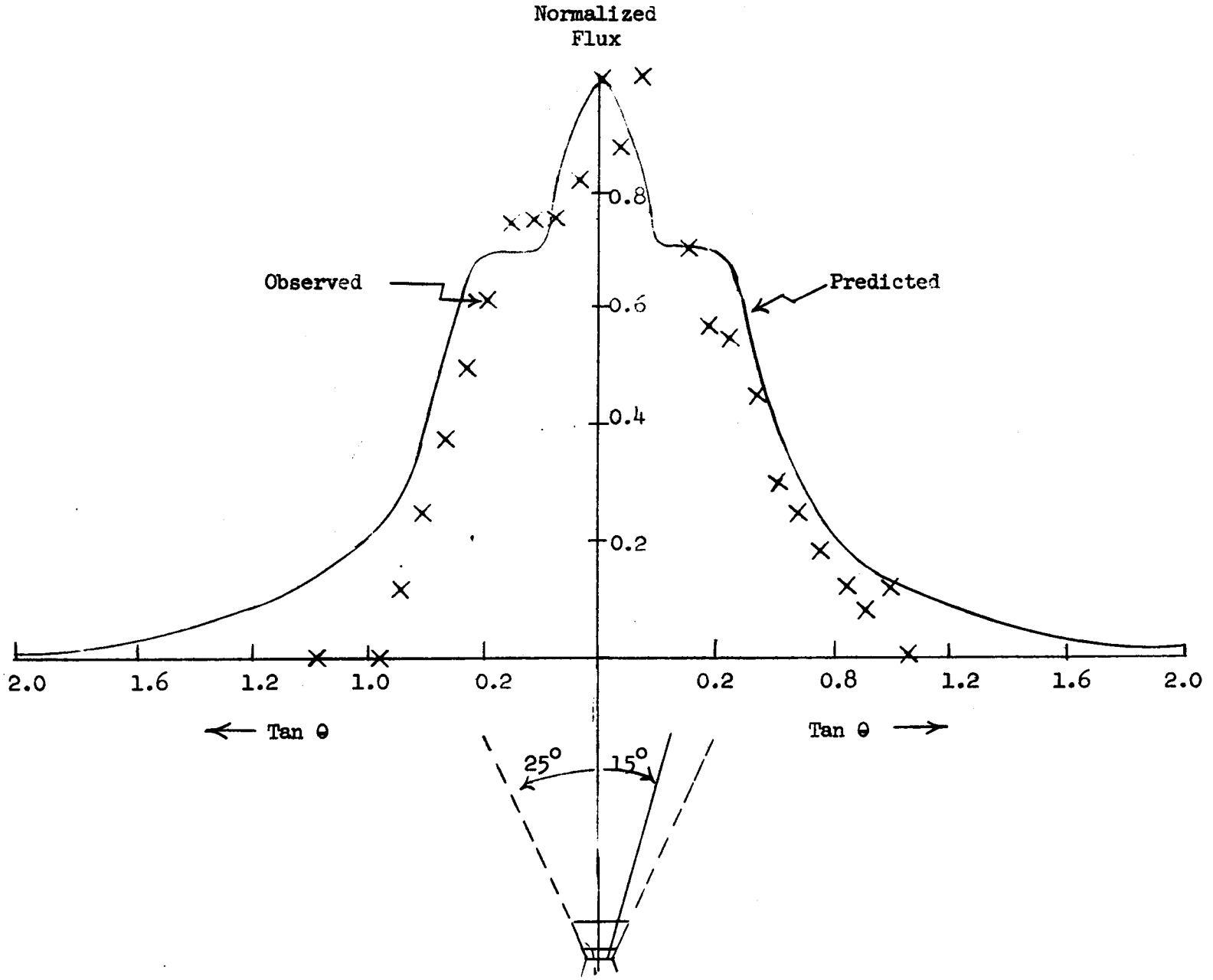


Fig. 55: Flow Pattern from a Multiple Orifice Source at Low Flow Rate

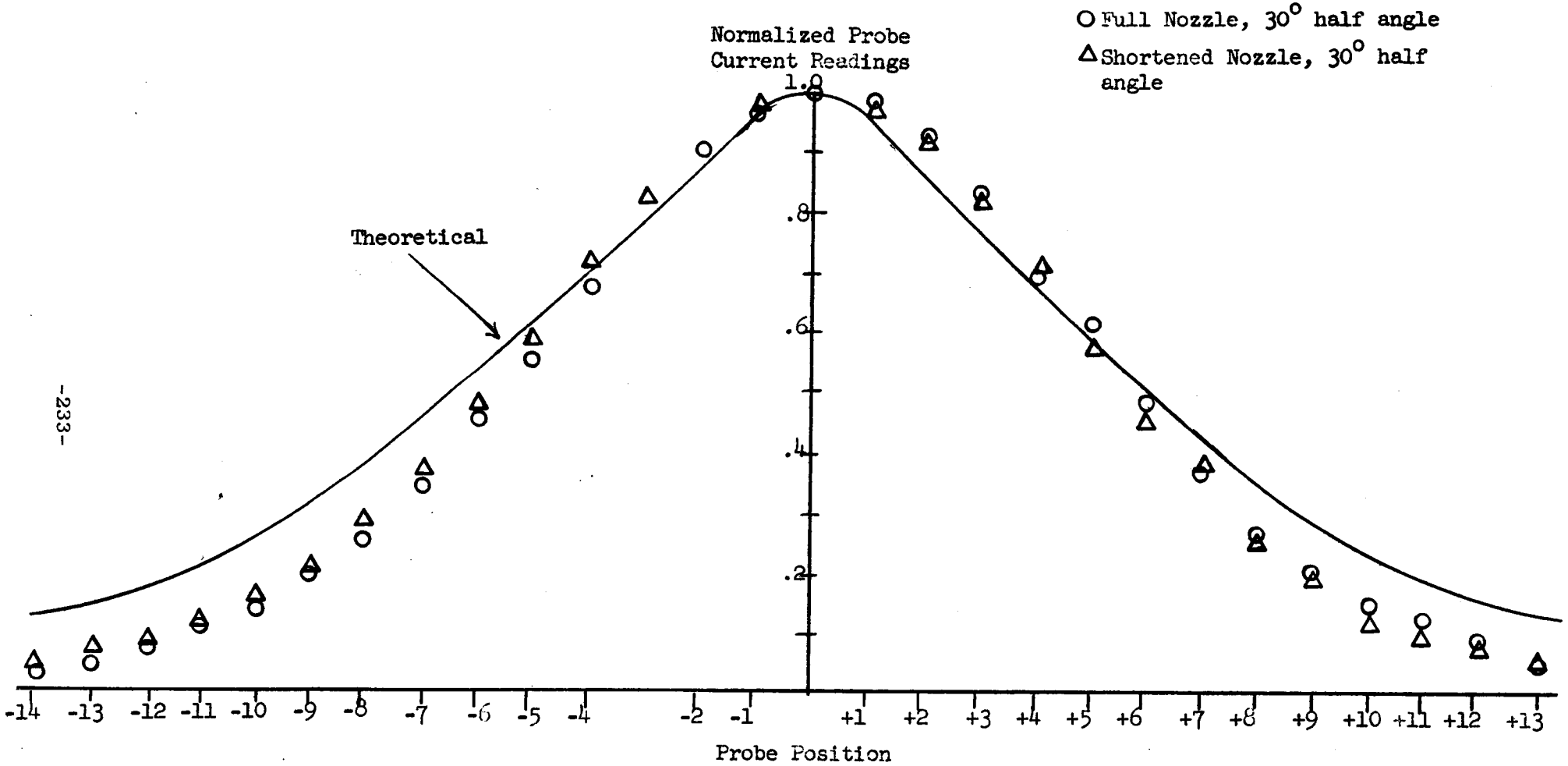


Fig. 56: Ion Density Pattern for Source VII. Tube Length/Radius Ratio = 2.5

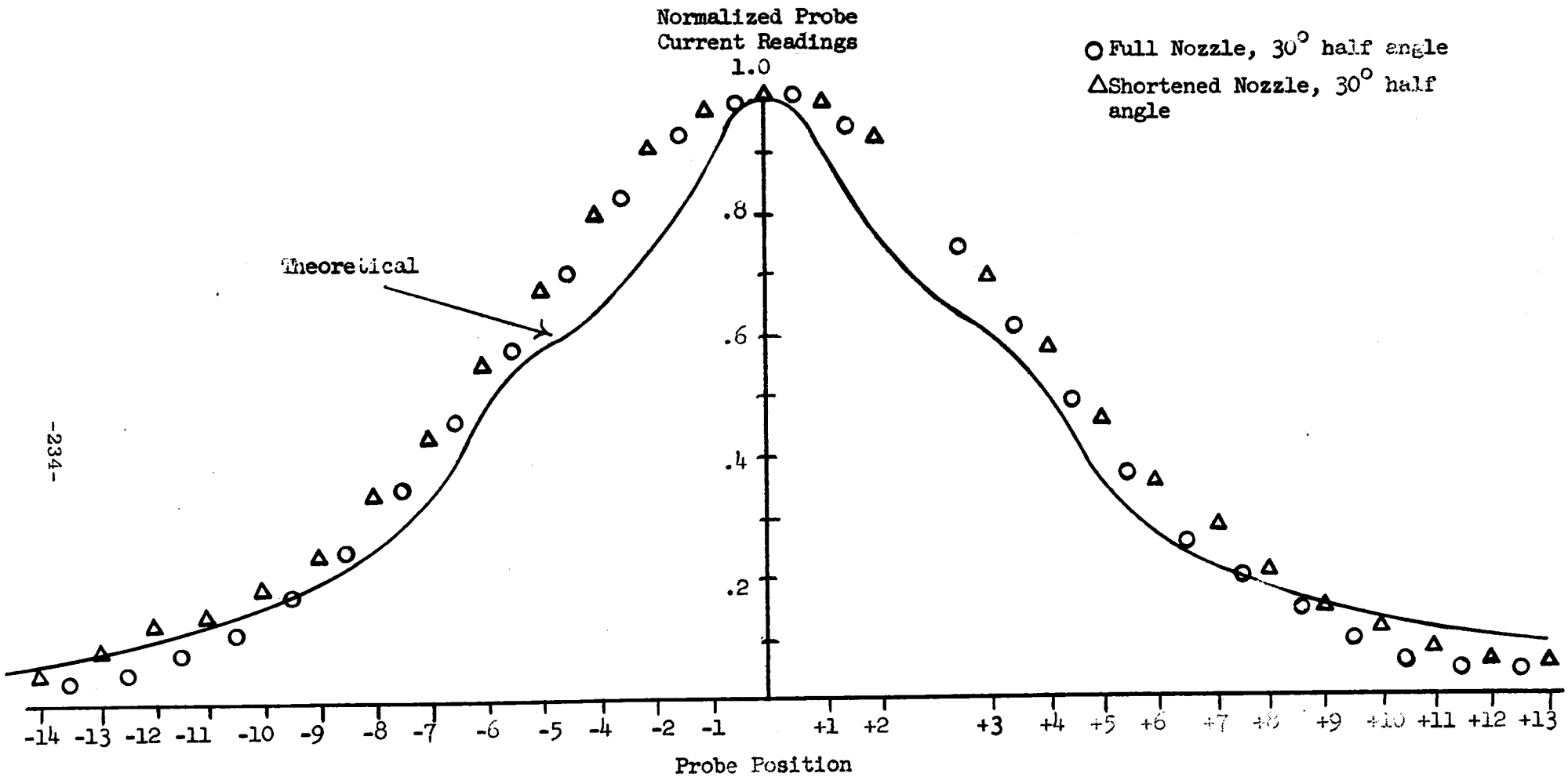


Fig. 57: Ion Density Pattern for Source VII. Tube Length/Radius Ratio = 5

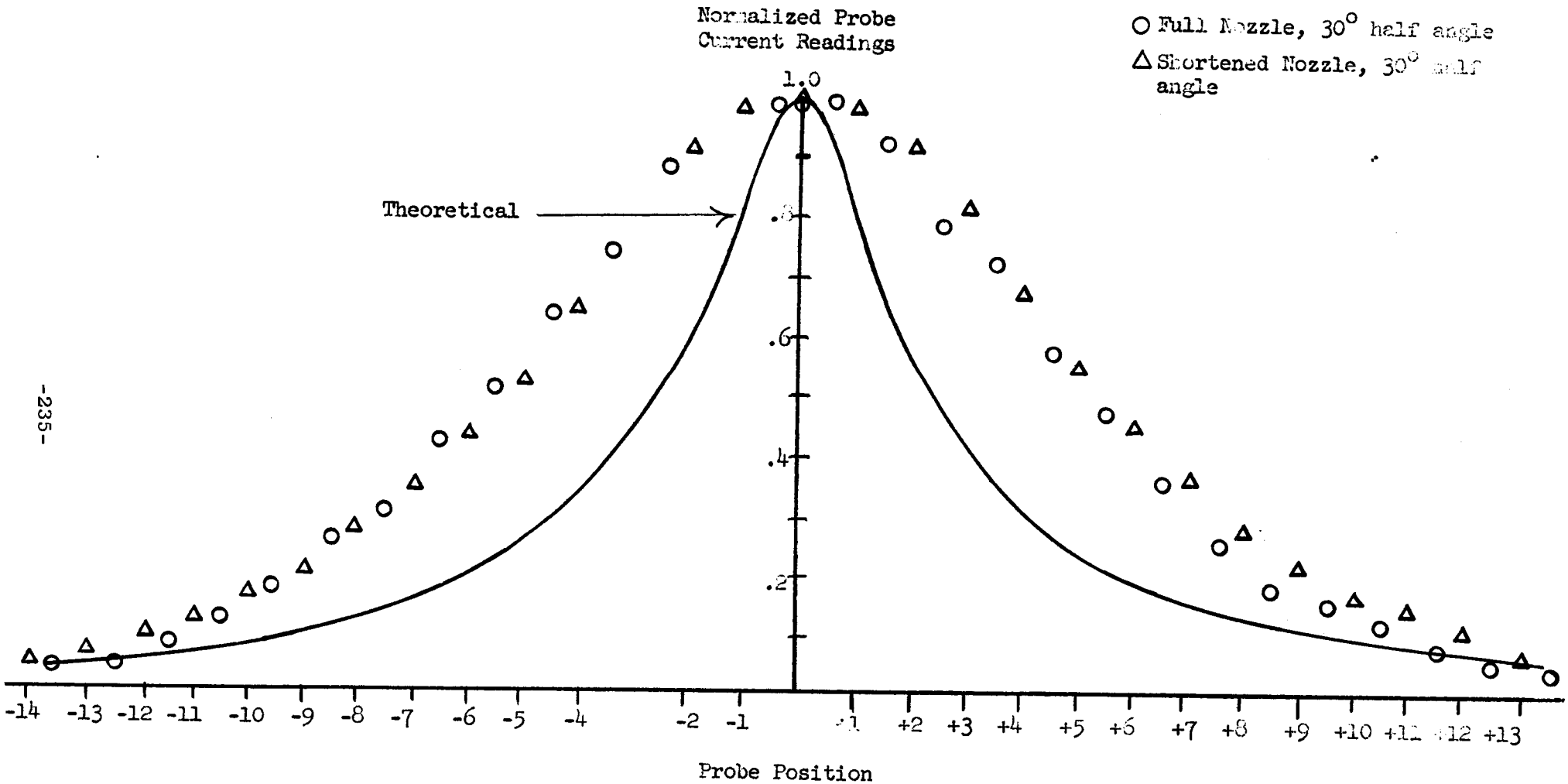


FIG. 58: Ion Density Pattern for Source VII. Tube Length/Radius Ratio = 10

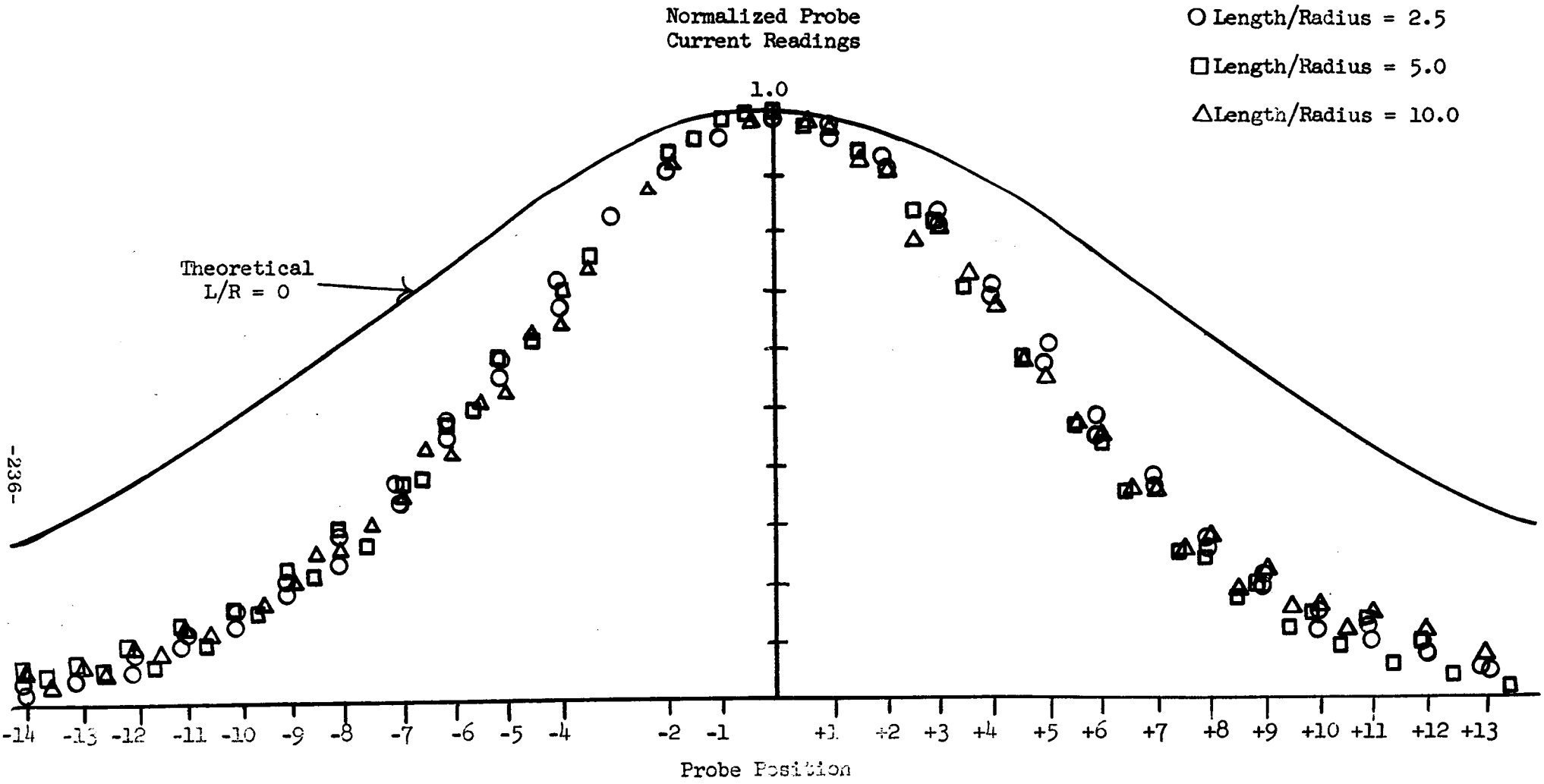


Fig. 59: Ion Density Patterns for Source VII. Variable Tube Dimensions

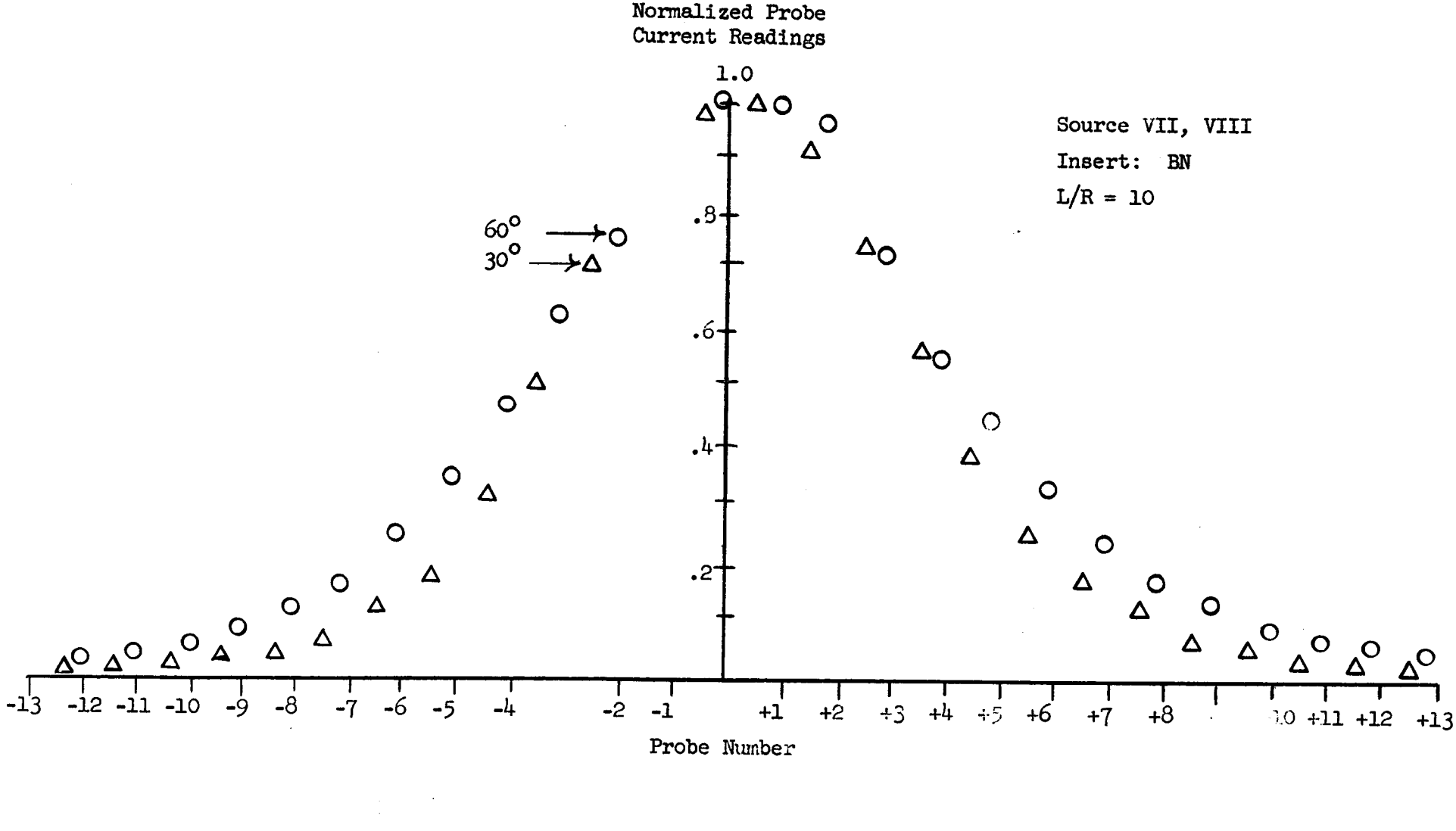


Fig. 60: Density Pattern Variation With Nozzle Half Angle

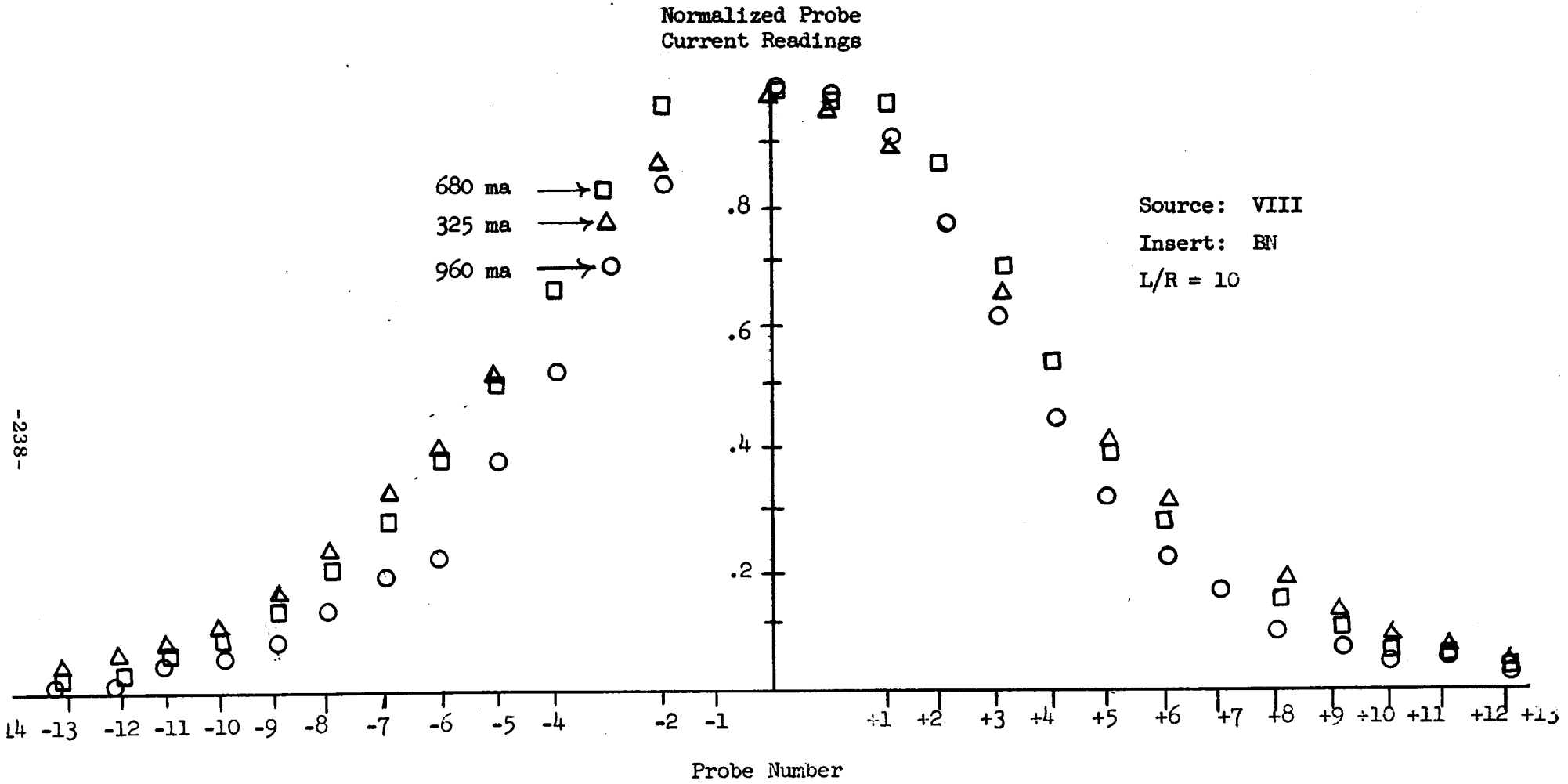


Fig. 61: Density Pattern Variation With Flow Rate

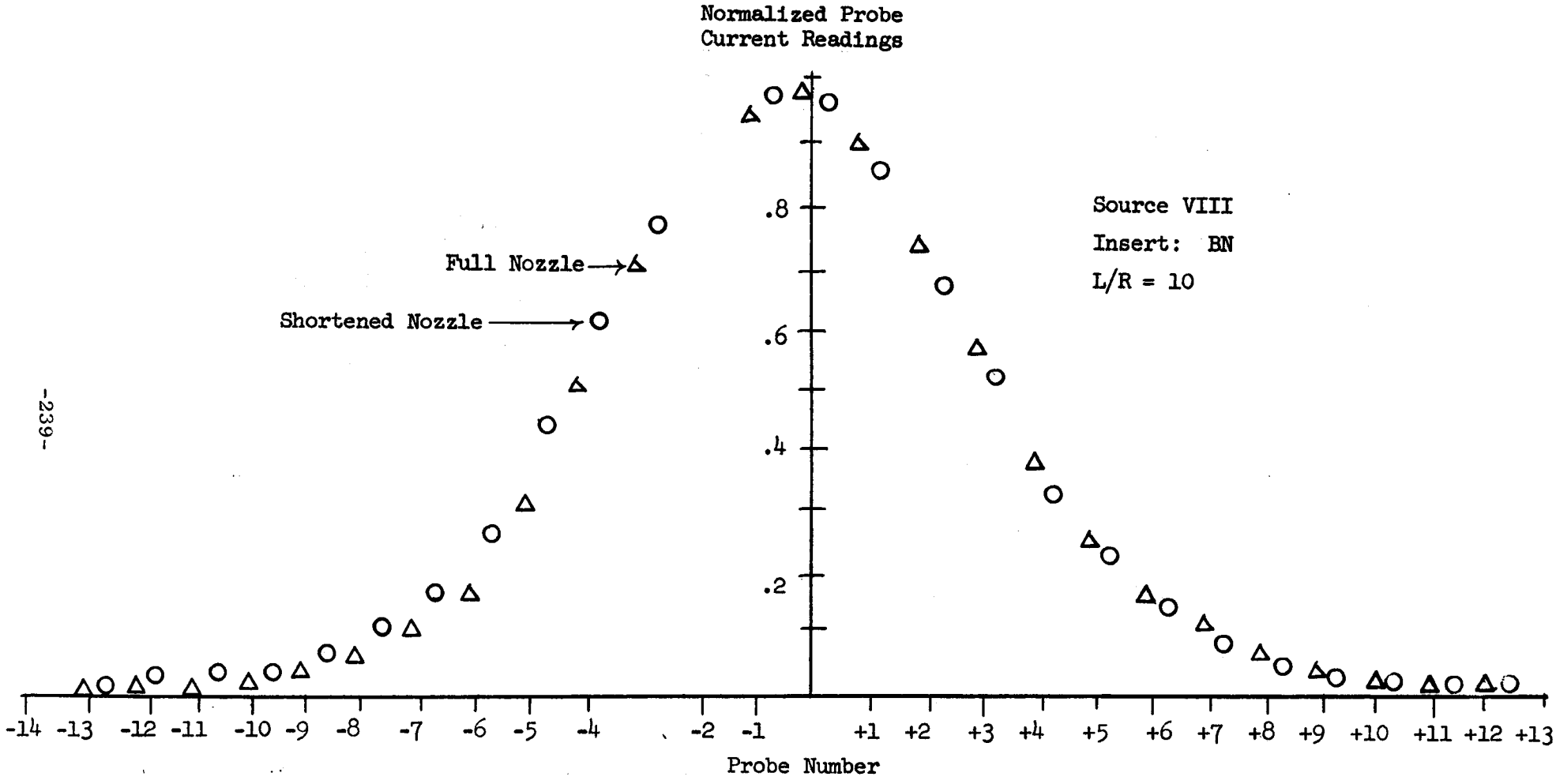


Fig. 62: The Effect of Nozzle Shortening

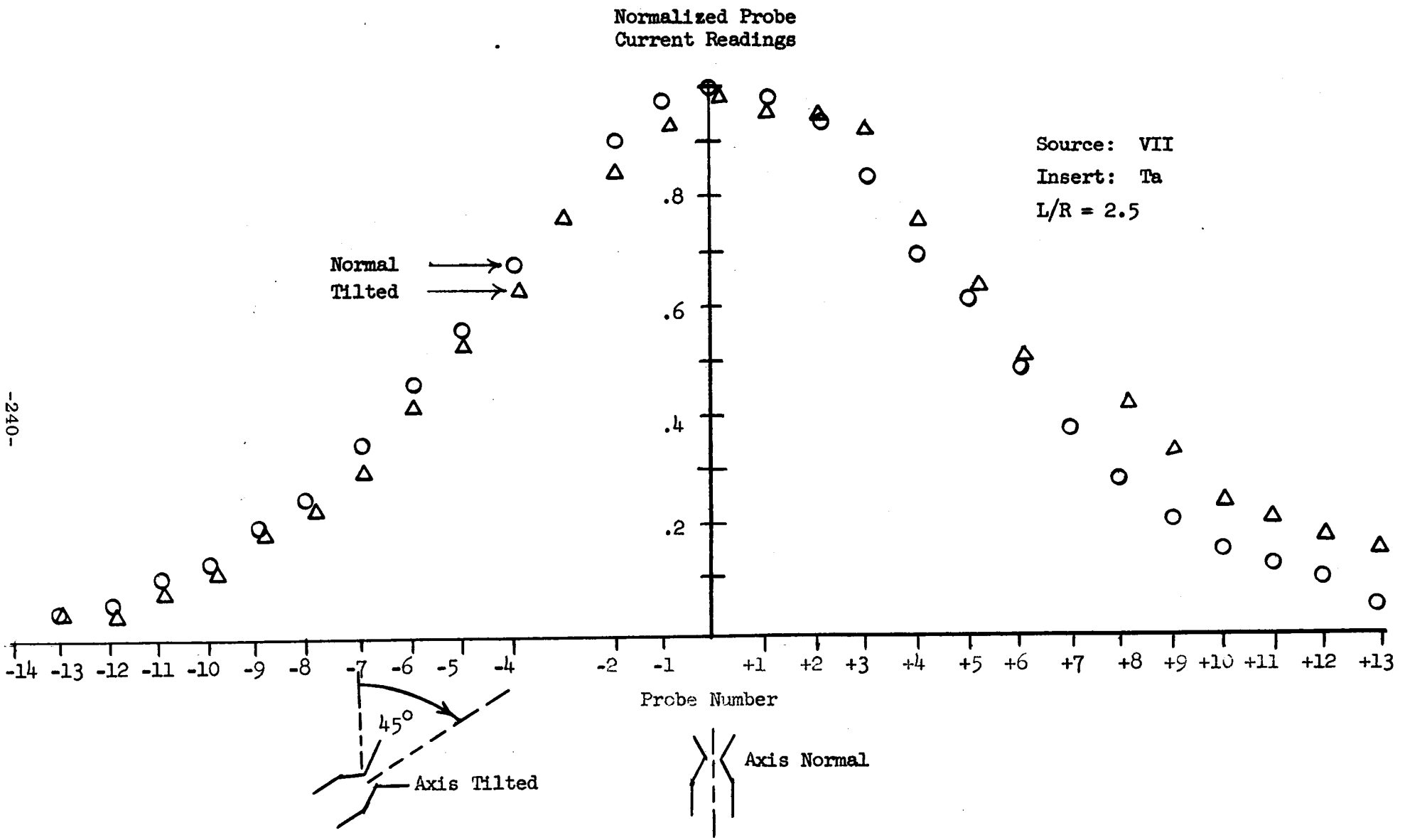


Fig. 63: Density Pattern Variation with Tilted Beam Axis

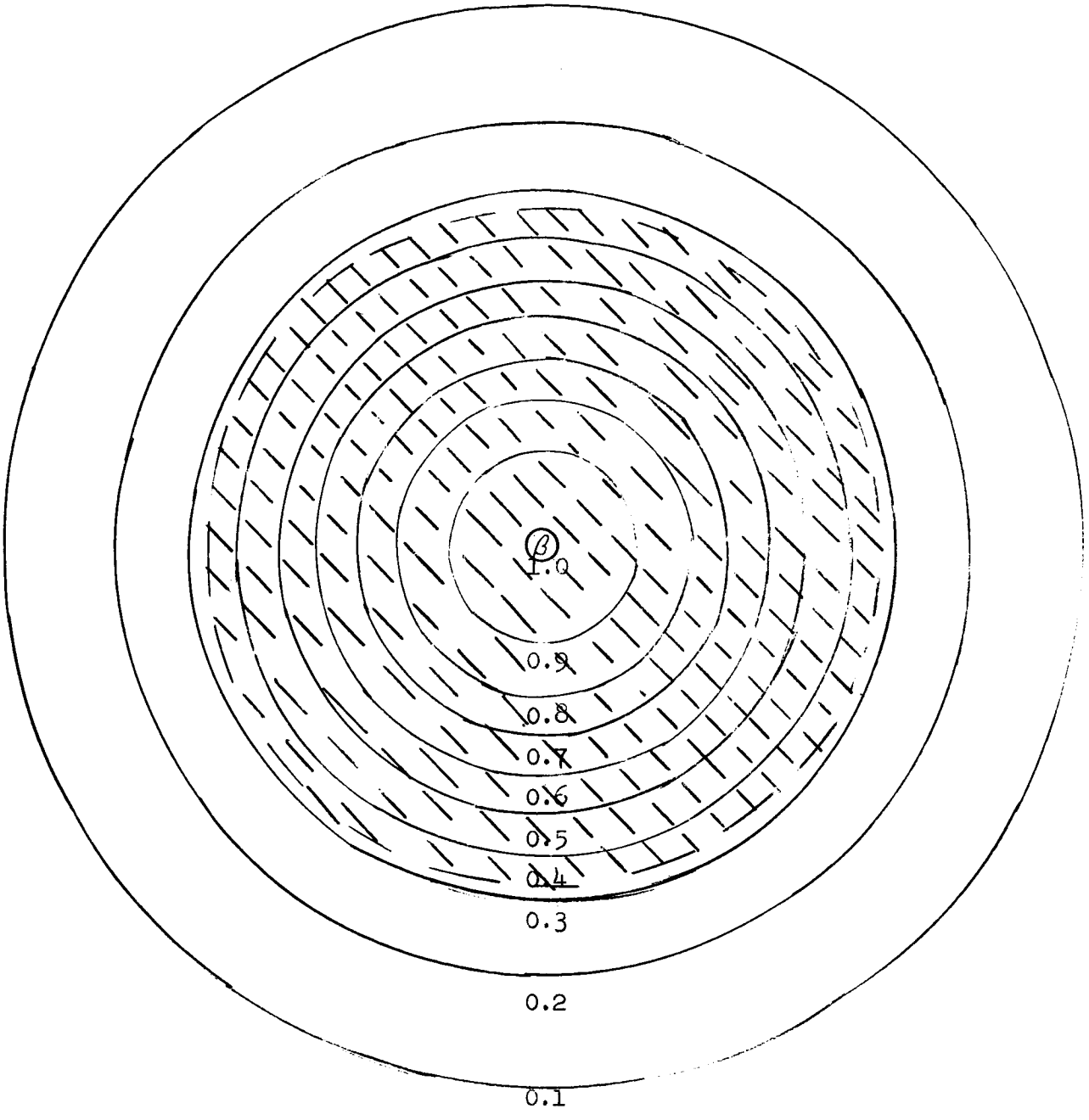


Fig. 64: A Single Source Flux Distribution. Source Located at ⊙. Shaded Area Within 3:1 Density Limits Represents 46.5% of Total Flow.

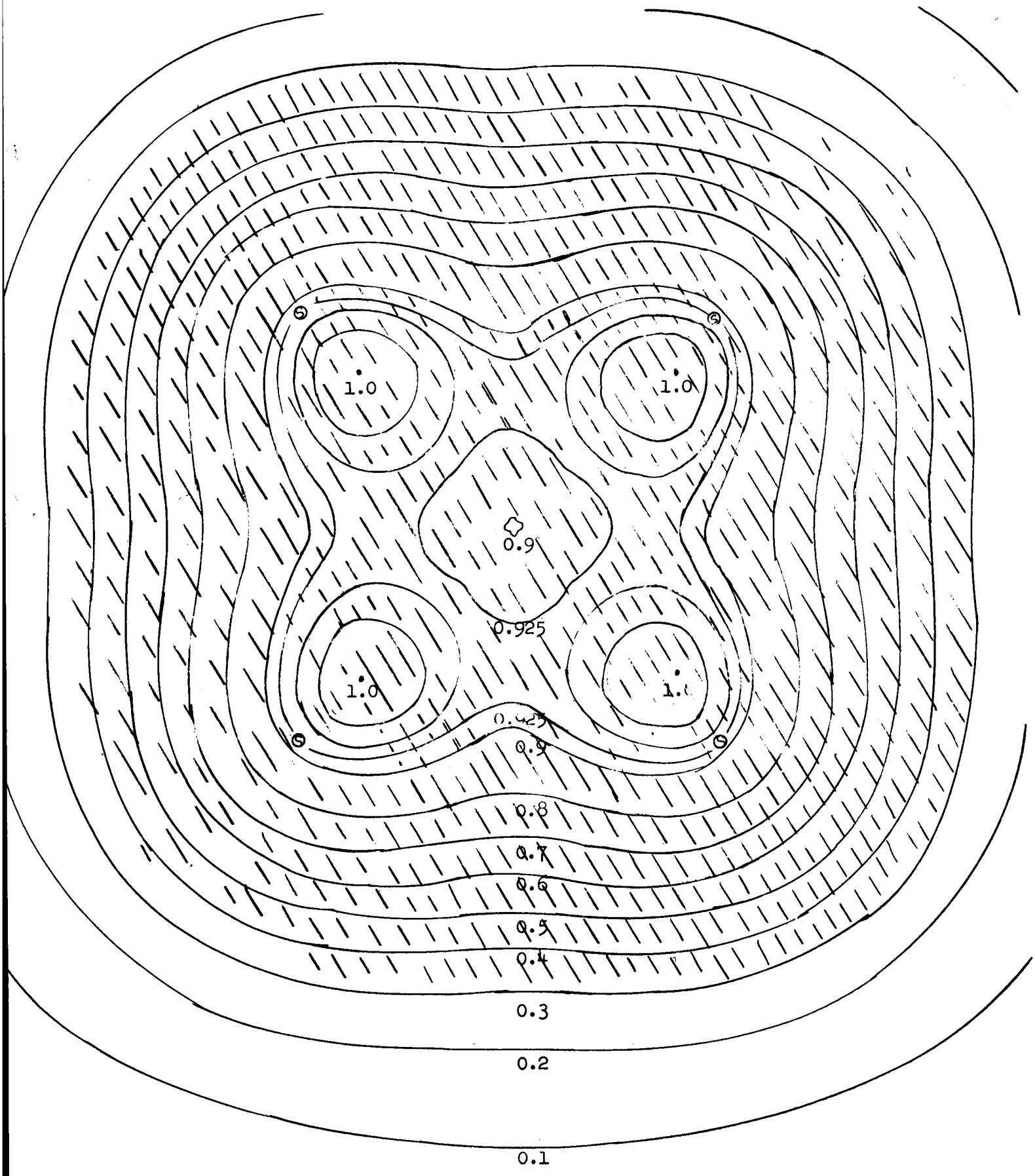


Fig. 65: Multiple Source Flux Distribution. Source Located at ⊙. Shaded Area Within 3:1 Density Limits Represents 78% of Total Flux.

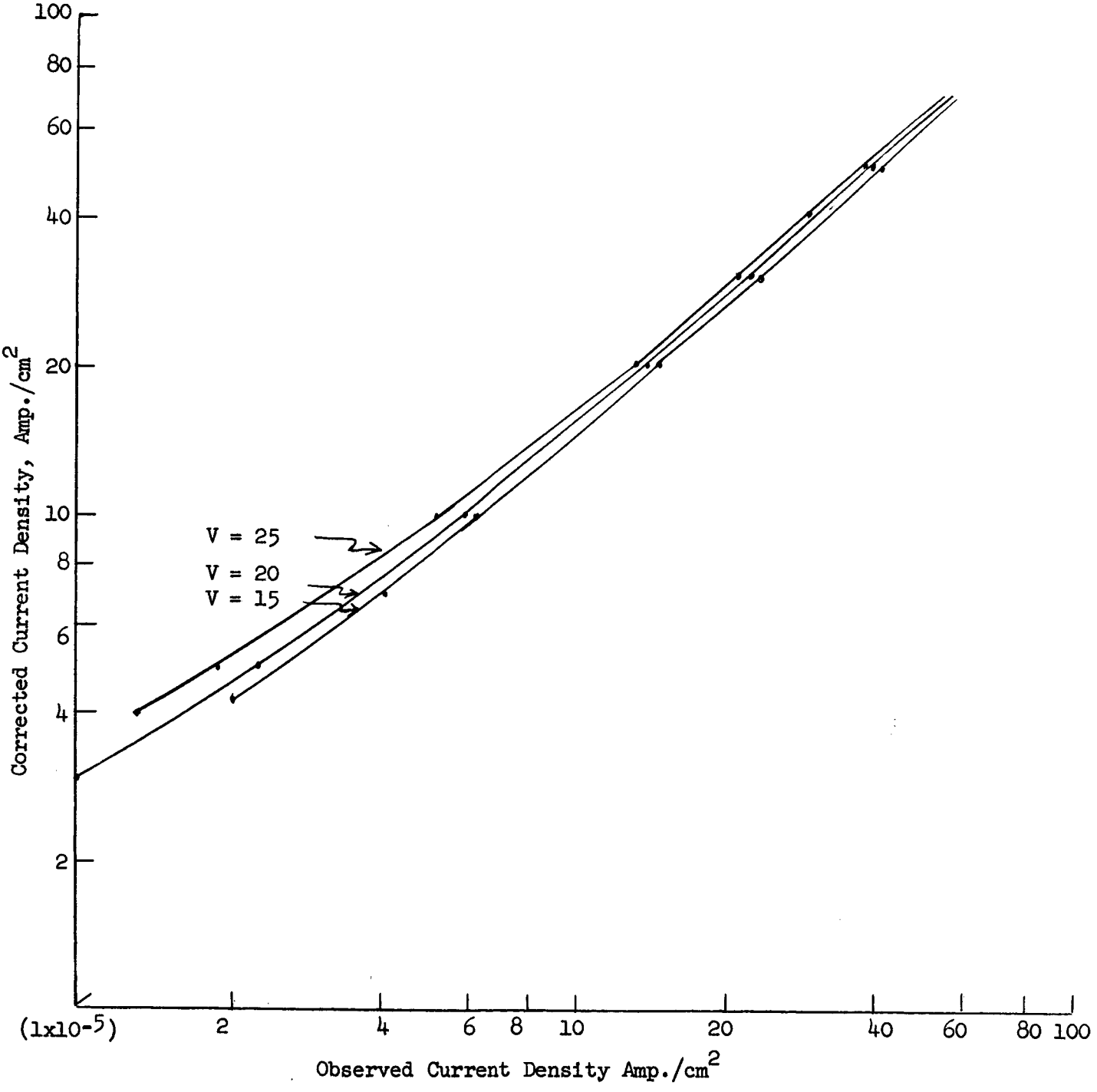


Fig. 66: Current Density Correction Curve for Plasma Sheath Effect

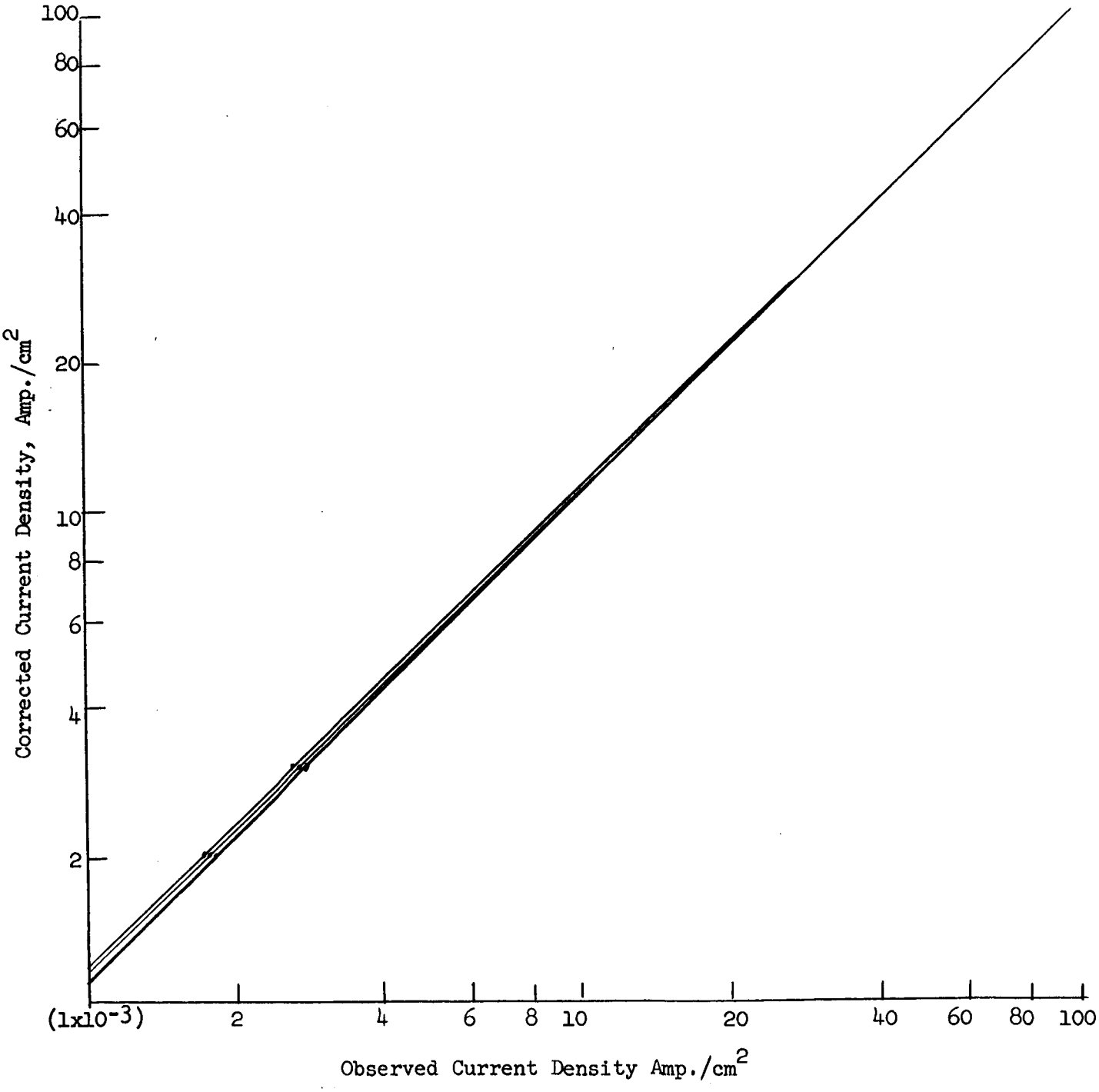


Fig. 66 (Cont'd): Current Density Correction Curve for Plasma Sheath Effect

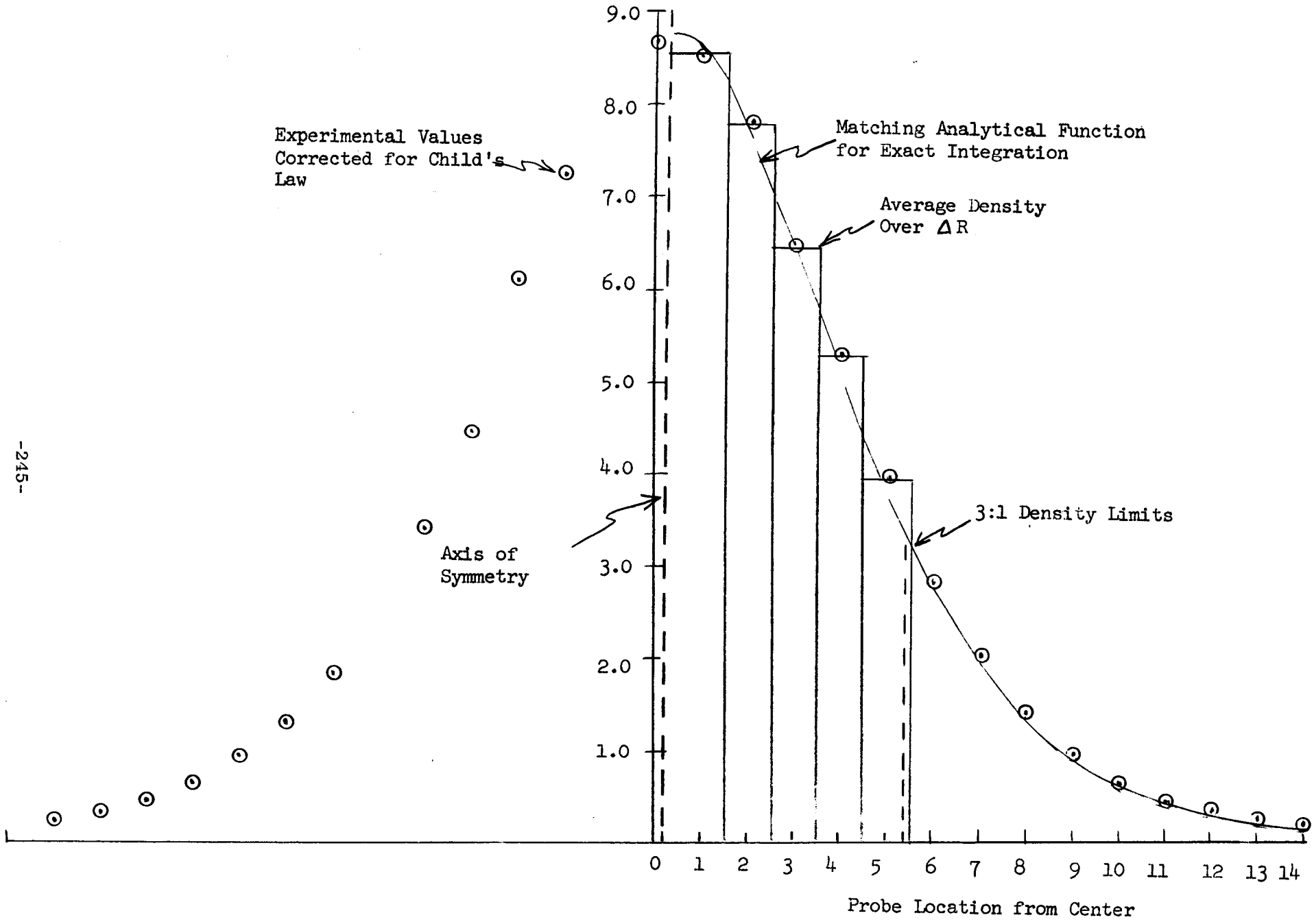


Fig. 67: A Selected Density Pattern and Matching Analytical Function

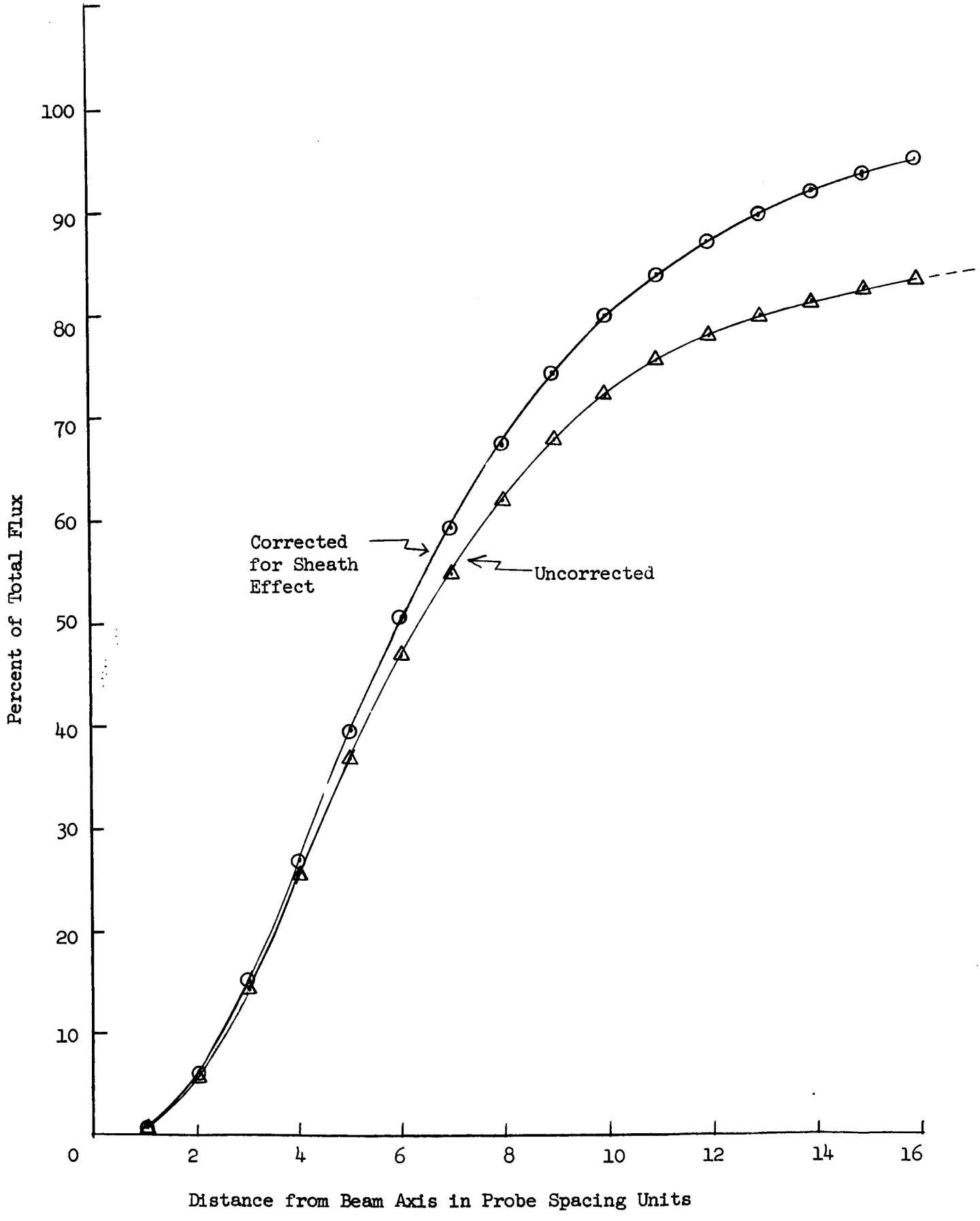


Fig. 68: Percent of Integrated Flow Within Different Radii

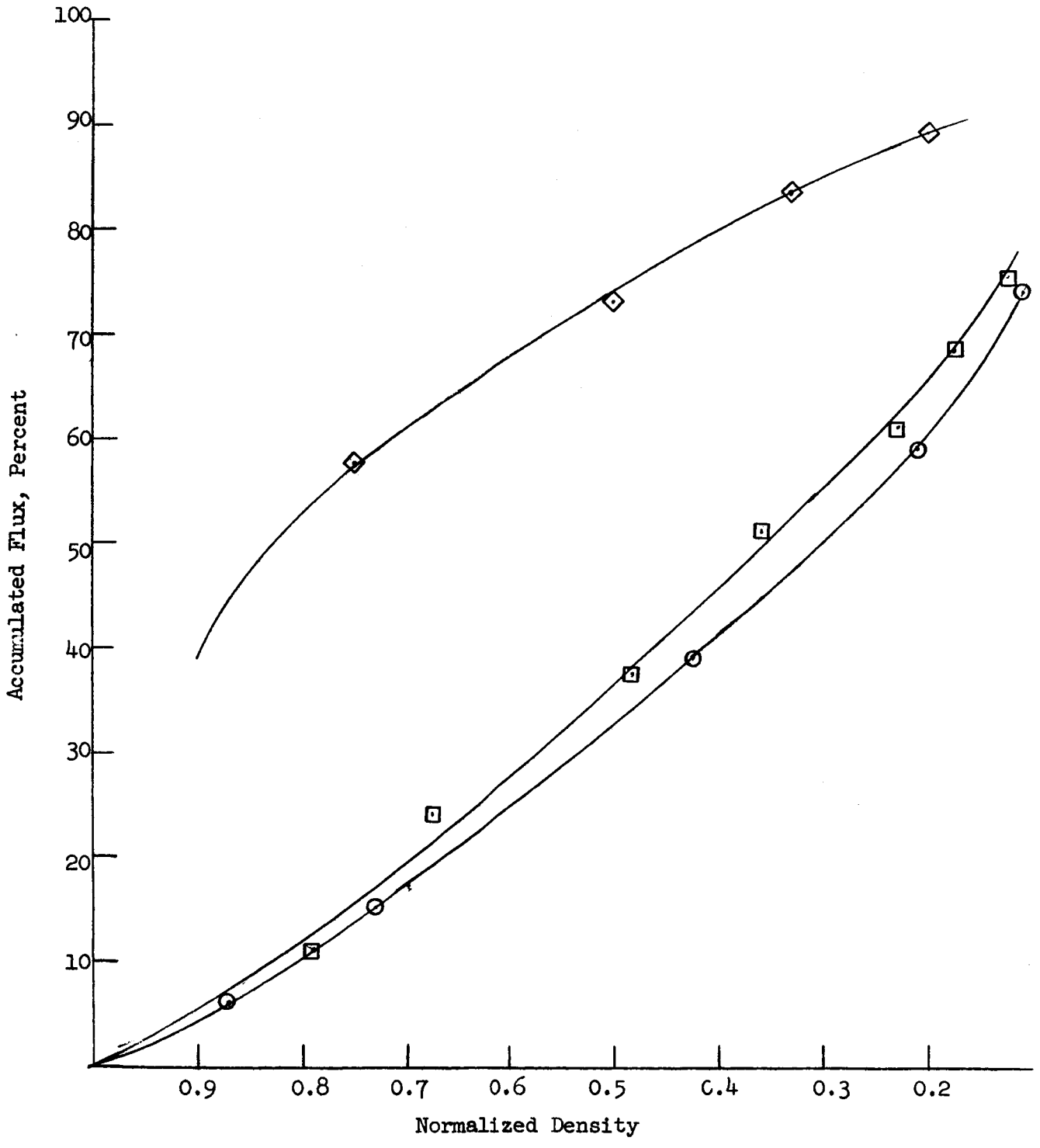


Fig. 69: Evaluation of Aerodynamic Flow Patterns

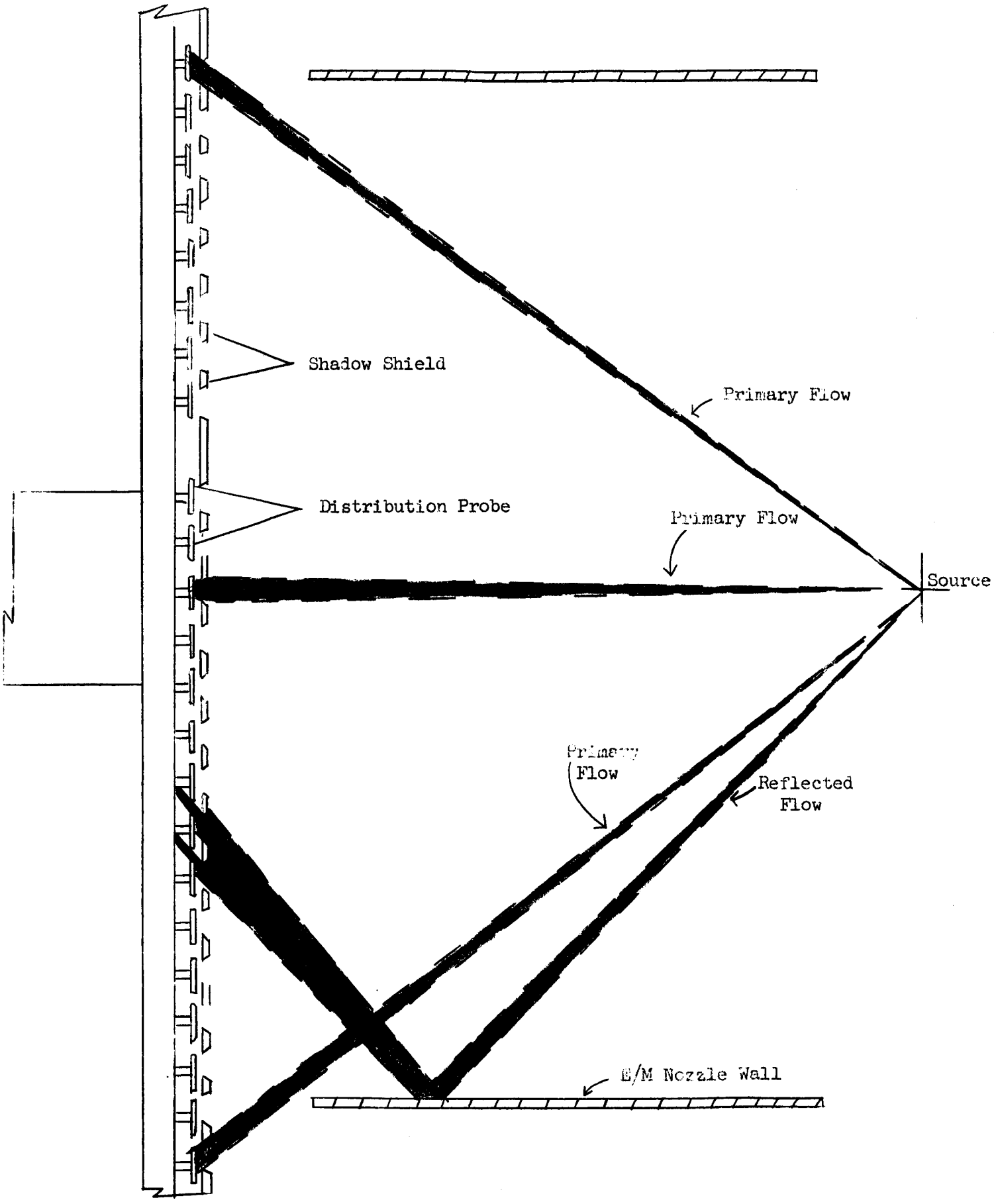


Fig. 70: Shadow Shield and Multiple Ion Probe Design

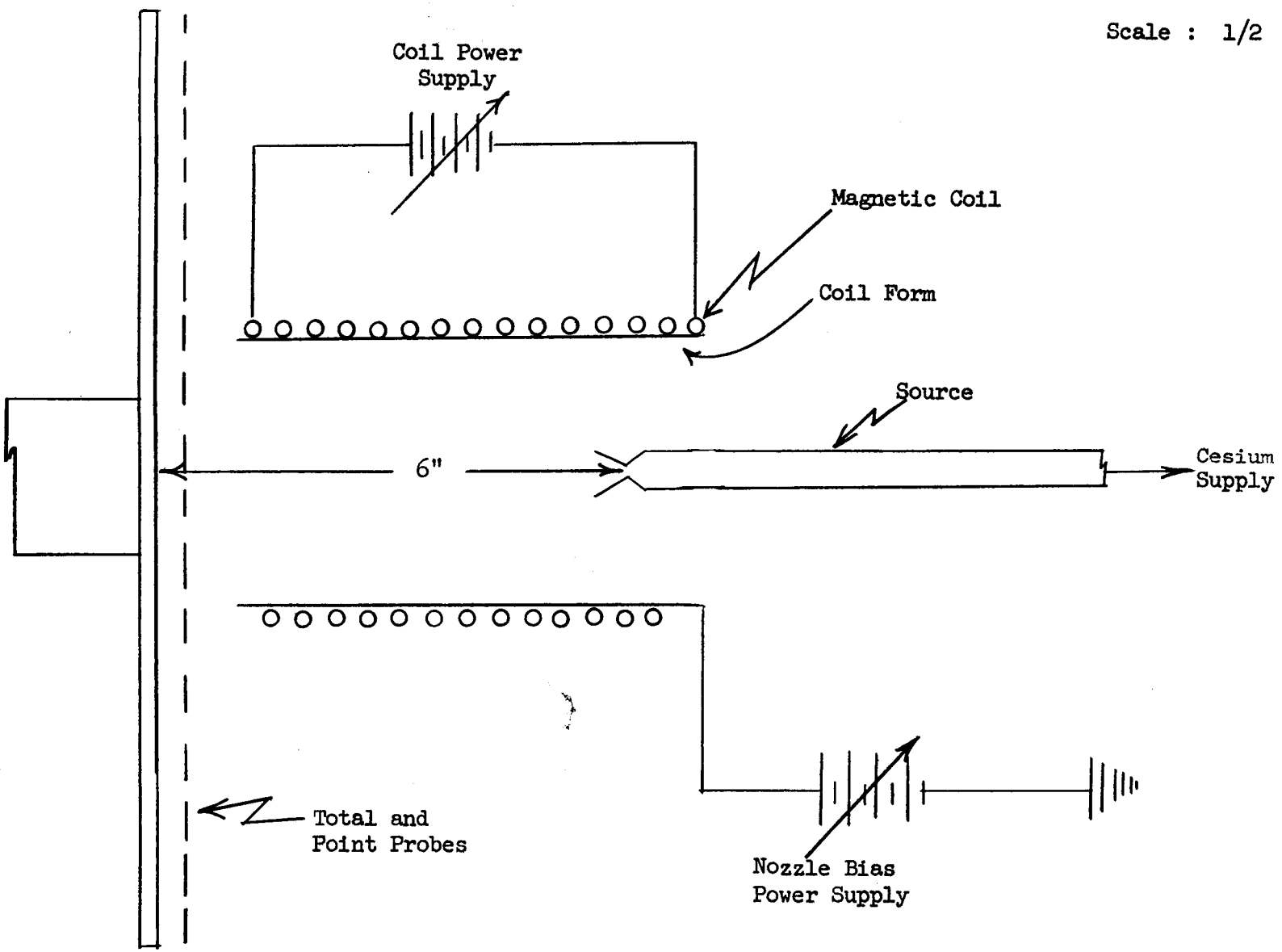


Fig. 71: Small Cylindrical Electromagnetic Nozzle

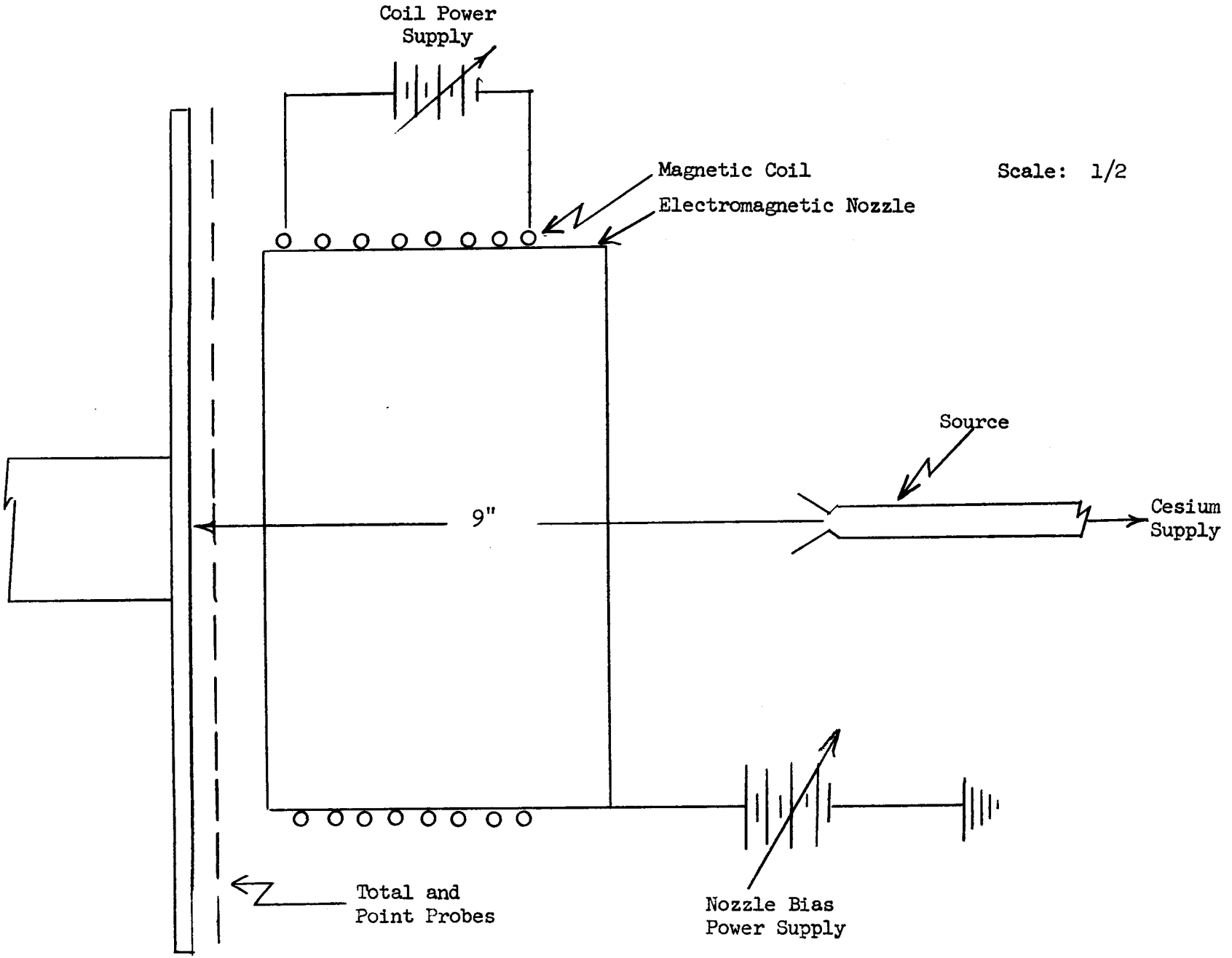


Fig. 72: Large Cylindrical Electromagnetic Nozzle

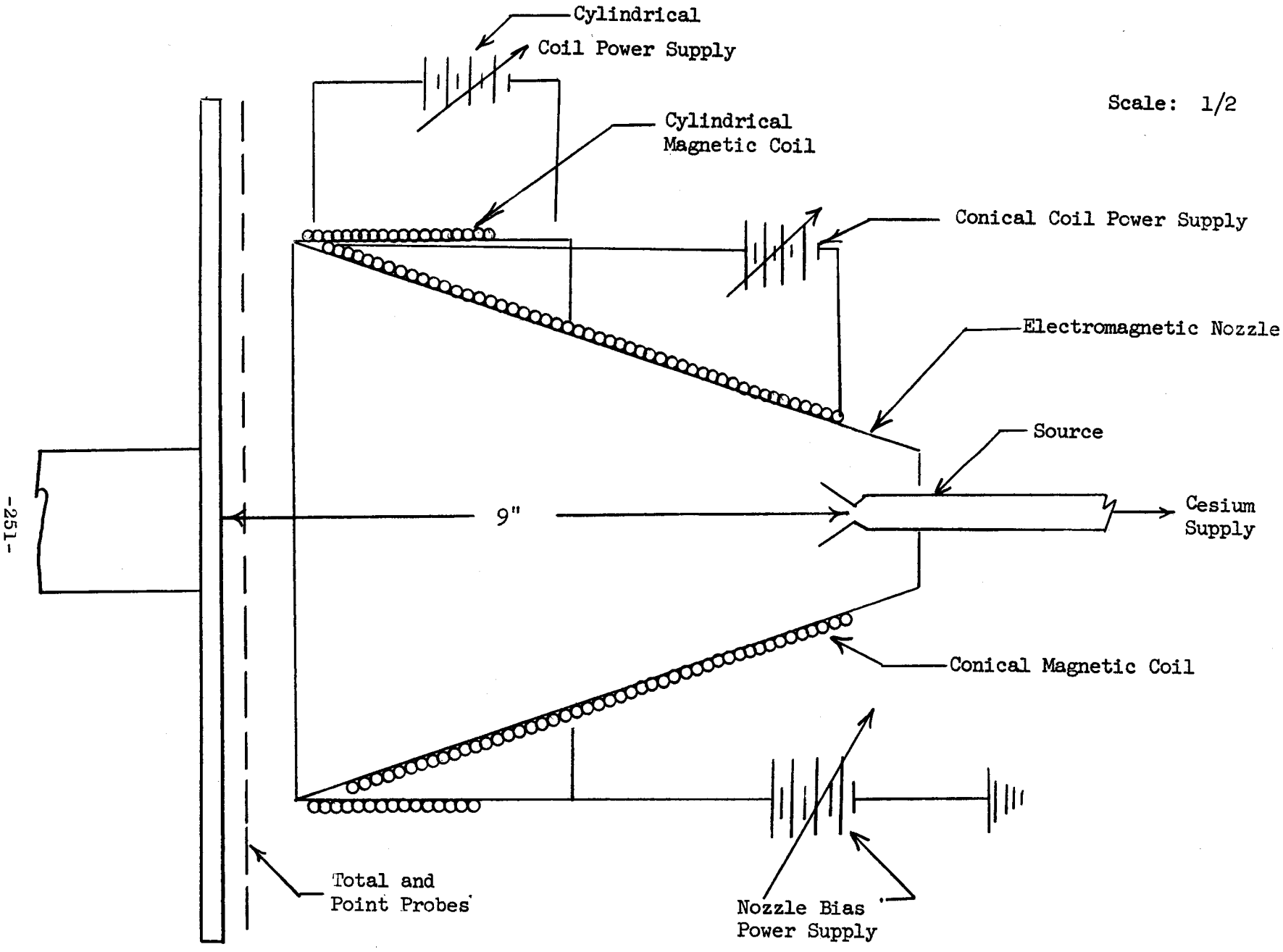


Fig. 73: Conical Electromagnetic Nozzle Design with Auxiliary Cylindrical Coil

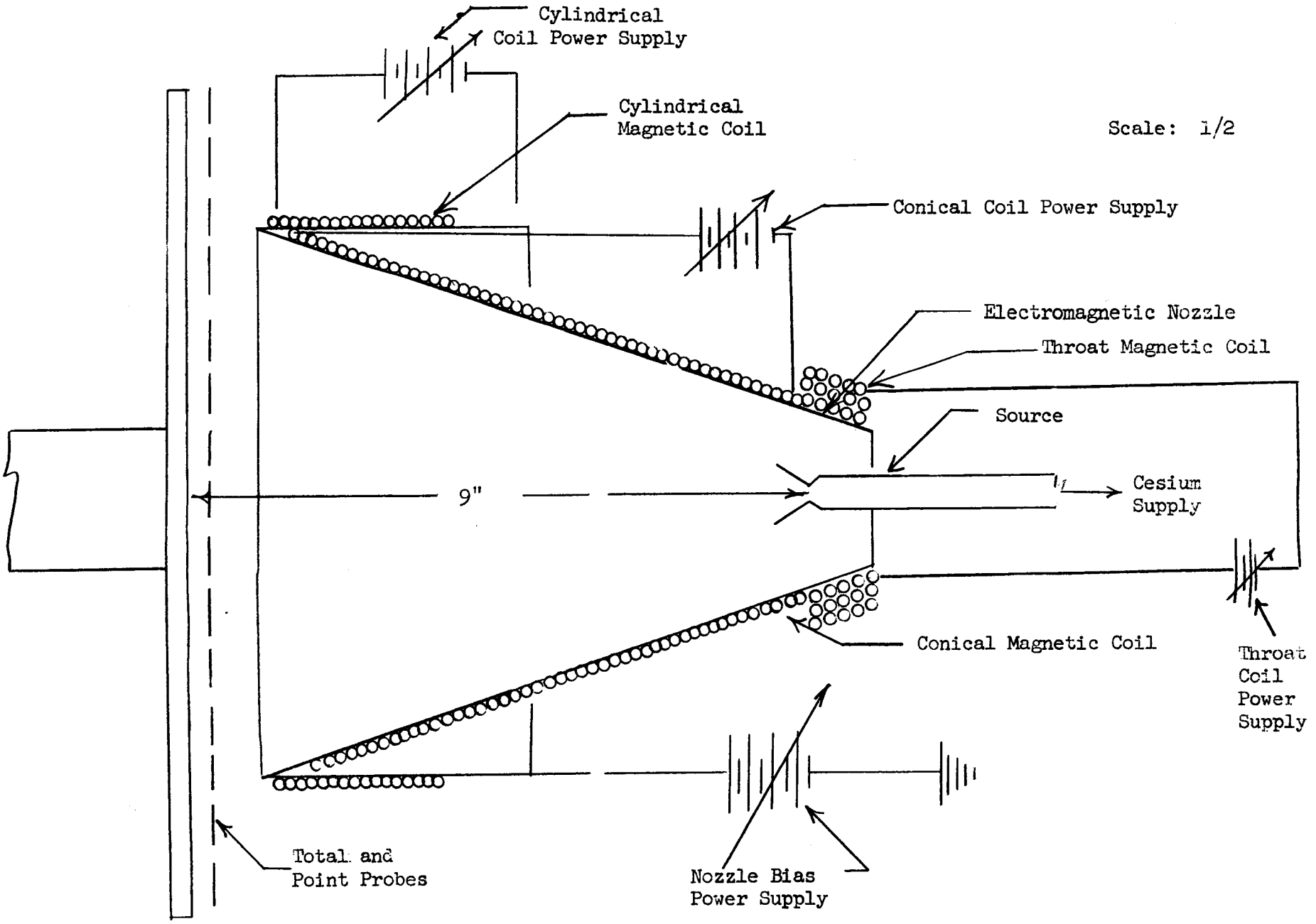


Fig. 74: Conical Electromagnetic Nozzle Design with Auxiliary Cylindrical Coil and Throat Coil

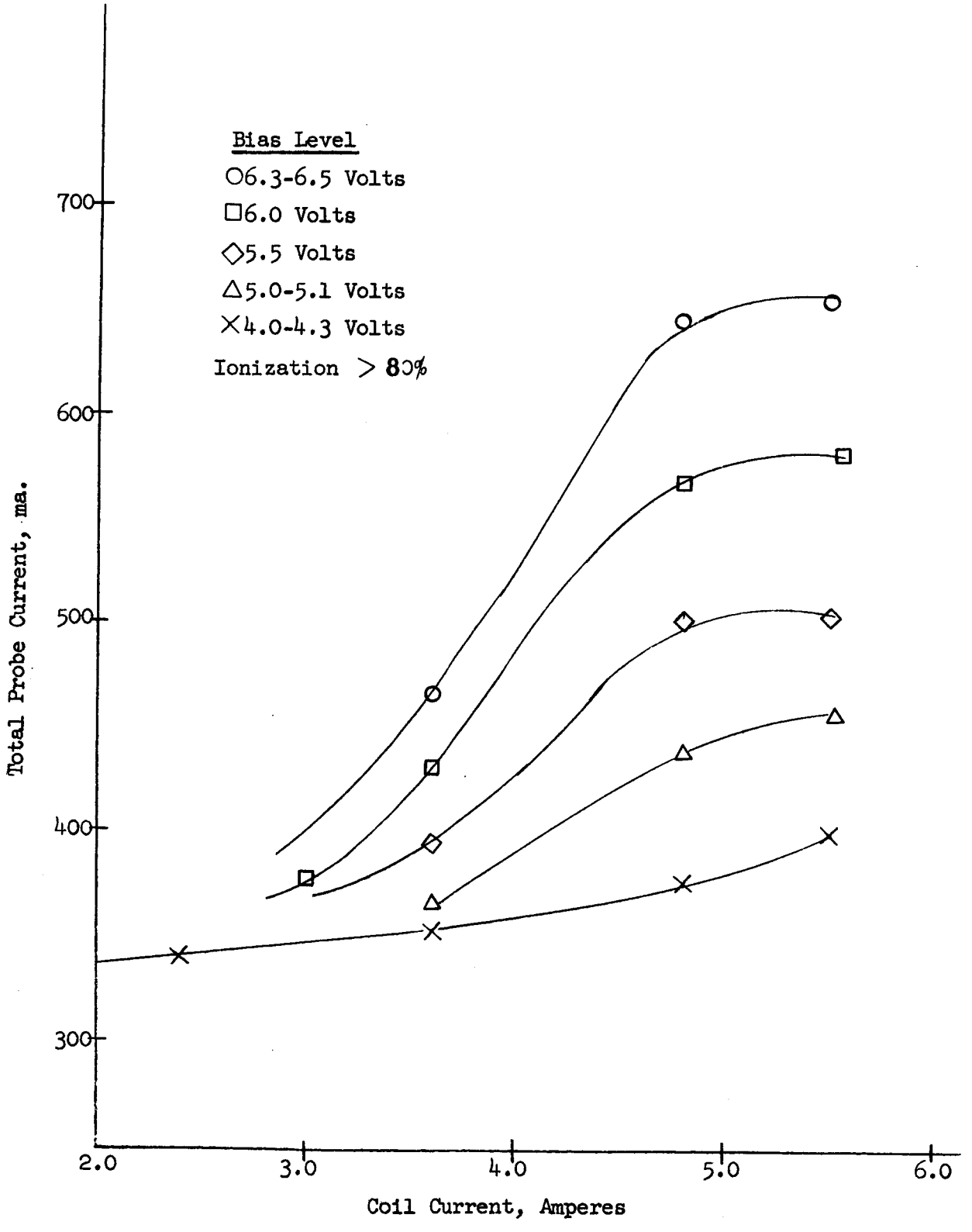


Fig. 75: Plasma Flow Control in a Small Solenoid

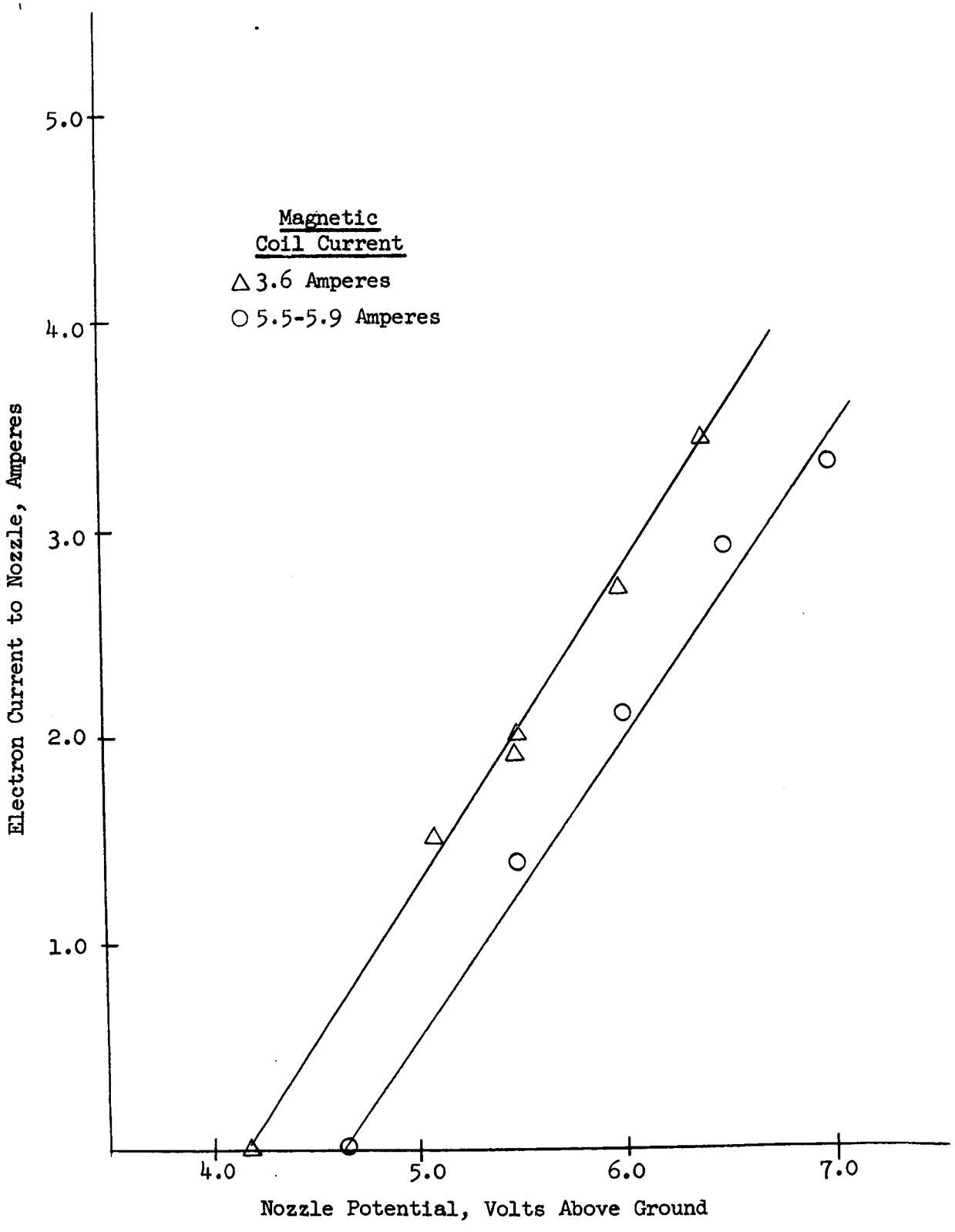


Fig. 76: Radial Electron Current Restriction in a Small Solenoid

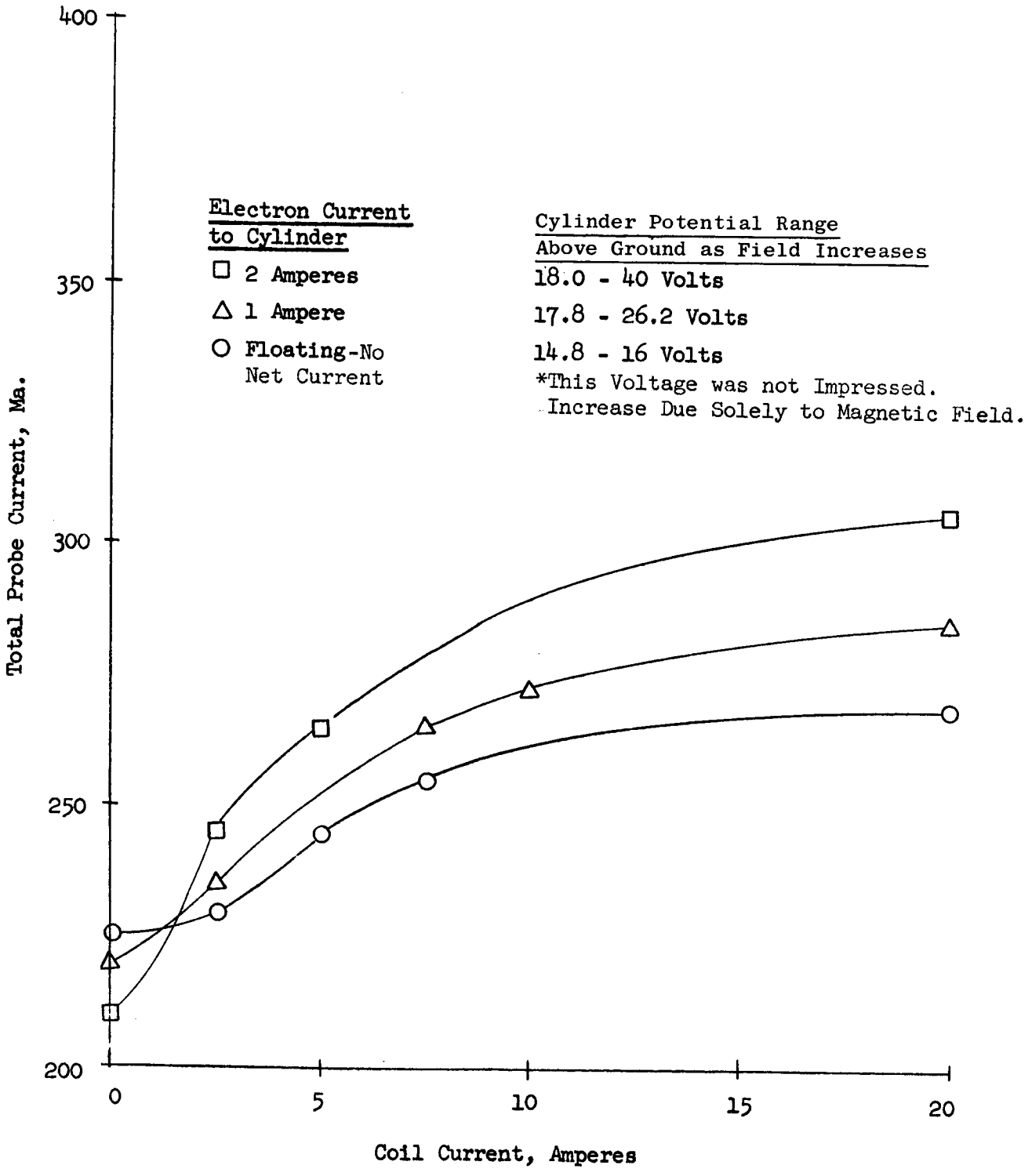


Fig. 77: Plasma Flow Control in an 8" Diameter Solenoid

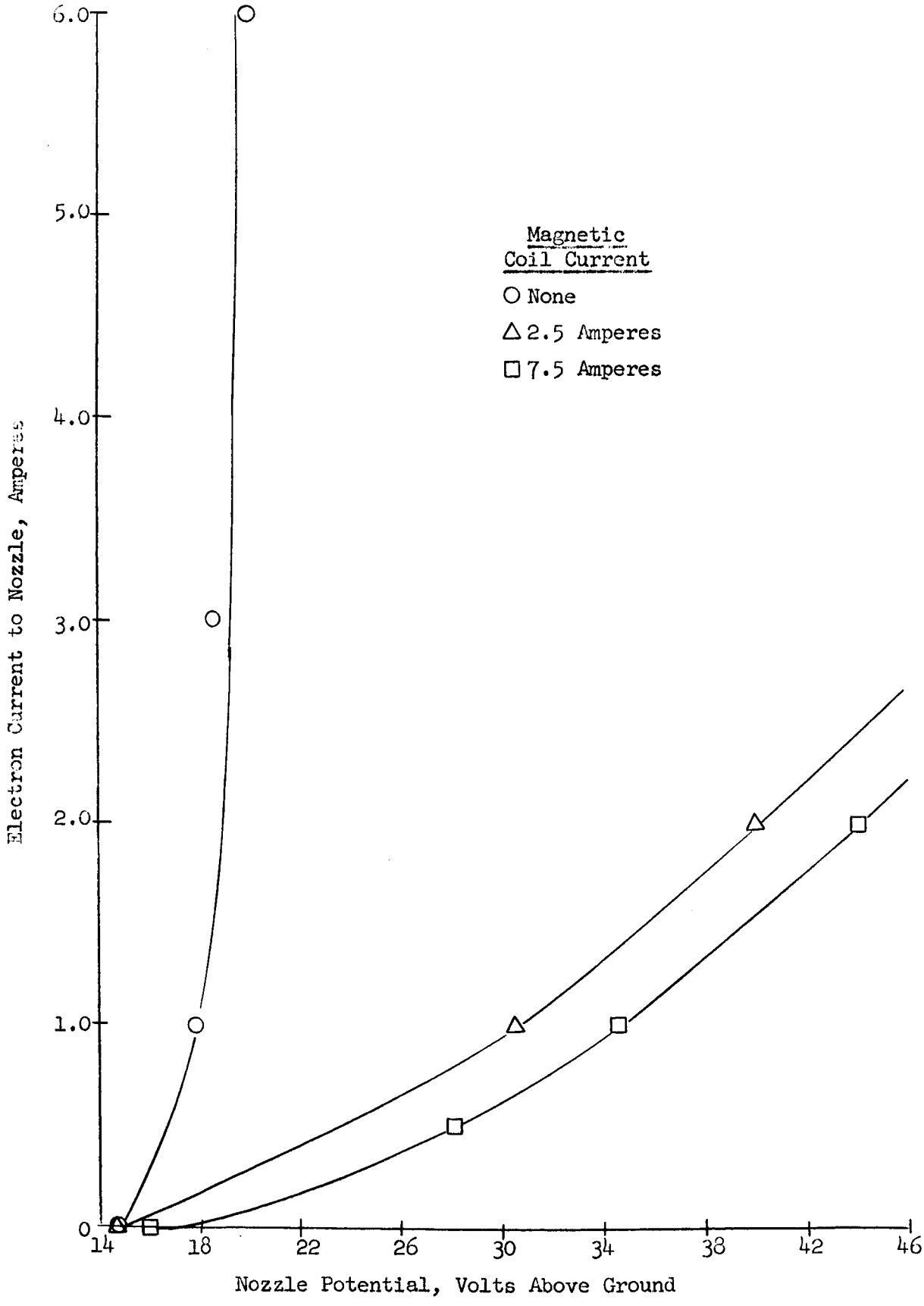


Fig. 78: Radial Electron Current Restriction in an 8" Diameter Solenoid

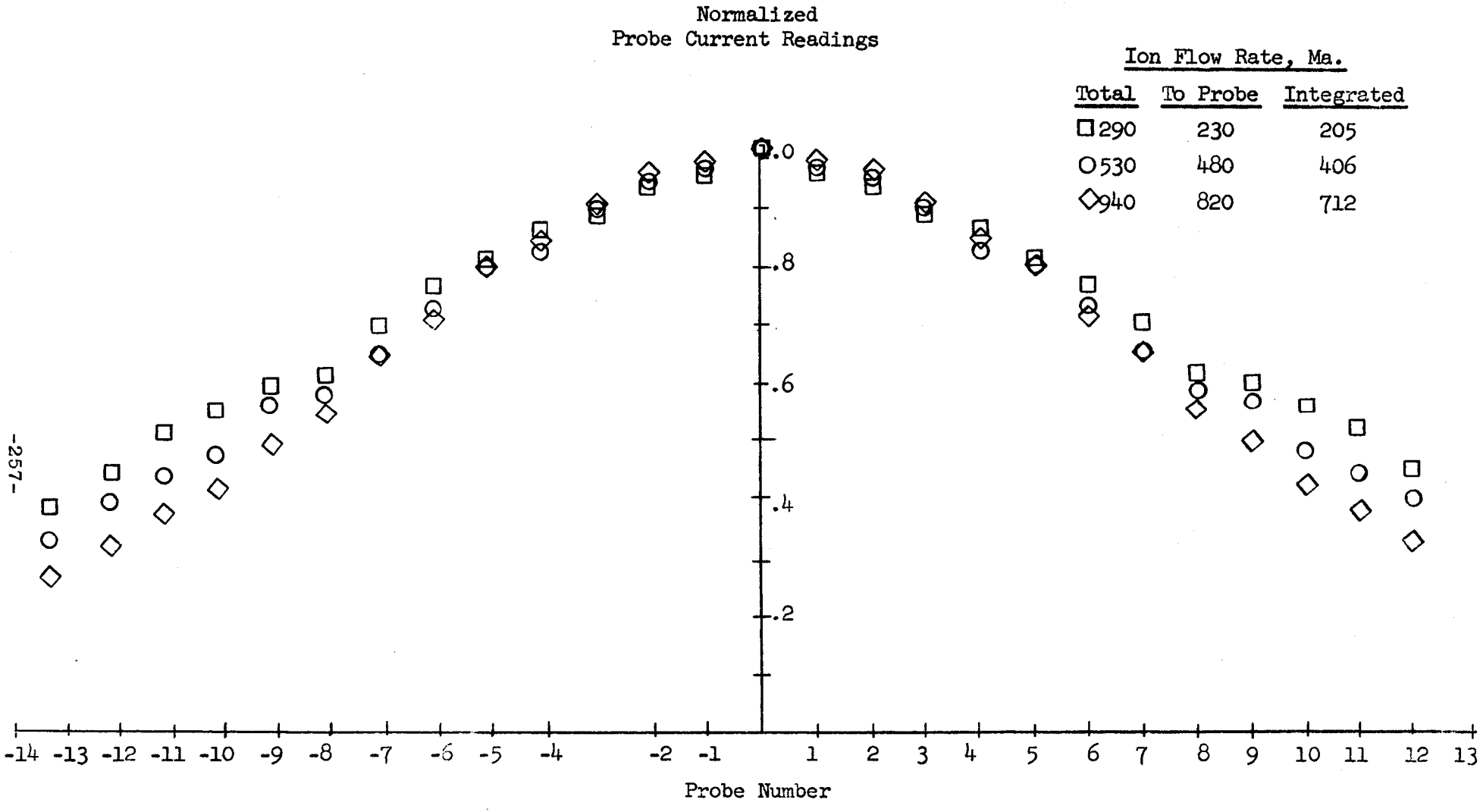


Fig. 79: Aerodynamic Density Pattern for Source X

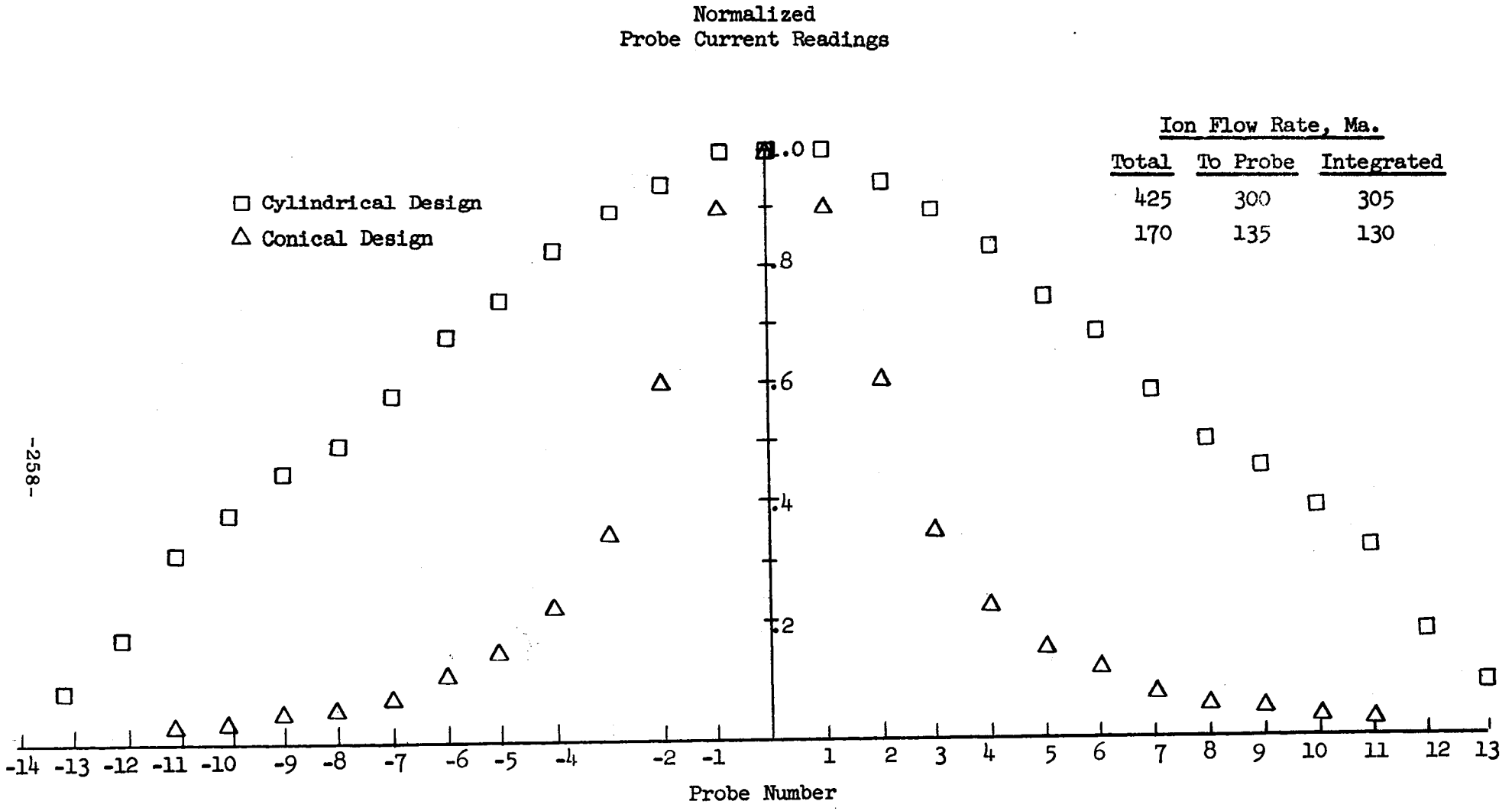


Fig. 80: Density Patterns of Simple Electromagnetic Devices

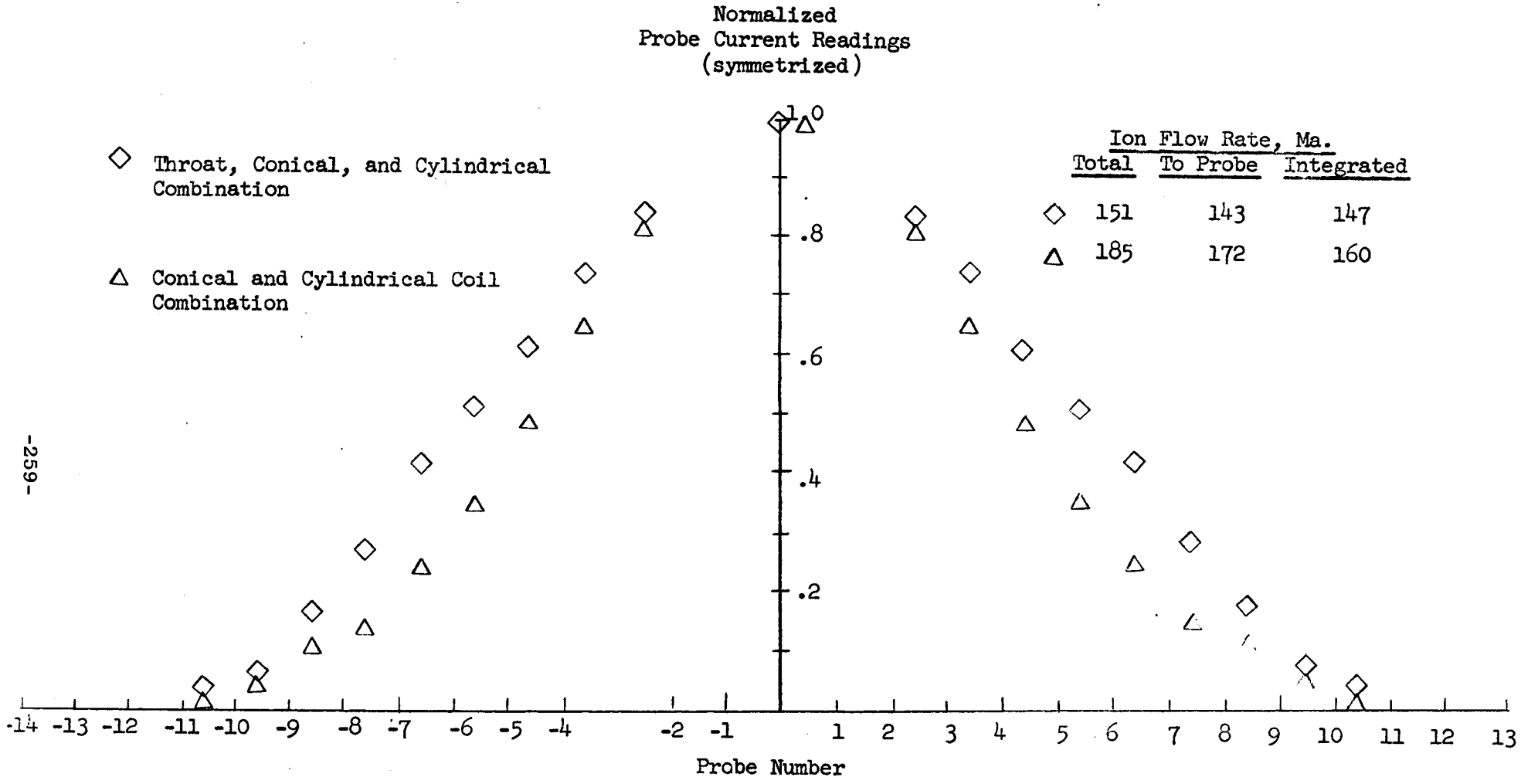


Fig. 81: Density Patterns for Electromagnetic Nozzle Configurations

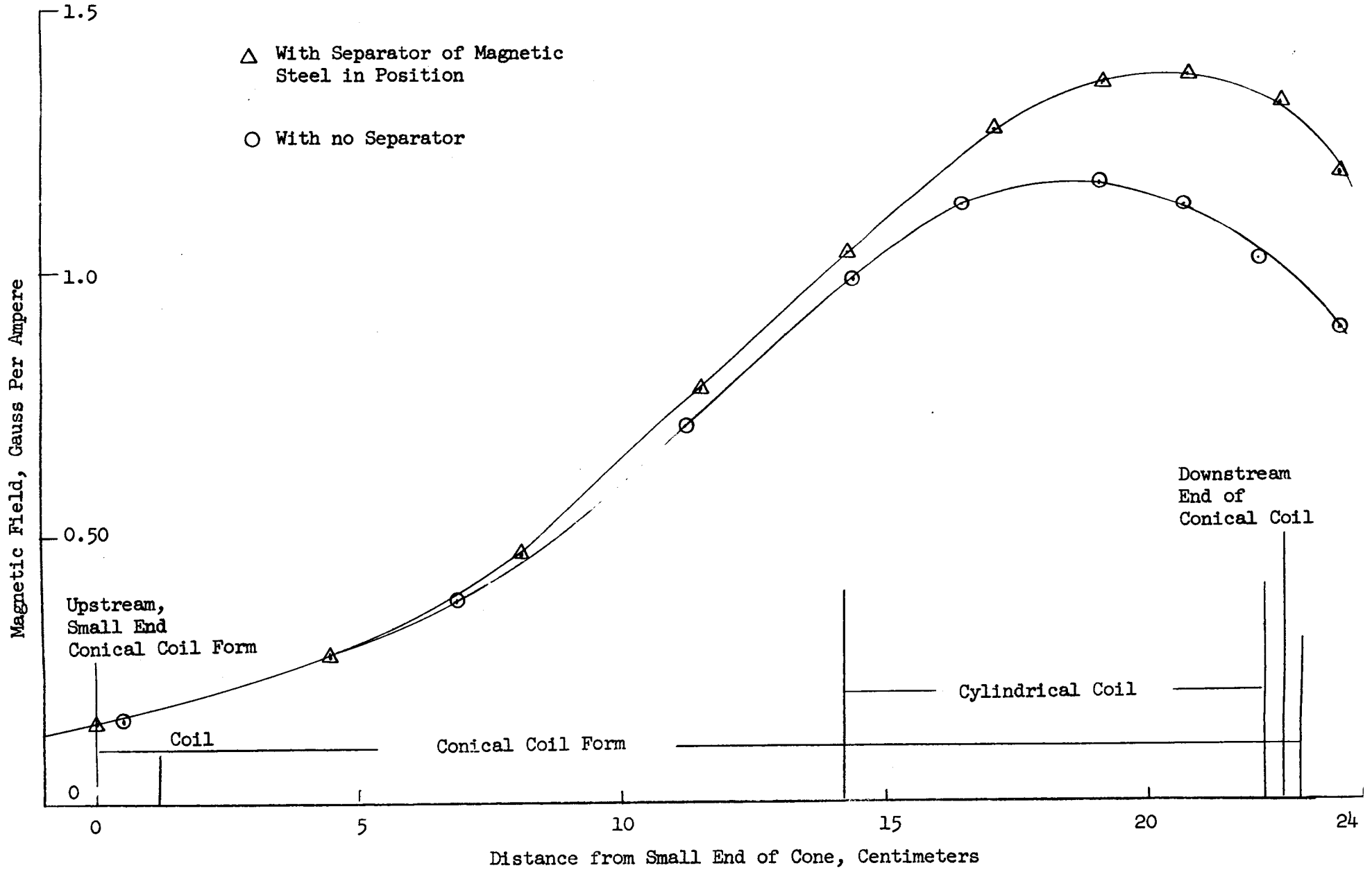


Fig. 82: Axial Magnetic Field Along Axis of Coaxial Magnet Coils with only Cylindrical Coil Energized

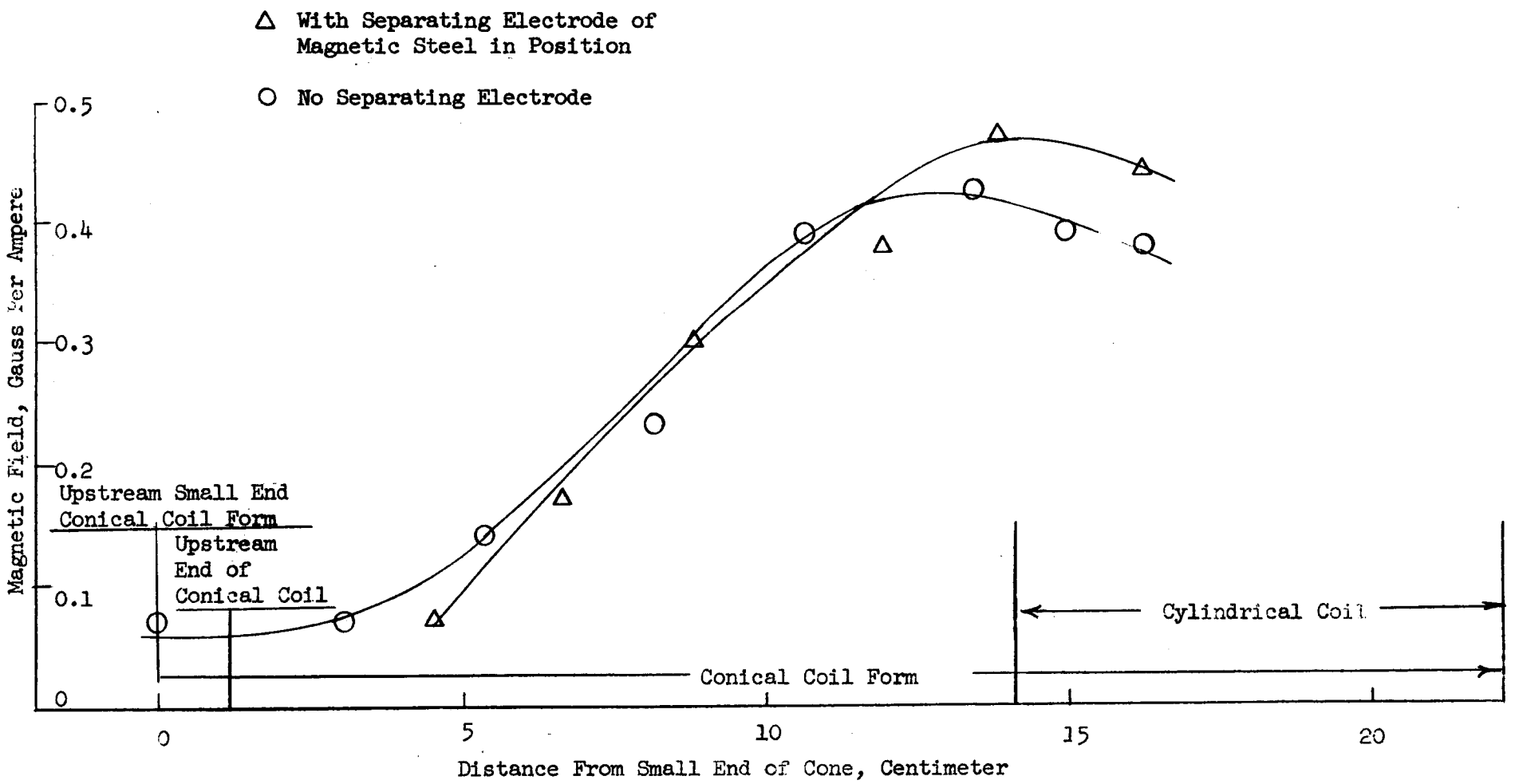


Fig. 83: Radial Magnetic Field Along Axis of Coaxial Magnet Coils with Only Cylindrical Coil Energized.

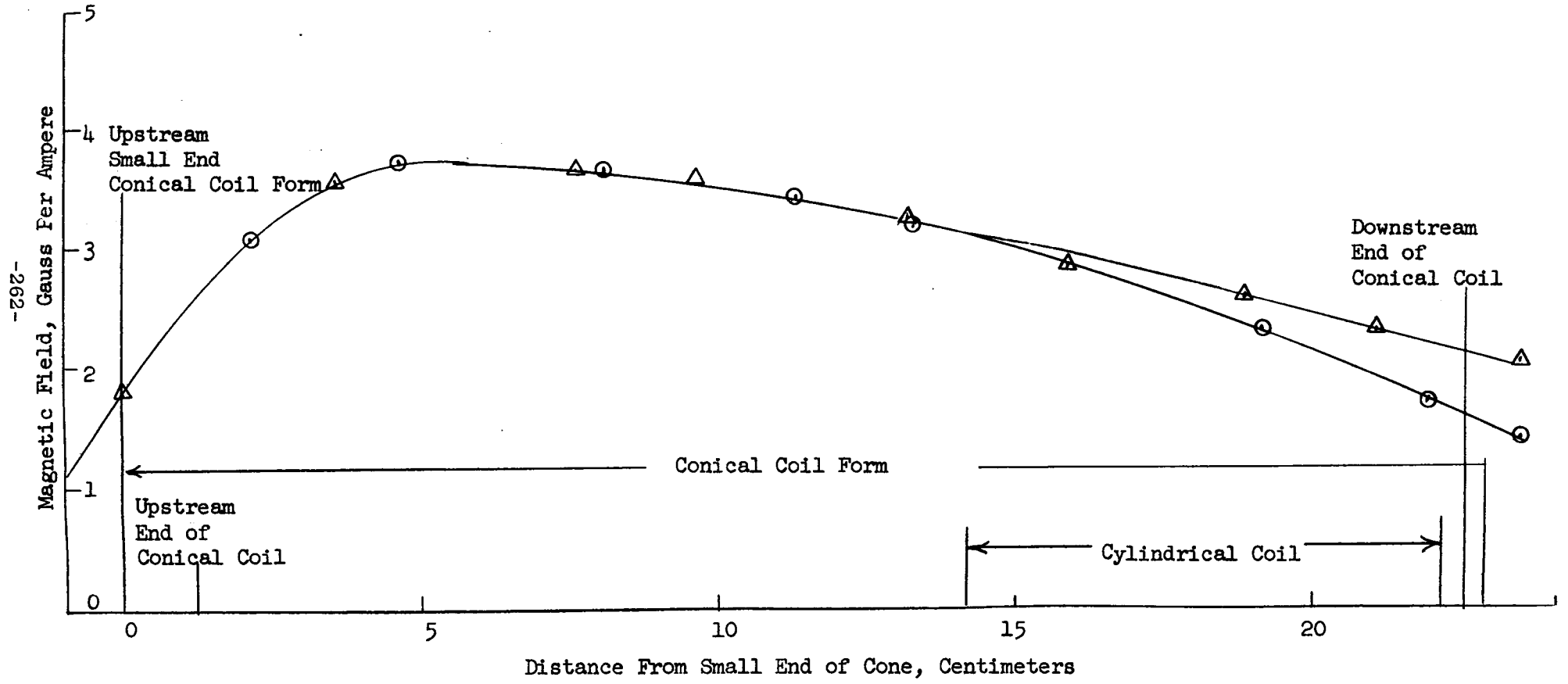


Fig. 84: Axial Magnetic Field Along Axis of Coaxial Magnet Coils with only Conical Coil Energized

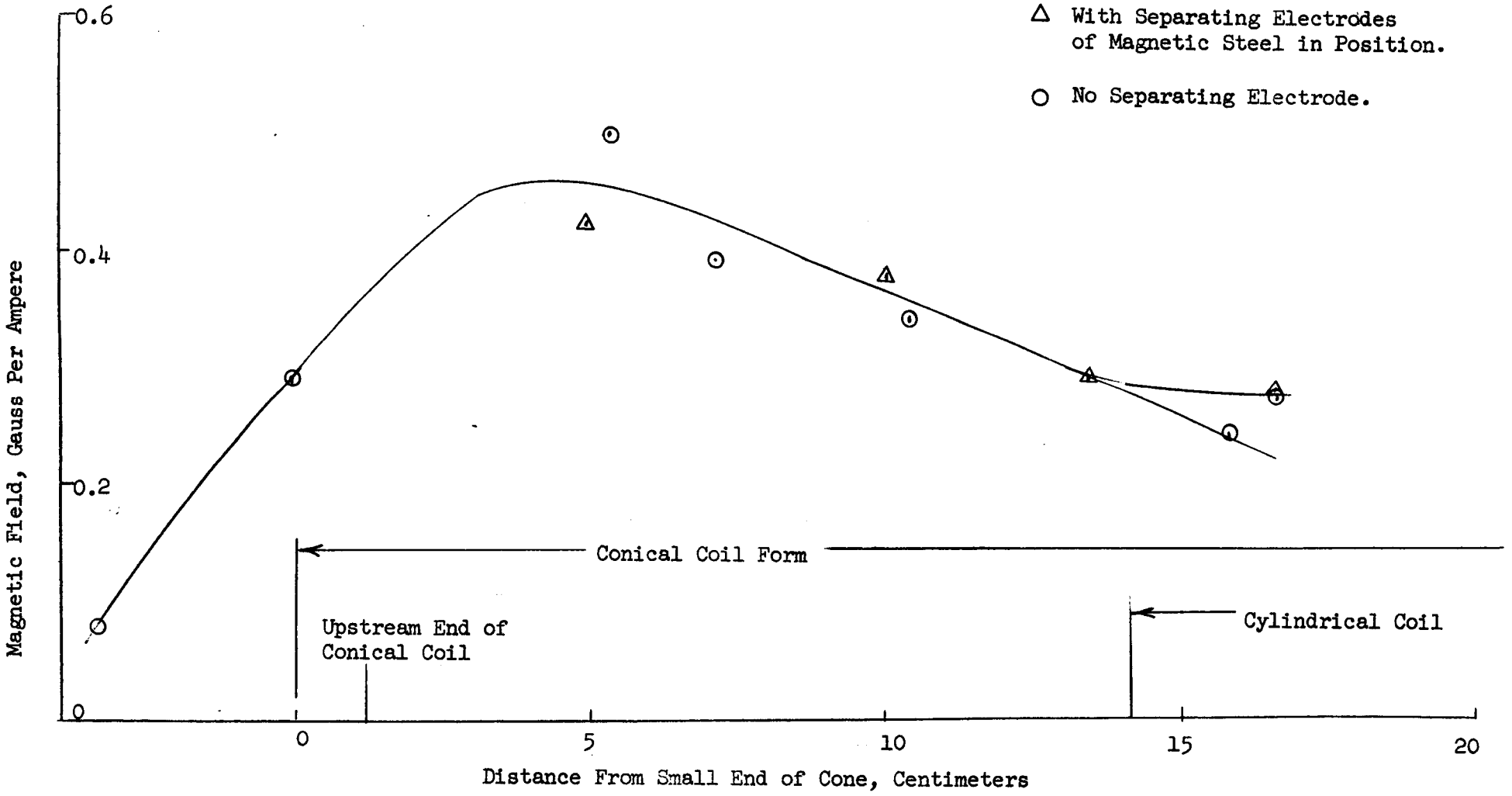


Fig. 85: Radial Magnetic Field Along Axis of Coaxial Magnet Coils with only Conical Coil Energized

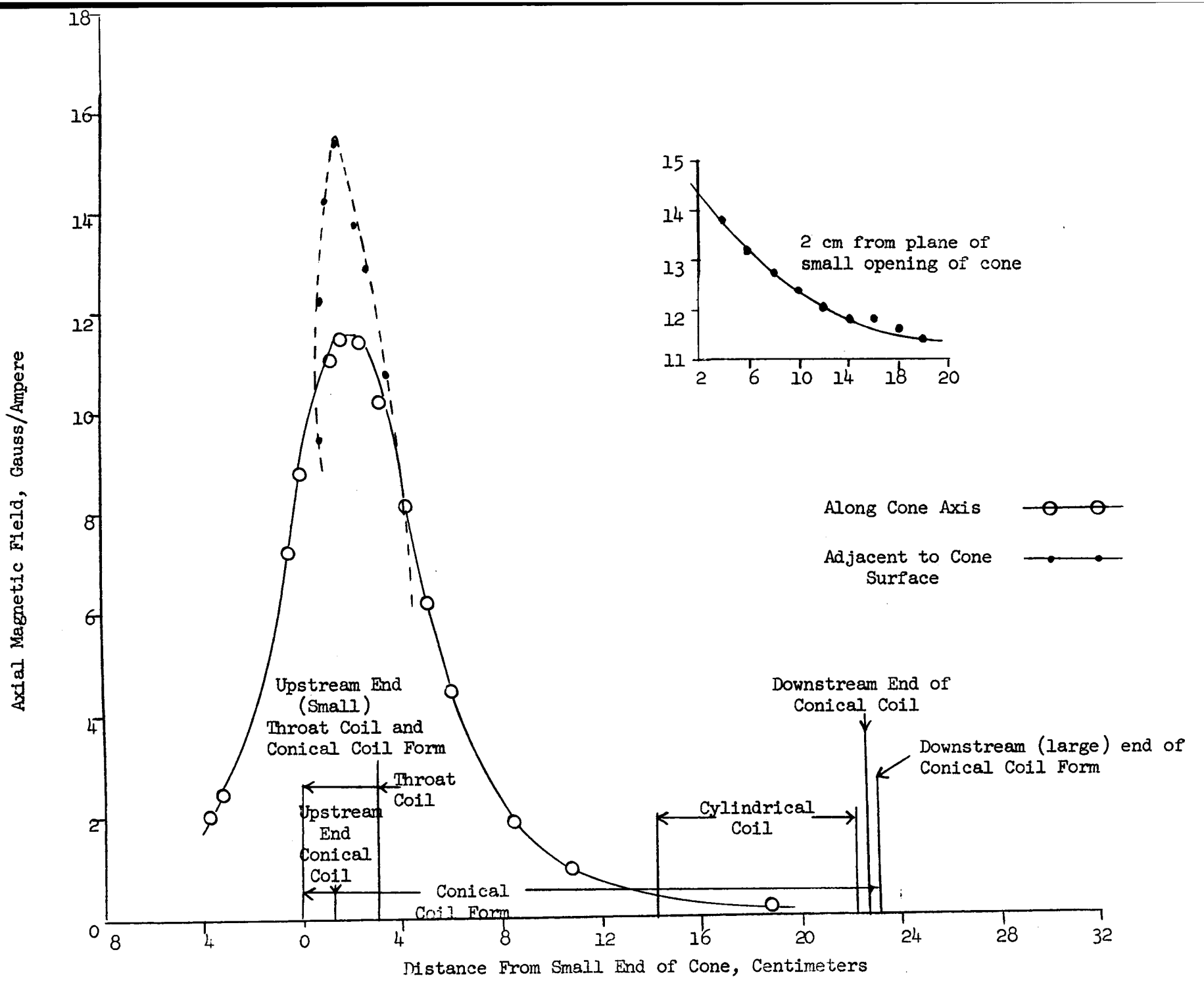


Fig. 86: Magnetic Field Characteristics of Wire Wound Throat Coil of Fig. 74.

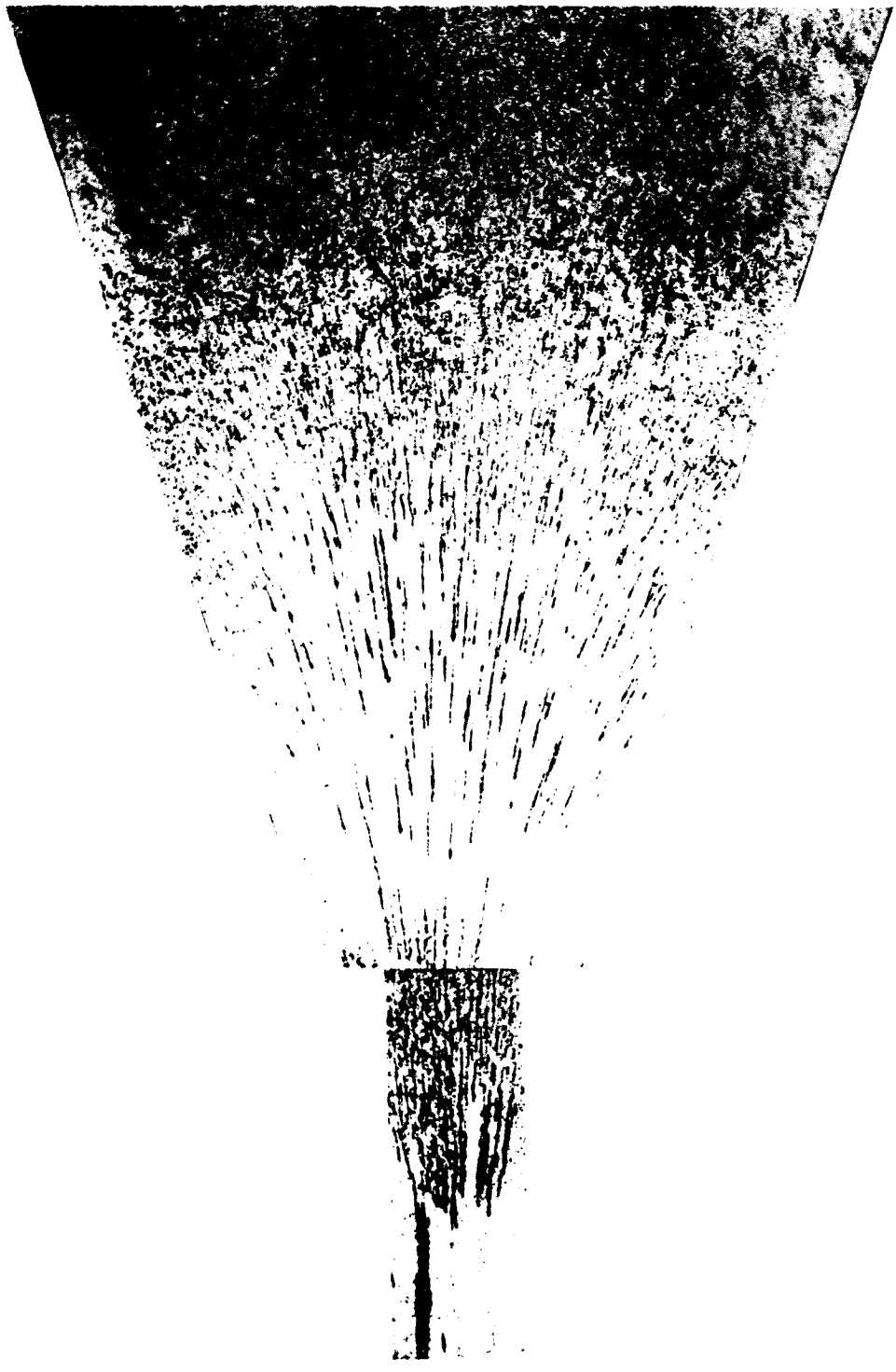


Fig. 88: Magnetic Field of the Throat Coil of Fig. 74

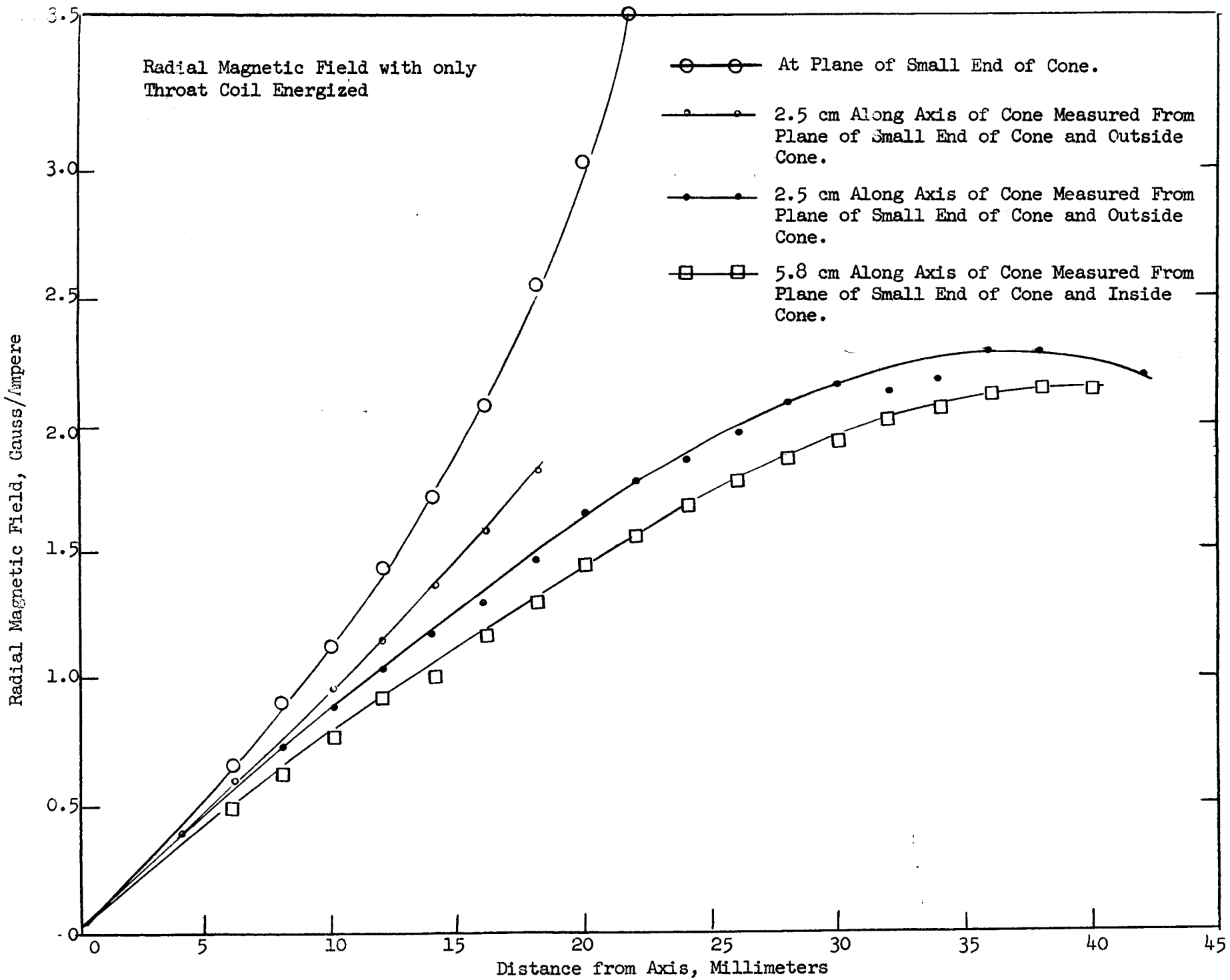


Fig. 87: Magnetic Field Characteristics of Wire Wound Throat Coil of Fig. 74.



Fig. 89: Magnetic Field of Conical Coil of Figs. 73 and 74



Fig. 90: Magnetic Field of the Downstream Solenoid of Figs. 73 and 74.

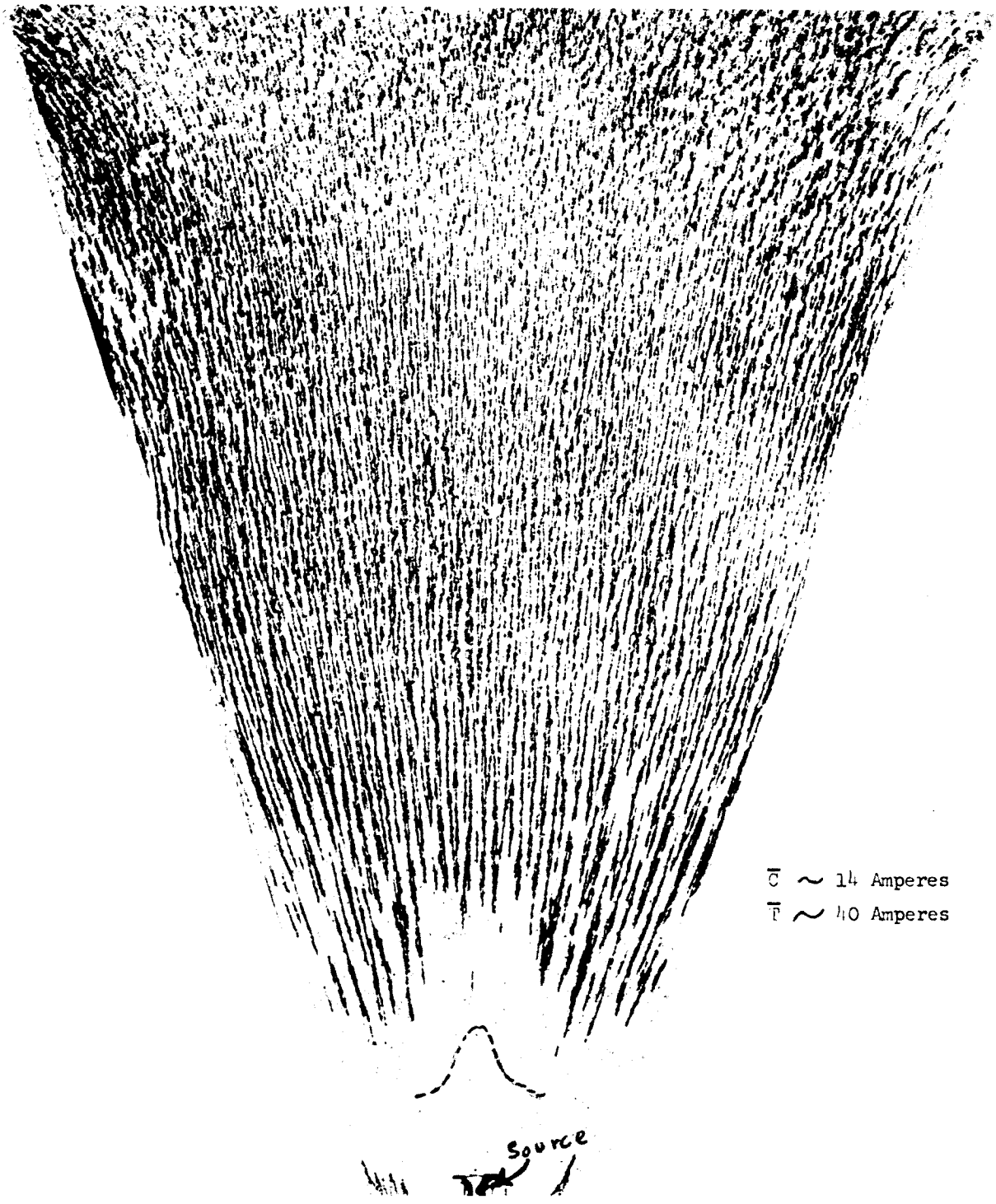


Fig. 91: Combined Magnetic Field of the Throat and Conical Windings

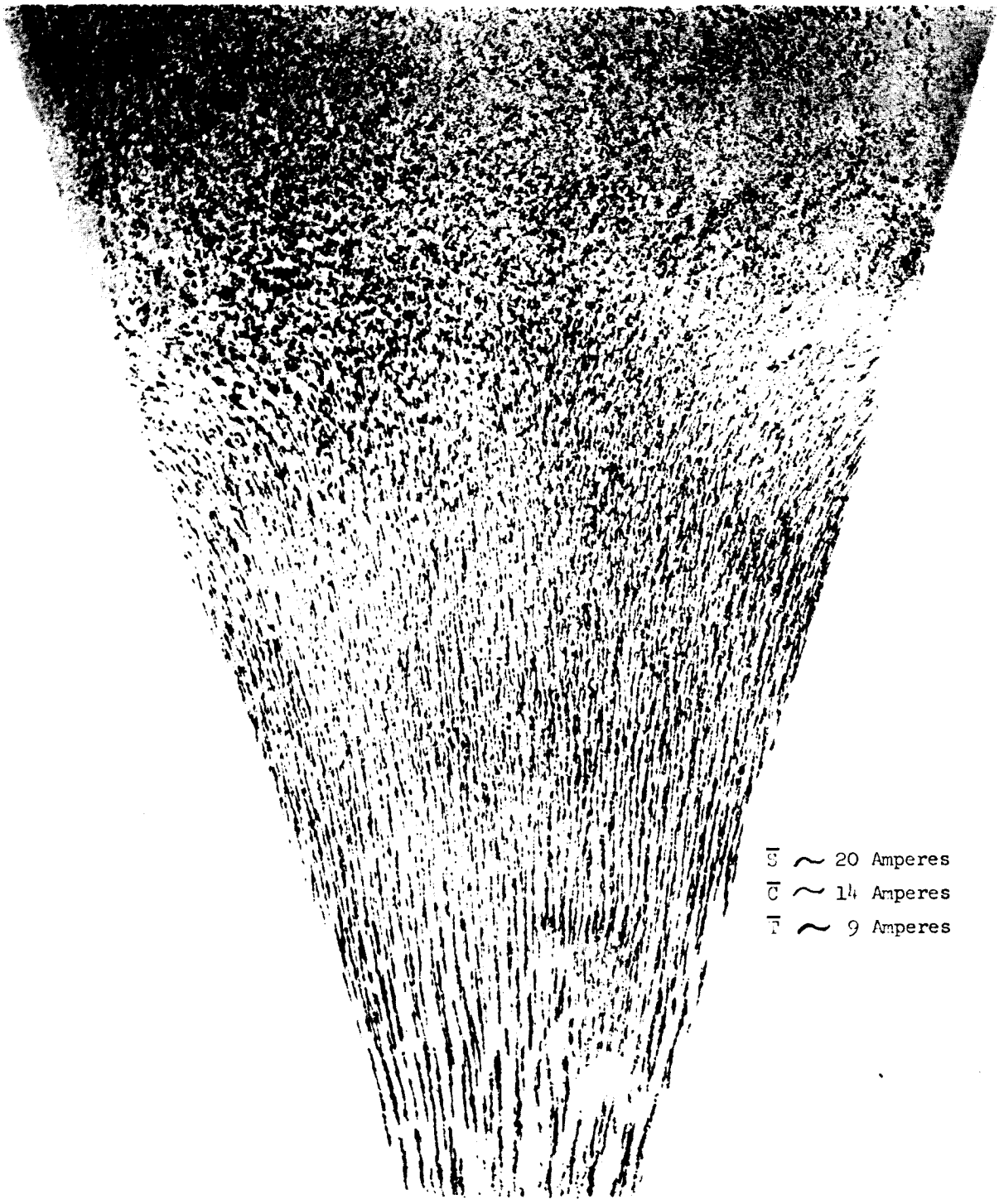


Fig. 92: Combined Magnetic Field of Throat, Conical, and Solenoid Windings

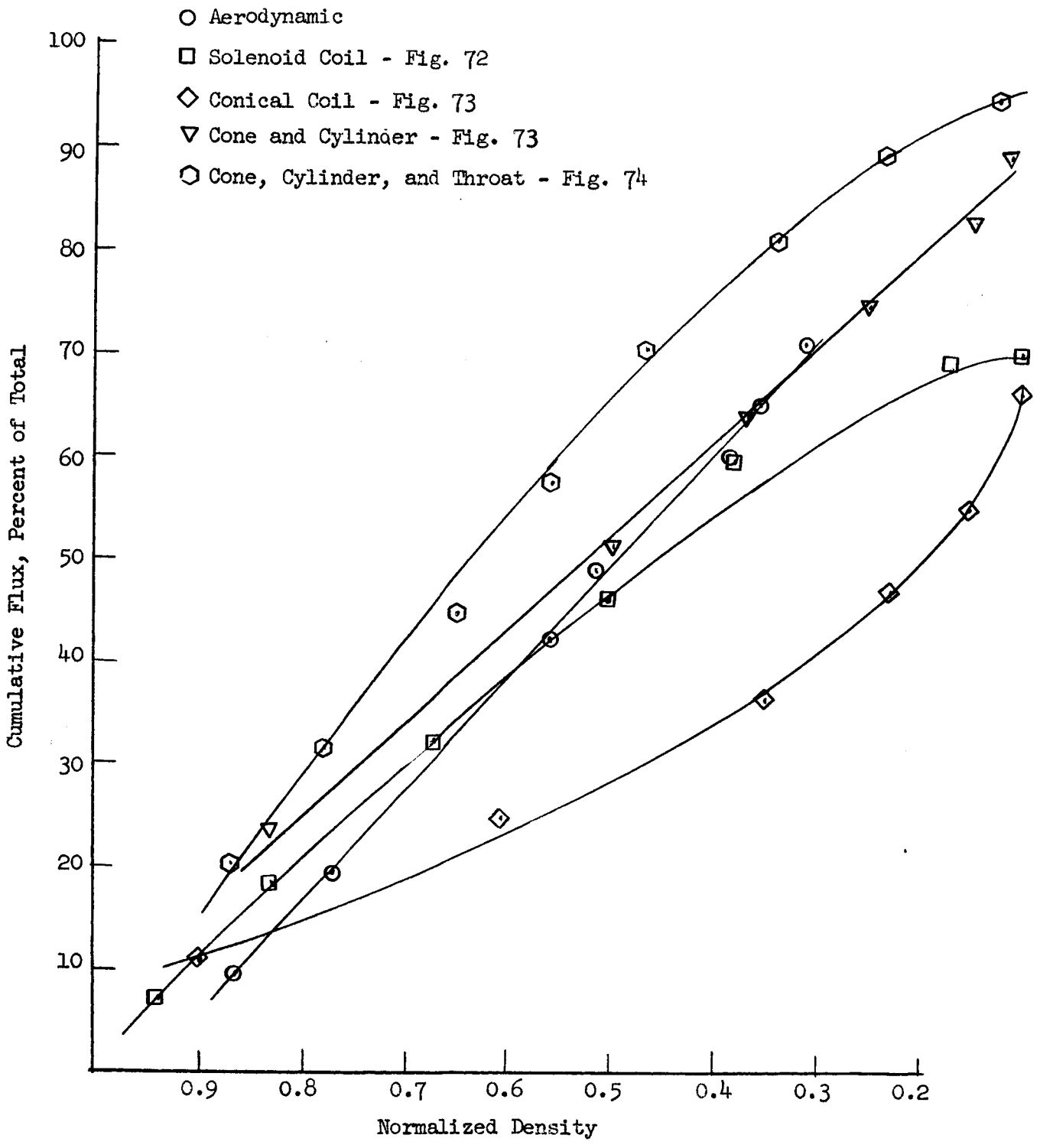


Fig. 93: Evaluation of Electromagnetic Steering

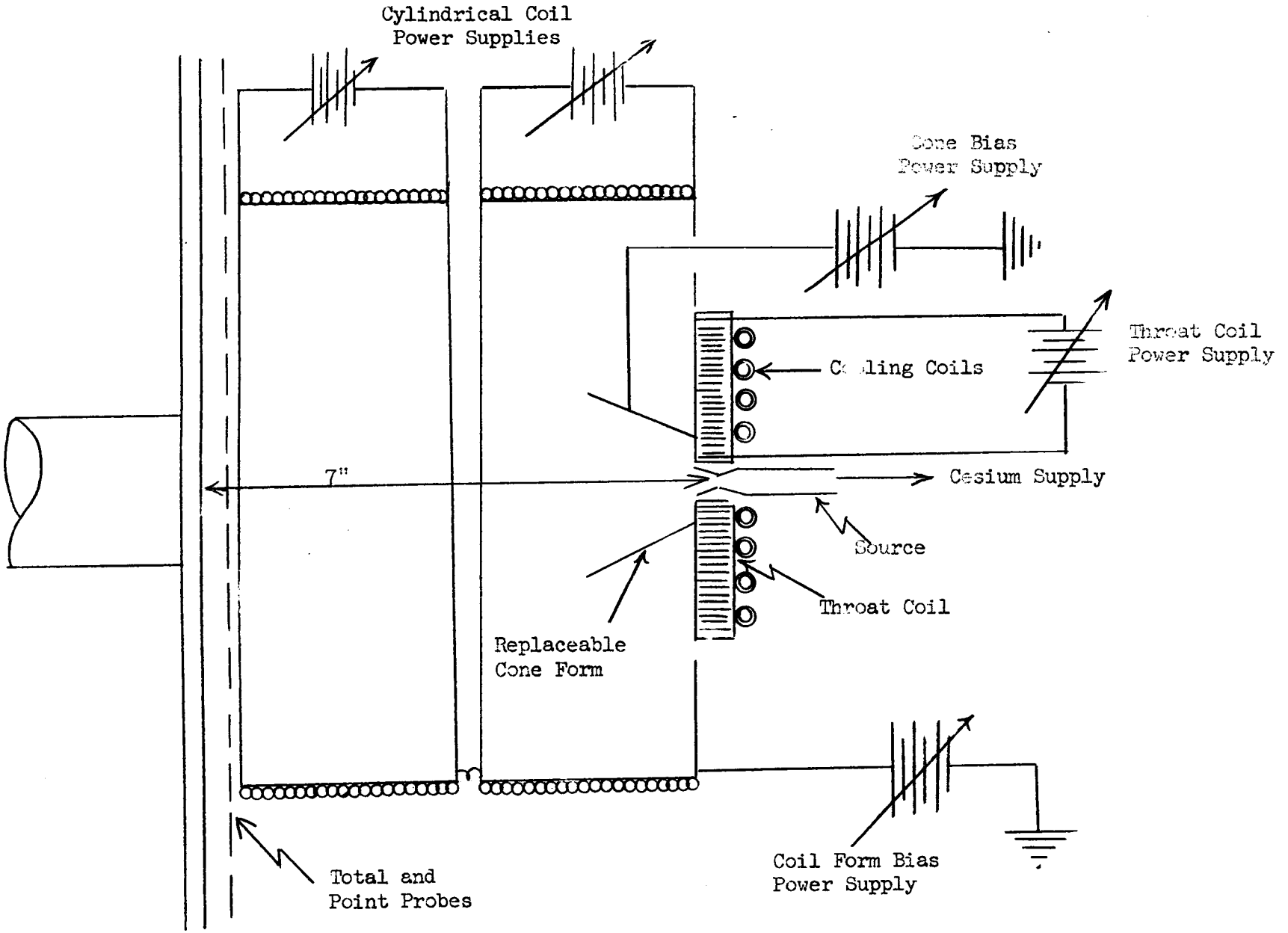


Fig. 94: Electromagnetic Nozzle Design Modification

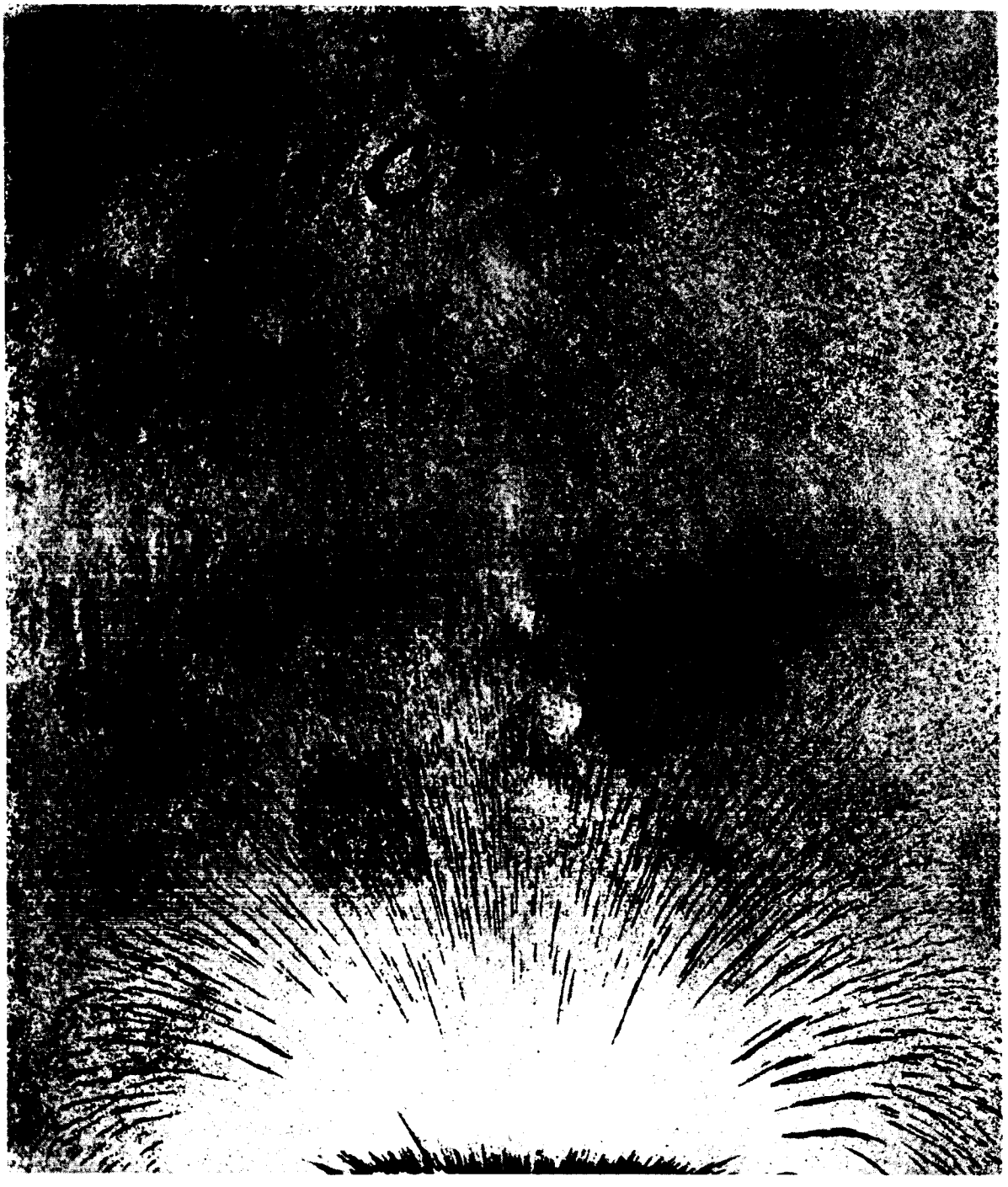


Fig. 95: Magnetic Field of the Throat Coil of Fig. 94

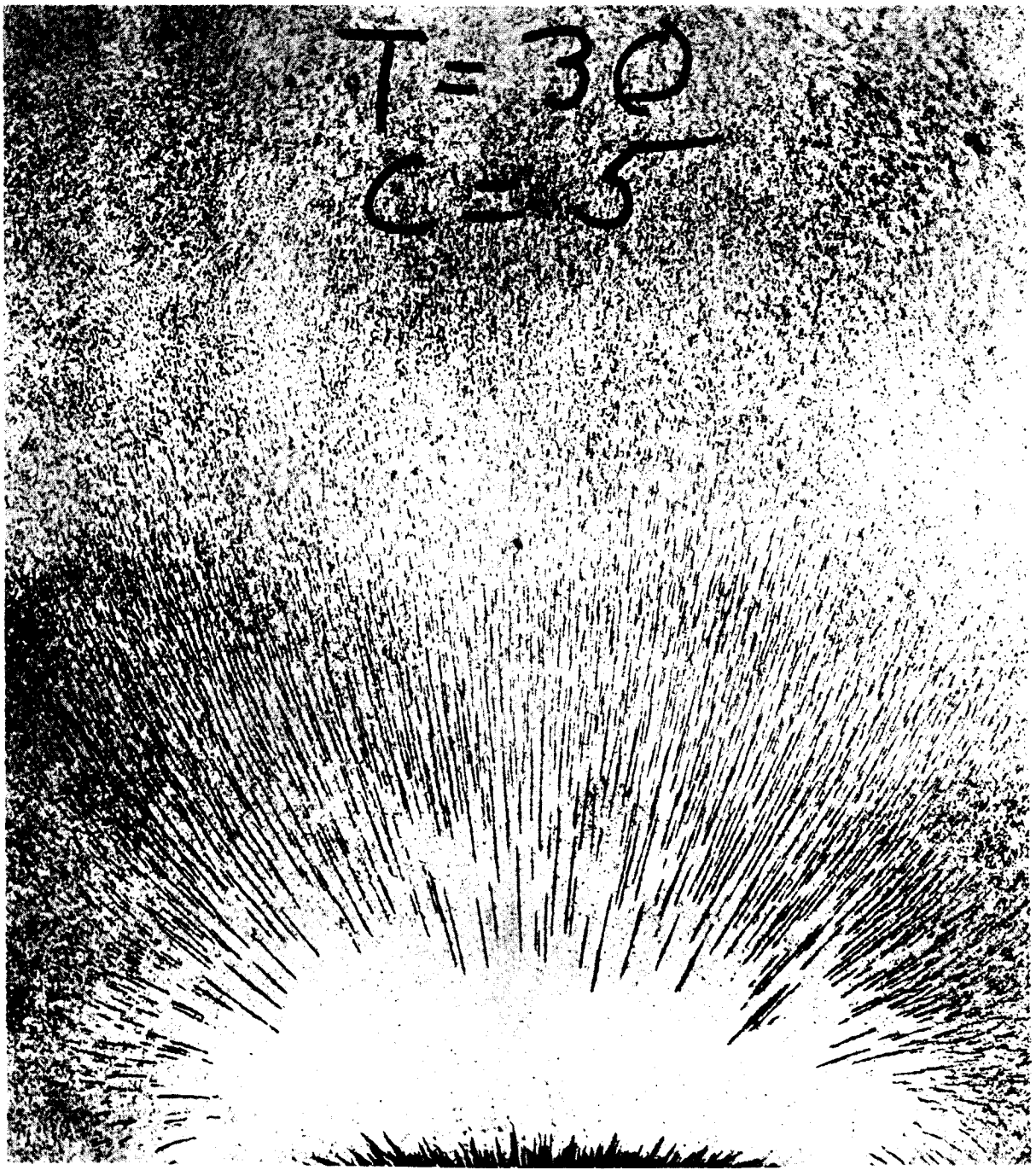


Fig. 96: Magnetic Field of the Throat Coil and Downstream Cylinder Coil of Fig. 94

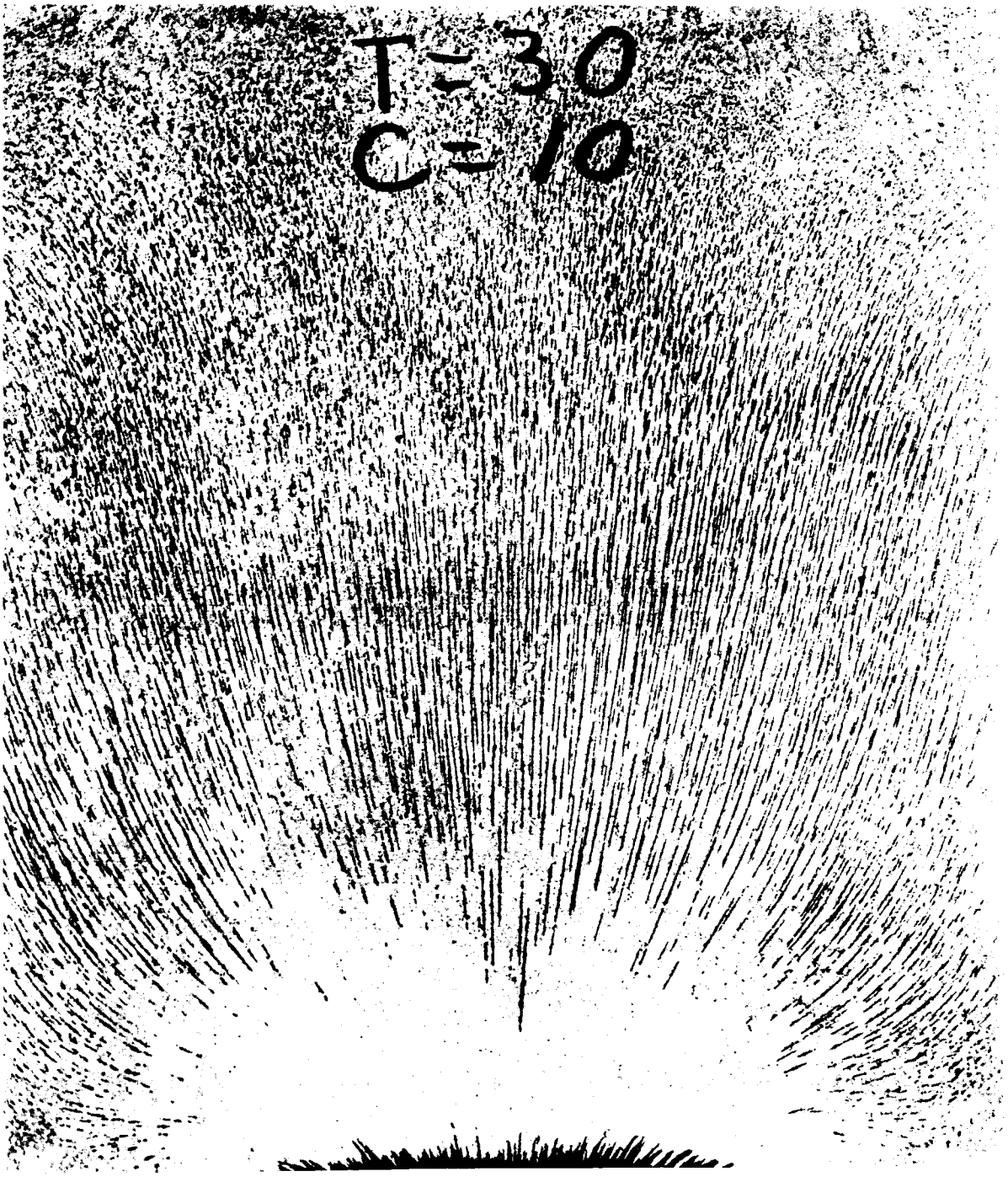


Fig. 97: Magnetic Field of the Throat Coil and Downstream Cylinder Coil of Fig. 94

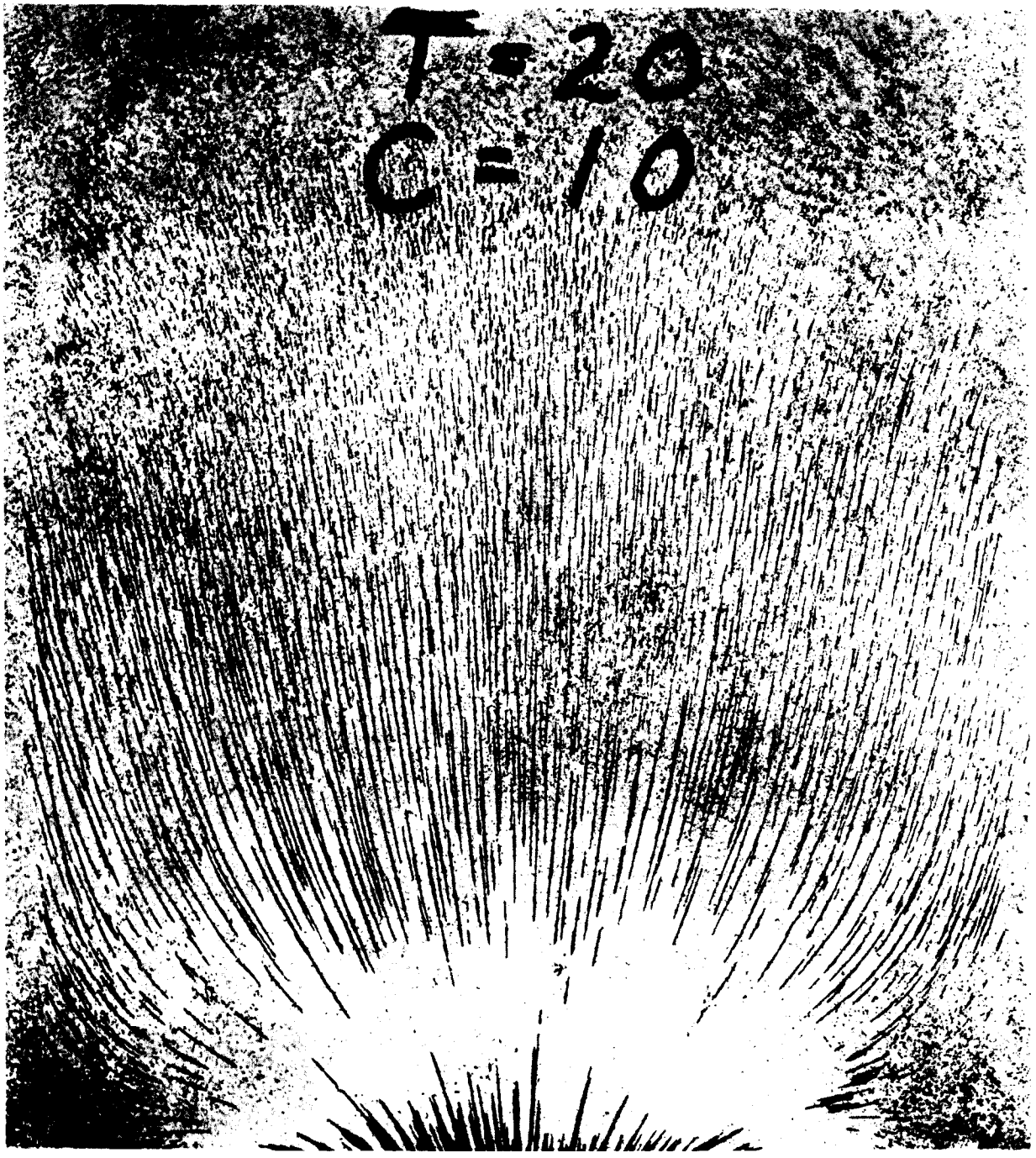


Fig. 98: Magnetic Field of the Throat Coil and Downstream Cylinder Coil of Fig. 94

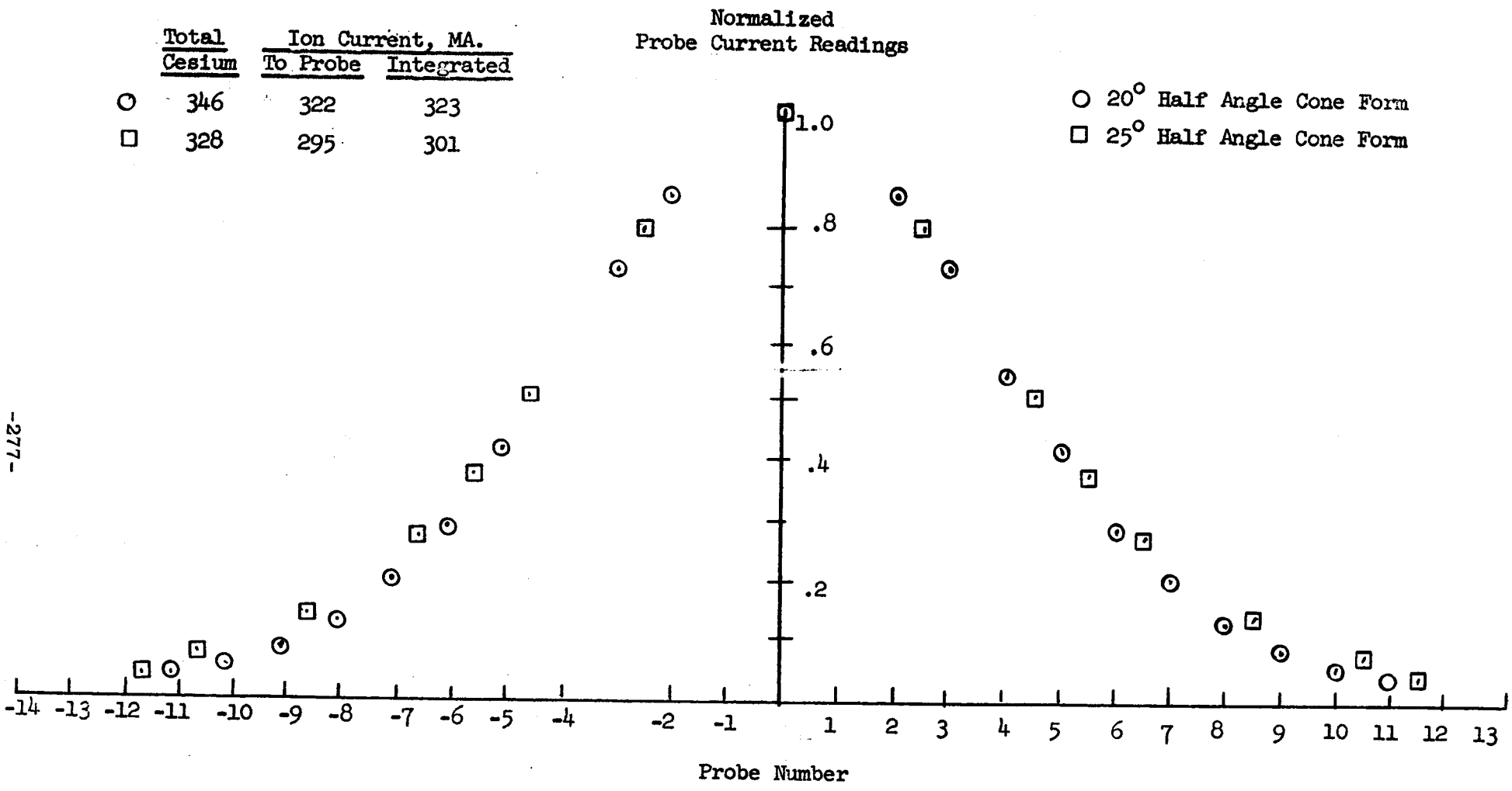


Fig. 99: Density Patterns of Electromagnetic Nozzle of Fig. 94.

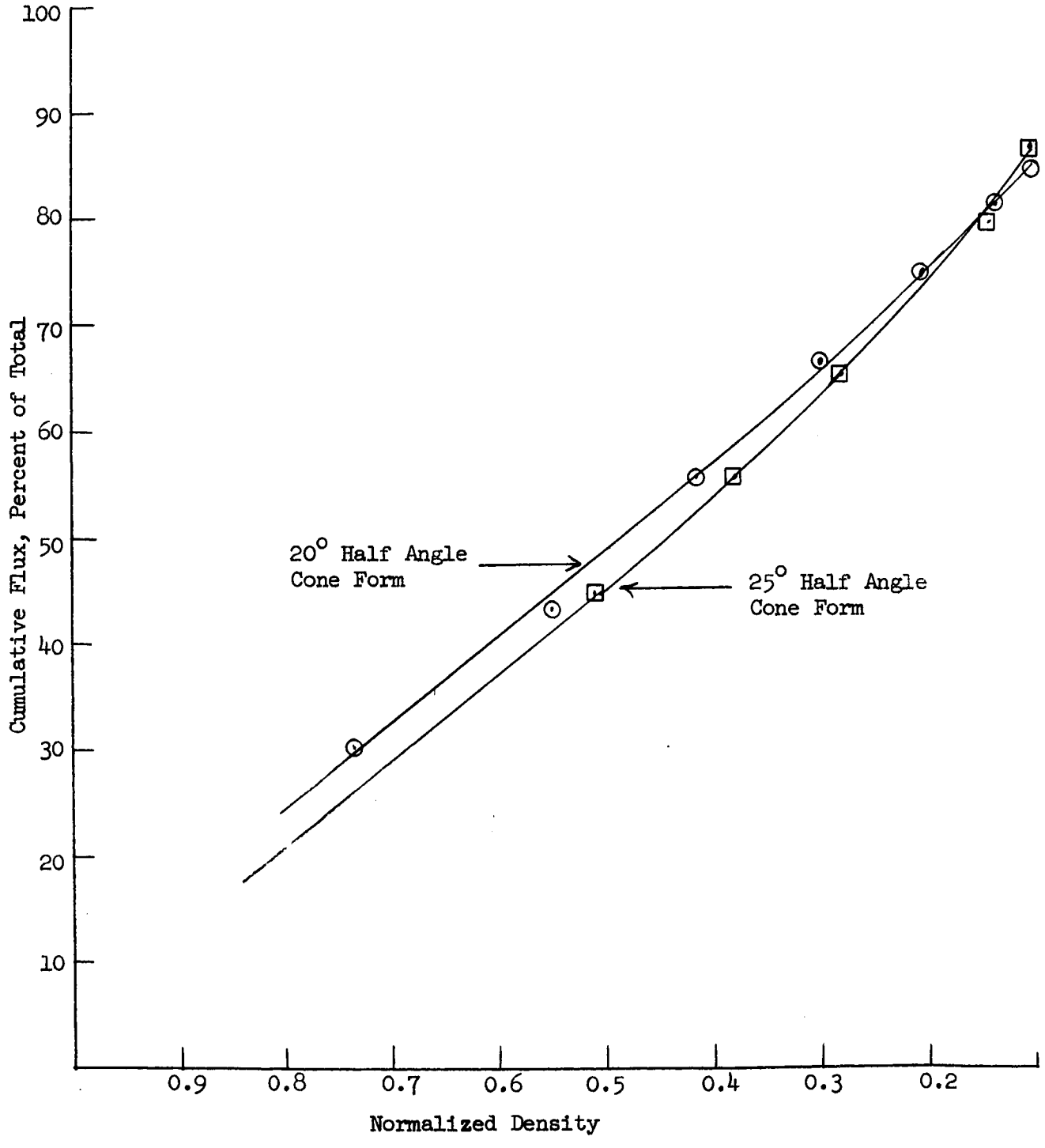


Fig. 100: Evaluation of Electromagnetic Nozzle of Fig. 94.

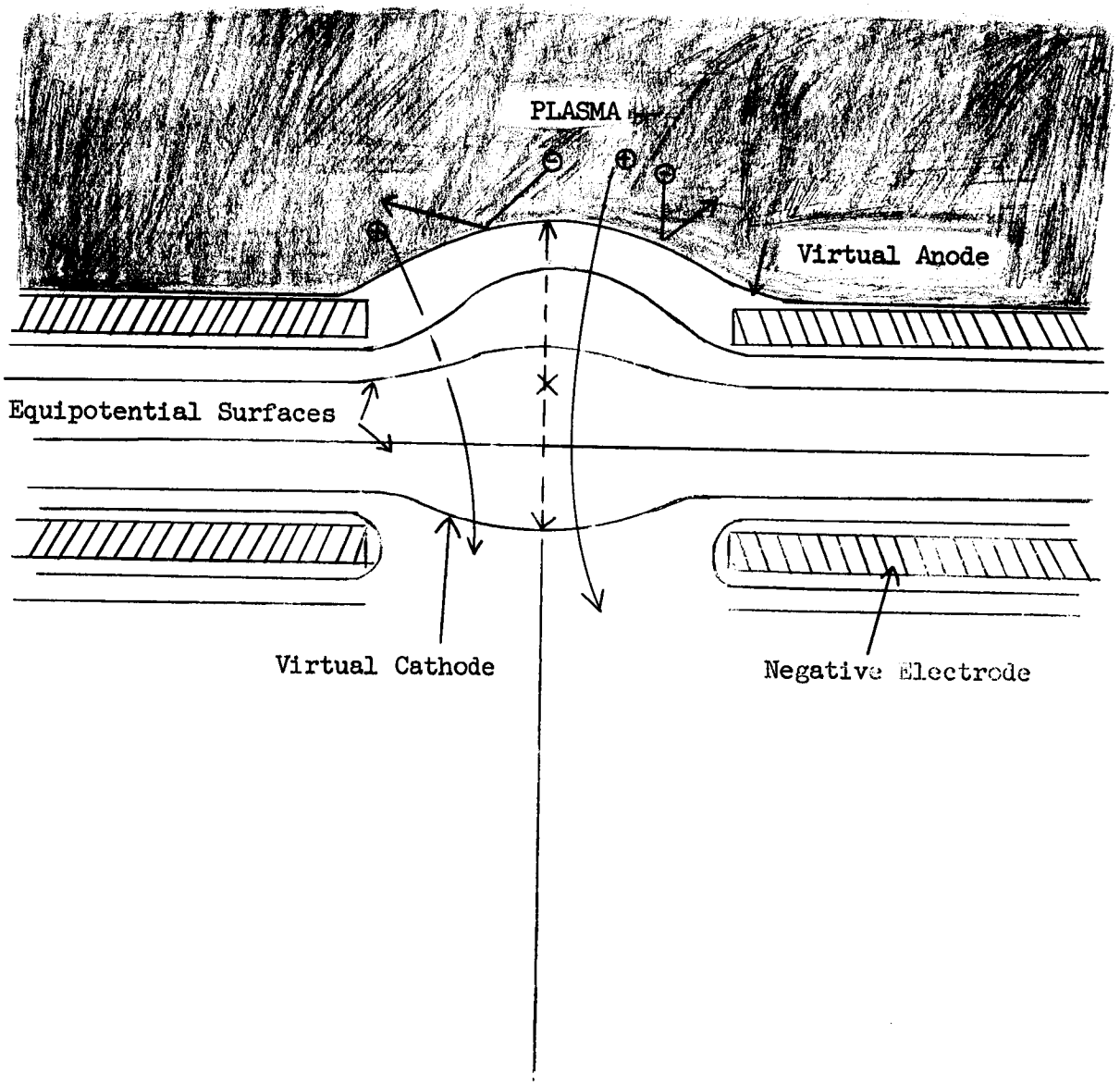
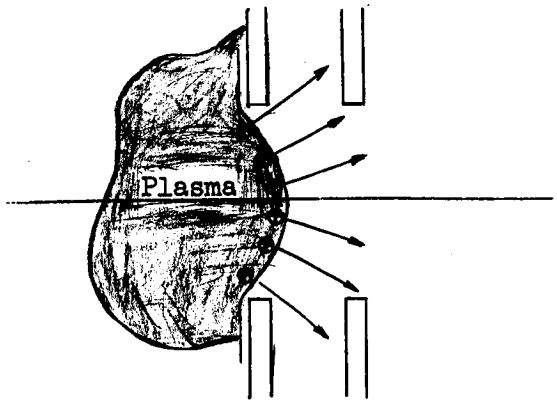
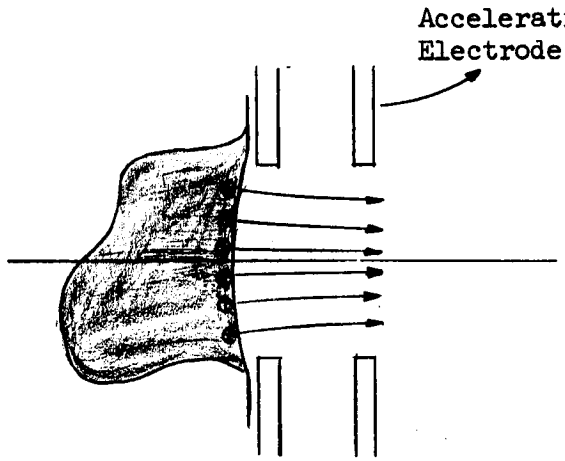


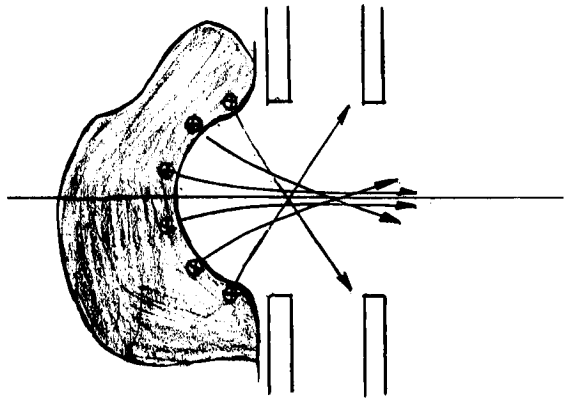
Fig. 101: Qualitative Field Characteristics of Perforated Plate Electrodes



Case I
Low Extraction Potential.
Throughput: <Geometrical
Optics: Under Focussed



Case II
Optimum Extraction Potential
Throughput: Geometrical.
Optics: Properly Focussed



Case III
High Extraction Potential.
Throughput: > Geometrical.
Optics: Over Focussed.

Fig. 102: Plasma Boundary Shapes Predicted by Classical Theory

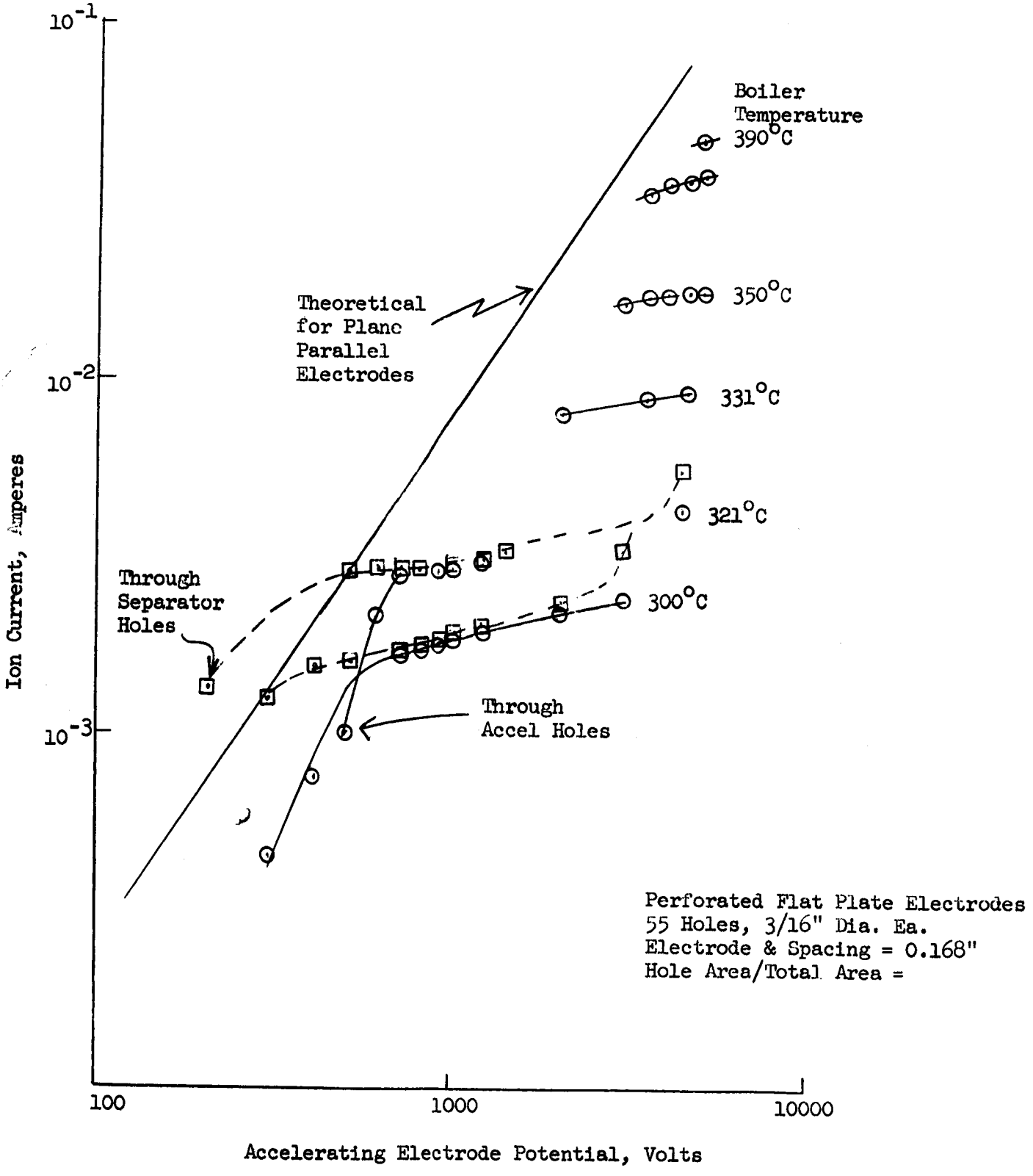


Fig. 103: Ion Currents vs. Accelerator Potential at Various Cesium Flow Rates

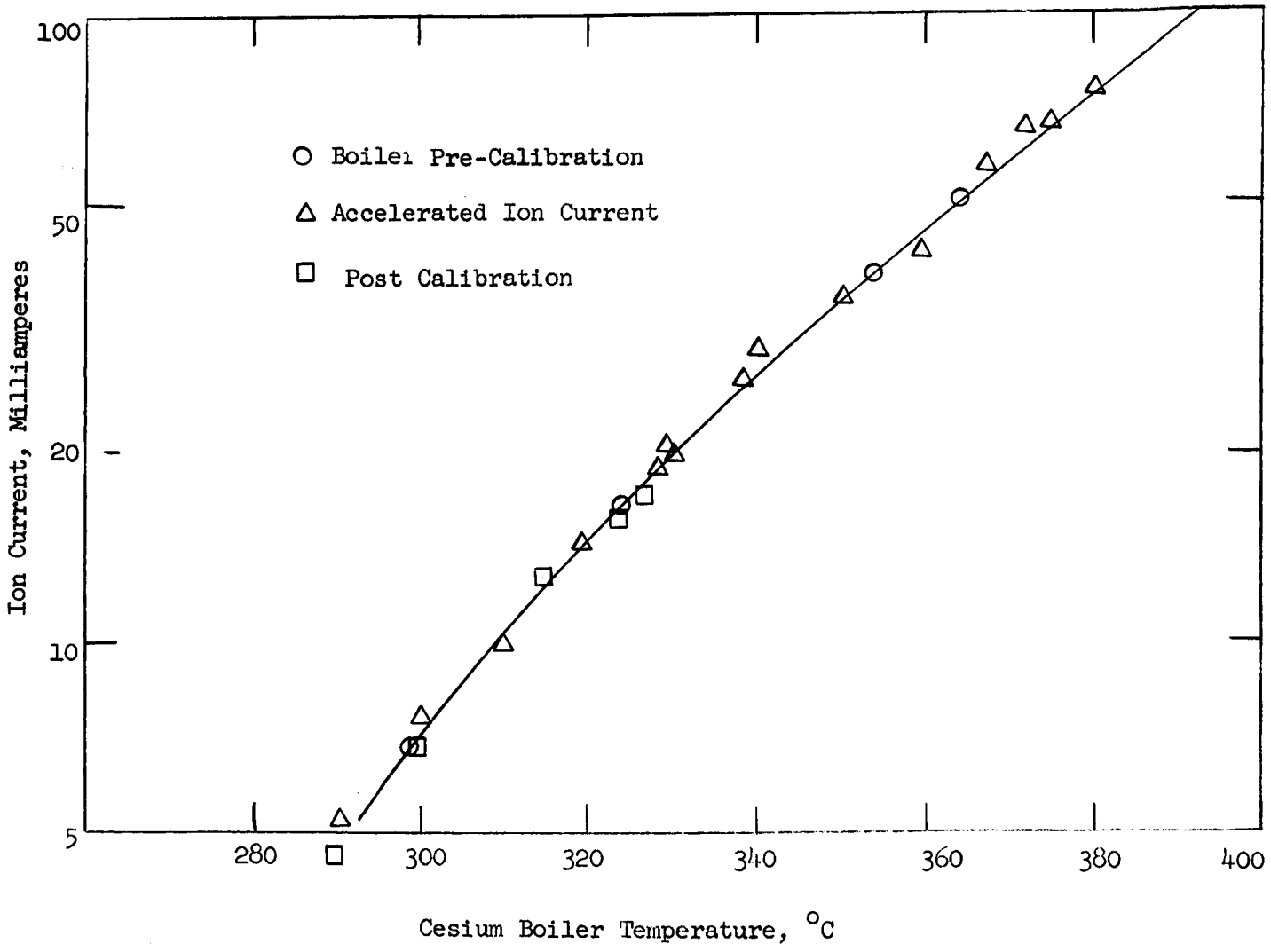


Fig. 104: Comparison of Measured Accelerated Ion Current with Total Incident Flow by Calibration.

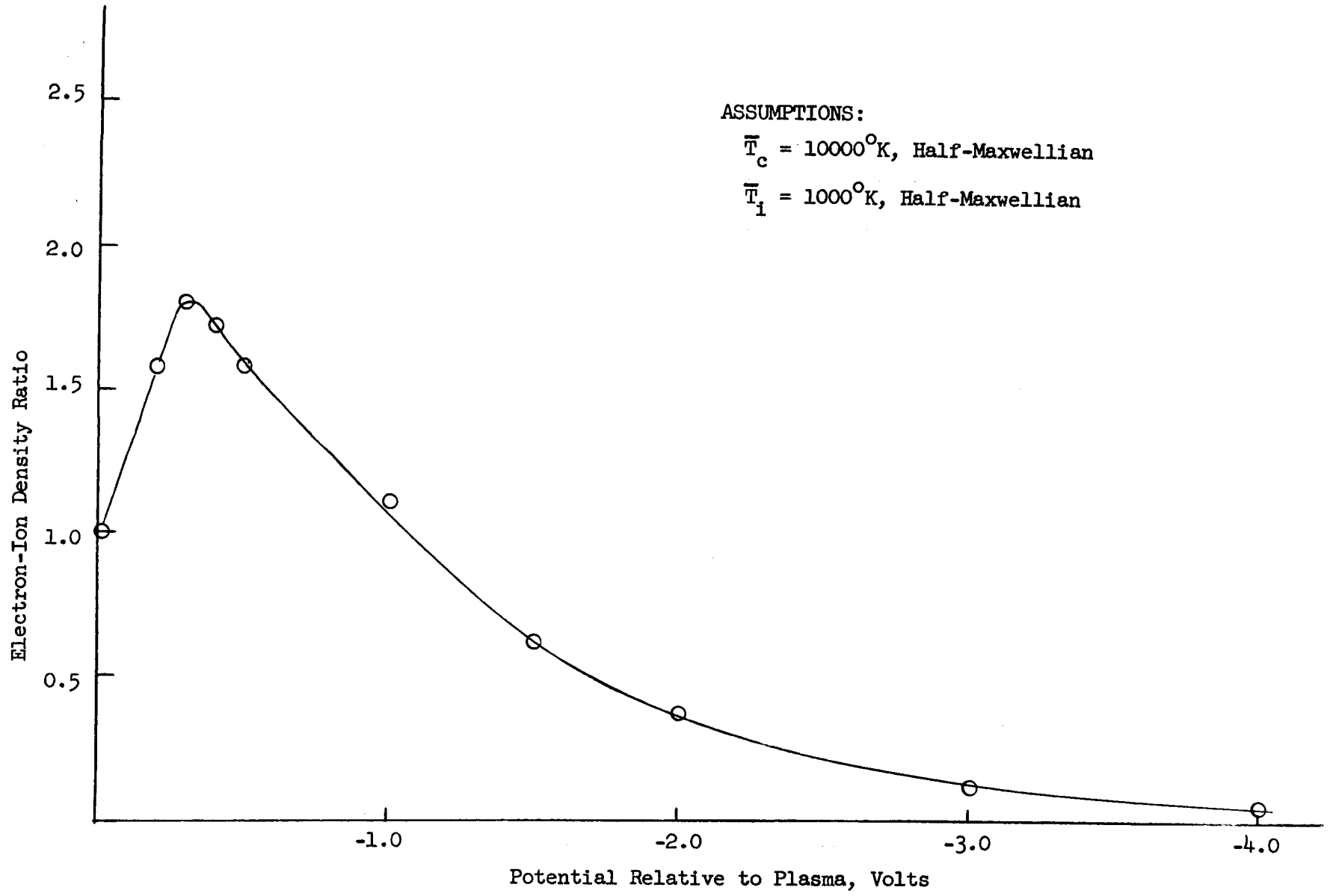
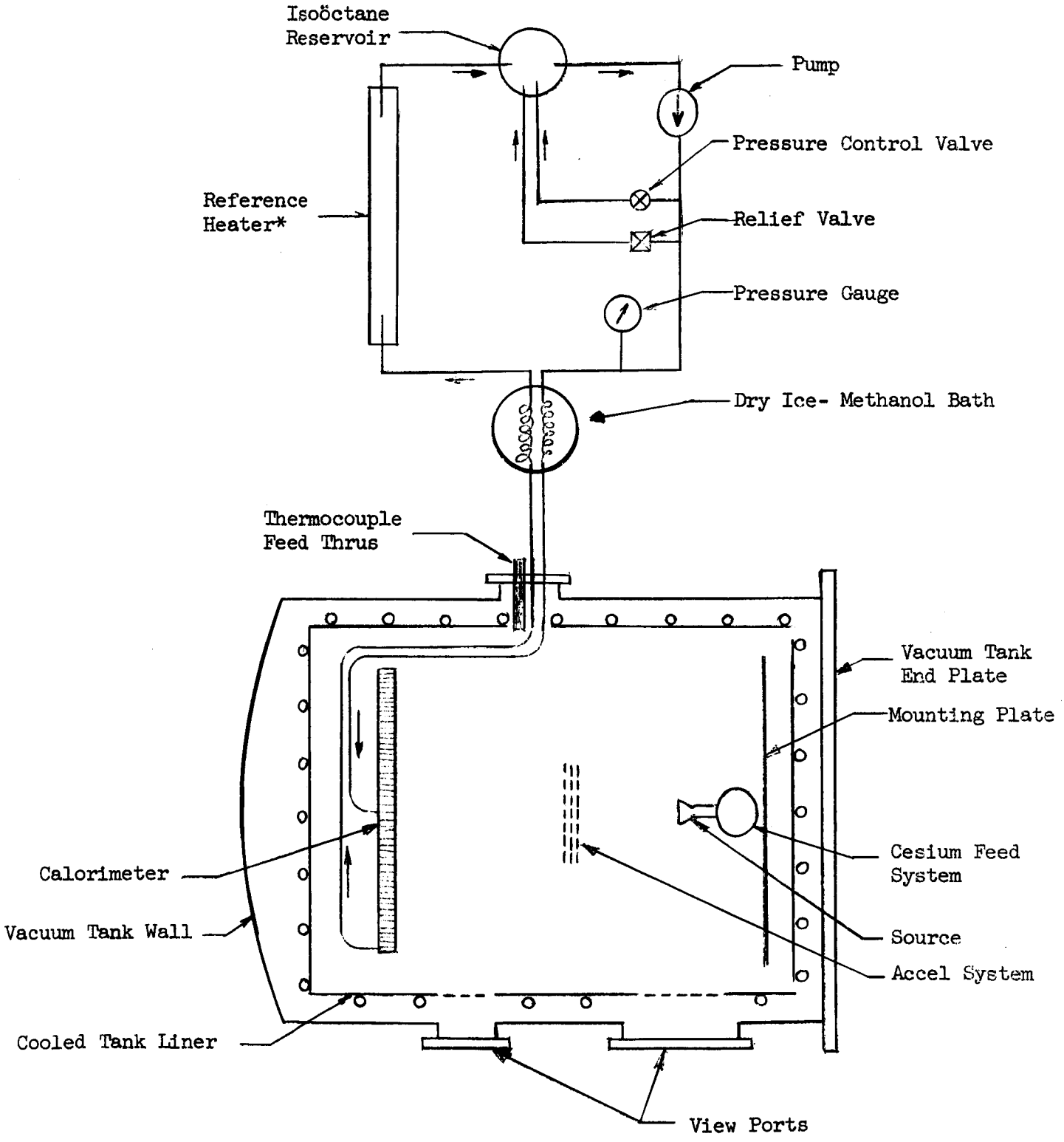


Fig. 105: Variation of Electron-Ion Density Ratio with Potential in the Transition Region from Neutral Plasma to Space Charge Limited Ion Flow.



*Detailed Description in Appendix I

Fig. 106: Vacuum System Used for Accelerator Studies and Engine Runs

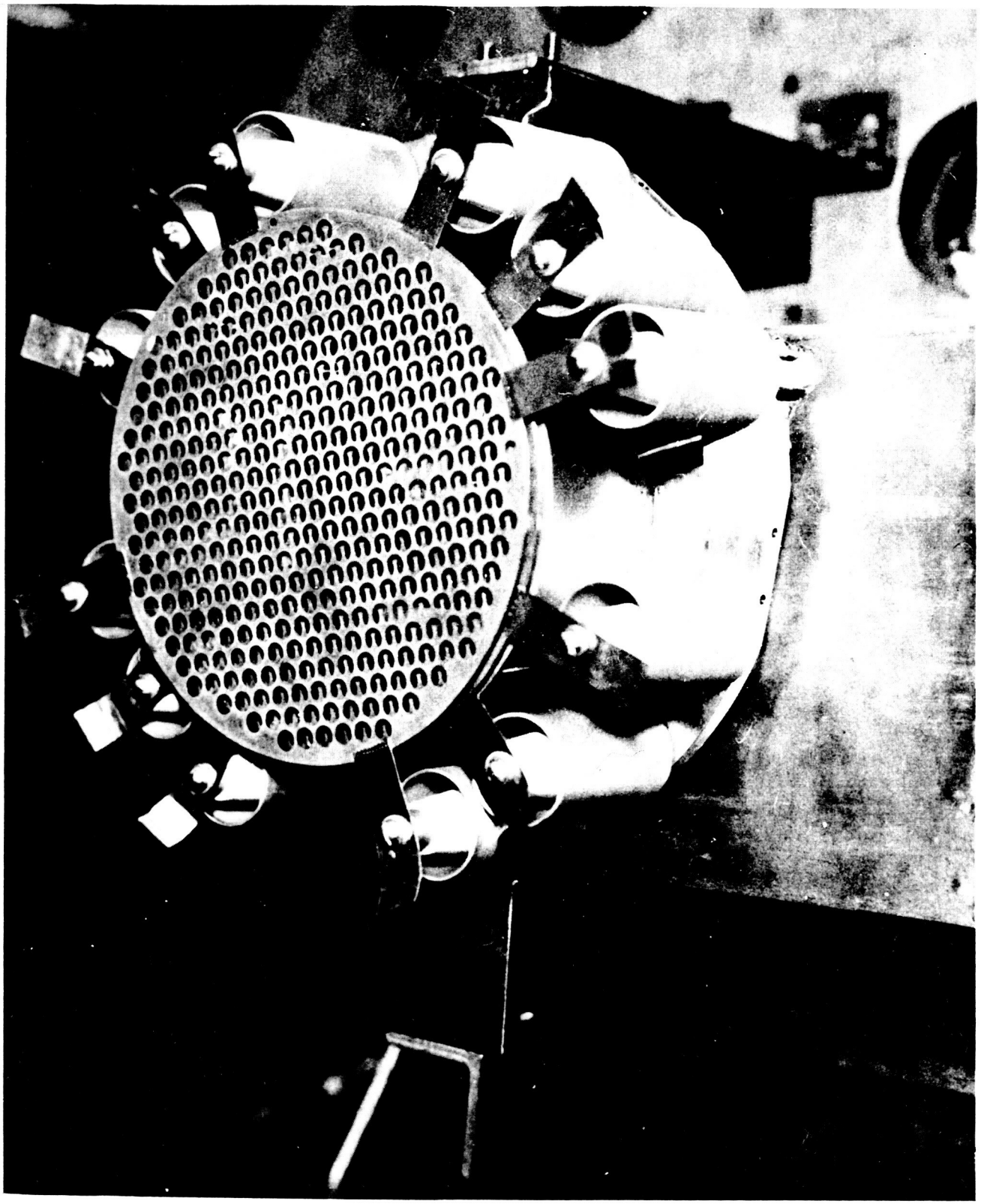


Fig. 107: Grid Suspension System for 19 Hole and 211 Hole Accelerator System

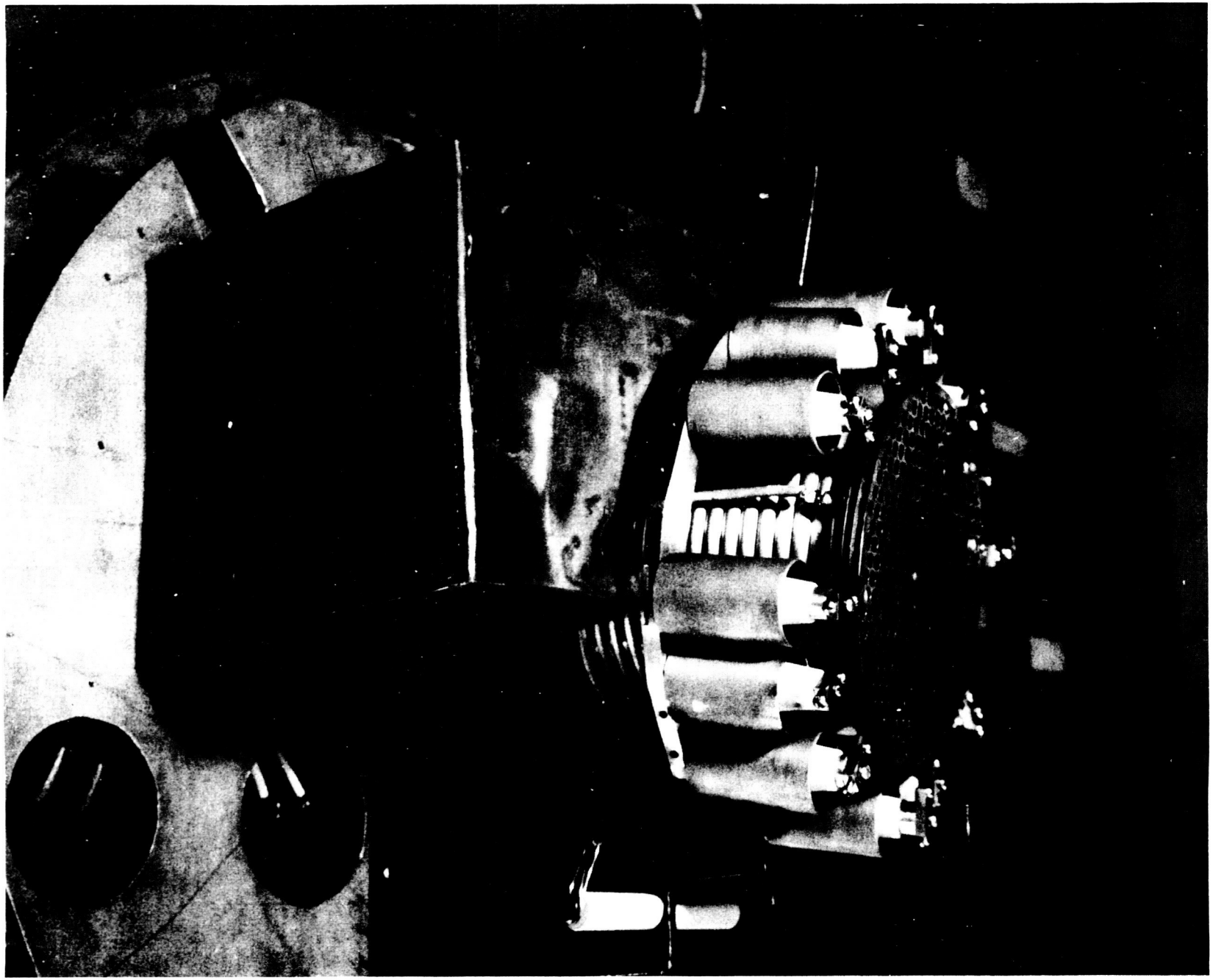


Fig 108: The Six Inch Accelerator System In Operating Position.

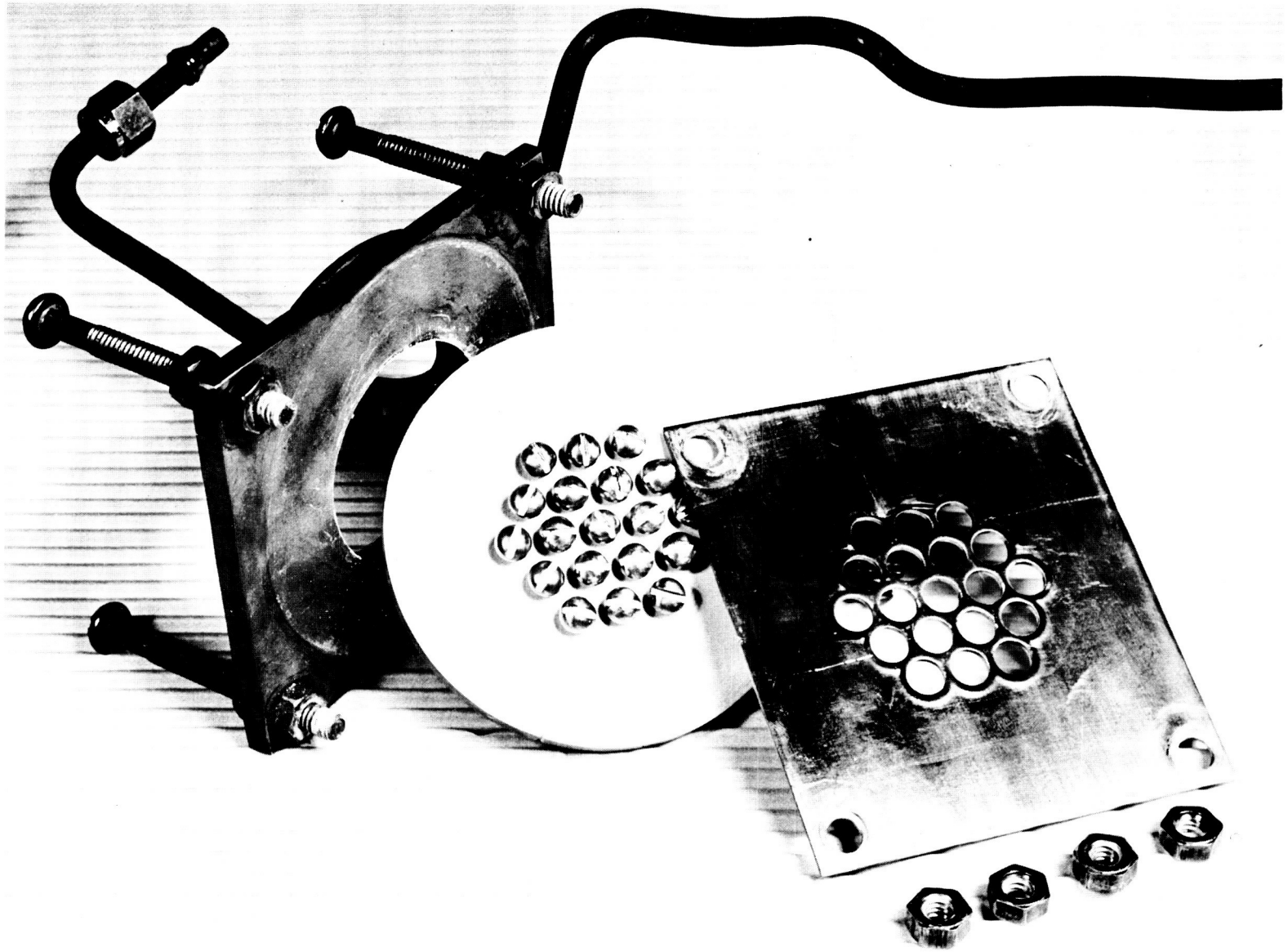
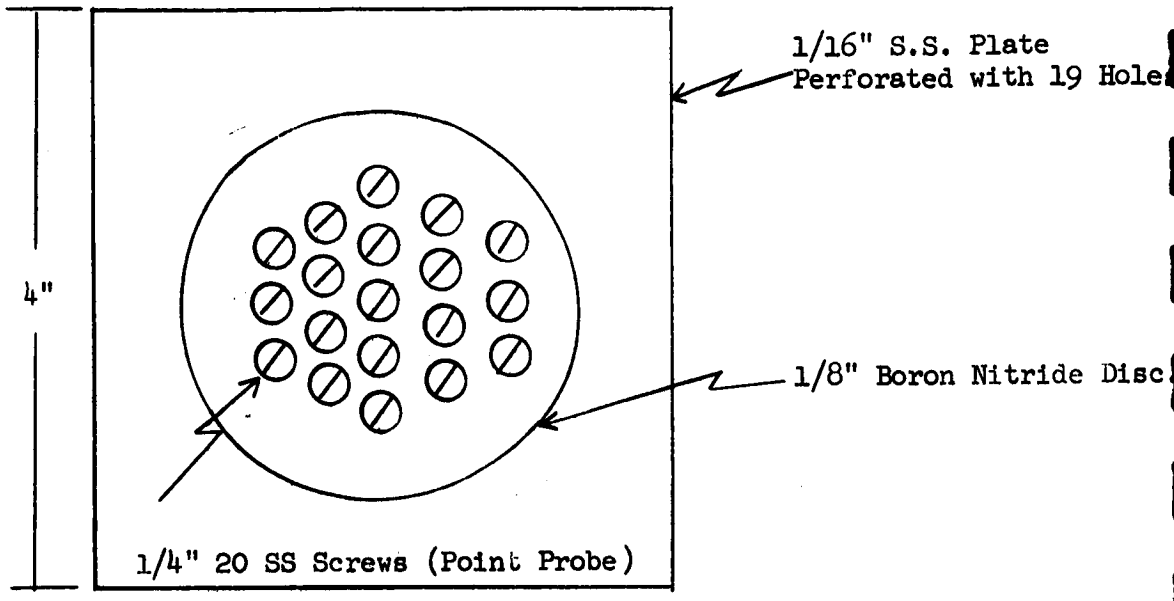
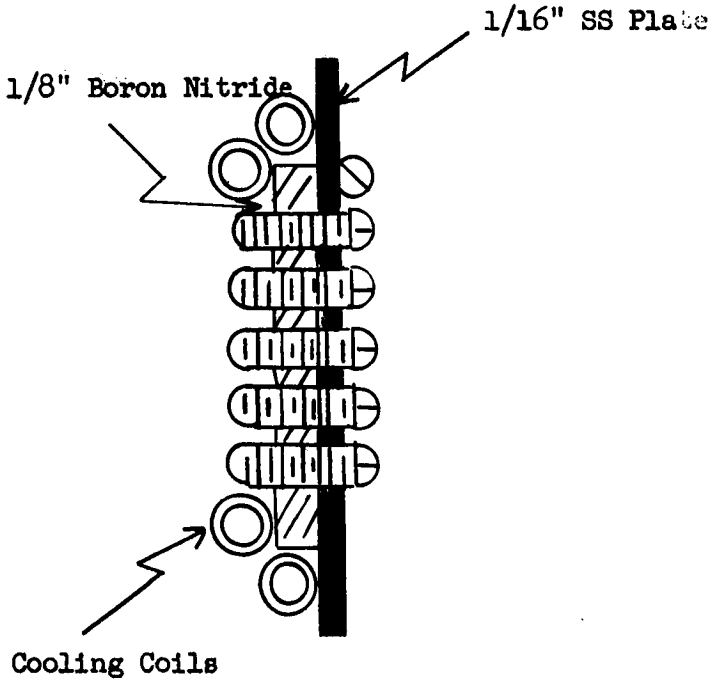


Fig. 109: The Ion Beam Examiner, Disassembled





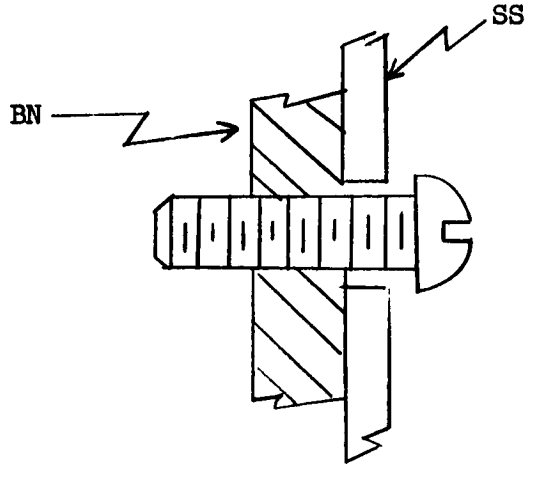


Fig. 110: Nineteen Point Ion Probe (Examiner)

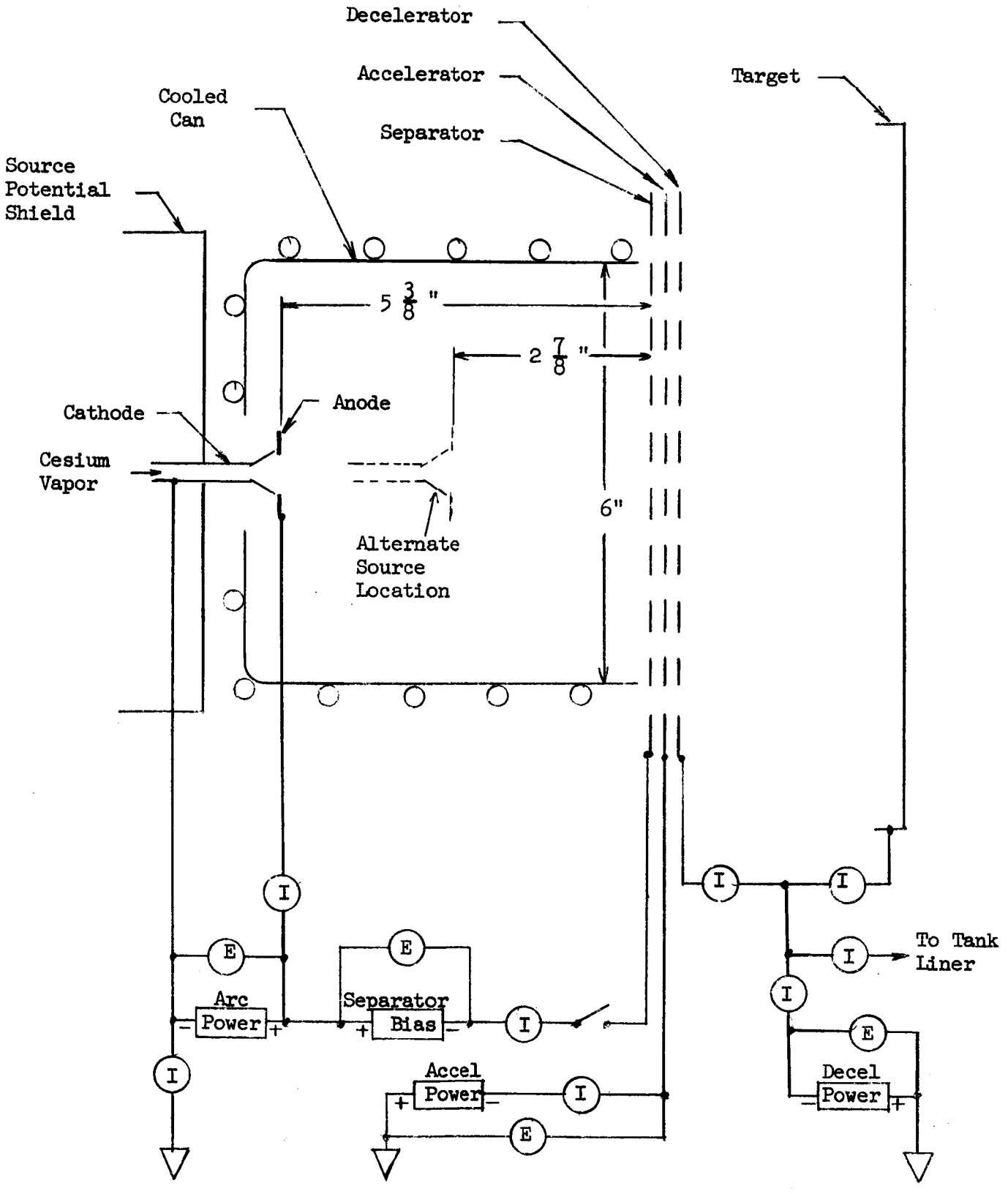


Fig. 111: Schematic Arrangement of the 6" Accelerator System Components

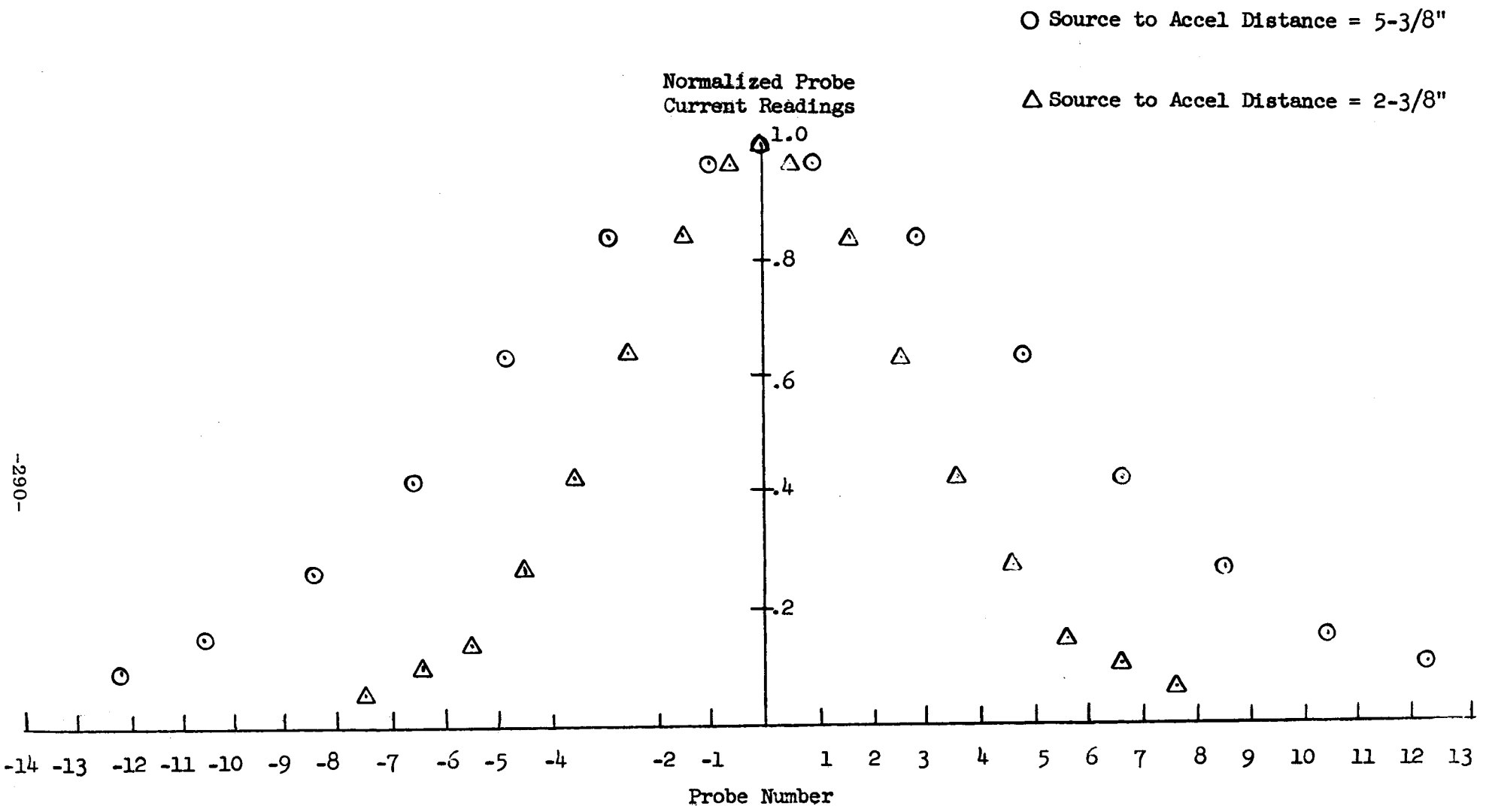


Fig. 112: Density Patterns for Source IX

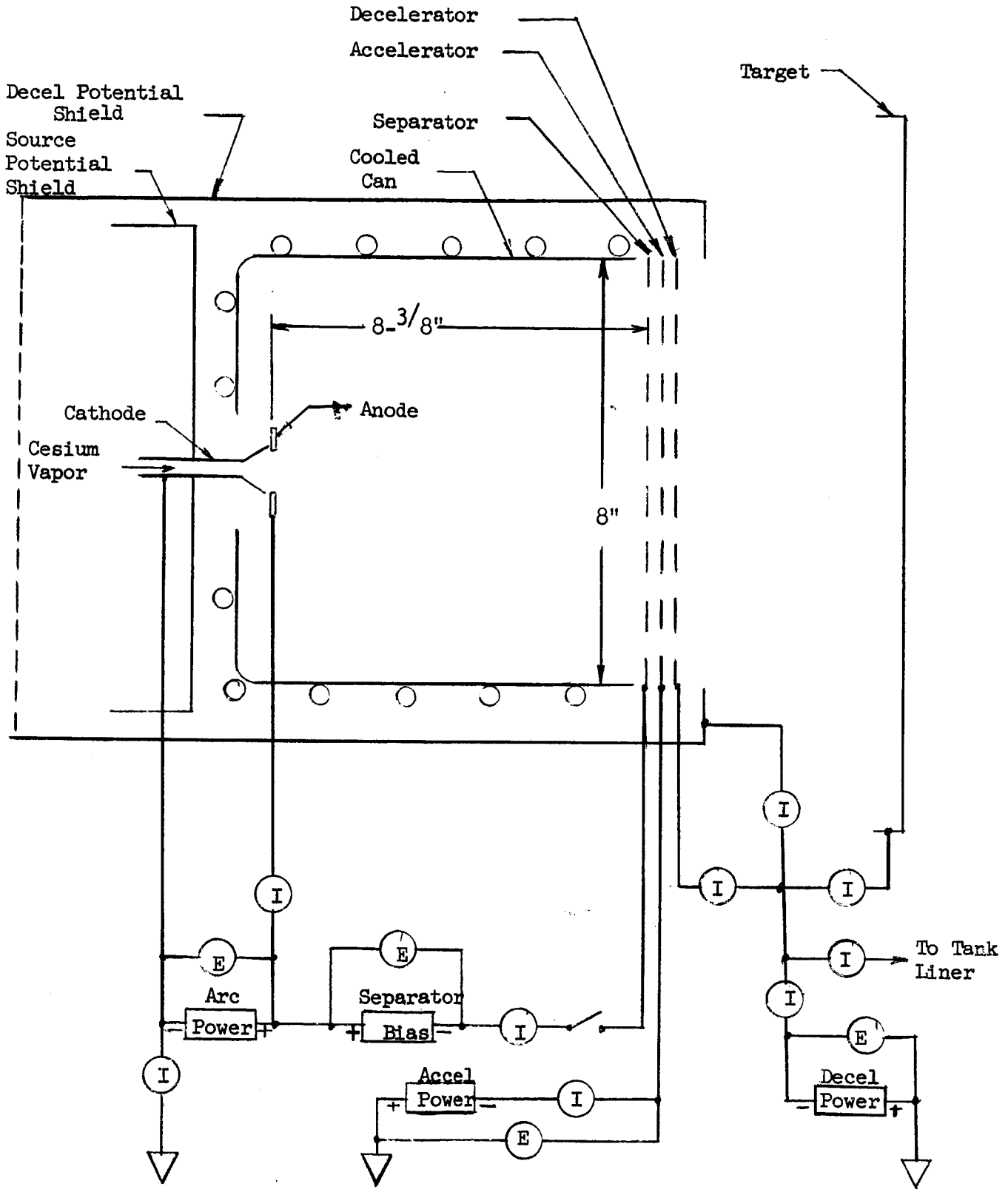


Fig. 113: Schematic Arrangement of the 8" Accelerator System Components

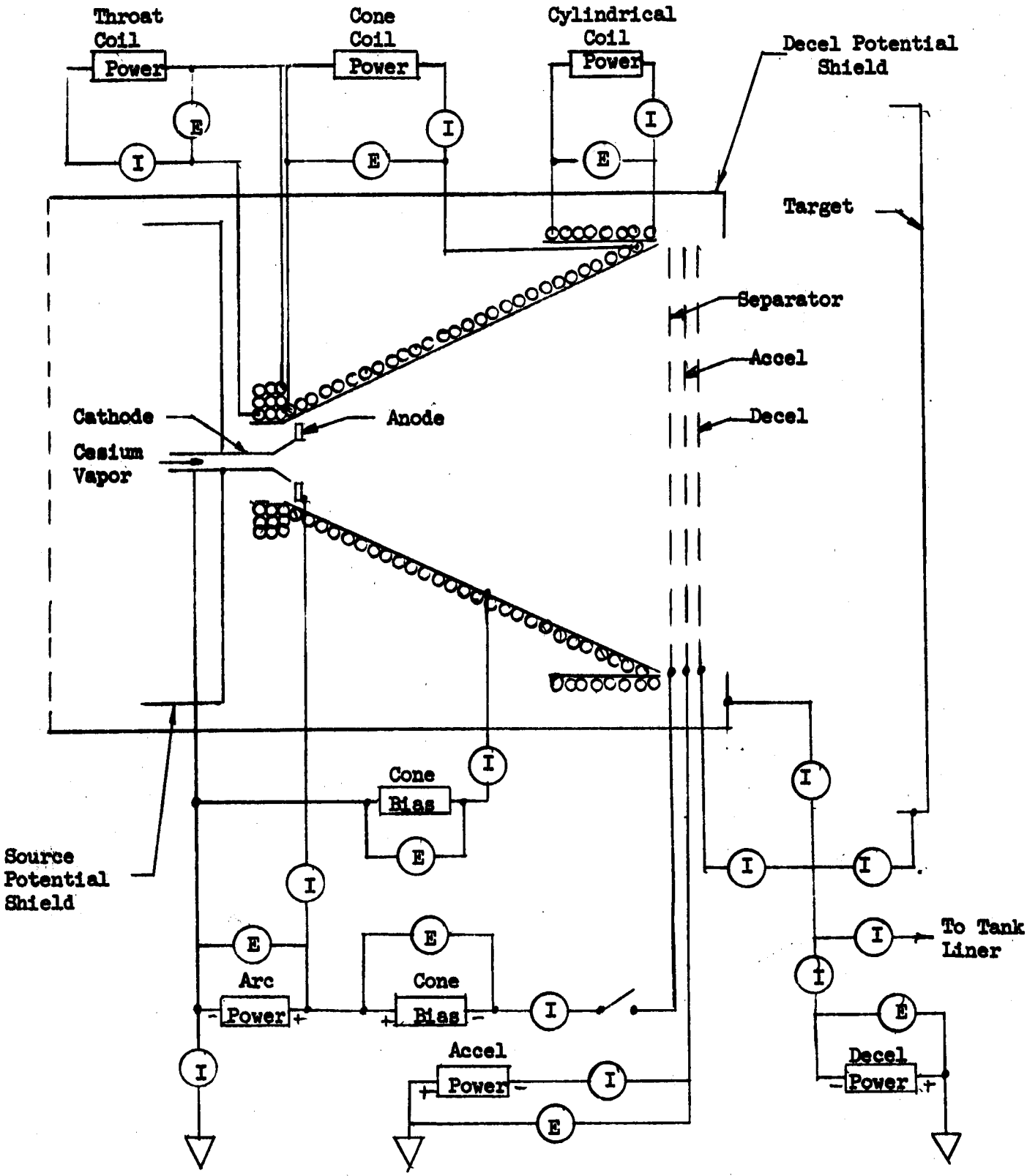


Fig. 114: Engine Configuration I

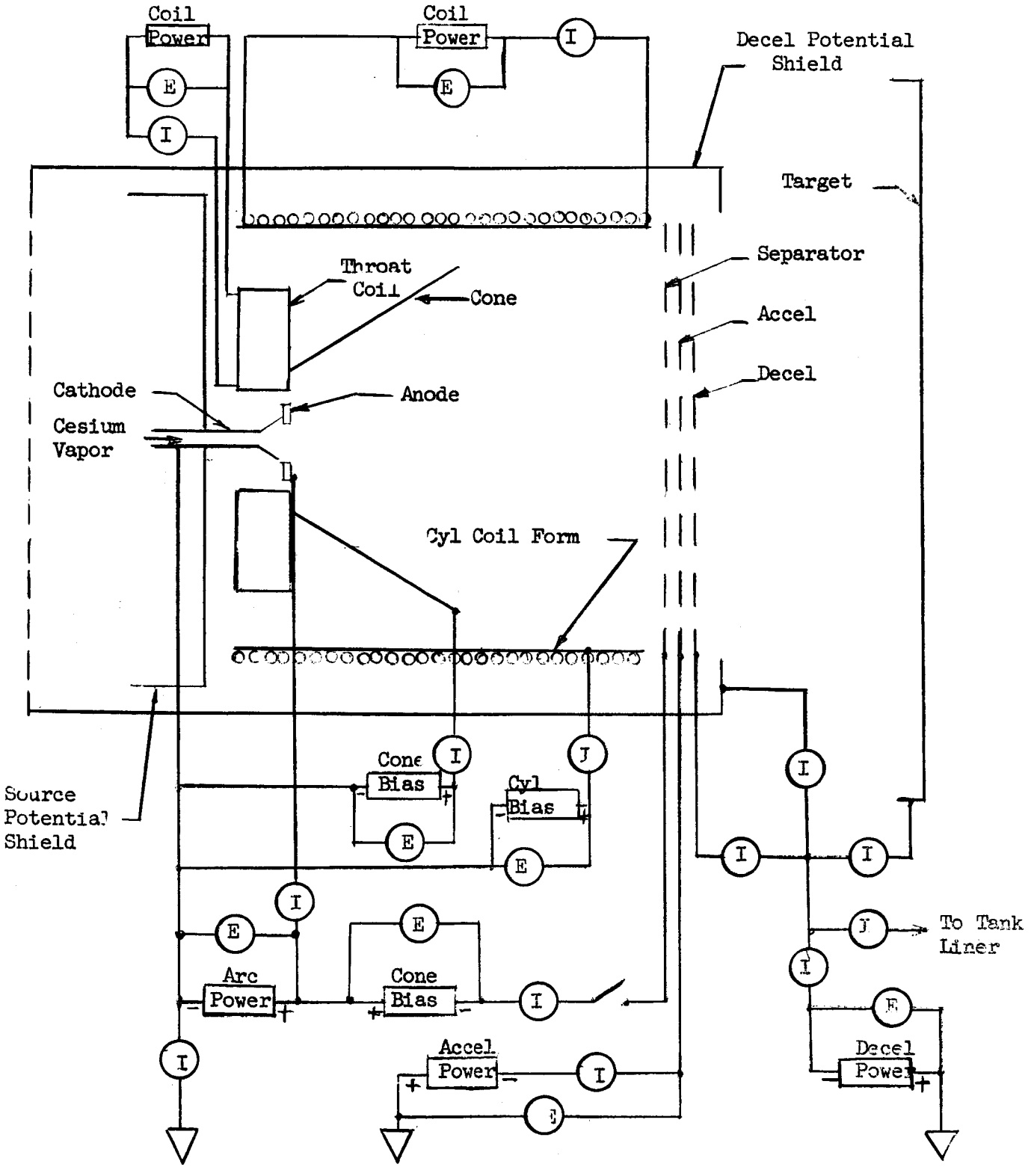


Fig. 115: Engine Configuration II

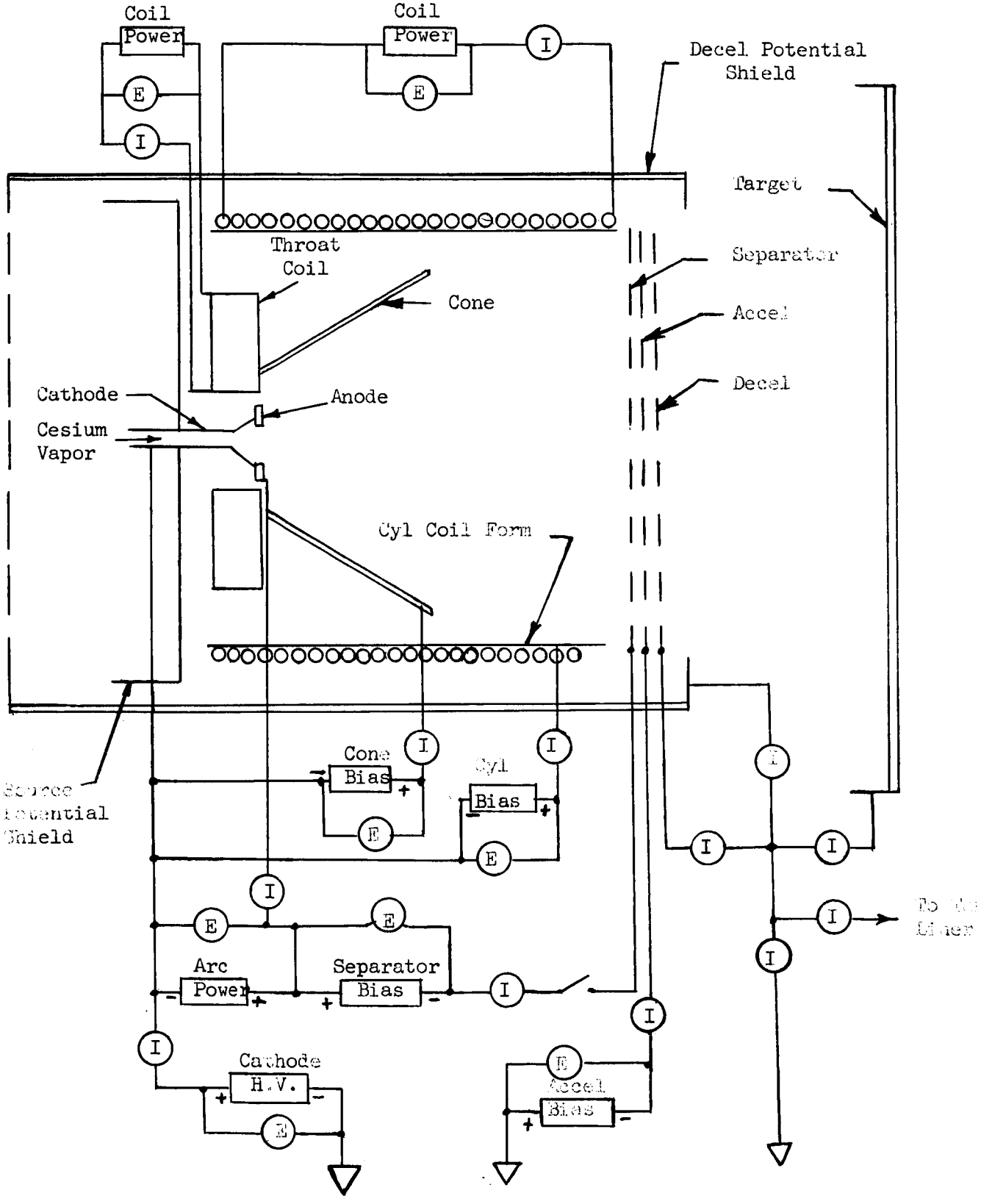


Fig. 116: Engine Configuration III

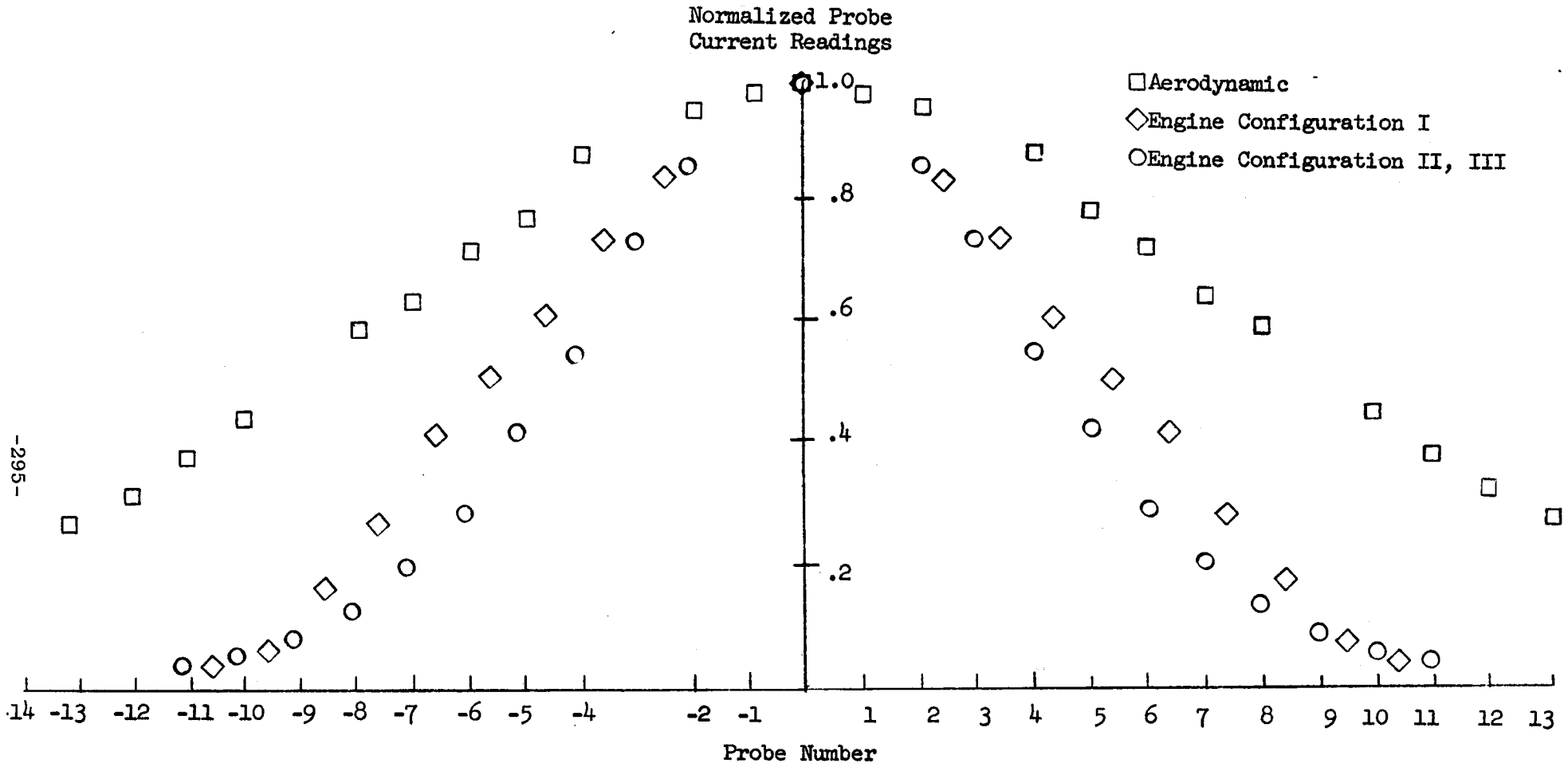


Fig. 117: Density Patterns for Source XI, Aerodynamic and Magnetically Controlled

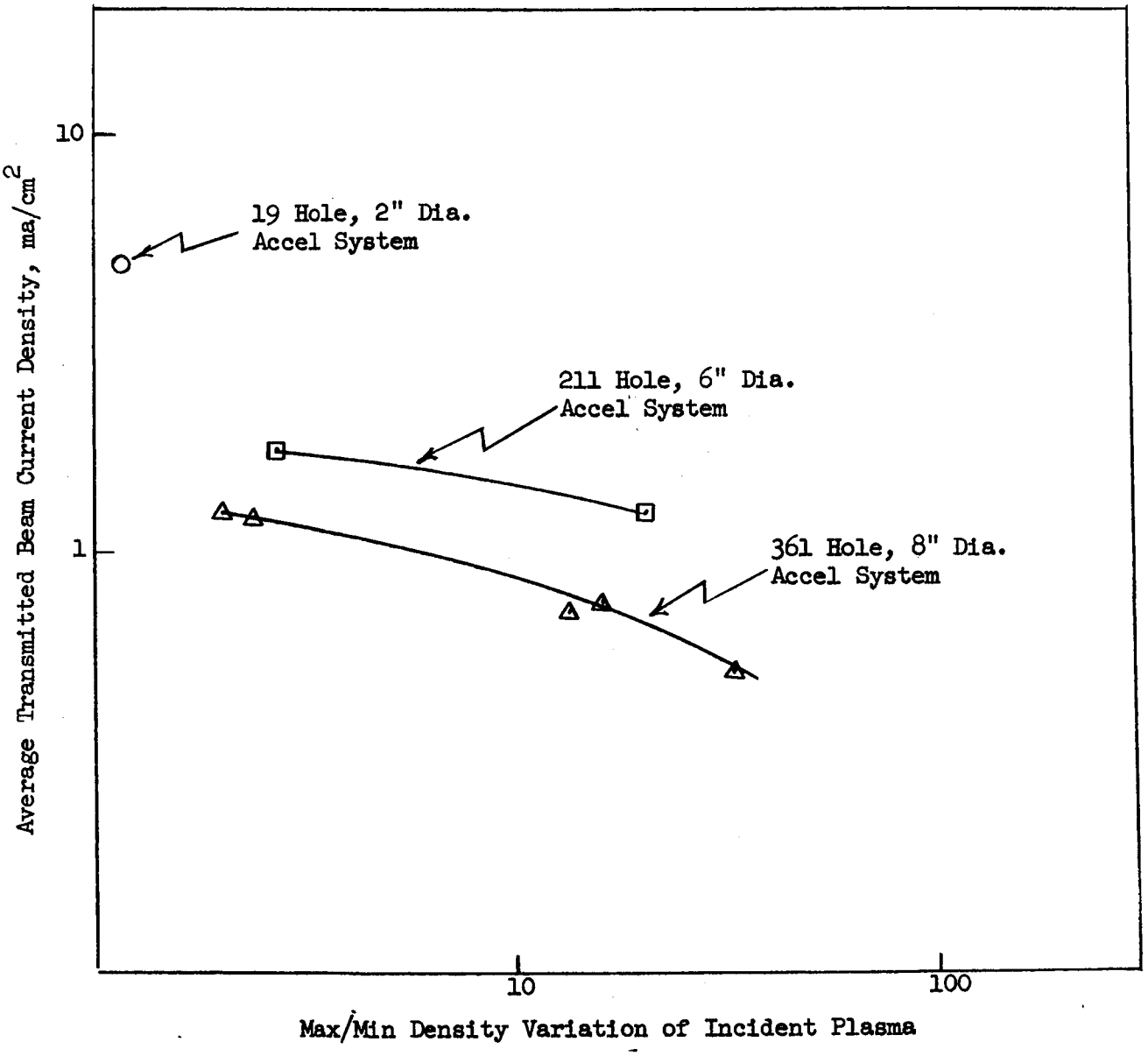


Fig. 118: Beam Current Density vs. Incident Density Ratio

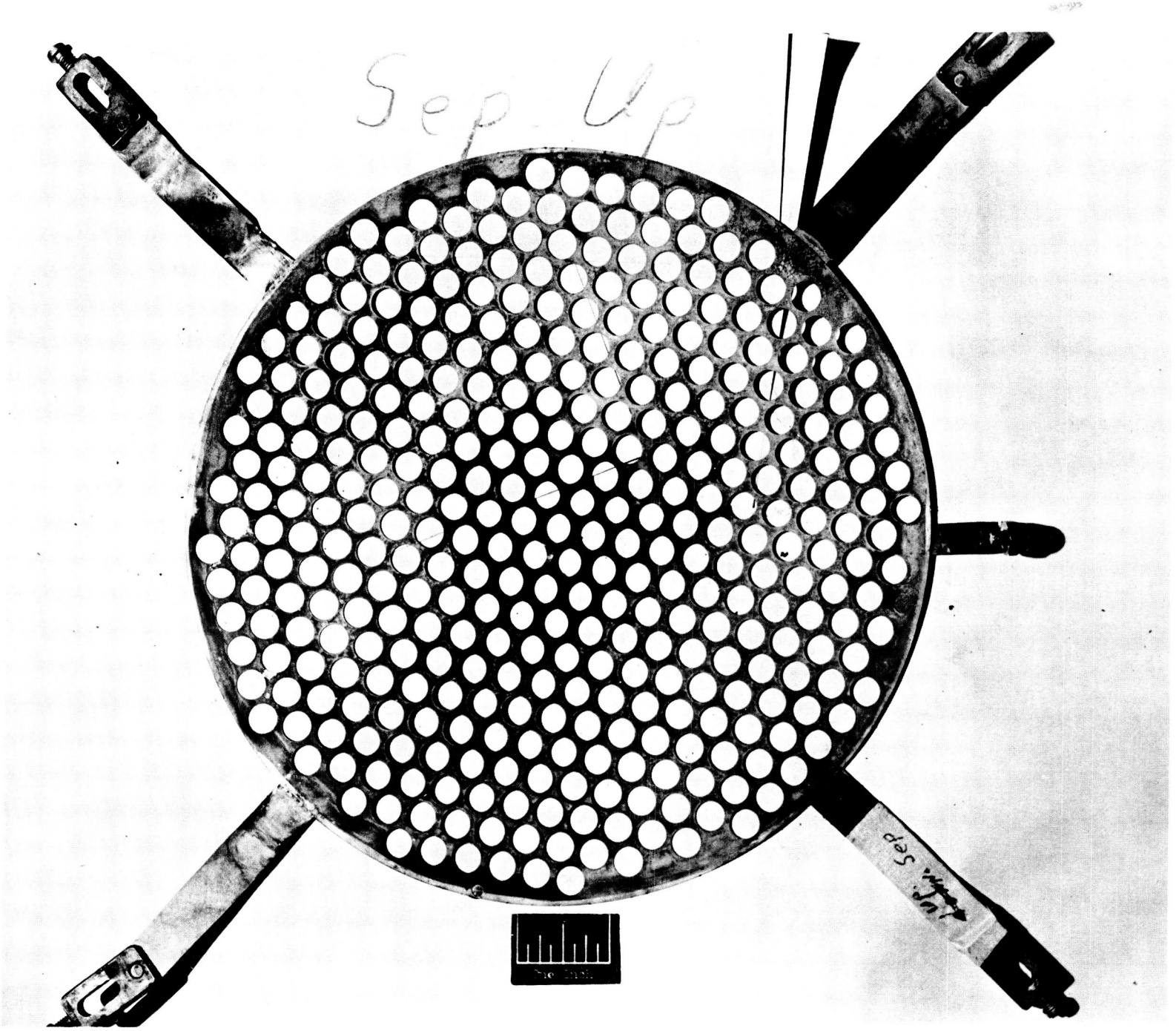


Fig. 119: Electrodes After EC III Run. Separator Upstream

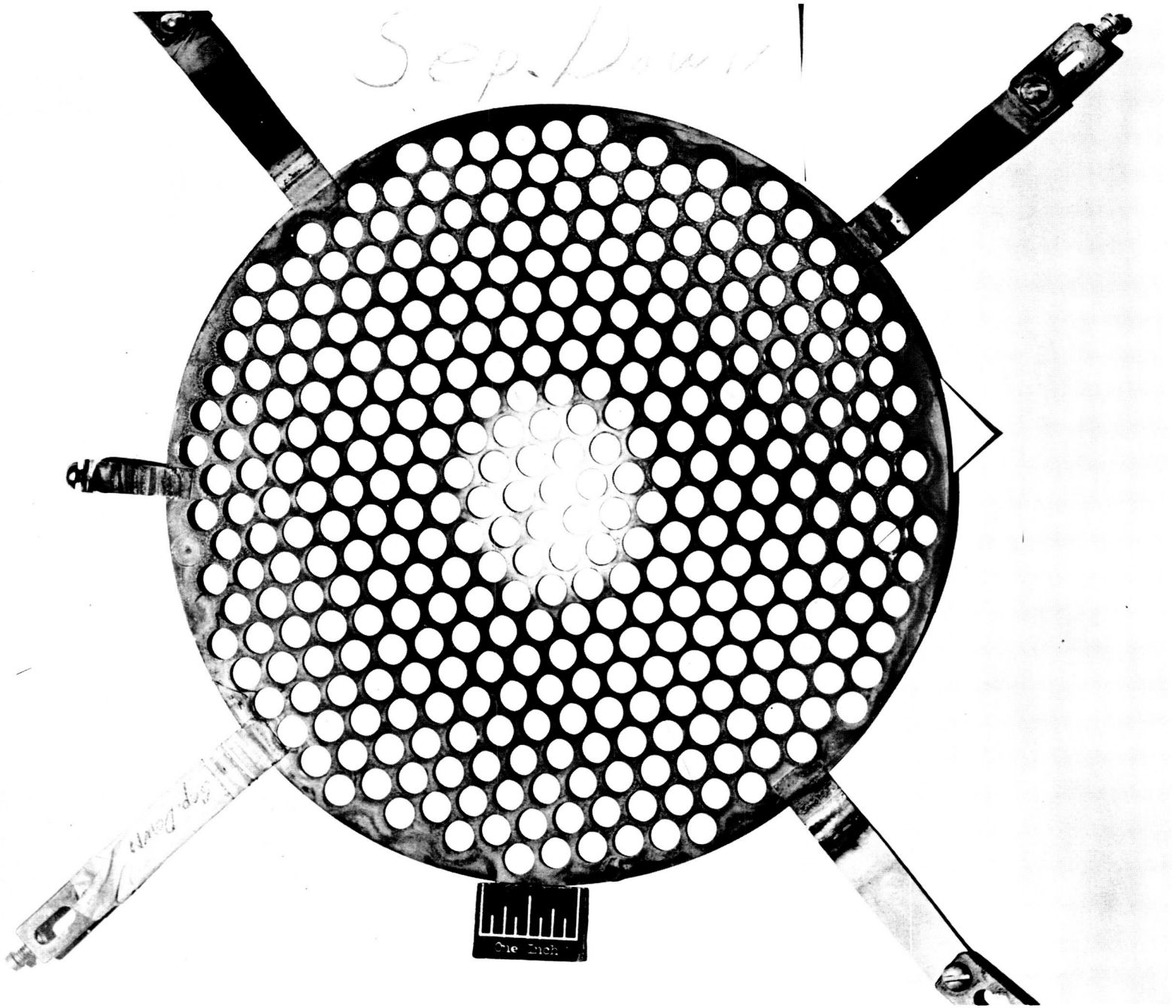


Fig. 120: Electrodes After EC III Run. Separator Downstream

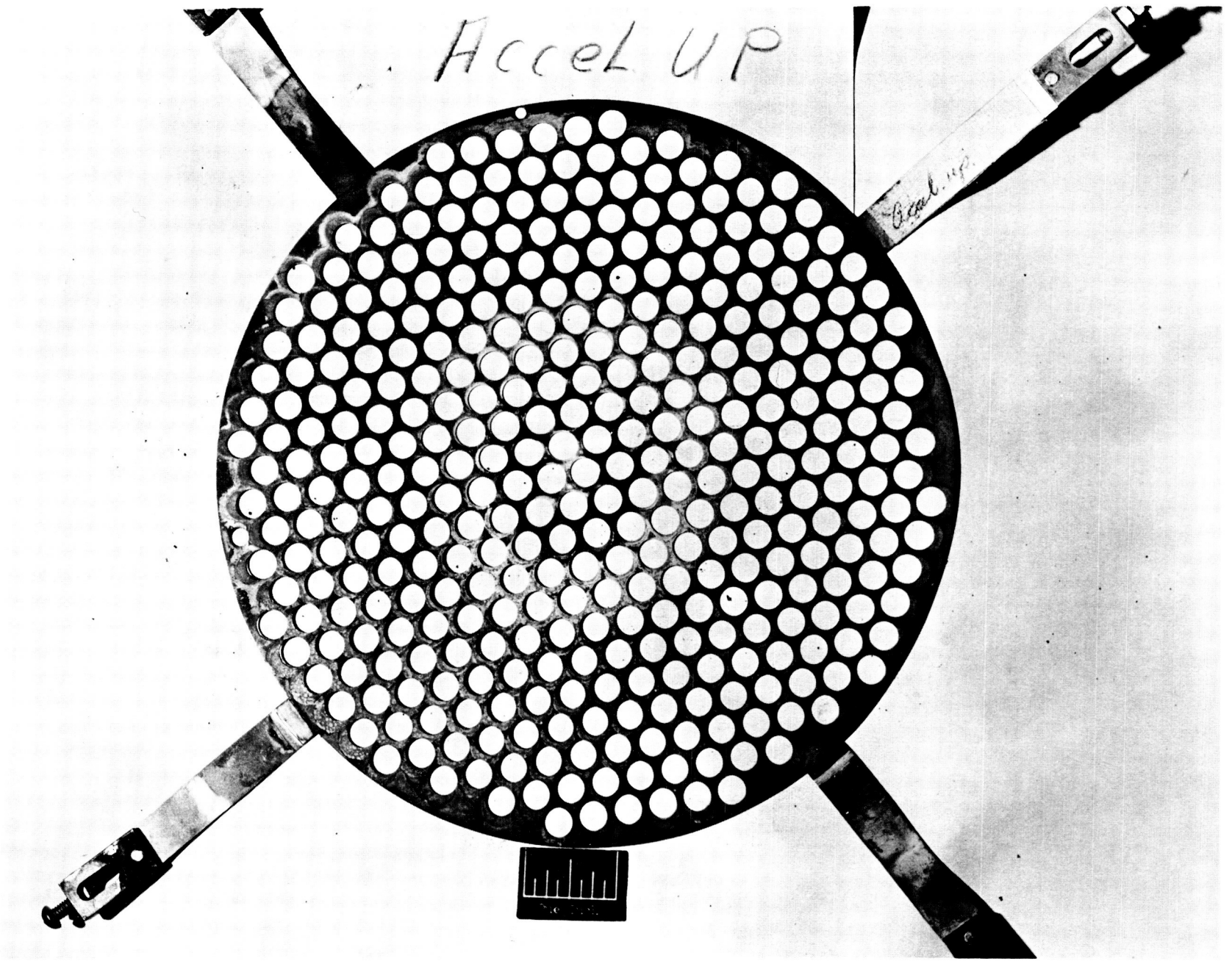


Fig. 121: Electrodes After EC III Run. Accelerator Upstream

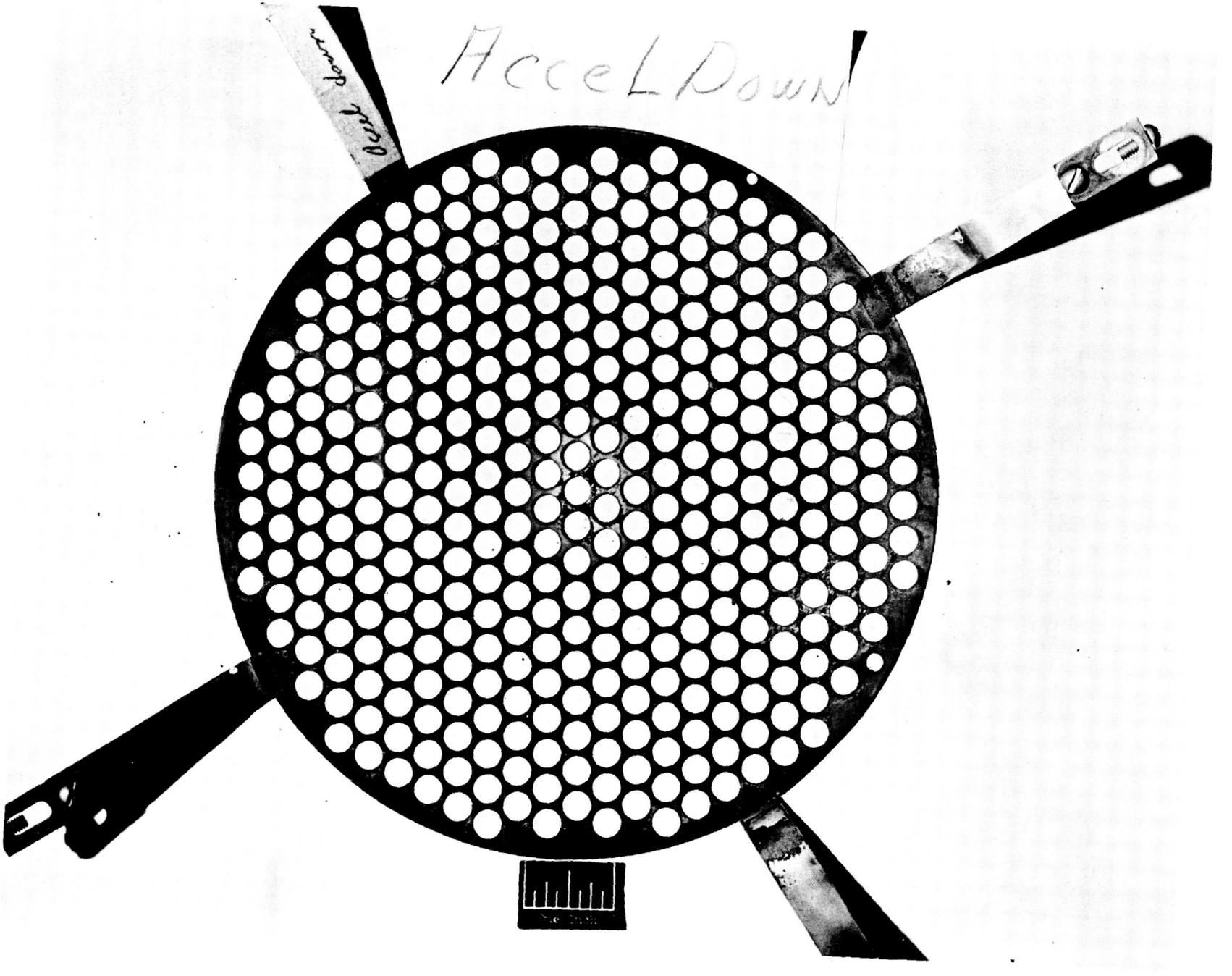


Fig. 122: Electrodes After EC III Run. Accelerator Downstream

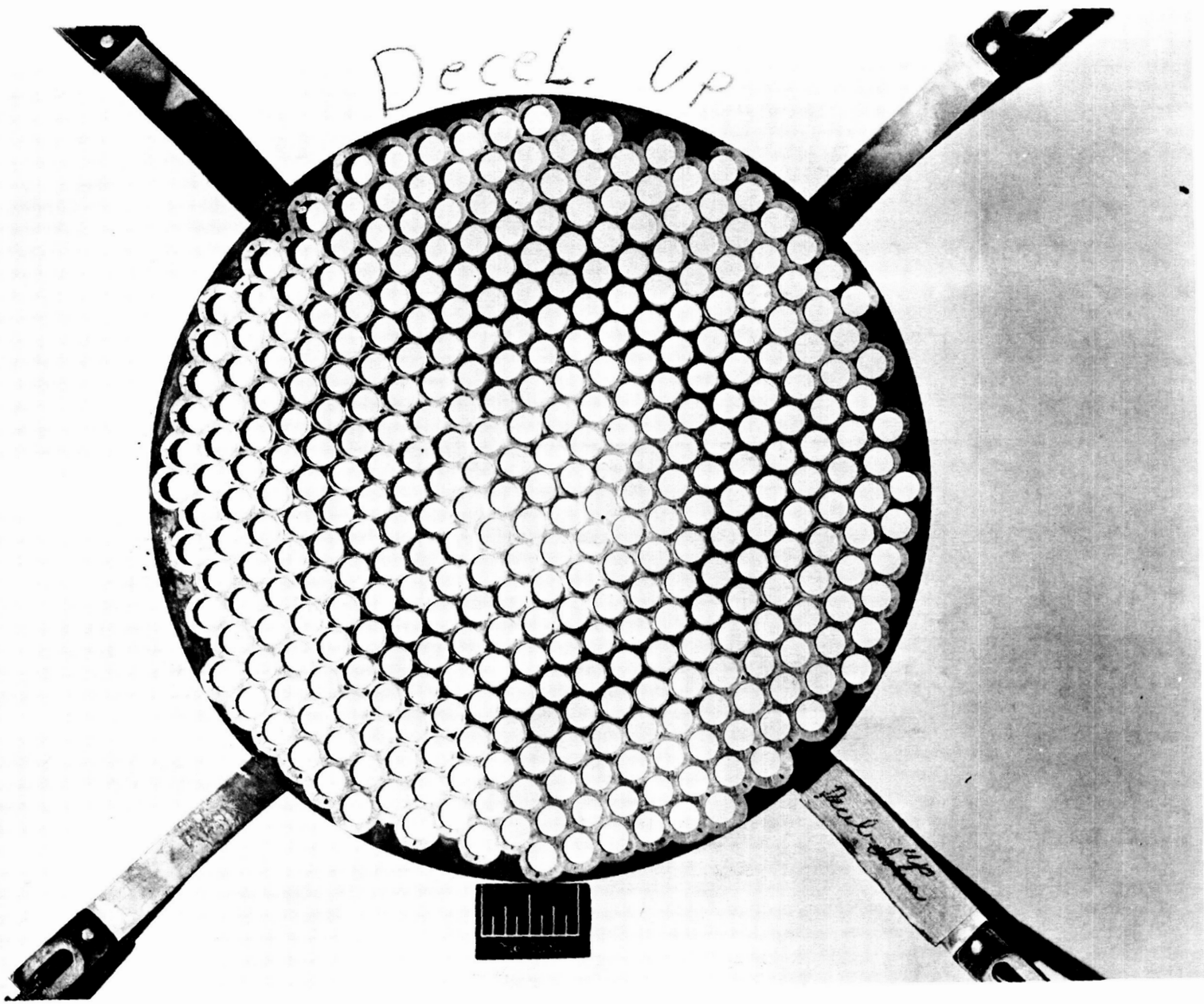


Fig. 123: Electrodes After EC III Run. Decelerator Upstream

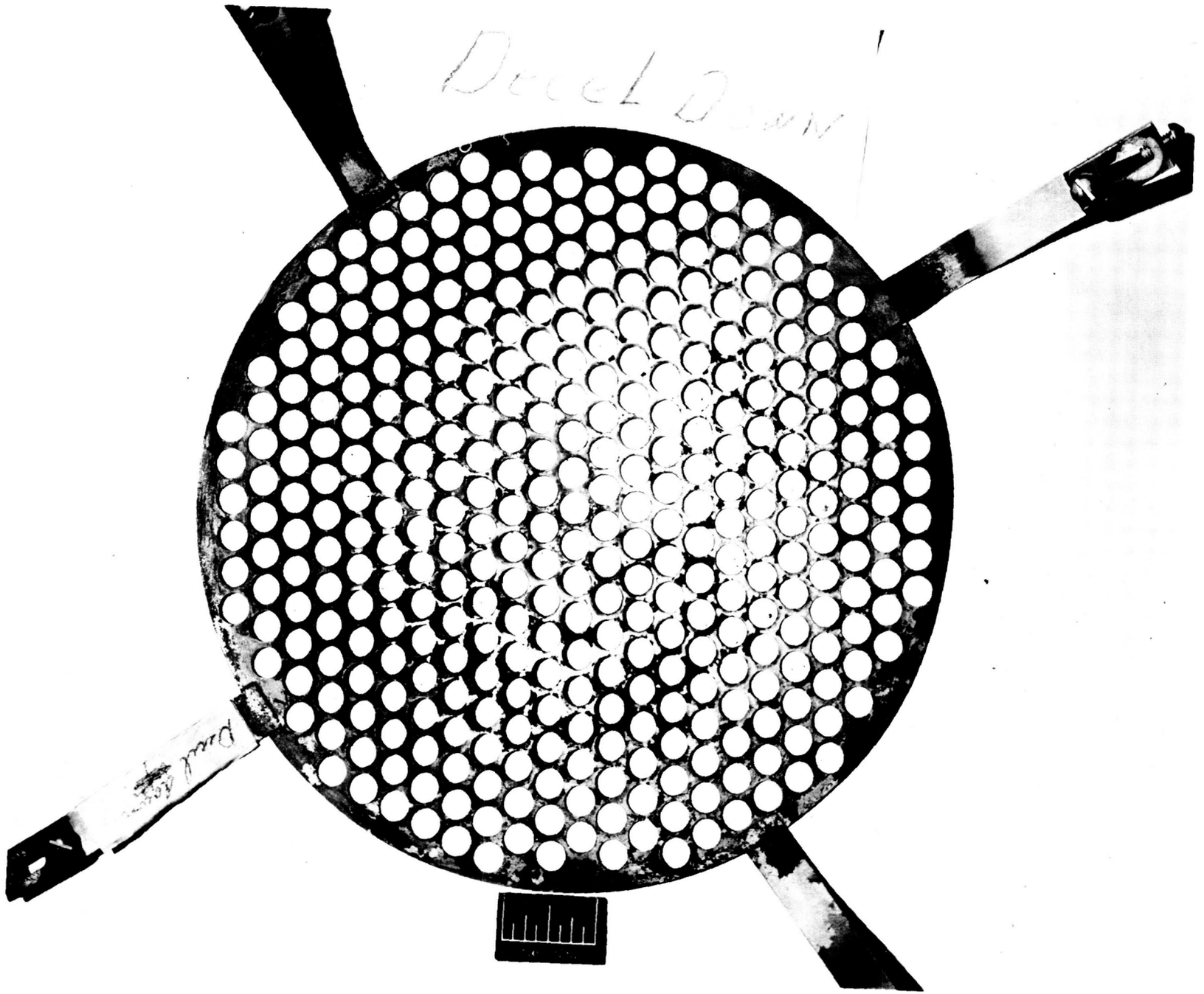


Fig. 124: Electrodes After EC III Run. Decelerator Downstream.

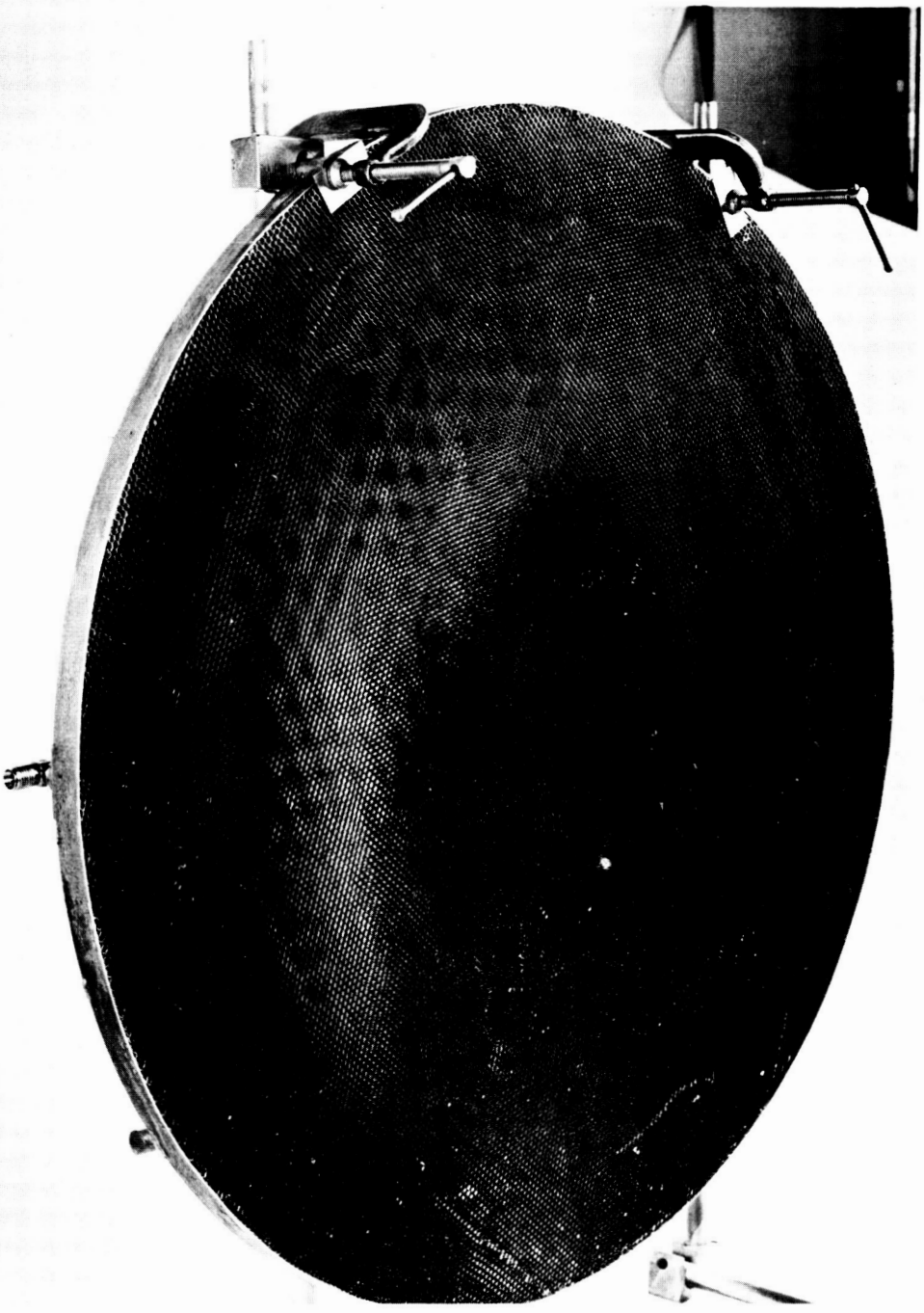


Fig. 125: The Target-Calorimeter After an Engine Run

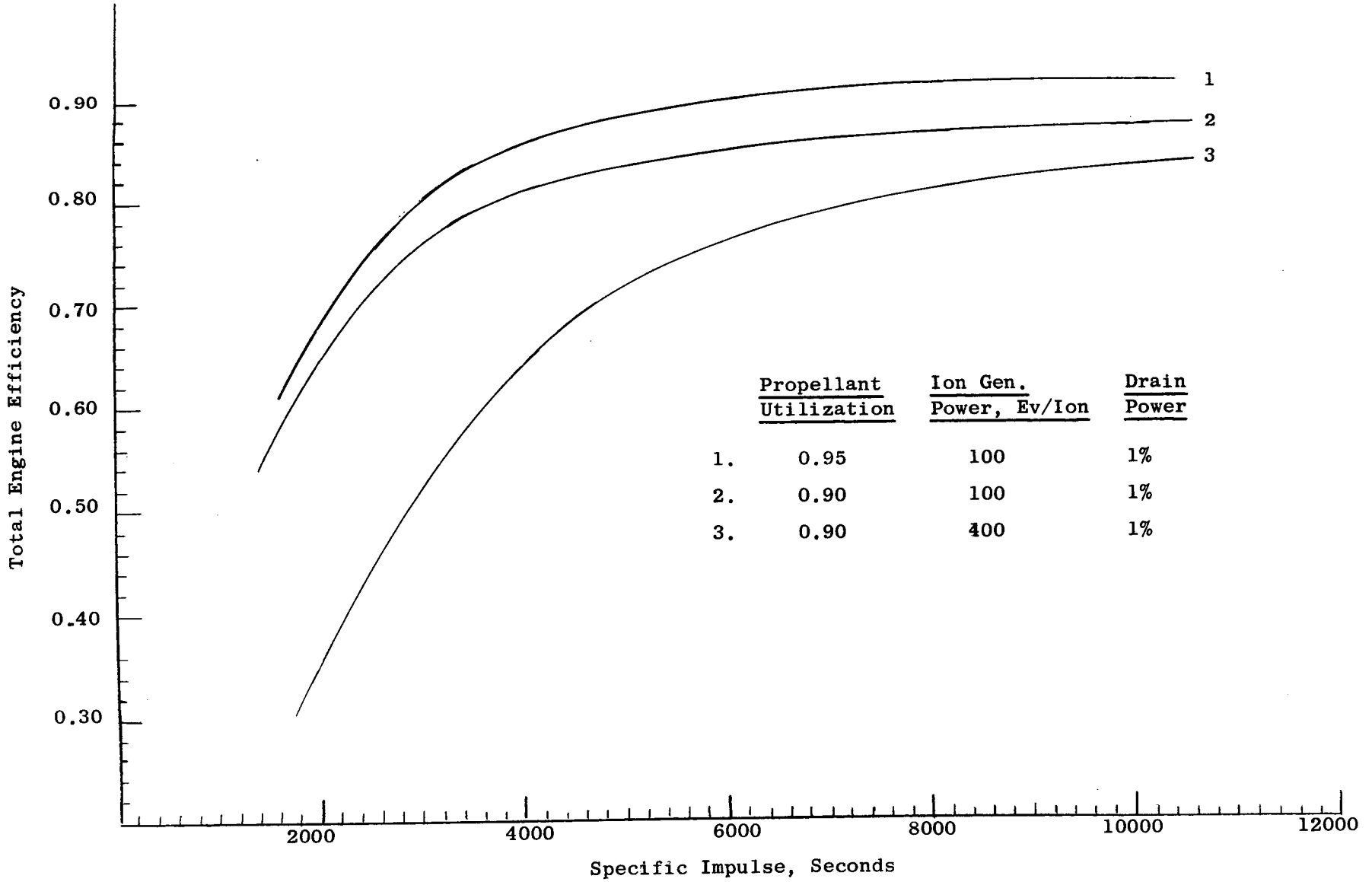


Fig. 126: Calculated Engine Efficiency for Two Values of Propellant Utilization and Two Values of Ion Generation Power

APPENDIX I

CALORIMETER VERIFICATION OF THE ION BEAM POWER IN THE PLASMA SEPARATOR ENGINE

by

B. A. Free, G. P. Kerr, and B. C. Merten

SUMMARY

A calorimeter based on temperature rise in a flowing coolant has been designed and tested. Beam power is compared independently with a heater calibrator in series with the calorimeter, and with the product of temperature rise, heat capacity, and calibrated flow rate of the coolant. Both methods confirm the beam power within 10% after radiation corrections are applied. Thermocouple measurements show that the conduction losses through the calorimeter supports and coolant leads are negligible. A radiation correction based on the Stefan-Boltzman formula has been derived and applied to correct for tare heat input to the calorimeter.

CALORIMETER DESIGN

Recently ion source and accelerator development reached a point where accurate calorimetric confirmation became of paramount importance. Consequently, the entire calorimeter was redesigned to increase accuracy to a point close to the limit for such measurements.

Overall Concept

A simplified coolant flow diagram is shown in Fig. 1. Pure isooctane (2, 2, 4 trimethyl-pentane) is pumped by means of a constant flow gear pump through a dry ice-methanol cooling bath and thence to the calorimeter. The fraction of the total coolant through the calorimeter is controlled by the valve and bypass arrangement shown, which regulates the upstream coolant

pressure. The return line from the calorimeter repasses through the cooling bath to insure comparable inlet temperatures in the calorimeter and calibrator heater.

Exactly the same fluid flow rate in both members is maintained by the series arrangement shown. The outlet line from the calibrator returns to the sump via a double throw valve which allows rerouting to a volume flow rate measuring device. All coolant lines, especially the inlets to the calorimeter and calibrator, are kept short and insulated to avoid unnecessary heat losses. The coolant is kept out of contact with air and the sump is equipped with a quantity of dessicant and a fine screen filter to avoid contamination of the coolant with water and dust. All leads to the sump discharge are below the liquid level to avoid inclusion of bubbles in the stream.

Heater-Calibrator Design

The design of the heater-calibrator is shown in Fig. 2. The purpose of this device is to provide a very accurate heat input to the flowing coolant. The heater-calibrator is constructed of thick walled glass tubing and nylon swagelok fittings, both of which are excellent thermal insulators. The coolant flows through the hollow power input leads to avoid any conductive lead losses and the bare-bead temperature measuring thermocouples are brought through the tee of the swagelok into a region of turbulence about 1-1/2" removed from the heater and shadow shielded from it. The heater is a 1/4" wide, 2' long nichrome ribbon which is silver brazed to the leads and twisted several full turns over its length to provide turbulence and swirl.

The entire device is suspended in a sealed wooden box and surrounded loosely on all sides with a mixture of fibrefrax, to prevent convection losses, and silica gel, to prevent condensation heat inputs. Tares on the calibrator at thermal equilibrium are invariably zero, showing that all extraneous heat losses or gains are negligible.

Calorimeter Design

The calorimeter design is shown in Fig. 3. It consists of two 2' diameter stainless steel plates separated by a one inch spiral stainless steel ribbon which forms a spiral passage 1 cm. wide from the center of the calorimeter to its outer edge. Inlet and outlet coolant lines consist of 1/4" stainless steel tubing, and all connections are made either by permanent welding or by swagelok fittings. A honeycomb of stainless steel is brazed to the front face in intimate contact with the steel plate. The calorimeter is mounted by means of three paraxial rods welded to its back face; these rods are in contact with the heavier vertical support rods only through line or point contacts made by support wires or pointed set screws in the insert.

TEMPERATURE MEASUREMENT AND CORRECTION

Thermocouple Calibrations

Chromel-alumel thermocouples, the use of which is validated by the latest ISA findings in this region, were calibrated in place by the use of selected freezing mixtures. The results are shown in Fig. 4.

The standard temperatures used were those of the solid CO_2/vapor equilibrium ($-78.5^{\circ}C$) modified by a barometric pressure (747 mm) correction to $-78.7^{\circ}C$; freezing chloroform ($-63.5^{\circ}C$); freezing carbon tetrachloride ($-22.9^{\circ}C$); and a pure ice bath. Quadruplicate readings on each thermocouple by two different operators checked within 0.02 mv maximum, corresponding to a maximum error of $0.5^{\circ}C$. In practice the accuracy was much better than this.

Conductive Heat Losses

Thermocouples are denoted on the calorimeter sketch by x and an arabic numeral. Conductive heat losses are evaluated by pairs 4 and 8, 3 and 2, and 3 and 1 by the standard formula:

$$(1) \quad W = 4.186\ k \frac{\Delta T}{\Delta X}\ A$$

where W is the conductive heat loss in watts, k the thermal conductivity in g cal sec^{-1} cm^{-2} $(^{\circ}C/cm)^{-1}$, ΔT the temperature differential, ΔX the distance differential along the conductor, and A the cross section normal to the heat flux vector.

Table 1 gives the maximum ΔT's observed across these pairs of thermocouples and the associated negligible conductive heat transfer losses.

TABLE 1

Conductive Heat Transfer Losses

TC Pair	ΔT	X, cm	A, cm^2	k	W, Watts
8, 4	$15^{o}C$	46	2.52	0.1	0.34
3, 2	$6^{o}C$	51	0.04	0.1	0.002
3, 1	$5^{o}C$	25	0.04	0.1	0.003

These results, and the fact that the heater-calibrator shows no tare readings, show that the calorimeter tares discussed below are radiative.

Radiative Losses

The existence and order of magnitude of radiative corrections to the calorimeter are shown by the size of the tare ΔT's measured without ion beam acceleration, and with the calorimeter surroundings in thermal equilibrium with the vacuum tank wall.

With no beam on, this tare is naturally larger than when the beam is on since the average calorimeter temperature is raised by the beam input. Typical

corrections are $\sim$70 watts at low temperature and $\sim$30-40 watts while running. Therefore, while no subtraction of the tare gives high results i.e., heat absorbed $>$ beam power, subtraction of the entire static tare gives low results. However, since the tares are radiative, the Stefan-Boltzman equation provides a convenient and accurate method of estimating running tares:

$$(2) \quad W = 5.672 \times 10^{-12} \epsilon \ (T^4 - T_s^4) \ A$$

where W is the net radiated power, ϵ is the emissivity, T is the effective calorimeter temperature, T_s is the effective temperature of the surroundings, and A is the radiating area of the calorimeter. The exact evaluation of this equation is hopeless, since the temperature varies widely over the surface of the calorimeter and surroundings, but a fairly accurate correction can be derived if we use the static tares to derive the effective surrounding temperature T_s, and then substitute for the temperature of the calorimeter a function of temperature, which varies with the beam input power across its face and with the spiral path length of the coolant.

Derivation of the Differential Stefan-Boltzman Equation

The average radius of a helical spiral path of width Δr is given by:

$$(3) \quad r = \frac{\theta}{2\pi} \Delta r + \frac{\Delta r}{2}$$

where θ is the total angle of the spiral, starting after the first complete revolution, and $\Delta r/2$ is the correction for starting the spiral. The differential spiral path length $d\ell$, neglecting the first irregular short length is:

$$(4)\quad d\ell = rd\theta = \frac{2\pi r}{\Delta r}\, dr$$

and by integration:

$$(5)\quad \ell = \left[\frac{\pi}{\Delta r}\, r^2\right]_{o}^{r}$$

Now the beam flux under consideration drops from any central value to one half of this value over a radial distance of 25 centimeters, the radius of the beam projected on the calorimeter. The assumption of a linear decay is very close to the true decay function and gives:

$$(6)\quad F_r = F_o\,(1 - \frac{r}{50})$$

Expressed as a function of ℓ, (6) becomes:

$$(7)\quad F_\ell = F_o\,(1 - \frac{1}{50}\sqrt{\frac{\ell\Delta r}{\pi}}) = F_o\,(1 - \frac{1}{50}\sqrt{\frac{\ell}{\pi}}) \text{ where } \Delta r = 1.$$

In the case of a static tare with no beam on the flux function is considered uniform, $F_\ell = C$.

The differential rise in temperature dT due to any heat input is given by:

$$(8)\quad dT = \frac{F_\ell \, d\ell}{\dot{m}\, Cp}$$

where $\dot{m}$ is the mass flow rate, Cp is the heat capacity of the coolant and $F\ell$ a suitable heat flux function of the spiral path length, e.g. equation (7)

Substitution of $F\ell = C$ into (8) and integrating gives:

$$(9)\quad \Delta T = \frac{C\Delta\ell}{\dot{m}\, Cp}$$

for the static tare temperature rise across the calorimeter.

Substitution of (7) into (8) and integrating gives:

$$(10)\quad \Delta T = \frac{F_o}{\dot{m}\, Cp} \int_o^{\ell} \left(1 - \frac{1}{50}\sqrt{\frac{\ell}{\pi}}\right) d\ell = \frac{F_o}{\dot{m}\, Cp}\left[\ell - \frac{2\pi}{3\,(50)}\left(\frac{\ell}{\pi}\right)^{3/2}\right]$$

for the running temperature rise with a beam density spread of 2:1.

The differential form of the Stefan-Boltzman equation for this case is given by:

$$(11)\quad dW = 5.672 \times 10^{-12} \sum \left[(T_{in} + \Delta T\ell)^4 - T_s^4\right] \quad d\ell$$

where T_{in} is the inlet temperature, T_ℓ is the temperature rise with coolant path, and $d\ell$ is numerically equal to the area differential because the path width equals unity. Integration of (11) gives the total power radiated across the area considered:

$$(12) \quad W = 5.672 \times 10^{-12} \int_o^{\ell} \left[(T_{in} + T_\ell)^4 - T_s^4 \right] \, d\ell$$

If a tare value for W is known by measurement, an effective value for T_s can be computed by substitution of (9) into (12) and solving for T_s.

If W is desired, equation (10) and an appropriate value for T_s is used in equation (12). The total radiated power is of course that radiated from or to the beam impingement area plus the area outside the perimeter of the beam.

RESULTS

Heater-Calibrator

The input power to the heater calibrator was checked by measuring the coolant flow rate and the temperature rise of the coolant across the heater by the equations:

$$(13)\quad W_{ab} = \dot{m} \int CpdT$$

$$(14)\quad W_{in} = VI$$

where W_{ab} is the heat absorbed by the coolant in watts, $\dot{m}$ is the mass flow rate, Cp is the heat capacity of the coolant in watt-seconds/$g^{o}C$, dT is the temperature differential, and W_{in} is the input watts to the heater in terms of V volts and I amperes.

The coolant is C.P. grade isooctane (2,2,4 - trimethyl pentane). Its density and heat capacity are accurately known and vary nearly linearly over the temperature range of interest. Working values of these properties were taken from data supplied by the Phillips Petroleum Company. The mass flow rate was determined accurately at the conclusion of each run with the power on, by collecting and measuring the volume of liquid passed during a timed interval. Volume and temperature were measured simultaneously.

The results are expressed in Table 2 and Fig. 5, which establishes the accuracy of either standard, i.e., electrical input power or heat absorbed by the coolant.

Calorimeter Measurements

Table 3 and Fig. 6 give the gross heat absorbed in the calorimeter as a function of the beam power, calculated in two ways. Equations (13) and (14), applied to the calorimeter, were used to compare heat absorbed, as measured by the product of coolant flow rate, heat capacity, and rise in temperature, with the beam power. The formula (with a minor correction for heat capacity):

$$(15) \quad W_C = W_H \frac{\Delta T_C}{\Delta T_H}$$

TABLE 2

Heat Absorbed by Coolant at Various Heater Power Levels

TEMP, °C In	TEMP, °C Out	Mass Flow, g/sec	Av. Heat Capacity Watt sec/g°C	Input, Watts	Absorbed, Watts
-60.8	-53.6	19.1	.420	157	177
-58.5	-47.0	20.2	.423	302	304
-57.2	-46.2	22.4	.425	321	320
-57.9	-46.2	21.5	.425	323	326
-65.6	-50.8	20.0	.420	360	378
-56.8	-44.8	26.4	.426	406	413
-54.1	-37.0	21.2	.430	470	473
-54.8	-37.2	21.1	.430	478	486

was used to calculate W_C the heat absorbed in the calorimeter, as a function of the input power to the heater-calibrator W_H, and the temperature rise ratio of the calorimeter to heater-calibrator $\Delta T_C / \Delta T_H$. It can be seen that the methods are identical for all practical purposes.

TABLE 3

Calorimeter Readings at Various Beam Power Levels

T, °C	Mass Flow g/sec.	Av. Heat Capacity Watts-sec/g °C	Measured Beam Power, Watts	Measured Heater Power, Watts	Heater ΔT, °C
8.9	14.0	1.76	158	157	7.2
12.7	14.9	1.77	292	302	11.5
8.5*	16.6	1.78	320	321	11.0
12.2	15.7	1.78	325	323	11.7
14.0	14.7	1.76	348	360	14.8
9.2*	19.2	1.78	426	406	12.0
16.5	15.4	1.80	448	470	17.1

*Tank liner cooled with liquid nitrogen.

With the reliability of the heater as a standard power input established, the need for subsequent measurement of flow rate is not necessary, since the flow rate must be identical at any time in the series-connected calorimeter and heater-calibrator. Since beam and heater power can be measured much faster with the present setup than can flow measurement, this eliminates a possible source of error due to small gradual changes in flow rate.

Tare Corrections

The method of calculating radiative corrections by the Stefan-Boltzman equation has already been described. Equations (9) and (12) were applied to a series of tare runs with the tank liner uncooled, and resulted in values for the effective temperature of the surroundings, T_s, of 249, 250, 252, and 267°K. The average value of 254°K is used in the following calculations.

A working form of equation (12) with all negligible terms dropped, is:

$$(12a)\quad W = 5.672 \times 10^{-12} \sum \left[(T_{in}^4 - T_s^4) \ell_b + 4 T_{in}^3 \frac{F_o}{\dot{m}\, Cp} \left(\frac{\ell_b^2}{2} - 3.01 \times 10^{-3} \ell_b^{5/2} \right) + 3 T_{in}^2 \left(\frac{F_o}{\dot{m}\, Cp} \right)^2 \ell_b^3 + 894 (T_{out}^4 - T_s^4) \right]$$

where W is the power radiated from one face of the calorimeter, ℓ_b is the spiral coolant path over the beam impingement area, F_o is the axial beam power in watts/cm^2 and 894 is the numerical value of the spiral path length and area outside the beam impingement area. This equation holds for a beam with 2:1 linear fall in current density over a beam radius of 25.4 cm.

Table 4 gives the pertinent experimental values for calculating the running tares for the corrected data points in Fig. 6. The corrected values are shown in Fig. 7.

Discussion

The results shown are not corrected for small heat losses due to sputtering, electron emission, or emissivity lower than unity, and the radiation corrections do not take into account the skin temperature elevation above the coolant temperature. Application of these corrections would raise the calorimeter power slightly, make the errors random instead of always negative, and result in better checks by a few percent.

Fig. 7 shows that the limits of the net calorimeter power/beam power ratio range from 1.01 to 0.82, with most of the data points checking within 10%. This range of accuracy is typical of this type of calorimeter.

At the relatively low beam power levels measured to date, the range of error is of the same magnitude as the radiation tare corrections, and the accuracy is expected to increase at future high power levels where the radiation tares become less significant. It is noteworthy that checks within 5% were obtained at the two highest beam power levels examined to date.

TABLE 4

Values of Elements for Calculating Radiative Tares

T_{in}^2, $^oK \times 10^{-4}$	T_{in}^3 $^oK \times 10^{-7}$	T_{in}^4 $^oK \times 10^{-9}$	T_{out}^4 $^oK \times 10^{-9}$	T_s^4, $^oK \times 10^{-9}$	ℓ_b, cm $\times 10^{-3}$	ℓ_b^2, cm $\times 10^{-6}$	$\ell_b^{5/2}$, cm $\times 10^{-8}$	ℓ_b^3, cm $\times 10^{-9}$	F_o, Watts/cm^2	$\dot{m}$ Cp, Watts/^oC	$F_o/\dot{m}Cp$ (^oC/cm^2) $\times 10^3$	$F_o/\dot{m}Cp$ (^oC/cm^2) $\times 10^5$	W, Watts Per Face
4.62	0.99	2.13	2.51	4.16	2.026	4.105	1.846	8.316	.118	24.6	4.80	2.30	-30
4.69	1.02	2.20	2.76	4.16	2.026	4.105	1.846	8.316	.218	26.4	8.25	6.81	-26
4.81	1.06	2.32	2.70	0.43*	2.026	4.105	1.846	8.316	.239	29.5	8.10	6.56	+37
4.65	1.00	2.16	2.70	4.16	2.026	4.105	1.846	8.316	.243	27.9	8.71	7.59	-27
4.44	0.93	1.97	2.54	4.16	2.026	4.105	1.846	8.316	.260	25.9	10.00	10.00	-30
4.73	1.03	2.23	2.64	0.43*	2.026	4.105	1.846	8.316	.318	34.2	9.30	8.65	+36
4.80	1.05	2.30	3.08	4.16	2.026	4.105	1.846	8.316	.335	27.7	12.10	14.60	-22

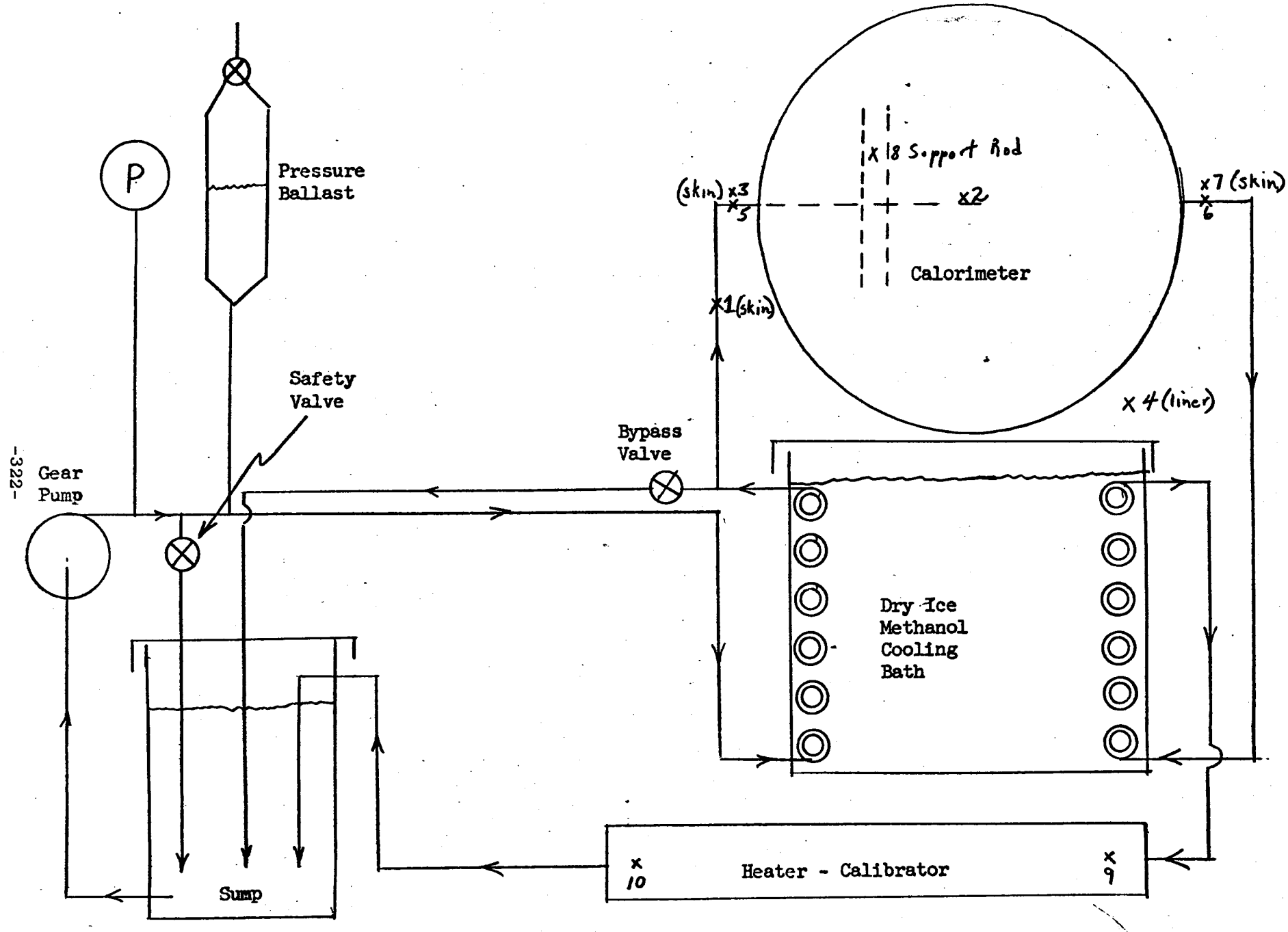


Fig. 1: Coolant Flow Diagram

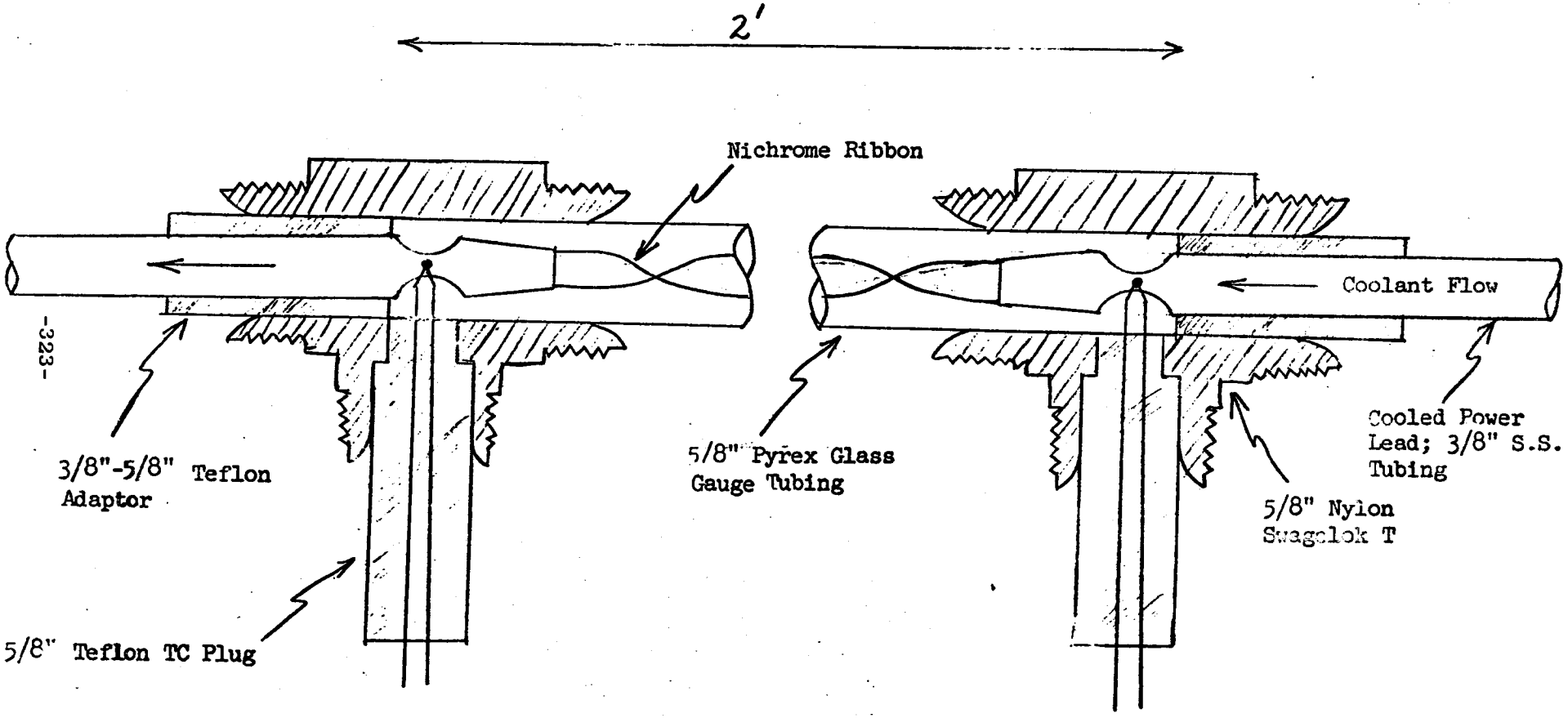


Fig. 2: Heater-Calibrator Design

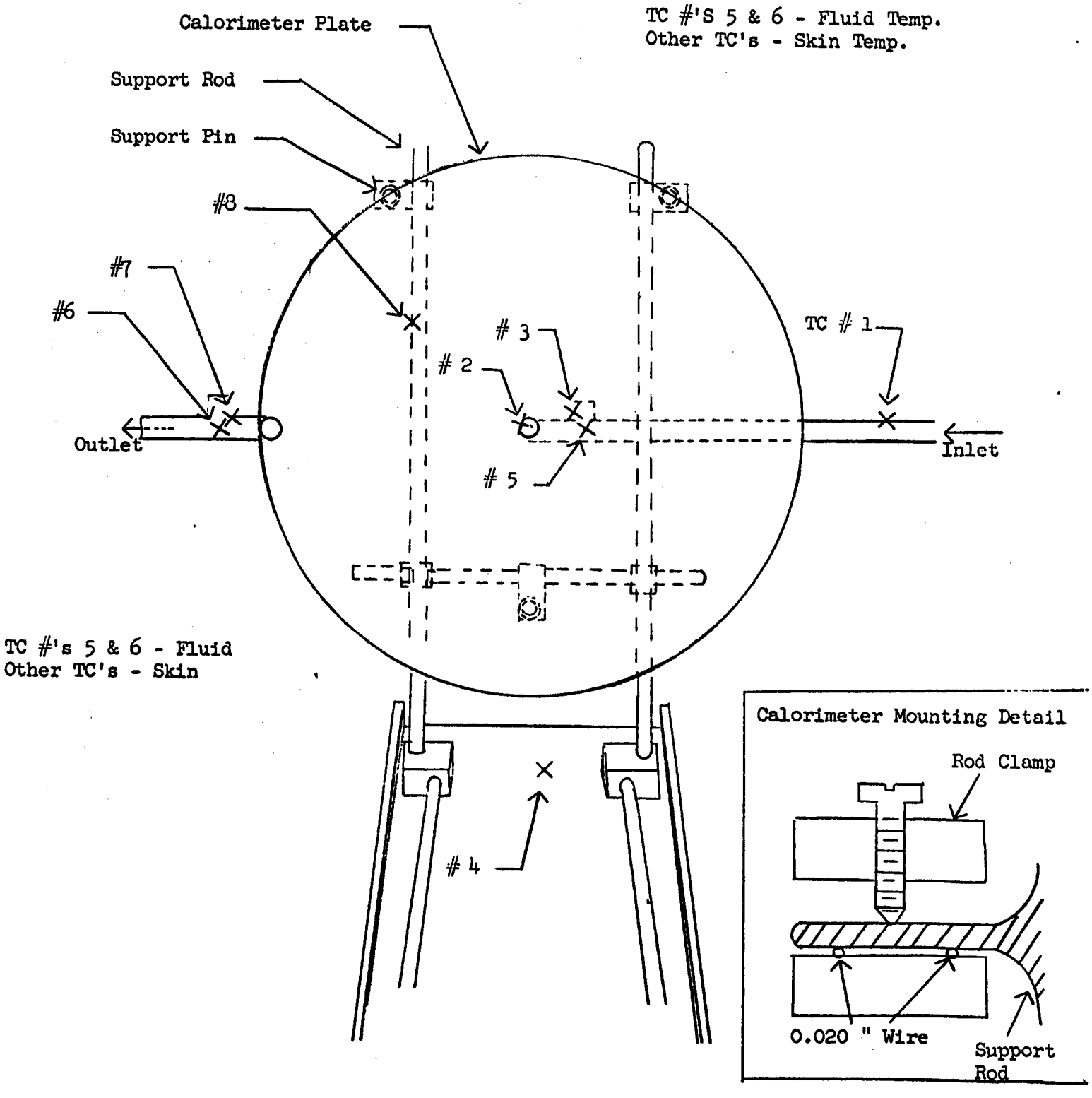


Figure 3: Calorimeter Design and Mounting

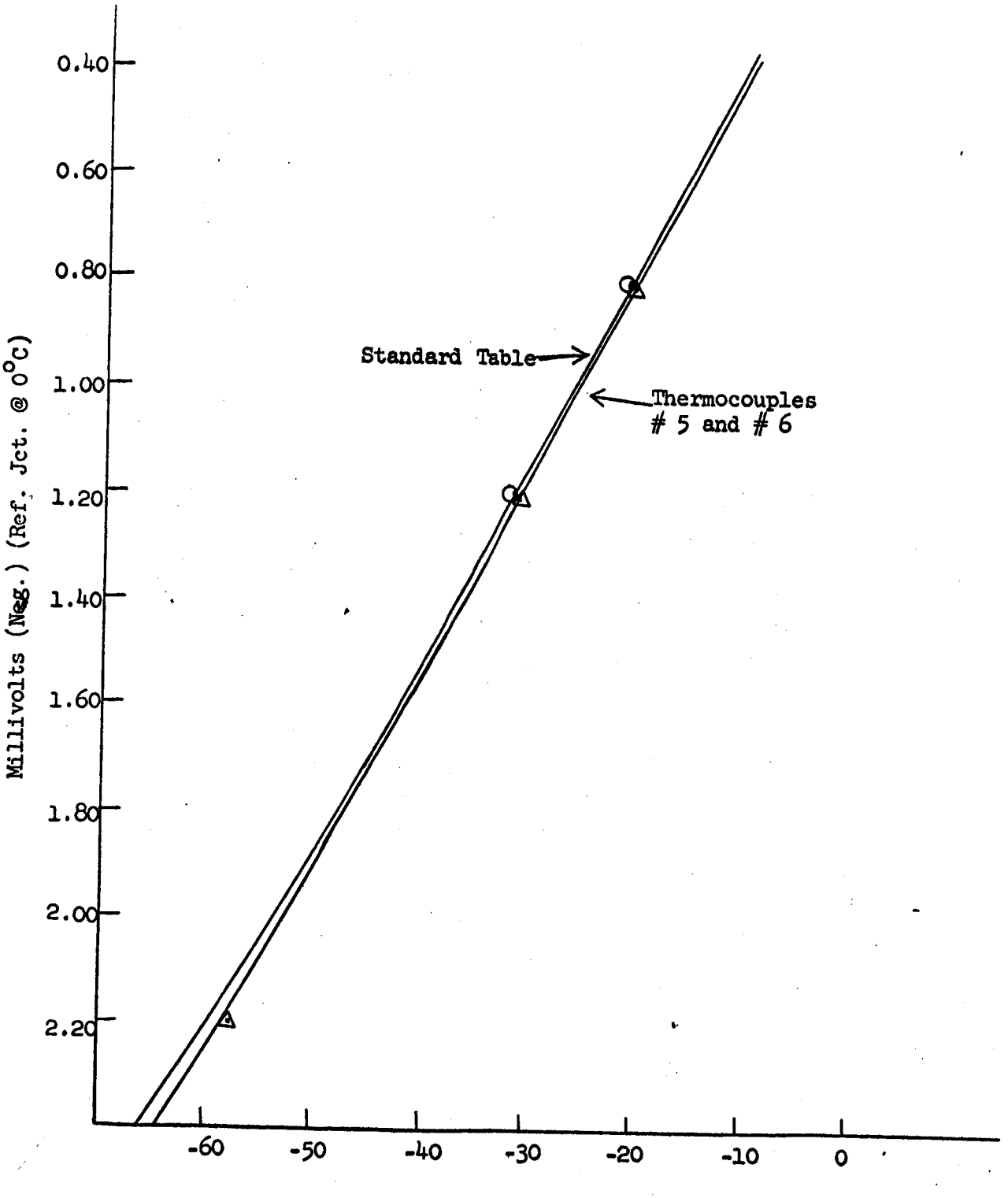


Figure 4: Calorimeter Thermocouple Calibration

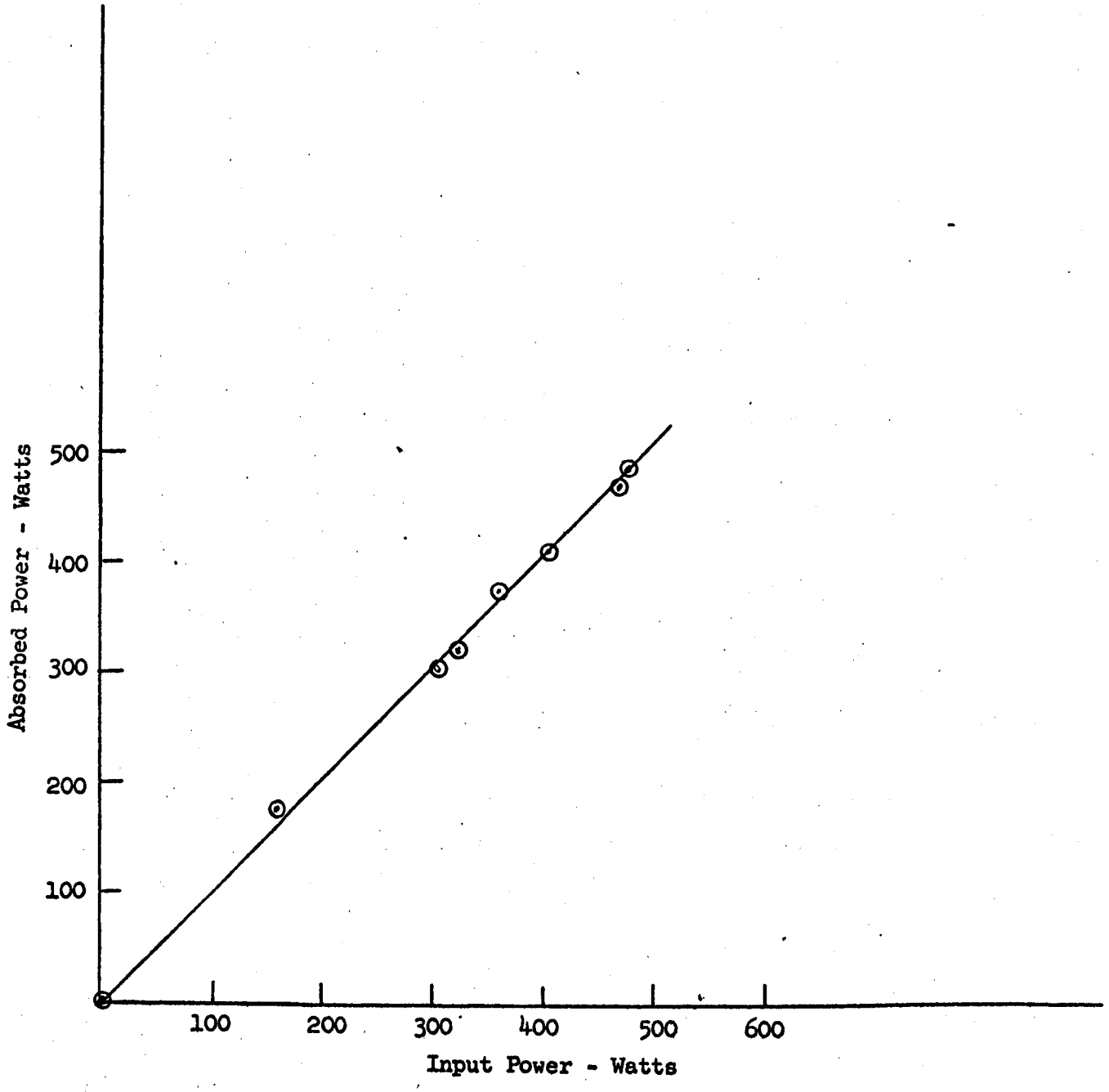


Figure 5: Calibrator Performance

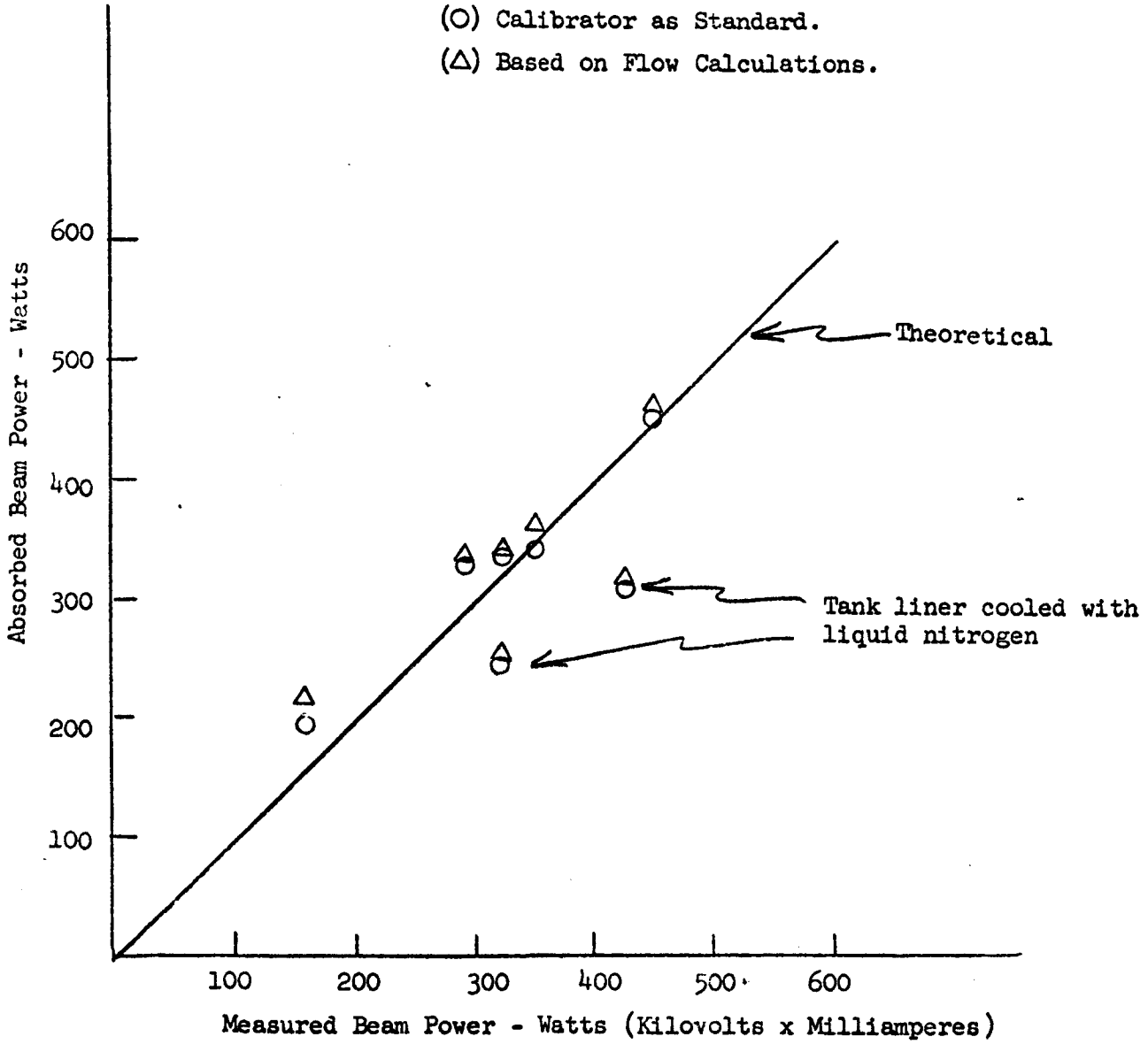


Figure 6: Comparison of Gross Values of Calorimeter-Absorbed Beam Power to Incident Beam Power

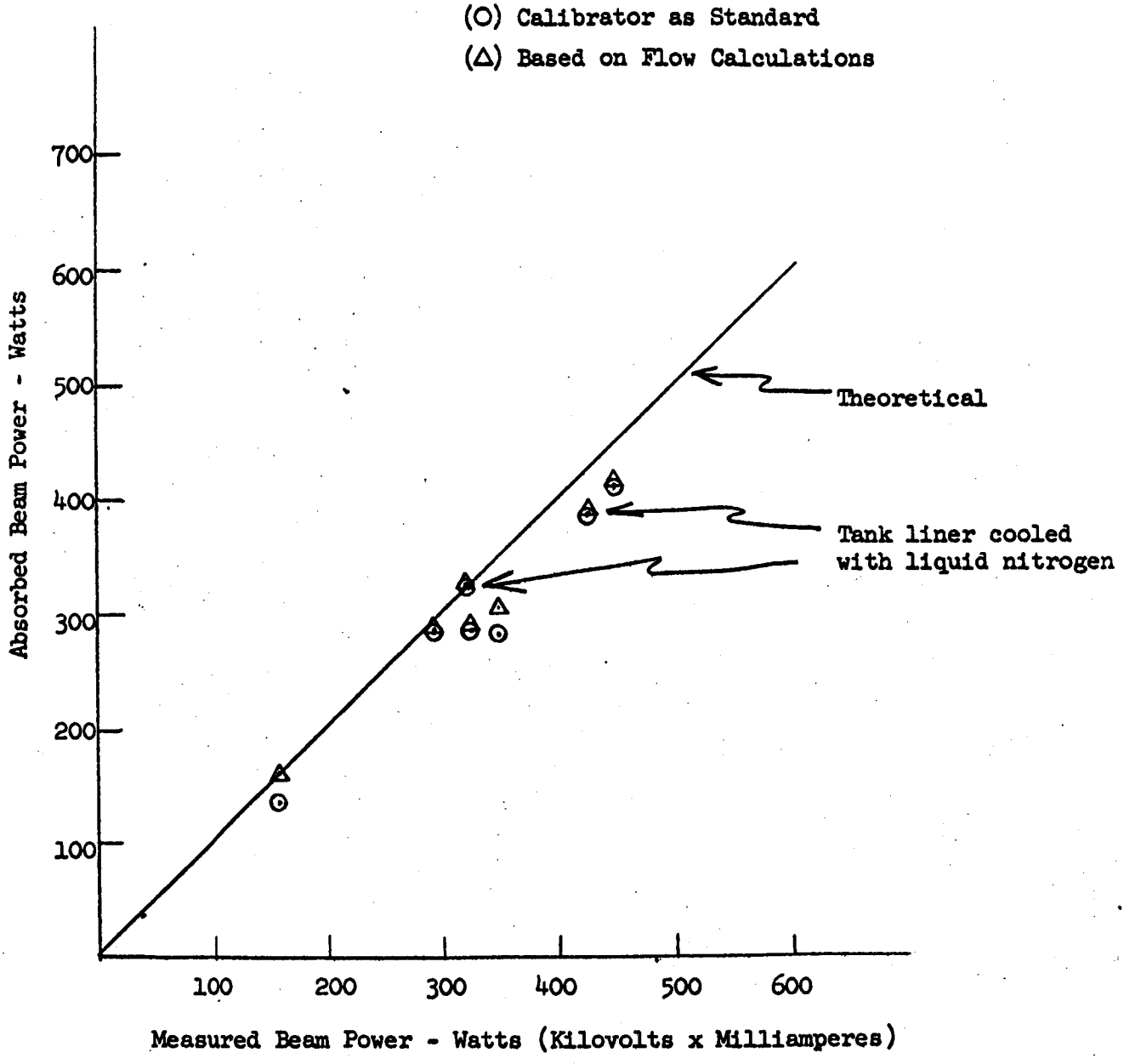


Figure 7: Comparison of Net Values of Calorimeter Absorbed Beam Power to Incident Beam Power

DM S-64-6

APPENDIX II

COMPARATIVE ION ENGINE MISSION PERFORMANCE CAPABILITIES

Harold Brown, Manager
Mission Analysis and Evaluation
Space Power and Propulsion Section
Building 701, N-12, Ext. 4873

NOMENCLATURE

a	Thrust Acceleration - meter/sec.^{2}
g	Sea Level Gravitation Constant - 79,000 miles/hr.^{2}
I_{sp}	Specific Impulse - seconds
J	Low Thrust Parameter - meters^2/sec.^{3}
L	Characteristic Length - miles
P	Power - KW
t	Trip Time - hours
t_P	Propulsion time - hours
T	Thrust - lbs.
$\triangle V$	Characteristic Velocity - f.p.s.
w	Powerplant Specific Weight - lbs/Kw
w_g	Spacecraft Guidance and Control System Weight Ratio
w_T	Propellant Task Weight Ratio
W_o	Initial Nuclear - Electric Spacecraft Weight - lbs.
W_1	Terminal Nuclear - Electric Spacecraft Weight - lbs.
W_{PL}	Net Payload Weight - lbs.
W_{PP}	Propellant Weight - lbs.
W_{PS}	Power Supply Weight - lbs.
η_{TH}	Thrustor Efficiency

Subject: Comparative Ion Engine Mission Performance Capabilities

Cincinnati, Ohio - August 28, 1964

1. INTRODUCTION

This memo presents the results of a comparison of the potential mission performance capabilities of the plasma separator ion engine with those of the electron bombardment ion engine in order to indicate the significance of the improved plasma separator engine efficiency characteristics recently demonstrated in our laboratory. Three electric propulsion missions have been used for this comparison - an unmanned Mars orbiter, an unmanned Jupiter orbiter, and a manned Mars round trip - in order to present the comparison over a substantial range of mission difficulty. The unmanned mission performance data are shown for a range of powerplant specific weights and trip time in order to permit engine comparisons at either constant trip time or constant payload. Similar, but less detailed data are presented for the Manned Mars Mission.

2. ENGINE ASSUMPTIONS

The electron bombardment engine performance characteristics have been obtained from Reference 1. These data are illustrated in Fig. 1 as a function of the propulsion system specific impulse. The propellant utilization efficiency and the overall thrustor efficiency are shown. The engine electrical efficiency can be obtained by dividing the propellant utilization efficiency into the thrustor efficiency. According to Reference 1, these data represent theoretical maximum performance obtainable by the bombardment engine.

The plasma separator engine performance characteristics are also shown in Fig. 1. Current tests over the range of 5000 to 8000 seconds specific impulse have demonstrated propellant utilization efficiencies of the order of 90% and that the efficiency is essentially independent of specific impulse. The electrical efficiency characteristics have been based upon the following demonstrated source performance at currents in excess of 300 ma.

Ion Generation and Flow Control - 70 eV/ion

Drain Power - 2% of Total Power

These efficiency characteristics have been combined with the propellant utilization efficiency to produce the overall thrustor efficiency characteristic illustrated in Fig. 1. Although complete engine tests have been limited by the current accelerator geometry to operation at currents less than 300 ma, overall thrustor efficiencies within 96% of those shown in Fig. 1 have been obtained.

Engine power requirements can be obtained from Fig. 1 and the equation:

$$(P/T) = \frac{I_{sp}}{45.86\,\eta_{TH}} \text{ , KW/lb} \qquad (1)$$

The resulting power requirements of each engine have been represented by the following empirical relationships:

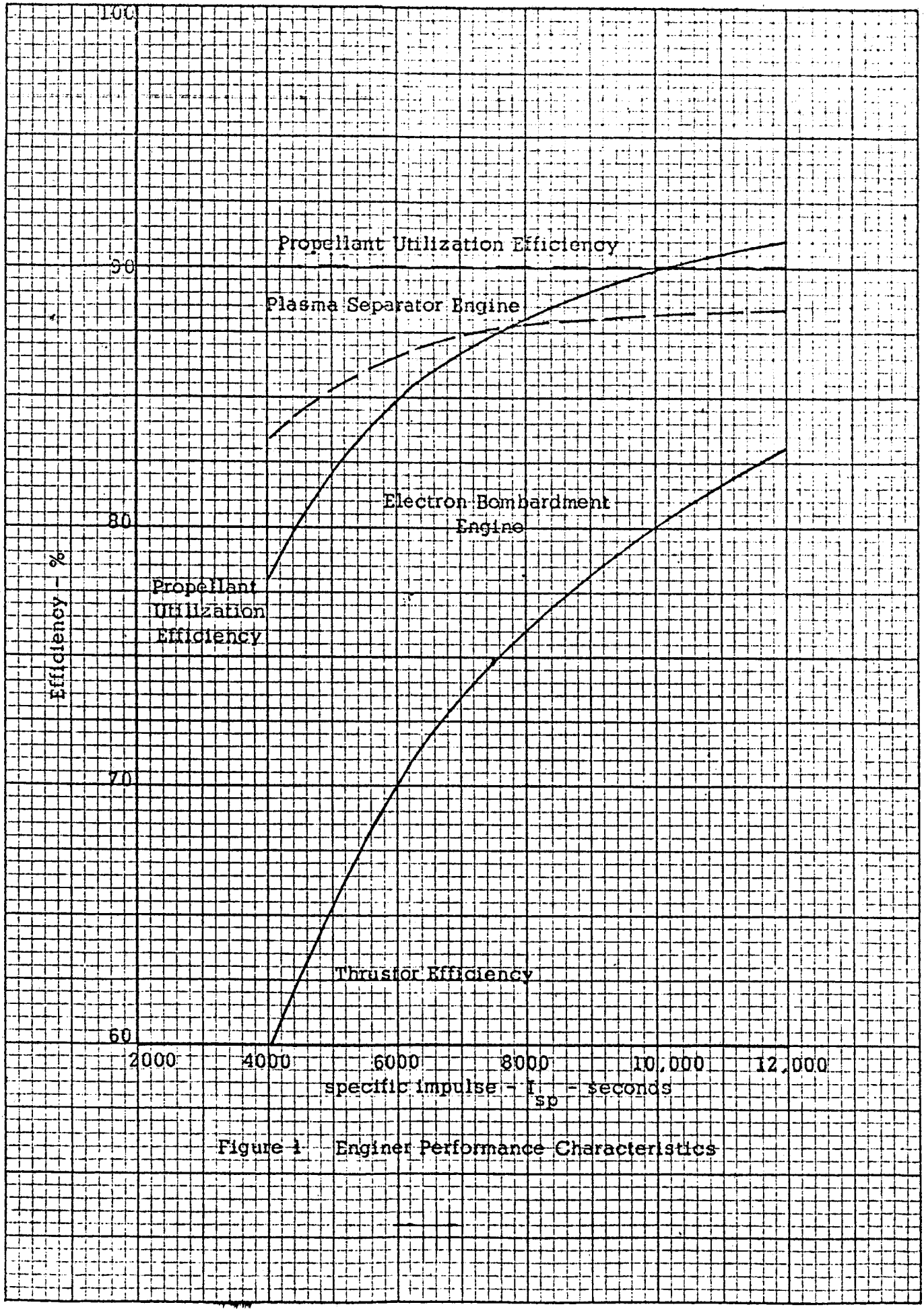


Figure 1 Engine Performance Characteristics

$$(P/T) = 48 + 2.15\ (10)^{-2}\ I_{sp} \quad \text{(Bombardment Engine)}$$

$$(P/T) = 7 + 2.40\ (10)^{-2}\ I_{sp} \quad \text{(Plasma Separator Engine)} \qquad (2)$$

A power conditioning system efficiency of 96% has been assumed for each engine to account for losses between the power generation system and the engine.

3. MISSION PROFILES

The engine performance characteristics of equations (2) have been used to generate mission performance capabilities for three electric propulsion missions. The Mars orbiter mission was selected as being representative of the relatively short-low characteristic velocity missions under consideration for electric propulsion. The following mission profile was assumed:

Mars Mission Profile

1. Boost to 300 m. Earth Orbit with Saturn 1B
2. Nuclear-Electric Propulsion to Earth Escape
3. Nuclear-Electric Propulsion to Parabolic Mars Approach (with intermediate heliocentric coast period)
4. Nuclear-Electric Propulsion Descent to 300 m. Circular Orbit about Mars

The Jupiter orbiter mission was selected as being representative of the relatively long - high characteristic velocity missions which are generally considered feasible only with electric propulsion. The mission profile differs from the above Mars mission only in the use of a larger boost vehicle and a substantially higher orbit altitude about Jupiter.

Jupiter Mission Profile

1. Boost to 300 m. Earth Orbit with Saturn V
2. Nuclear-Electric Propulsion to Earth Escape
3. Nuclear-Electric Propulsion to Parabolic Jupiter Approach (with intermediate heliocentric coast period)
4. Nuclear-Electric Propulsion Descent to 1,100,000 m. Circular Orbit about Jupiter

Note that the terminal altitude selected will bring the payload to the vicinity of Callisto, the outermost of Jupiter's four major moons.

The Manned Mars Round-Trip mission combines the worst aspects of each of the others in that it requires a relatively short trip time with a high characteristic velocity requirement. The current approach under investigation in our study contract - NAS8-11423 - involves the following mission profile.

Manned Mars Mission Profile

1. Boost to 300 m. Earth Orbit with several Saturn V's and Assemble
2. Boost beyond Earth Escape with 250,000 lb. Thrust Nuclear Rocket
3. Nuclear-Electric Propulsion to Parabolic Mars Approach (with intermediate heliocentric coast period)
4. Nuclear-Electric Propulsion Descent to 300 m. Circular Mars Orbit
5. Orbit Mars for 40 Days - 100,000 lb Excursion Module Lands on Mars with 3 Man Crew and Returns Crew to Orbiter
6. Nuclear-Electric Propulsion to Mars Escape (Excursion Module is left at Mars)
7. Nuclear-Electric Propulsion to Hyperbolic Earth Approach (with intermediate heliocentric coast period)
8. Re-enter Earth's Atmosphere at 50,000 f.p.s.

This approach has been used in comparing the above engines.

4. ANALYSIS

In order to obtain a valid comparison of the potential performance capabilities of the engines, it is necessary to optimize the nuclear-electric spacecraft thrust-weight ratio (or power-weight ratio) and engine specific impulse as a function of the individual mission characteristic velocity-trip time requirements, the powerplant specific weight, and the assumed engine efficiency characteristic. The unmanned-one way missions permit the use

of a relatively straightforward two-step optimization process. The added complexity of the manned-round trip mission, on the other hand, requires the use of a more sophisticated multi-dimensional optimization process. Each of these techniques will be described in more detail in the following sections.

a. Unmanned One-Way Missions

The results of our recent Navigator Study (Reference 2) have shown that the characteristic velocity requirements for the heliocentric phase of optimum planetary rendezvous trajectories are dependent only on the heliocentric trip time. It is furthermore shown that the characteristic velocity requirements for the geocentric earth escape and the planetary capture phases are dependent primarily on the initial earth orbital altitude and the terminal planetary orbital altitude. These results suggest than an optimization at constant characteristic velocity should produce results which are equivalent to an optimization at constant heliocentric or total trip time.

The gross payload ratio of a nuclear-electric spacecraft is first defined as:

$$W_{PL}/W_o = 1 - (1 + w_T)\,(W_{PP}/W_o) - (W_{PS}/W_o) - w_g \qquad (3)$$

The propellant and powerplant weight fractions are then defined in terms of the mission or thrustor parameters as follows:

$$W_{PP}/W_o = 1 - (W_1/W_o) = 1 - e^{-\Delta V/g\, I_{sp}} \tag{4}$$

$$W_{PS}/W_o = w\,(T/W_o)(P/T) = w\,(T/W_o)(A\, I_{sp} + B) \tag{5}$$

Equations (4) and (5) can then be substituted into equation (3):

$$W_{PL}/W_o = 1 - (1 + w_T) - w_g - (1 + w_T)e^{-\Delta V/g\, I_{sp}} - w(T/W_o)(A\, I_{sp} + B) \tag{6}$$

The resulting equation (6) can then be differentiated with respect to specific impulse at constant characteristic velocity and thrust-weight ratio and equated to zero to maximize the payload ratio.

$$\frac{d(W_{PL}/W_o)}{d\, I_{sp}} = 0 = (1 + w_T)\left(\frac{\Delta V}{g I_{sp}^2}\right)(e^{-\Delta V/g\, I_{sp}}) - w\, A\, (T/W_o) \tag{7}$$

Equation (7) can then be solved for the thrust-weight ratio corresponding to the optimum specific impulse - characteristic velocity combination:

$$(T/W_o) = \frac{(1 + w_T)(W_1/W_o)\,\Delta V}{A\, g\, w\, I_{sp}^2} \tag{8}$$

The use of equation (8), therefore, represents the first step of the two-step optimization process. Note that this step is completely independent of the mission requirements.

The second step in the optimization process serves to identify the optimum specific impulse - characteristic velocity - trip time relationship for the specific mission under investigation. The heliocentric mission requirements are obtained by converting the conventional low-thrust parameter:

$$J = \int a^2 \, dt \tag{9}$$

into the characteristic length of Reference (3) through the equation:

$$L = \sqrt{\frac{Jt^3}{12}} \tag{10}$$

Table 1 summarizes the variation of J (as obtained from Reference 4) and L (as calculated by equation 10) with trip time for the Mars and Jupiter missions investigated. These data were represented empirically by equations of the form:

$$L = C_1 t^2 + C_2 t + C_3 \tag{11}$$

The characteristic length can, however, be expressed in terms of the thrustor parameters as follows:

$$L = \frac{g I_{sp}}{(T/W_o)} \left[(1 - \sqrt{W_1/W_o})^2 - \frac{(T/W_o)}{g I_{sp}} (t - t_p) \ln W_1/W_o \right] \tag{12}$$

where

$$W_1/W_o = e^{-\Delta V/g\, I_{sp}} \qquad (13)$$

Equations (11) and (12) can then be equated and solved for the trip time:

$$t = \frac{1}{2C_1}\left[\Delta V - C_2 - \sqrt{(\Delta V - C_2)^2 - 4C_1(C_3 - D)}\right] \qquad (14)$$

where:

$$D = \frac{g\, I_{sp}^{\,2}}{(\quad W_o)}\left[(1 - \sqrt{W_1/W_o})^2 + \frac{1}{2}(1 - W_1/W_o)\ \ln W_1/W_o\right] \qquad (15)$$

Note that equations (10) through (15) apply only to the heliocentric phase of the missions and, consequently, the geocentric and planetary phases must be obtained separately. These were obtained from the data of Reference (2).

The actual process was carried out by assuming an arbitrary matrix of specific impulse and characteristic velocity and utilizing equations (1), (3), (14), and (15) to determine the payload and the overall trip time. The results were then plotted against specific impulse for lines of constant characteristic velocity as illustrated in Fig. 2 and 3. Constant trip time lines were then obtained from Fig. 2 and superimposed on the data of Fig. 1. The optimum payload at constant trip time is then readily evident.

The results obtained from this process for the one-way Mars and Jupiter orbiter missions are described in Section 5.

TABLE I

Heliocentric Mission Requirements for Optimum Rendezvous Trajectories

Mission	Heliocentric Trip Time t-days	Low Thrust Parameter J-meters^2/sec.^{3}	Characteristic Length L-million miles
Mars	120	28.38	31.8
	150	13.28	30.4
	180	7.05	29.2
	210	4.146	28.2
	240	2.675	27.7
	255	2.221	27.6
Jupiter	180	974.7	343.5
	360	105.37	319.4
	540	29.19	308.8
	720	12.627	312.7
	900	7.298	332.3

b. Manned Round-Trip Missions

Manned-round-trip missions are complicated by the need to optimize the propulsion parameters for both the outbound and inbound heliocentric legs and by the requirement to rendezvous with the Earth on the return leg. This last factor necessitates the use of non-optimum one-way trajectories in order to obtain an overall central angle for the trajectory which matches the Earth's central angle during the round-trip. These considerations result in five additional parameters - for a total of seven-which must be optimized for a valid solution.

This problem has been solved by the use of the multi-dimensional LEADER optimization process (Reference 5). The following parameters were used as independent variables to be determined by the optimization process:

1. Vehicle Initial Gross Weight in Orbit
2. Outbound Heliocentric Mass Ratio
3. Outbound Propellant Flow Rate
4. Outbound Velocity Ratio - $\frac{\text{Nuclear Rocket Hyperbolic Excess Vel.}}{\text{Nuclear-Electric Jet Velocity}}$
5. Outbound Coast Time to Trip Time Ratio
6. Inbound Nuclear-Electric Jet Velocity
7. Earth Arrival Date

Note that the Earth arrival date was allowed to vary only over a launch window of 3000 hours in any selected synodic period. These parameters serve as input to a mathematical model of the Manned Mars Mission which evaluates some 60 auxiliary powerplant and mission parameters including, for example, launch date, power rating, intermediate trip times, and payload at constant powerplant

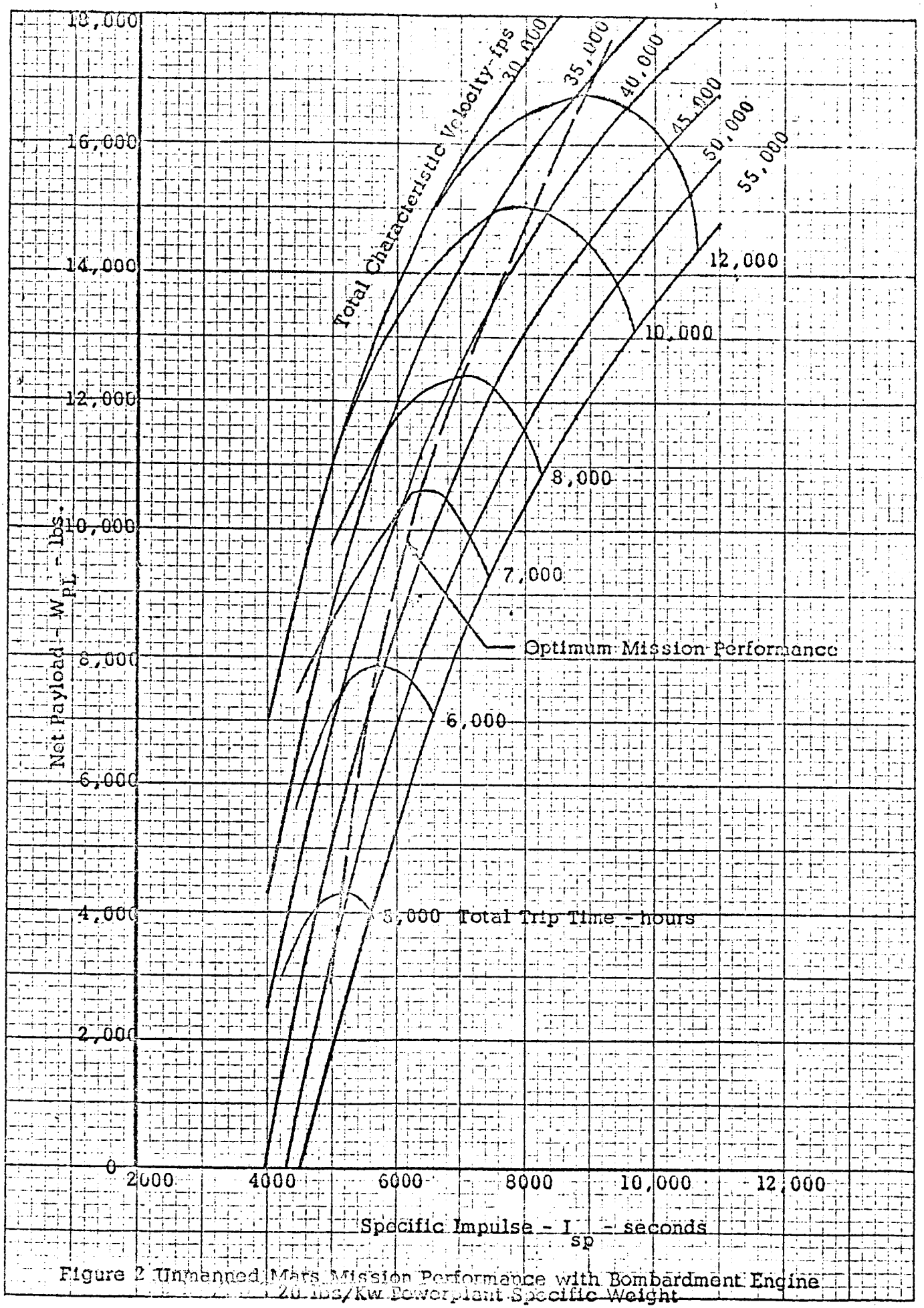


Figure 2 Unmanned Mars Mission Performance with Bombardment Engine
20 lbs/Kw Powerplant Specific Weight

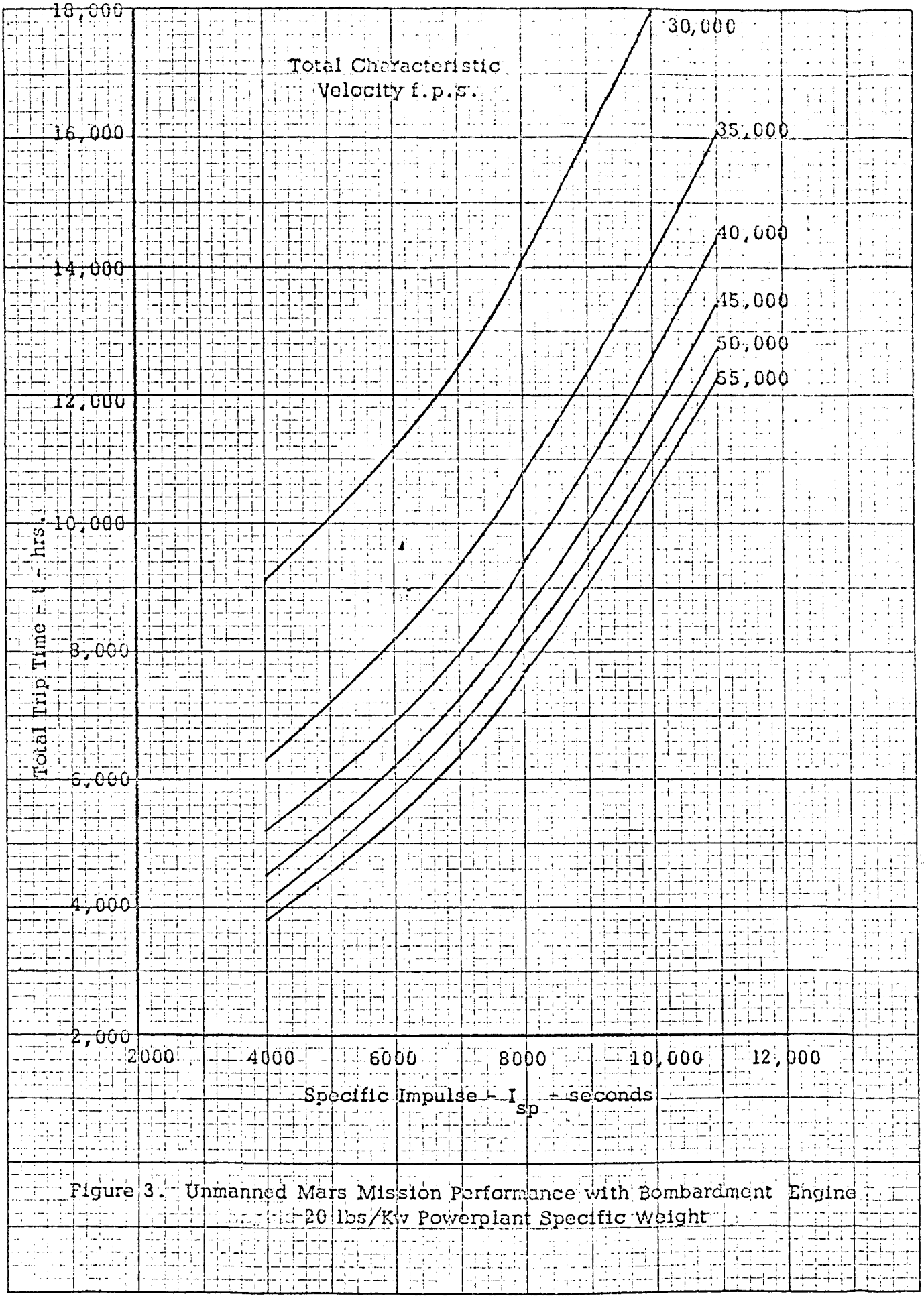


Figure 3. Unmanned Mars Mission Performance with Bombardment Engine 20 lbs/Kw Powerplant Specific Weight

specific weight and round-trip time. The LEADER process varies the independent variables until the initial gross weight in orbit is minimized for a specified return payload.

The Mission Model is based upon the following assumptions:

1. Circular Earth orbit and elliptical Mars orbit.
2. Earth, vehicle, and Mars orbits are co-planar
3. Propulsion requirements for elliptical Mars rendezvous are based upon the data of Reference 4.
4. Propulsion requirements for non-optimum central angle Mars rendezvous are based upon the data of Reference 6.
5. The elliptical effects and the non-optimum central angle effects can be directly superimposed on each other.
6. The characteristic length concept of Reference 4 can be used to convert the variable thrust data of Reference 4 and 6 to constant thrust requirements.
7. Constant thrust propulsion with optimum heliocentric coast is used.

The Manned Mars Mission results are also described in Section 5.

70X100 1/10 Inch Division
GENERAL ELECTRIC COMPANY, SCHENECTADY, N. Y., U.S.A.
PN 321 A (8/60)

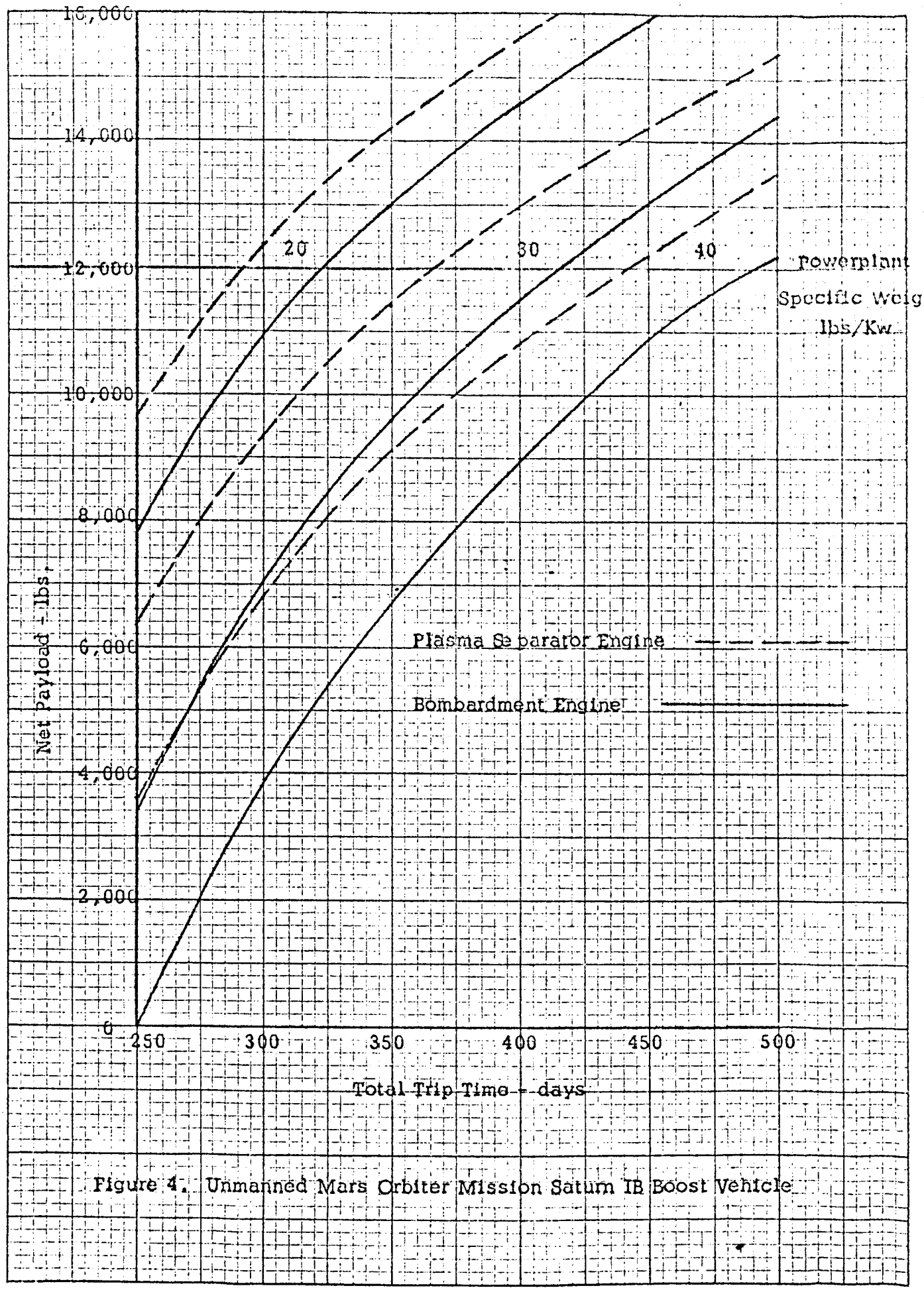


Figure 4. Unmanned Mars Orbiter Mission Saturn IB Boost Vehicle

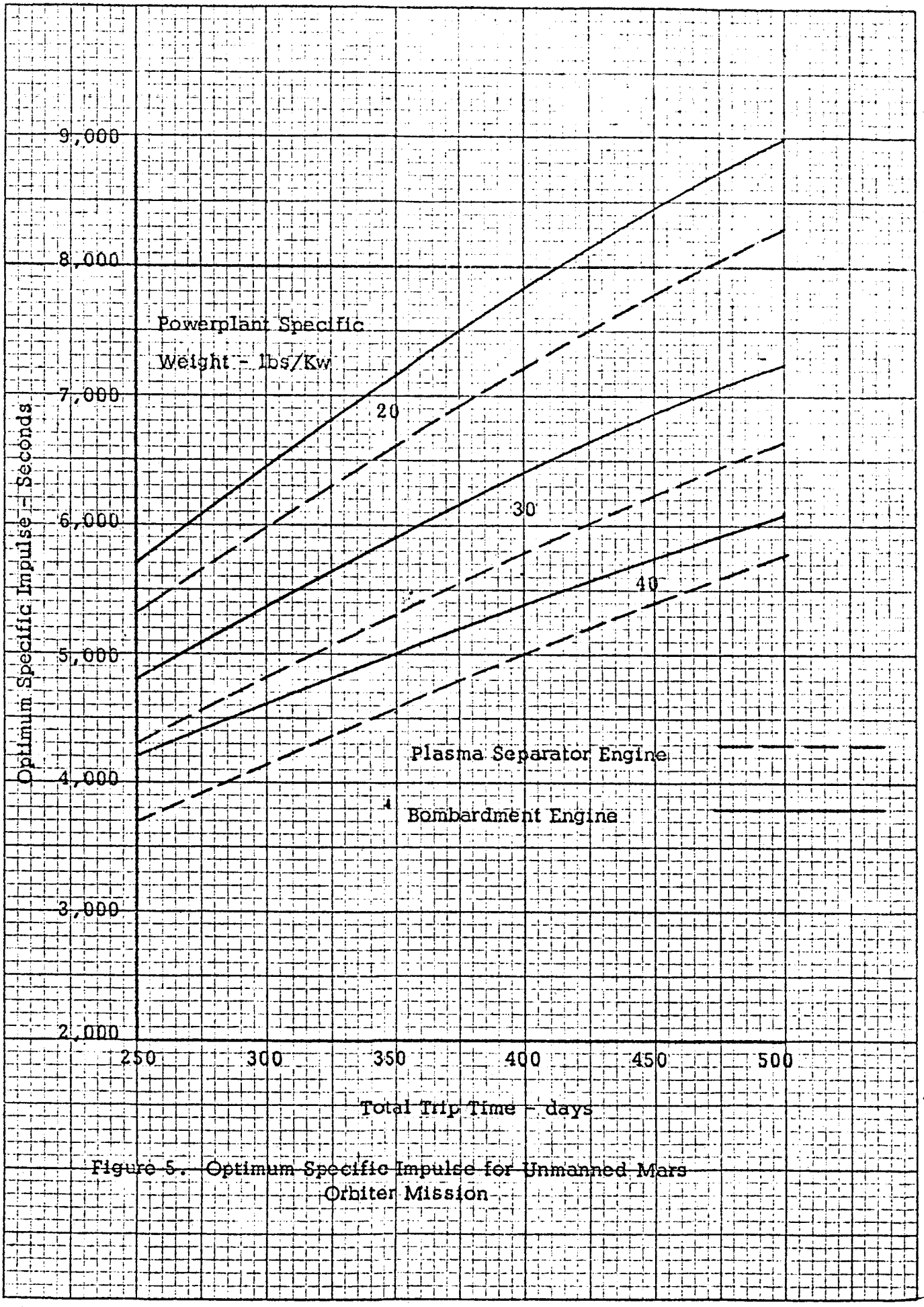


Figure 5. Optimum Specific Impulse for Unmanned Mars Orbiter Mission

5. RESULTS

The results of the unmanned Mars mission studies are summarized in Figs. 4 and 5. Fig. 4 contains the payload variation with trip time for both engines and for powerplant specific weights of 20, 30, and 40 lb/Kw. The plasma separator engine is seen to produce higher payloads than the bombardment engine at constant trip time - payload improvements of the order of 1000 to 4000 lbs are available. At constant payload, on the other hand, the plasma separator engine offers a 50 day reduction in trip time. It is most significant, however, that the improved efficiency of the plasma separator engine is equivalent to a 5 to 10 lb/Kw reduction in powerplant specific weight over the 20 to 40 lb/Kw range investigated. Fig. 5 illustrates the optimum specific impulse range associated with the data of Fig. 4. Note that it covers the range of 3600 to 9000 seconds.

The results of the unmanned Jupiter mission studies are summarized in Figs. 6 and 7. Fig. 6 contains the net payload capabilities of each engine over a trip time range of 550 to 1000 days and for powerplant specific weights of 20, 30, and 40 lb/Kw. At constant trip time, the plasma separator engine provides an improvement of 3000 to 6000 lb. in the net payload. At constant payload, on the other hand, the plasma separator permits a reduction of 30 to 70 days in the total trip time requirement. At constant trip time and constant payload, the improved plasma separator engine efficiency is seen to be equivalent to a 5 to 8 lb/Kw reduction in powerplant specific weight. The slightly lower percent improvement realized for the Jupiter mission are due primarily to the higher optimum specific impulse range required for the

mission. Fig. 7 indicates that this specific impulse range is roughly 2000 to 3000 seconds higher than the corresponding data illustrated in Fig. 5 for the Mars mission.

The Manned Mars Mission results are summarized in Table 2 for a power-plant specific weight of 30 lbs/Kw. Comparative data are shown for both the electron bombardment engine and the plasma separator engine for an optimum 600 day round-trip in the 1975 launch window. The most significant difference between the two sets of data are in the initial orbital vehicle weight requirements and in the power requirements. The 1.4 million pound initial orbital vehicle weight for the electron bombardment engine will require an orbital assembly of 6 Saturn V boosters at 235,000 lbs. per booster. The plasma separator engine, on the other hand, will require either 5 Saturn V boosters at 207,000 lbs per booster or 4 Saturn V's at 260,000 lbs per booster. The use of the plasma separator engine can, therefore, result in a savings of 1 to 2 Saturn V boosters at about 50 million dollars per booster.

As a result of the decreased spacecraft weight and of the improved plasma separator engine conversion efficiency characteristics, the power requirements for the plasma separator vehicle are only 62% of the power requirements for the electron bombardment vehicle. The actual results are 4.3 MW for the plasma separator and 6.9 MW for the electron bombardment engine. It is also significant to note that the optimum specific impulse requirements are of the order of 3000 to 3300 seconds on the outbound leg of 4300 to 4400 seconds on the inbound leg. In each case, the lower numbers are required by the bombardment engine and the upper numbers by the plasma separator engine.

TABLE 2

Manned Mars Round Trip Mission Capabilities
Powerplant Specific Weight of 30 lb/Kw

Engine	Electron Bombardment	Plasma Separator
Launch Date	7 July 1975	5 July 1975
Trip Times - days		
Outbound	197	197
Mars Descent	36	34
Exploration	40	40
Mars Escape	33	30
Inbound	294	299
Total	600	600
Weight - lbs.		
Initial Orbital Vehicle	1,410,000	1,034,000
Initial Nuclear-Electric Vehicle	853,000	638,000
Mars Excursion Module	100,000	100,000
Mission Module	100,000	100,000
Nuclear-Electric Propulsion & Tankage	446,000	309,000
Powerplant	207,000	129,000
Power Rating - MW	6.91	4.29
Specific Impulse - sec.		
Outbound Engine	2960	3275
Inbound Engine	4315	4375
Thrust - lbs.		
Outbound Engine	59	43
Inbound Engine	47	37
Propulsion Time - hours		
Outbound Engine	3770	3715
Inbound Engine	3355	2835
Nuclear Rocket Characteristic Velocity-f.p.s.	14,500	13,500
Mission Termination Date	26 Feb. 1977	24 Feb. 1977

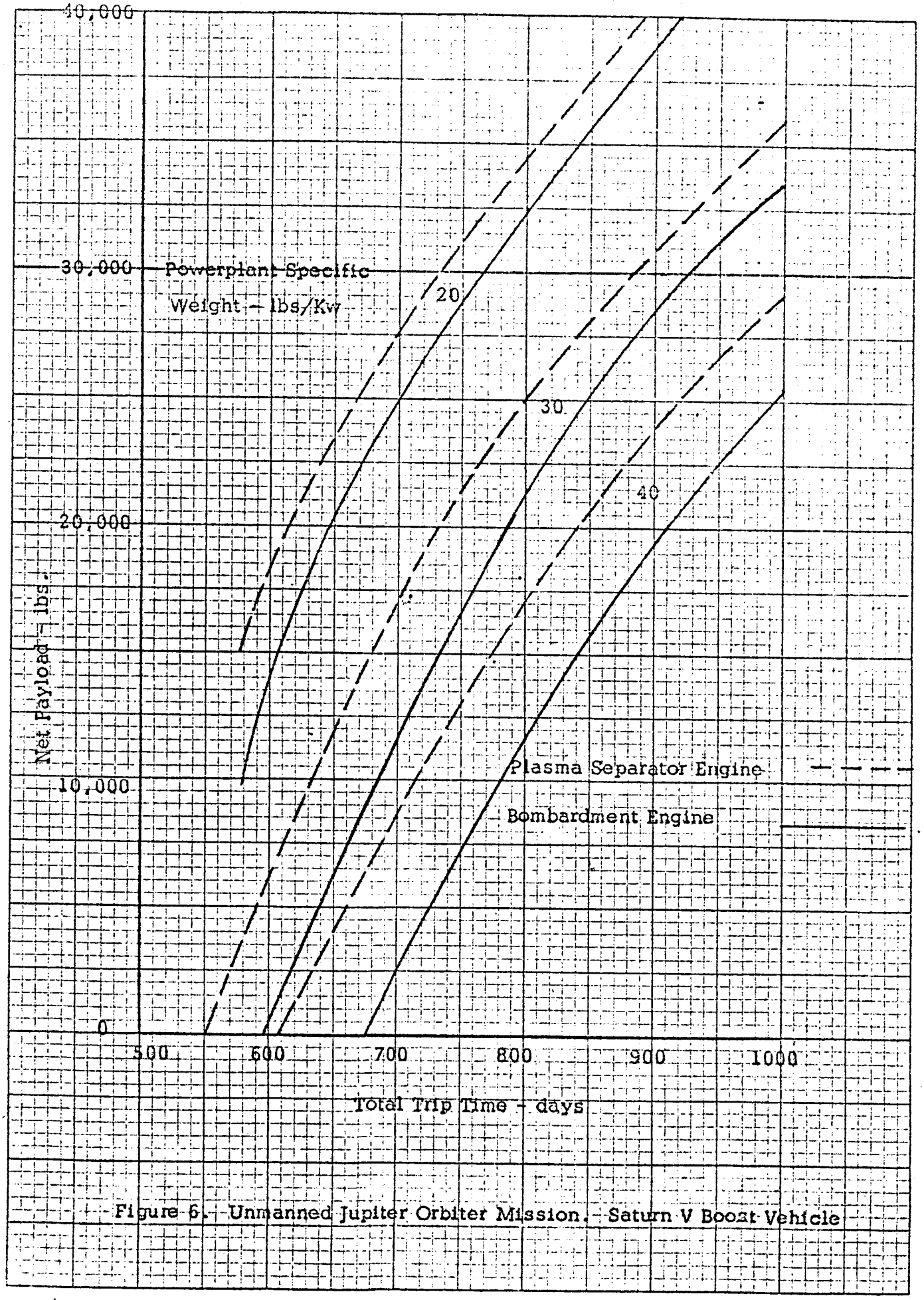


Figure 6. Unmanned Jupiter Orbiter Mission. - Saturn V Boost Vehicle

70X100 8-10 Inch Divisions
GENERAL ELECTRIC COMPANY, SCHENECTADY, N. Y., U.S.A.

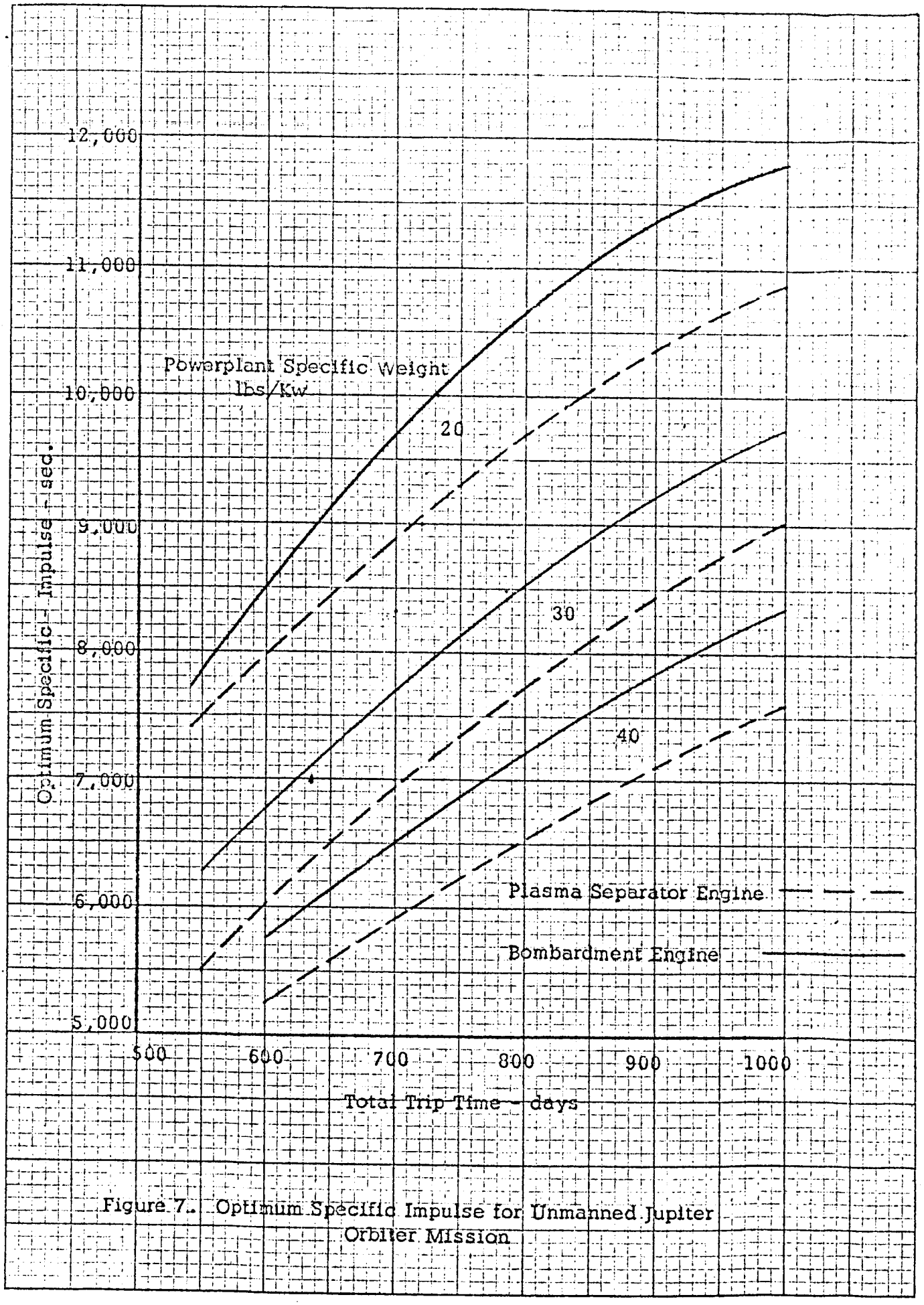


Figure 7. Optimum Specific Impulse for Unmanned Jupiter Orbiter Mission

6. CONCLUSIONS

The higher efficiency characteristics of the plasma separator engine result in substantial gains in mission performance capabilities over those of the electron bombardment engine. The following improvements were obtained for the missions investigated:

a. Manned Mars Mission - Combined Nuclear Rocket and Nuclear-Electric Propulsion

1. Reduction in initial orbital vehicle weight requirements from 1.4 million lbs to 1.0 million lbs. This reduction in orbital weight requirements reduces the number of Saturn V boosters required for the mission from 6 to 4.
2. Reduction in nuclear-electric powerplant rating from 6.9 MW to 4.3 MW at an assumed powerplant specific weight of 30 lbs/Kw.

b. Unmanned Mars and Jupiter Orbiter Missions-Nuclear-Electric Propulsion

1. The equivalent of a 25% reduction in powerplant specific weight at constant trip time and constant payload in the powerplant specific weight range of 20 to 40 lbs/Kw.

2. A comparable increase in payload at constant trip time and powerplant specific weight or decrease in trip time at constant payload and specific weight.

Harold Brown, Manager
Mission Analysis and Evaluation
Space Power and Propulsion Section
Building 700 - N-12 - Ext. 4873

REFERENCES

1. Reader, P. D. and Mickelson, W. R., "Experimental Systems Studies of Large Modules and Arrays of Electrostatic Thrustors", AIAA Preprint No. 64-503, June 1964.

2. Brown, H. and Widmer, T. F., "Research on Spacecraft and Powerplant Integration Problems - Mission Analysis Topical Report", Contract No. NAS 3-2533, General Electric Company, February, 1964.

3. Zola, C. L., "Trajectory Methods in Mission Analysis for Low-Thrust Vehicles", NASA Lewis TP 20-63, January 1964.

4. Melbourne, W. G., "Interplanetary Trajectories and Payload Capabilities of Advanced Propulsion Vehicle", JPL Technical Report No. 32-68, March, 1961.

5. Brown, H., "Spacecraft Electric Generating and Propulsion System Integration Study", Technical Documentary Report No. ASD-TDR-63-428, Contract No. AF33(657)-8488, General Electric Company, August, 1963.

6. Sauer, C. G., and Melbourne, W. G., "Optimum Earth-To-Mars Roundtrip Trajectories Utilizing a Low Thrust Power-Limited Propulsion System", JPL Technical Report No. 32-376, March 1963.

REPORT DISTRIBUTION LIST FOR
CONTRACT NAS3-3561

NASA-Lewis Research Center
Spacecraft Technology Procurement Section
21000 Brookpark Road
Cleveland, Ohio 44135
Attention: John H. DeFord — 1

NASA-Lewis Research Center
Electromagnetic Propulsion Division
21000 Brookpark Road
Cleveland, Ohio 44135
Attention: H. R. Kaufman — 1

NASA-Lewis Research Center
Electromagnetic Propulsion Division
21000 Brookpark Road
Cleveland, Ohio 44135
Attention: P. D. Reader — 1

NASA-Lewis Research Center
Electromagnetic Propulsion Division
21000 Brookpark Road
Cleveland, Ohio 44135
Attention: W. E. Moeckel — 1

NASA-Lewis Research Center
Spacecraft Technology Division
21000 Brookpark Road
Cleveland, Ohio 44135
Attention: S. Jones — 1

NASA-Lewis Research Center
Spacecraft Technology Division
21000 Brookpark Road
Cleveland, Ohio 44135
Attention: D. L. Lockwood — 1

NASA-Lewis Research Center
Spacecraft Technology Division
21000 Brookpark Road
Cleveland, Ohio 44135
Attention: J. H. Childs — 2

NASA-Lewis Research Center
Spacecraft Technology Division
21000 Brookpark Road
Cleveland, Ohio 44135
Attention: J. A. Wolters — 1

NASA-Lewis Research Center
Spacecraft Technology Division
21000 Brookpark Road
Cleveland, Ohio 44135
Attention: R. R. Nicholls 1

NASA-Lewis Research Center
Technology Utilization Office
21000 Brookpark Road
Cleveland, Ohio 44135
Attention: John Weber 1

NASA-Lewis Research Center
Technical Information Division
21000 Brookpark Road
Cleveland, Ohio 44135 1

NASA Headquarters
FOB-10B
600 Independence Avenue, S.W.
Washington, D.C. 20546
Attention: RNT/James Lazar 2

NASA Marshall Space Flight Center
Huntsville, Alabama 35812
Attention: M-RP-DIR/Dr. E. Stuhlinger 1

NASA Langley Research Center
Langley Field, Virginia
Attention: Technical Library 1

Headquarters - USAF
Air Force Office of Scientific Research
Washington, D.C. 20525
Attention: Dr. M. Slawsky 1

Commander
Aeronautical Systems Division
Wright-Patterson Air Force Base, Ohio 45433
Attention: AFAPL (APIE)/Robert Supp 1

NASA-Lewis Research Center
21000 Brookpark Road
Cleveland, Ohio 44135
Attention: Library 2

NASA-Lewis Research Center
21000 Brookpark Road
Cleveland, Ohio 44135
Attention: Reports Control Office 1

AFWL
Kirtland AFB, New Mexico
Attention: WLPC/Capt. C. F. Ellis — 1

Jet Propulsion Laboratory
Pasadena, California
Attention: J. J. Paulson — 1

Aerospace Corporation
P.O. Box 95085
Los Angeles, California 90045
Attention: Library Technical Documents Group — 1

North American Aviation, Inc.
12214 Lakewood Avenue
Downey, California
Attention: Technical Information Center
Dept. 4096-314 — 1

Colorado State University
Fort Collins, Colorado
Attention: L. Baldwin — 1

Hughes Research Laboratories
3011 Malibu Canyon Road
Malibu, California 90265
Attention: Dr. G. R. Brewer — 1

Hughes Research Laboratories
3011 Malibu Canyon Road
Malibu, California 90265
Attention: Mr. R. C. Knechtli — 1

Ion Physics Corporation
Burlington, Massachusetts
Attention: Dr. S. V. Nablo — 1

Field Emission Corporation
611 Third Street
McMinnville, Oregon
Attention: Dr. F. M. Charbonnier — 1

United Aircraft Corporation
Research Department
East Hartford, Connecticut
Attention: Dr. R. G. Meyerand, Jr. — 1

Space Technology Laboratories
8433 Fallbrook Avenue
Canoga Park, California
Attention: Dr. D. B. Langmuir — 1

Westinghouse Astronuclear Laboratories
Pittsburgh, Pennsylvania 15234
Attention: H. W. Szymanowski, Manager
Electrical Propulsion Laboratory — 1

Aerojet General
San Ramon, California
Attention: Dr. J. S. Luce — 1

Electro-Optical Systems, Inc.
125 North Vinedo Avenue
Pasadena, California
Attention: Dr. A. T. Forrestor — 1

TRW Electromechanical Division
Thompson Ramo Wooldridge Inc.
23555 Euclid Avenue
Cleveland, Ohio 44117
Attention: Mr. R. T. Craig — 1

Rocketdyne
6633 Canoga Avenue
Canoga Park, California
Attention: Mr. J. F. Hon — 1

MSA Research Corporation
Callery, Pennsylvania
Attention: Dr. R. C. Werner — 1

U.S. Atomic Energy Commission
Division of Technical Information Extension
P.O. Box 62
Oak Ridge, Tennessee 37831 — 1

NASA Scientific and Technical Information Facility
Box 5700
Bethesda, Maryland
Attention: NASA Rep. RQT 2448 — 6 + 1 Repro

Information Processing Section
Wright-Patterson AFB, Ohio
Attention: ASRCEM — 1

NASA-Lewis Research Center
Spacecraft Technology Division
21000 Brookpark Road
Cleveland, Ohio 44135
Attention: John Ferrante — 5